AN INVESTIGATION OF HALOGENATED COPPER PHTHALOCYANINE PIGMENTS USING TRANSMISSION ELECTRON MICROSCOPY

by Paul McColgan

submitted for the degree of Ph.D in the University of Glasgow.

March 1990.

ProQuest LLC.
789 East Eisenhower Parkway
P.O. Box 1346
Ann Arbor, MI 48106 – 1346

Acknowledgements

I am extremely grateful to everyone who helped in the work described in this thesis. In particular for his guidance and help, I am deeply indebted to my supervisor, Professor J. N. Chapman. Thanks also to Professor R. P. Ferrier for making available the facilities within the Solid State Physics Group in the Department of Physics and Astronomy at Glasgow University.

During my stay at ICI Grangemouth I received valuable insight into the industrial background to the project from Dr. David Vass and Mr Bert McKay as well as many others.

I would like to thank Dr W. A. P. Nicholson for designing the low temperature x-ray rod used in this project. Thanks also go to Mr J. Simms, Mr. A. Howie and Miss. M. Low for maintenance of the microscope facilities at Glasgow. I am also grateful to Mr. I. M^{c}Vicar for assistance in producing the photographic prints and to Mrs. M. Waterson for stencilling many of the diagrams. Many thanks to my room-mates George and Frank, and to David, Kevin and Stephen for many useful discussions. I would also like to thank my parents for support and encouragement.

Finally, I would like to thank SERC together with ICI for the provision of a CASE award and equipment.

DECLARATION

This thesis has been composed by myself and is a record of work carried out by me in the Department of Physics and Astronomy at the University of Glasgow. The various materials studied in this project were supplied by Dr. Vass of ICI. Some of the work described has been presented in the following papers.

The use of differential phase contrast imaging for investigating particles.

P. McColgan and J. N. Chapman, Eurem Proceeding York 1988, eds P. J. Goodhew and H. G. Dickinson, 1, 185.

Elemental analysis of halogenated copper phthalocyanine samples at low temperatures.

P. McColgan J. N. Chapman and W. A. P Nicholson SCANNING 89/EM West proceedings (Long Beach, 1989)

Low Temperature EDX microanalysis of halogenated copper phthalocyanine samples.

P. McColgan J. N. Chapman and W. A. P Nicholson submitted for publication in J. Microsc.

This thesis has not been submitted in any previous application for a degree.

CONTENTS

Summary

Halogenated copper phthalocyanines are an important class of organic materials, widely used in pigmentary form in paints, plastics, dyes and printing inks. The properties of these materials are strongly dependent on the size and chemical composition of the individual pigmentary particles. As individual pigmentary particles are typically 50nm, analytical techniques of high spatial resolution are required to investigate them. Electron microscopy is capable of providing structural and compositional information on the required scale and is thus well suited to the investigation of these materials. The industrial preparation of the pigmentary material is described in chapter 1, together with a brief introduction to the analytical techniques available in electron microscopy. The information that can be obtained using electron beam techniques is,however, limited by damage the material suffers during electron irradiation. This results in a loss of crystallinity and mass as the sample is irradiated. Care must therefore be taken when analysing radiation sensitive materials to ensure that the results obtained pertain to the as-prepared and not the damaged material. As radiation damage imposes severe limits on the investigation of organic materials by electron microscopy, chapter 2 gives a review of the major aspects of the damage processes together with particular damage studies of various phthalocyanines. In chapter 3, the theory of diffraction and imaging in the CTEM and STEM instruments used in this work is described. The results obtained from the CTEM diffraction and imaging studies of the pigment are presented in chapter 4. In chapter 5, results obtained using the Differential Phase Contrast (DPC) imaging mode in a STEM are presented. Advantages of this technique include its efficient use of electrons and the simultaneous availability of

information on specimen topography and internal structure.

Considerations relevant to energy dispersive x-ray (EDX) microanalysis are discussed in chapter 6. However, as discussed above, damage results in the breaking of chemical bonds leading in this case to the loss of peripheral halogen atoms and thus to a reduction in the halogen to copper ratio. As diffusion processes are strongly temperature dependent, cooling the sample should reduce the rate of halogen loss. To investigate this a specially designed low temperature x-ray rod was used. The experimental procedure adopted for EDX microanalysis is described in detail in chapter 7. It involved the acquisition of series of spectra at room and low temperature from the various pigmentary samples. This had two advantages. Firstly it provided accurate information on the halogen to copper ratios through extrapolation of each series to zero dose from which the undamaged composition was recovered. Additionally it allowed a comparison to be made between room and low temperature microanalysis under carefully controlled experimental conditions. This is important in assessing the improvements conferred by low temperature microanalysis. Finally in chapter 8, general conclusions are drawn on the work described in this thesis along with suggestions for possible continuation of the work.

Chapter 1

INTRODUCTION TO THE PHTHALOCYANINES AND ELECTRON MICROSCOPY

1.1 Introduction

The phthalocyanines are an important class of organic materials widely used as colouring pigments. The most important of these are based on copper phthalocyanine (Cu Pc). This possesses a blue colour, but this may be changed by the substitution of halogen atoms for the hydrogen atoms around the periphery of the molecule. The structure and bonding in phthalocyanine and its halogenated derivatives is described in section 1.2. The industrial preparation of halogenated copper phthalocyanine (X-Cu Pc) pigments, together with the associated problems, is described in section 1.3. Typically, problems involve variations in the shade and strength of the pigment between batches prepared under nominally identical preparation conditions. The shade of the pigment is sensitive to the type and quantity of halogen added; a highly chlorinated sample is a strong blue green colour. As the concentration of bromine atoms increases this passes gradually through to a yellow green shade. The strength is dependent on the size, shape and internal crystalline structure of the individual pigmentary particles. There is therefore a considerable incentive for investigating these properties on a microscopic scale to characterise the materials and determine how variations arise. As individual pigmentary particles have dimensions of typically 50nm, investigation of their structure and composition requires imaging and analytical techniques of high spatial resolution. Electron microscopy can provide information on the specimen structure and composition on the

required scale. The information obtainable and problems associated with the technique are described briefly in section 1.4. The elemental analysis technique used to obtain compositional information from the pigmentary materials is described in section 1.5. The preparation of specimens suitable for examination in the electron microscope is described in section 1.6.

1.2 The phthalocyanines

As noted in the introduction phthalocyanines are widely used as pigments. They also find application as catalysts, gas sensors and show potential for electronic and photoelectric applications. A comprehensive review of the phthalocyanines is found in (Moser & Thomas, 1983). The molecular structure of the phthalocyanines is shown in figure 1.1. The central position can be occupied by two hydrogen atoms or a single metal atom. Copper is the most frequently used but platinum, silicon, nickel and aluminum have been coordinated in this position. Five membered porphyrin rings are connected to the inner four nitrogens. The outer four nitrogens have lone pairs of electrons which can have a considerable influence on substitutional reactions, as occurs in the halogenation process. There are then four benzene type rings; the influence of these benzene rings on the stability of the phthalocyanines to electron irradiation will be discussed in chapter 2. Finally there are sixteen peripheral atomic sites in the molecule can be occupied by hydrogen atoms or halogen atoms or both, with chlorine and bromine being the most commonly substituted halogens. The ring structures, containing double or unsaturated bonds, can result in electron delocalisation throughout the rings in the form of π–orbitals. Overlap of the π–orbitals provides the bonding between planes of molecules, resulting in a strong tendency for the molecules to stack on top of each other with their delocalised ring structures

overlapping, (Drummond et. al., 1981; Kobayashi et. al., 1982). This gives rise to long needle shaped molecular columns which are then attracted to each other by weaker Van der Waals forces. In Cu Pc and its halogenated derivatives bonding between molecules shows a marked anisotropy, with stearic or shape effects having a significant role in determining the resultant crystal structure. A consequence of the weak bonding in molecular crystals is the existence of several crystal phases of comparable lattice energies, (Horn & Honigman, 1974; Fryer, 1977).

1.3 Industrial preparation of halogenated coper phthalocyanine pigments and their properties

Cu Pc as manufactured industrially is a useful blue pigment. Substitution of halogen atoms for the hydrogen atoms around the periphery of the molecule considerably increases the strength of the pigment and enables the production of a wide variety of commercially important green shades. In terms of cost, optical strength, shade and fastness properties no other class of pigment can compete in the blue/green colour area. Due to these highly desirable features there is considerable incentive for halogenating Cu Pc on an industrial scale.

The general features of the industrial process will be described but as the final pigment is a commercially important product precise details of the reaction process are omitted. There are two major stages. Firstly the raw copper phthalocyanine in the form of needle shaped crystals is halogenated to the required level giving an intermediate compound consisting of large particles in the range 0.5μm to 50μm, with mean dimension ~5μm. The strength of the pigment is intimately connected with the particle size, the optimum dimensions for individual pigmentary particles being ~50nm, (Brockes, 1964). As the intermediate material has dimensions considerably

greater than this value, its strength is correspondingly low. In an attempt to alter the particle size to a value closer to the optimum, the intermediate material is subjected to a pigmentation process. This involves reacting the intermediate material with various solvents and surfactants which leads to lattice expansion and internal disruption of the intermediate material. The result is that larger particles are split at weaker areas where defects are present. Rather fortuitously this process yields a large number of smaller pigmentary particles of roughly the optimum particle size. The final stage of the process involves washing the material in water and dilute sulphuric acid to remove any impurities which may have been introduced. As the pigment is a commercial product the properties should be highly reproducible, enabling routine application. This requires that under standard conditions the pigmentation process should give a particular size distribution and result in the desired shade. Unfortunately the industrial preparation does not always meet these requirements with variations in both the strength and shade of the final pigment arising under nominally identical preparation conditions. There is therefore considerable incentive for investigating the factors which determine the size, shape and composition of the pigmentary particles to explain how the observed variations can arise.

1.4 Introduction to electron microscopy

In the introduction it was emphasised that information of the highest possible spatial resolution was required to investigate the internal structure of individual pigmentary particles. The aims of this section is firstly, to give a brief introduction to diffraction and imaging techniques available in electron microscopy that can provide information of the required resolution and secondly to discuss the problem of radiation damage, which is the major

obstacle in obtaining structural and compositional information on organic materials.

The electron microscope can be used to form electron diffraction patterns, containing high resolution structural information. This is possible due to the flexible nature of the imaging system. By altering the strength of the intermediate lens, the diffraction pattern which is formed close to the back focal plane can be transferred to the final viewing screen. Recording electron diffraction patterns offers significant advantages for structural investigations of radiation sensitive materials. The diffraction pattern for crystalline specimens takes the form of a discrete array of spots. By contrast, in an image the same electron flux is spread out over the entire area. For this reason a diffraction pattern containing high resolution detail <0.1 nm can be recorded using a fraction of the dose required to record a high resolution image. Diffraction patterns can be recorded from areas typically ($\sim 1 \mu m^2$) using a dose of $\sim 10^{-3}$ Ccm^{-2}. The information obtainable from electron diffraction patterns is discussed in chapter 3. The results obtained from the various materials investigated are presented in chapter 4.

Lattice imaging can also be used to provide information on the crystalline structure of the pigmentary particles; additionally imaging techniques allow the relation between the internal structure and the external habit to be investigated. The theory relating to lattice imaging in the conventional transmission electron microscope (CTEM) and the scanning transmission electron microscope (STEM) is described in chapter 3. The major disadvantage of STEM lattice imaging is it represents an inefficient use of electrons. More specifically the dose to which the specimen must be subjected to achieve comparable images is substantially greater than in the CTEM, making it ill-suited to the investigation of radiation sensitive materials. A new technique based on the differential phase contrast (DPC) mode of

microscopy, is described in chapter 5. The advantages of this technique include its efficient use of electrons and the simultaneous availability of information on specimen topography and structure. Lattice images obtained using the CTEM are presented in chapter 4 and images obtained using the DPC mode are presented in chapter 5. A comparison of the various imaging modes available in the CTEM and STEM is discussed in chapter 5.

In passing, it should be noted that the scanning tunnelling microscope (STM) has been used recently to obtain images of isolated Cu Pc molecules on a copper [100] substrate Lippel et. al. (1989). Some problems exist with this technique, including a build up of molecules on the tip and movement of molecules due to the tip. However with rapid advances in this technique expected, it will be a powerful technique for imaging isolated molecules.

Severe difficulties are encountered when trying to obtain high resolution information from organic materials by electron microscopy. This is due to the process of radiation damage. When the electron beam is incident on a thin specimen there are several interactions which can occur. The beam can pass through the specimen unaffected or undergo one of two types of scattering processes, either elastic or inelastic scattering. In the former process, which carries most of the high resolution information, the electrons interact directly with the field of the atomic nuclei transferring little energy to the atoms. In inelastic scattering however, the incident electrons interact with orbital electrons. Due to their identical masses, this can lead to the transfer of large amounts of energy. The resulting molecular excitations and ionisation causes structural and chemical disorder in the sample. Investigation of radiation damage by a number of investigators has indicated that its effect may in some cases be reduced, but seldom eliminated. This is discussed more fully in chapter 2. Radiation damage effects must therefore be taken into account to ensure that the conclusions reached pertain to the undamaged and not the damaged structure.

A measure of the sensitivity of a material to electron irradiation is given by its characteristic dose. To obtain information on the undamaged material it is neccesary to use a dose less than that which causes unacceptable damage to the specimen. A bright field lattice image with resolution of 1nm and a signal to noise ratio of 5 requires a dose of ~1Ccm^{-2}, (Cosslett, 1978). This is significantly higher than the critical dose for a wide variety of specimens, thus precluding direct imaging of their structure by electron microscopy. The exceptional stability of fully halogenated Cu Pc's, as witnessed by their ability to withstand doses >25Ccm^{-2} indicates that for these samples it is not only possible to record a bright field lattice image, but a large number of such images before the crystal is completely damaged. Thus it is possible to monitor the radiation damage process directly with phase contrast microscopy. Due to their exceptional radiation resistance, X-Cu Pc's have been extensively investigated. Molecular images have been obtained by Uyeda et. al. (1978) and Smith et. al. (1986) in which atomic detail is convincing. Lattice images of the pigmentary material have been obtained by Fryer (1980), and have shown comparable lattice spacings to the epitaxial material and a wide variety of defects.

1.5 Elemental analysis in the electron microscope

It has been stressed in this chapter that the properties of the pigment are strongly dependent on the chemical composition. In particular the shade is determined by the halogen content. It is therefore important to use analytical techniques which enable the acquisition of information on specimen composition with the greatest possible accuracy. A suitable analytical technique for determining specimen composition is energy dispersive x-ray (EDX) microanalysis. This technique is based on detecting and quantifying

the characteristic x-rays produced by the interaction of the electron beam with the atoms in the irradiated volume of specimen. However, interaction of the electron beam with the sample results in the breaking of chemical bonds, leading to loss of peripheral halogen atoms as a result of diffusion. Thus there is a reduction in the halogen to copper ratio as irradiation proceeds. To obtain accurate analyses from small volumes of sample, as is neccesary if there is a possibility that there are compositional variations on a microscopic scale, the rate of halogen loss must be reduced. Elemental loss can be reduced by simply restricting the electron dose to which the specimen is subjected. However this results in statistically insignificant counts in the x-ray peaks. The relationship between the statistical accuracy of an analysis, electron dose and the volume of material analysed is addressed in chapter 7. The loss of peripheral halogen during electron irradiation is controlled largely by diffusion of the liberated species following bond breakage. As diffusion is strongly temperature dependent, lowering the temperature should reduce the rate of halogen loss and enable a more meaningful analysis to be undertaken. This option is considered in detail in chapter 6. The various pigmentary samples under investigation were cooled using a specially designed low temperature x-ray rod. Results presented in chapter 7 show that a considerable improvement in the confinement of the halogen atoms could be obtained by cooling the sample to liquid nitrogen temperatures, with a corresponding increase in analytical accuracy.

1.6 Specimen preparation

The majority of studies of X-Cu Pc's have involved epitaxially prepared specimens. This technique involves evaporating the material from a molybdenum boat under high vacuum onto a freshly cleaved KCl substrate.

The regular arrangement of the potassium and chlorine ions sets up an ionic field which interacts with the π-electron rings of the molecule constraining it to lie in a well defined position. As the substrate is at a temperature of ~300°C, the molecules are relatively mobile and have a strong tendency to form an ordered base layer. Subsequent layers build up a perfect crystal extensive in the a-b plane or molecular plane, and thin in the c-direction, corresponding to the column axis.

In order to examine the structure of the pigment by electron microscopy it is neccesary to use a preparation technique which does not change it in any manner. Fortunately X-Cu Pc's are insoluble in almost all solvents, apart from concentrated sulphuric acid. The pigmentary material may therefore be dispersed in a liquid without affecting its structure. In this work a 35% ethanol/water mixture was found suitable. The experimental apparatus used in preparation of electron microscope samples is shown in figure 1.2. Specimens were prepared using the following procedure. The pigment in the form of a dry powder was mixed with several drops of dispersol T, a sodium based dispersing agent supplied by I.C.I. This mixture was then rubbed out several hundred times with a flexible palette knife, several drops of a 35% ethanol/water mixture being added periodically to prevent the paste from drying out. The mixture was then further diluted with the ethanol/water mixture until a bright green transparent dispersion was obtained. The pigmentary dispersion was placed in a glass tube and the system sealed with a rubber cork. Spray tubes were prepared by extruding fine bore glass tubes. Nitrogen gas was fed from a standard gas cylinder creating a region of low pressure above the capillary tube, causing liquid to be drawn up the tube and a spray formed. The emergent spray was directed over an electrical hot-plate. This removed the ethanol/water mixture and the dry dispersed powder impinged on the suitably prepared grids. The particle density was assessed by masking the area surrounding the grids with filter paper. A suitable density

was obtained when the filter paper achieved a light green shade. Two types of grid were used in specimen preparation. For imaging, holey carbon covered 400 mesh copper grids were used. These are useful at low magnification for focussing and correcting astigmatism. At higher magnification the phase contrast of the carbon film itself provided a more accurate test. For EDX studies 75 mesh titanium grids were used. A difficulty with using carbon coated 75-mesh titanium grids, was that the carbon film broke under the force of the spray. The grids were therefore covered by a thin carbon coated formvar film.

The final stage in the preparation of specimens involved evaporating a further thin layer of carbon over the pigmentary material thus encapsulating the specimen. This prevented charging and has been shown to reduce the effects of radiation damage by confining gaseous species which would otherwise be lost from the specimen surface (Fryer & Holland, 1984).

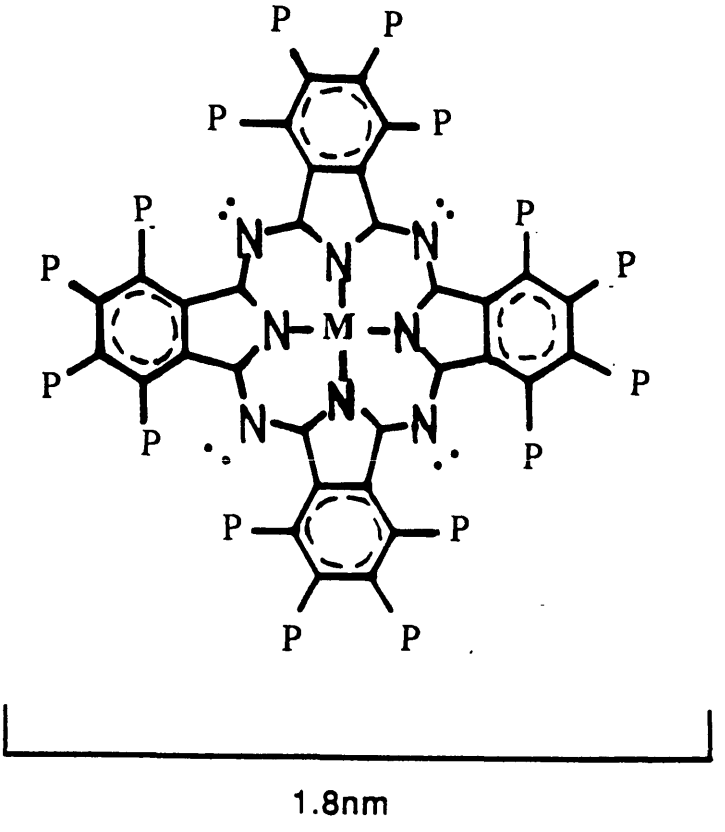

Figure 1.1: Molecular structure of phthalocyanines

M denotes a metal or two hydrogen atoms,
P denotes a peripheral atomic site which can be occupied either by hydrogen or halogen atoms.
: denotes a lone pair of electrons.

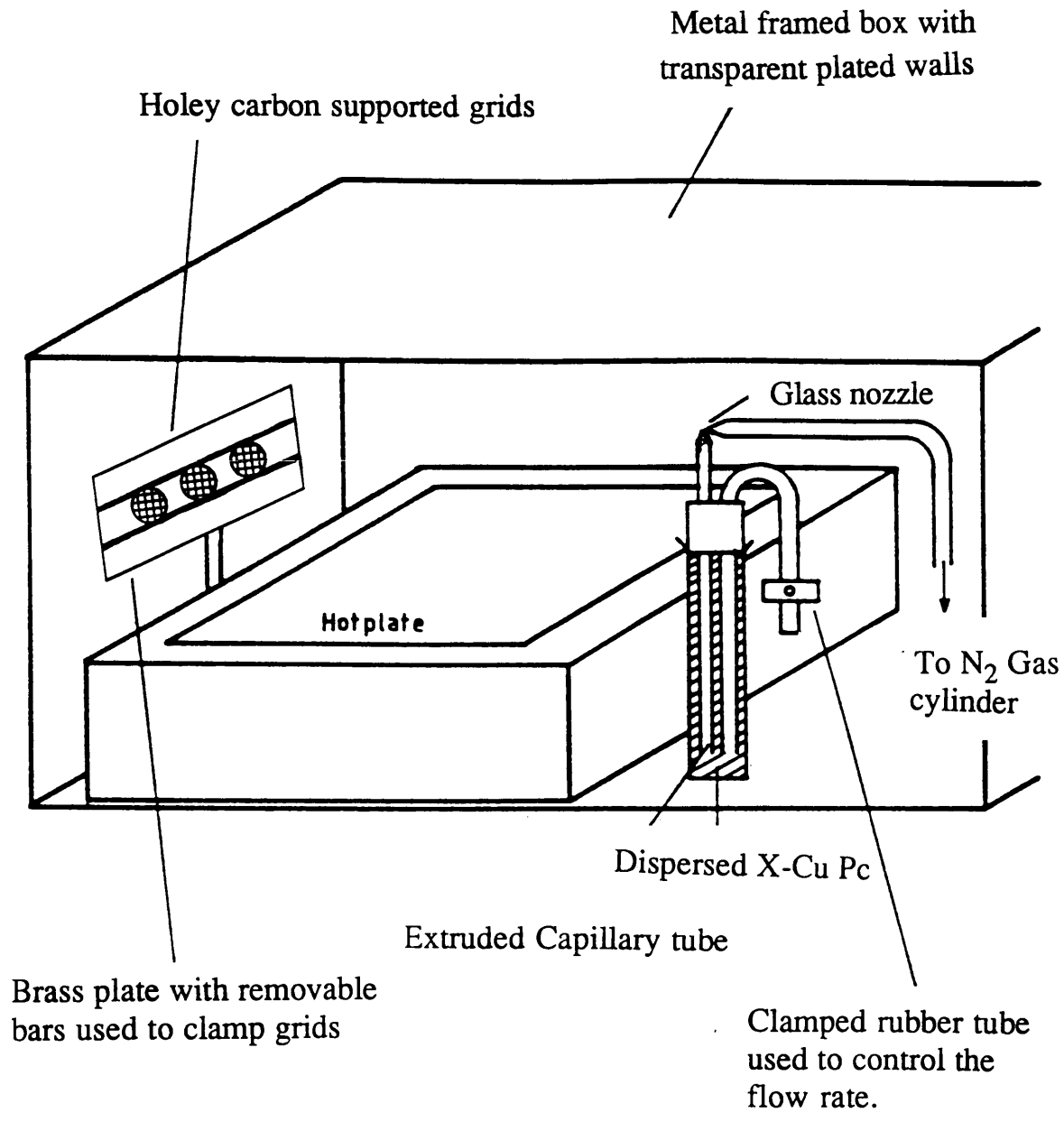

Figure 1.2: Apparatus used to prepare X-Cu Pc specimens.
Entire system is enclosed within a fume cupboard.

Chapter 2

RADIATION DAMAGE IN ORGANIC SPECIMENS

2.1 Introduction

There are two general types of interaction that an electron can experience when traversing a thin specimen. The first is elastic scattering. In this process the incident electron interacts with the atomic nuclei and can provide structural information on the specimen without inducing damage. The other is inelastic scattering, in which case the incident electron interacts (primarily but not exclusively) with the orbital electrons in the structure. Due to their identical masses, the energy transfer can be large, resulting in molecular excitation and ionisation. These scattering processes are described in section 2.2.

A consequence of the aforementioned energy transfer is that many specimens, particularly organic samples, damage upon irradiation by the electron beam. This damage results in a loss of crystallinity and mass which become more pronounced as irradiation proceeds. Radiation damage therefore imposes severe difficulties in the investigation of organic specimens by electron microscopy. In an attempt to understand and characterise the damage processes, investigations using a variety of experimental techniques have been undertaken. The aim of these investigations was to provide information on the basic damage mechanism and to monitor its effect as irradiation proceeds. They are discussed briefly in section 2.3. In section 2.4, the consequences of damage, including a discussion of the limits imposed on elemental analysis and imaging techniques using a restricted electron dose are addressed. As

radiation damage imposes severe constraints on the investigation of organic materials, techniques which reduce the effect experienced by the specimen are of considerable interest. This enables a greater incident electron dose to be used, with a corresponding increase in analytical sensitivity. It is discussed in section 2.5. To enable the results presented in chapters 4-7 of this thesis to be explained it is instructive to examine various studies of radiation damage in Cu Pc and its halogenated derivatives; these are described in section 2.6. They are helpful in allowing a comparison and correlation of results obtained in this work with those from other techniques and investigations.

2.2 Elastic and Inelastic scattering processes

Extensive articles (Reimer 1984, Colliex & Mory 1984, Egerton 1986) have been written on elastic and inelastic scattering processes. The aim of this section therefore is to give a short description of the salient features of these processes. The energy transfer ΔE in elastic scattering is given by Cosslett(1970),

$$\Delta E = \frac{2E(E + 2m_0c^2)}{Mc^2} \sin^2 \frac{\theta}{2} \qquad (2.1)$$

where E_0 is the incident electron energy m_0c^2 and Mc^2 are the rest masses of the electron and atom respectively and θ is the angle through which the electron is scattered. It can be seen from equation 2.1, that the energy loss is negligible for small scattering angles. However, for higher electron energies and larger scattering angles ΔE can be greater than the displacement energy E_D required to remove an atom from its site. To transfer sufficient energy there is a corresponding threshold value for the incident electron energy. Using a bond energy of 5eV for carbon, Cosslett (1970) calculated the threshold energy for displacement of a carbon atom to be ~27keV. The cross-section for this knock-on process is, however, orders of magnitude smaller than the elastic (σ_{el}) or inelastic cross-section (σ_{inel}) and so is of lesser importance. However it should be noted that light element loss has been reported from metal-oxides, carbides and nitrides using the high current densities achievable with a field emission source, (Crozier et. al. 1984; Thomas et. al. 1984). In inelastic scattering, interaction of the incident electron beam with the orbital electrons can give rise to considerable energy losses. The rate of energy loss of an electron traversing a thin specimen can be expressed using the relativistic form of the Bethe formula (Glaeser, 1975),this is given by

$$\frac{dE}{dX} = 0.1535\frac{\rho}{\beta^2}\frac{Z}{A}\log\left[\frac{T^2(T+2)E_o^2}{2I^2} + (1-\beta^2) + \frac{(T^2/8 - (2T+1)\log 2)}{(T+1)^2}\right] \qquad (2.2)$$

where ρ is the density of the specimen, β is equal to v/c, where v and c are the velocities of the electron and light respectively, Z is the atomic number, A is the atomic mass and T is the electron kinetic energy divided by the electron rest mass and I is the mean ionisation energy. A good approximation is to use

$$\frac{dE}{dX} \propto \beta^{-2} \qquad (2.3)$$

A consequence of this energy transfer to the specimen is that it can result in molecular excitation and ionisation giving rise to bond breakage. The latter process leads to the formation of radicals and the diffusion of liberated species resulting in considerable structural and chemical disruption to the specimen.

The proportion of inelastic to elastic collisions relates the damage to information content Egerton (1976) has obtained experimentally the relationship

$$\frac{\sigma_{inel}}{\sigma_{el}} \approx \frac{26\sum_j Z_j^{1/3} N_j}{\sum_j Z_j^{4/3} N_j} \qquad (2.4)$$

where N_j is the number of atoms of type j and atomic number Z_j. In low

atomic number elements the total inelastic cross-section is greater than the elastic cross-section, for example $\sigma_{inel}/\sigma_{el}$~3 for carbon at 100keV. A consequence of the high probability of inelastic scattering is that primary damage processes are virtually unavoidable under normal imaging conditions.

2.3 Experimental studies of radiation damage in organic materials

Methods of investigating radiation damage can be divided into two categories. The first set of measurements performed in-situ in the electron microscope involve monitoring the variation of the characteristic signals (diffraction spot intensities, lattice fringes and EDX spectra) with electron irradiation. This provides information relating the observed damage to the incident dose, but provides little information on the basic damage mechanism. In contrast the second set of measurements are capable of providing information at a much earlier stage of the damage process. These techniques include electron energy loss spectroscopy (EELS), infra-red absorption (IRA) and electron spin resonance (ESR). In both sets of measurements the behaviour is characterised in terms of the variation of the detected signal with electron dose. The dose value most frequently used to quantify the damage is $D_{1/e}$ which corresponds to a reduction in the signal intensity to 1/e of its initial value. Values of this parameter for a variety of organic materials are presented in Table 2.1.

In the first group of measurements, electron diffraction is a convenient and sensitive indicator of structural damage in crystalline samples. Fading of the diffraction spots occurs as a consequence of either molecules suffering internal disruption or their orientation with respect to one another being altered, the determining parameter being whether inter or

intra-molecular bonds are most readily broken. Measuring the values for disappearance of the high and low order diffraction spots provides information on the dose sustainable by the specimen before severe structural disorder occurs, (Kobayashi & Sakaoku, 1965; Reimer & Spruth, 1978; Clark et. al. 1980).

Chemical disorder, as indicated by loss of volatile components, can be observed by changes in the electron transparency of the specimen during electron irradiation. This can be related to mass loss via Beer's Law, as discussed by Bahr et. al. (1965) and Ramamurti et. al. (1975). Monitoring the decrease in the bremsstrahlung component in the EDX spectrum also reveals mass loss. Using this method Hall & Gupta (1974), showed that up to 40% of the mass of organic specimens could be lost within a few seconds of electron irradiation.

The second set of measurements are capable of providing information at an earlier stage of the damage mechanism. In EELS, the energy distribution of the transmitted electrons provides information on specimen composition and structure. Fine structure is observed at low energies (1-10eV) and superimposed on absorption edges corresponding to inner electron shells. This provides information on the bonding in the specimen (Isaacson et. al., 1973). The signals here usually decay more slowly than do the spots in electron diffraction patterns indicating that bonds between molecules are in general broken more readily than those within a molecule. EELS has also been used to monitor the loss of elements from samples during electron irradiation; this is discussed in section 2.5. Infrared absorption can be used to detect structure changes within single molecules, and provides information on the rotation and vibration band structure. Disappearance of absorption maxima at relatively low doses indicates that cross-linking and scission of bonds

occur, (Reimer, 1965, Bahr et. al., 1965). The I-R studies of Baumeister et. al. (1976), showed that certain bonds in molecules were more prone to attack. Carbon-carbon bonds were found to be stable whereas carbon bonded to hydrogen or hydroxyl groups were found to be more susceptible to rupture. Compounds with benzene rings were exceptionally stable under electron irradiation. The resonating electron configuration enables the energy losses to be spread over the whole benzene ring instead of acting locally, thus decreasing the probability of bond rupture.

A second technique which has provided valuable information on the basic damage mechanism is electron spin resonance (ESR). By examining the ESR spectrum the paramagnetic species which are produced after primary ionisation can be identified Box (1961). Radical formation and subsequent migration have been shown to be important secondary processes in the overall damage scheme. Results from Box (1975) showed that ionizing radiation had a considerably less detrimental effect on the molecular architecture of the sample when cooled to liquid helium temperatures. The implications from these studies were that results obtained at very low temperatures were truly representative of the native structure and that partially damaged molecules in sufficiently low concentrations can be stabilized within the structure at low temperature, though bond reformation resulting in no net damage is clearly not efficient in all cases. Results from these investigations provided much of the impetus for the cryotechniques developed in electron microscopy as discussed in greater detail in section 2.5.

2.4 Consequences of radiation damage

As discussed previously, a problem arises when investigating radiation

sensitive specimens as the detected signal varies as the specimen is irradiated. If reliable information on specimen structure or composition is to be obtained, it is neccesary to restrict the electron dose to a value less than a certain 'critical value', which is determined by the amount of damage that can be tolerated without affecting the results to the accuracy required. The signal acquired, whether it is an image or a spectrum, is the result of recording a number of discrete quanta such as electrons or photons whose number is directly dependent on the incident dose. A consequence of this is that there is a fundamental limit to the accuracy obtainable. This is due to the finite number of counts contributing to the signal. The accuracy is determined by Poisson Statistics; for a given number of counts N, there is an associated error $N^{1/2}$, leading to a fractional error which is given by $N^{-1/2}$. Therefore for a given volume of specimen and a maximum permissible dose D, a limit is placed on the number of counts N and consequently on the accuracy with which the signal can be measured. The aim of this section is to examine the constraints imposed by radiation damage on the detected signal; for the main analytical techniques employed in this project, these were EDX and imaging.

The relationship between the detected signal S and the electron dose D (electrons/ unit area) is given by,

$$S = \sigma D n v f \qquad (2.5)$$

where σ is the cross-section for the generation of S, n is the number density of molecules giving rise to S, v is the volume of material analysed, and f is the efficiency with which S is detected. Analysis of equation 2.5, indicates that in order to obtain a signal S of the desired statistical accuracy using a given electron dose D, a limit is placed on the minimum

volume of material analysed. This aspect is discussed in detail in chapter 6 for EDX.

In the case of imaging, the relationship between the size of object detectable and the dose required has been discussed by Glaeser (1971), and is given by,

$$D_{min} = \frac{e\chi^2}{f d^2 C^2} \qquad (2.6)$$

where e is the electron charge, C the object contrast, d the minimum object size, f the utilization factor, D_{min} the minimum electron dose required and χ the signal to noise ratio, typically 5 (Rose, 1948).

A consequence of the dose constraints discussed above is that to obtain information pertaining to the undamaged material the smallest possible electron dose should be used. This requires that exposure outwith image acquisition should be minimised at all costs. Minimal dose systems (MDS) were developed to implement these requirements. Using this technique the specimen is initially scanned at low magnification with a low illumination level. Upon finding a suitable area of specimen, the position is recorded, and then moved outwith the field of view. Focusing and astigmatism corrections are then performed on a nearby area of specimen and the exposure level selected. The shutter is then opened and the beam is automatically deflected onto the previously defined area of specimen with the preset exposure level and defocus. This technique was used by Williams & Fisher (1970), who observed the helical structure of the tobacco mosaic virus (TMV) for the first time in their images of negatively stained particles. An improved version of this technique has been used by Fujiyoshi et. al. (1980) to obtain high resolution molecular

images of zinc phthalocyanine and silver-tetracyanoquinodimethane (Ag-TNCQ) using total doses of ~1Ccm^{-2} and 0.3Ccm^{-2} respectively. Due to the success of this technique, MDS packages are now fitted as standard on most modern microscopes. Results obtained using this technique are described in chapter 4. It is self evident that if one wishes to record high resolution images one must work with an electron dose less than that which destroys the sought after high resolution information. However, in many cases this entails using a very low electron exposure, resulting in a statistically ill defined image. In cases of periodic structures, such as crystalline arrays of n-repeating units, averaging over a large number of identical sub units allows the extraction of high resolution information (Unwin & Henderson, 1975; Kirkland & Siegal, 1980). Examination of equation 2.1, shows that the dose required can be reduced by a factor of 1/N where N is the number of repeating units. This technique can also be applied, with care, to non-periodic specimens using cross-correlation methods (Kessel et. al., 1980).

As the image is to be recorded it is useful to examine the methods by which this can be achieved. The commonest approach involves using photographic emulsions. The response of several commercial photographic emulsions has been investigated by Chiu & Glaeser (1980) and Downing & Grano (1982). The results indicated a wide variation in the resolution, speed and fog level attainable using different emulsions. X-ray emulsions were shown to have excellent characteristics, magnifications of 150,000 times being adequate for 3Å resolution despite the coarse grain size of the film. Additionally their high speed and low fog level makes them ideal for low dose imaging (<1Ccm^{-2}). The investigations of Chiu & Glaeser (1980), showed that for very low dose imaging <10^{-3} Ccm^{-2}, 25μm thick nuclear track emulsion (NBT3) is significantly better at transferring high spatial frequency information

than any other commercially available emulsion.

A recent alternative to photographic emulsions involves digital pick-up systems using TV image tubes (Smith et. al., 1985) or solid state image devices such as charge coupled device (CCD) arrays, (Roberts et. al., 1982; Chapman et. al., 1989). The advantage of these systems is that they allow focussing and astigmatism correction to be achieved at very low illumination levels. Recent advances in processing techniques also allow automatic correction of astigmatism (Kostel et. al., 1988). Additionally dynamical events can be recorded in real time and stored on video tape or fed direct to a computer, for real time image processing or subsequent analysis. Extensive reviews of these systems are given by, Herrmann (1984) and Herrmann & Krahl (1986).

2.5 Methods of reducing the effects of radiation damage on organic materials

In order to achieve greater accuracy using any of the analytical techniques described, it becomes neccesary to use a greater incident electron dose. This, however, can only be achieved if methods are available which prolong the useful lifetime of the specimen. The aim of this section is to discuss methods which reduce the effects of damage experienced by the specimen.

Radiation damage has been previously discussed as a two stage process. The primary damage results in ionisation or excitation of the molecule; in some materials this results in bond breakage leading to secondary damage processes such as diffusion which then lead to considerable degradation of the structure. The observed damage can therefore be reduced by lowering the probability or the effects of either of these processes.

To reduce the primary damage, higher accelerating voltages have been advocated, the rationale for this being that higher energy electrons interact more weakly with the specimen and thereby deposit less energy upon traversing the specimen, as shown by the β^{-2} dependence in equation 2.3. For a change in accelerating voltage of 100kV to 1MV the predicted decrease in primary damage is ~2.3 (Glaseser, 1971). Experimental evidence for this dependence has been obtained by Grubb & Groves (1971), Howitt et. al. (1976) and Martinez et. al. (1982). However the reduction in inelastic scattering is largely offset by a corresponding decrease in elastic scattering amplitude.

As the final damage rate is strongly dependent on the rate of secondary processes, slowing down these secondary processes should reduce the effects of damage. Changes in the structure and composition of the specimen are thought to be dependent on the diffusion of highly reactive radicals following bond breakage. As diffusion processes are strongly temperature dependent, lowering the specimen temperature offers the possibility of reducing the effects of damage. Improved stabilities of organic specimens at lower temperatures have been reported by a number of investigators. Using electron diffraction as the monitoring technique, Grubb & Groves (1971) observed a three-fold gain in the sustainable dose of polyethylene upon cooling to 18K. Salih & Cosslett (1974) investigated the damage response of several organic specimens using electron diffraction. They found that the dose required to cause equivalent damage at room temperature was ~3-4 times lower at liquid helium temperatures. Siegal (1972), using a liquid helium cooled cryostat in which the specimen was well insulated from any external heat sources, showed that the dose required for complete fading of the electron diffraction pattern of tetracene and paraffin was increased by a factor of 3-4, upon cooling to

liquid helium temperatures. Additionally he showed that the crystals on warming from 4K released hydrogen and disintegrated. The implication from these results was that cooling to 4K virtually immobilised displaced atoms, and stabilised radical or ionised species. However upon returning the samples to room temperature the observed damage is the same as that obtained if the sample had been irradiated with the same electron dose at room temperature. This implied that primary damage process were not influenced by specimen cooling.

In the previous studies described the improvement in the sustainable dose observed upon cooling to liquid helium temperature amounts to less than an order of magnitude. Improvements by factors as large as a 100 or more were reported for some biological specimens at 4.2 K (Knapek and Dubochet., 1980), but these results were not confirmed in subsequent work (Lepault et. al., 1983) and a multilaboratory collaboration has been unable to find any clear indication that the critical dose at 4.2 K is measurably improved over that at 150 K (International Experimental Study Group., 1986)

Egerton (1979), (1980) has shown that the reduction of temperature has a considerably greater influence on the loss of low molecular weight gaseous elements than it does on structural stability. For example, for collodion there was a ~80 and 120 fold decrease in O_2 and N_2 loss from the specimen at 77K compared to room temperature, whilst structural studies would indicate an improvement in stability of ~3. The difference between the two sets of measurements can be explained in terms of the relative importance of diffusion in each case. Confining the released radicals in the analysed volume minimises the elemental loss; this, however, can still result in gross structural changes to the specimen, as witnessed in the diffraction pattern. The improvement between room and low temperature analysis for a number of investigations, using a variety

of experimental techniques, are presented in Table 2.2.

Another technique advocated to reduce the effects of damage involves encapsulating the specimen between thin conducting films. Salih & Cosslett (1974) showed that the sustainable dose of coronene and anathracene was increased by typically a factor of 3-5, when the samples were coated in carbon or gold films. Fryer & Holland (1984) investigated the use of carbon films to encapsulate the specimens. They found that carbon encapsulation decreased the radiation sensitivity for a wide range of organic specimens by typically a factor of 3. The improved stability was a consequence of confining gaseous species which would otherwise be lost from the specimen surface. This has been further investigated by Egerton & Crozier (1987) using both electron diffraction and (EELS). The advantages of EELS is that the rate of loss of volatile species can be measured directly. Results from the investigations confirmed that the rate of loss of molecular fragments was reduced by encapsulating the specimen.

The results presented in this section have shown that the effects of radiation damage can be reduced using one, or a combination, of the schemes outlined above. This has several advantages, firstly it enables information to be obtained pertaining to the undamaged and not the damaged material and, additionally, it reduces the severe constraints imposed by radiation damage, enabling a greater incident dose to be used with a corresponding increase in analytical sensitivity.

2.6 Studies of radiation damage in various phthalocyanines

The exceptional stability of Cu Pc and its halogenated derivatives as shown in Table 2.1, has led to extensive investigation of the structure and

response of these materials using a variety of experimental techniques. Reimer (1960), using the radiation induced changes in the ultraviolet absorption spectrum and in the electron diffraction pattern, measured the characteristic dose of Cu Pc to be ~1-2Ccm^{-2}. Isaacson et. al. (1973) investigated the response of the diffraction pattern and energy loss spectrum. Plotting the intensity of the energy loss and diffraction peaks on a logarithmic scale, they showed that both the 5eV energy loss and 5.7Å diffraction peak decreased exponentially with dose. This was consistent with a 'single hit', model in which damage is produced by a single energy loss event, rather than a succession of events. The response of the 12.5Å, diffraction peak did not decrease exponentially. After an initial decrease it became relatively stable with increasing electron dose. This was explained by postulating the stabilization of copper atoms in a matrix of damaged organic material. Clark et. al. (1979), investigated the detailed response of various diffracted beams, these were compared to a theoretically calculated model of the fading of theelectrondiffraction pattern based on the 'single hit' model previously described. Excellent agreement between theory and experiment was obtained for the majority of the data, with anomalous behaviour of the low order spots explained on the basis of long range order being preserved in the damaged structure as a result of cross-linking of bonds between adjacent molecules.

Using EELS Egerton (1980), showed that on exposure to 80keV electrons, the carbon concentration remained constant, whereas the nitrogen concentration decreased exponentially with a characteristic dose $D_{1/e}$ ~0.8 Ccm^{-2}.

Table 2.1 shows that epitaxial Cl-Cu Pc is the most resistant of all organic materials, with a dose of ~60 Ccm^{-2}, being required before all long range order is lost in the electron diffraction pattern. With such a

large stability Uyeda et. al. (1972) were able to obtain the first molecular images while later studies (Uyeda et. al., 1978; Smith et. al., 1988) clearly showed the position of the chlorine and bromine atoms as well as the central copper atoms. Multi-slice calculations have been used extensively to compare experimentally obtained and simulated images, (Uyeda & Ishizuka 1974; Kirkland et. al., 1984, 1985). Excellent agreement was obtained between the experimentally obtained and simulated images. Murata (1978) using molecular imaging and optical diffraction analysis was able to show that damage did not occur homogeneously across the entire crystal, but occurred in localized areas and along preferred directions notably [100] and [110]. The advantage of optical diffraction analysis, as compared to electron diffraction is information can be obtained from areas as small as $100Å^2$, whereas areas typically $1\mu m^2$ are required for electron diffraction. Additionally fine detail often not visible in the micrograph can be detected in the optical diffraction pattern. Clark et. al. (1979) investigated the response of the bright field lattice image and the diffraction pattern to electron irradiation. Two versions of epitaxially prepared Cl-Cu Pc were studied, these were a fully chlorinated sample (referred to as A-type) and a sample of approximate composition $Cl_{14.5}$ $H_{1.5}$ Cu Pc (referred to as B-type). The bright field images showed that damage appeared to spread at an approximately constant rate in the form of an advancing front. In the A-type material this front spread only from the edges of the particles inwards, whereas in the B-type material, the images soon appeared speckled due to the formation of a large number of smaller damage regions. As irradiation proceeded, damage progressed inwards from the edges and also rapidly outward from newly created damage sites until the whole crystal was consumed. These results suggested that the observed rate of damage was strongly dependent on the specimen environment. Based on the ideas of 'caging', Clark et. al. (1979)

considered that a given molecule could only be damaged if its nearest neighbours were damaged, thus allowing diffusion of the large chlorine atoms. In order to initiate damage in this model a surface layer of molecules around the edge of the particles were taken to be damaged. The probability for damage increased as a given molecule became surrounded by damaged units and indeed this model predicted a linear advance of damage from a growth front.

Using EDX Clark et. al. (1979) measured the rate of chlorine loss with electron irradiation from these two specimens. In the A-type material ~20% of chlorine was lost after a dose of ~100Ccm^{-2} whereas ~40% was lost in the B-type after an equivalent dose. These results, showing more rapid loss in the lower chlorinated material, were in agreement with the caging ideas previously described. In contrast to these results Kobayashi et. al. (1982), investigated the loss of chlorine from a fully chlorinated epitaxial sample using EELS. As the electron dose increased the chlorine concentration decreased continuously. At the stage of damage where the diffraction spots from the crystal disappeared, ~75% of the chlorine still remained, with further irradiation (total dose ~100 Ccm^{-2}) all the chlorine disappeared.

Material	$D_{1/e}$ (Ccm^{-2})	E(keV)	Method	Reference
Amino acids				
Glycine	$1.5x10^{-3}$	60	ED	Reimer (1960)
l-Valine	$1.5x10^{-3}$	80	ED	Glaeser (1971)
Aliphatic hydrocarbons				
Paraffin	$(3\text{-}5)x10^{-3}$	60	ED	Reimer (1960)
Polyvinylformal	$1x10^{-2}$	100	ED	Bahr et. al. (1965)
Bases of nucleic acids				
Adenosine	$1x10^{-2}$	80	ED	Reimer (1978)
Cytosine	$4x10^{-2}$	20	EELS	Crewe et. al. (1970)
Aromatic Compounds				
Anthracene	$(6\text{-}8)x10^{-2}$	60	ED	Reimer (1960)
Coronene	$5x10^{-2}$	100	ED	Siegal (1972)
Phthalocyanine	$1x10^{-1}$	100	ED	Reimer (1960)
Cu Pc	0.8	100	EELS (N_2 Loss)	Egerton (1979)
Cu Pc	1-2	100	ED	Reimer (1960)
*Cl_{16}Cu Pc	25-35	100	ED	Uyeda et. al. (1972)
*Cl_{16}Cu Pc	60	100	ED	Clark (1979)

ED Electron Diffraction; EELS Electron Energy Loss Spectroscopy; * complete fading of diffraction pattern.

Table 2.1: Characteristic doses for a variety of organic materials and experimental techniques.

Material	Temperature (K)	Low to Room Temperature Improvement	Technique	Reference
Polythene	100	1	Diffraction	Kobayashi & Sakaoku (1965)
	18	3.3	"	Grubb & Groves (1971)
	4	30	"	Knapek (1982)
Catalase	150	3	"	Glaeser & Taylor (1978)
Cl_{16} Cu Pc	100	1.7	Diffraction	Harada et al. (1972)
	100	3	EELS	Egerton (1986)
Collodion	100	5	EELS (C loss)	Egerton (1986)
	100	80	EELS (0_2 Loss)	Egerton (1986)
	100	120	EELS (N_2 Loss)	Egerton (1986)
Purple Membrane	100	5-7	Diffraction	Hayward & Glaeser (1980)

Table 2.2: Effect of low temperature on the radiation sensitivity of a variety of organic materials.

Chapter 3

INSTRUMENTATION AND IMAGE FORMATION IN THE ELECTRON MICROSCOPE

3.1 Introduction

The aim of this chapter is to outline the main features and operational modes of the CTEM and STEM which were used in this project. A brief description of the major components of the CTEM is presented in section 3.2. The formation of an electron diffraction pattern in the CTEM is described in section 3.3 and the information obtainable from such diffraction patterns is considered in section 3.4. This information includes assessment of the extent of crystalline ordering in the specimen and determination of crystal type and lattice spacings.

Image formation in the CTEM is discussed in section 3.5, where it is shown that, under certain conditions, imaging in the electron microscope can be described by a linear transfer theory, the transfer function being determined by the electron optical properties of the microscope. The form and importance of these transfer functions is considered in detail in this section.

The major components of the STEM, and the basic principles of image formation in the STEM are described in sections 3.6 and 3.7 respectively. In these sections it is shown that the STEM is capable of producing similar images to the CTEM when operated under conditions satisfying the reciprocity principle. For certain imaging modes, such as standard lattice imaging, the STEM is markedly inferior in terms of the efficiency of

electron utilisation. For radiation resistant materials this is not a serious problem as the dwell time can be increased until an image of comparable contrast and signal to noise ratio is obtained. However, in the investigation of radiation sensitive specimens it is of considerable importance as the achievement of comparable images in the STEM requires irradiating the specimen with a considerably greater electron dose, leading to a corresponding increase in the damage experienced by the specimen.

To alleviate these difficulties a new technique based on the differential phase contrast (DPC) mode of electron microscopy was developed. The principles of image formation using this technique are discussed in section 3.8. Advantages of the DPC technique include its efficient use of electrons and the simultaneous availability of high contrast lattice fringes and information on specimen topography. These features make it a powerful technique for the investigation of radiation sensitive specimens. The form of the transfer function for DPC imaging is discussed in section 3.9.

Due to the importance of efficient imaging modes in the investigation of beam sensitive specimens it is instructive to discuss the relative efficiencies of the various imaging modes available in the CTEM and STEM. This is considered in section 3.10.

3.2 The conventional transmission electron microscope (CTEM)

A schematic diagram of a CTEM is shown in figure 3.1, the instrument used being a JEOL 1200EX. At the top of the microscope column, (which is at a vacuum of ~10^{-6} Torr) is a gun in which the cathode is a heated filament which acts as the electron source. In this work a lanthanum hexaboride (LaB_6) filament was used instead of the conventional tungsten filament due to its increased brightness (B_o~10^{10}Am^{-2}sr^{-1} compared to B_o~10^{9}Am^{-2}sr^{-1} for

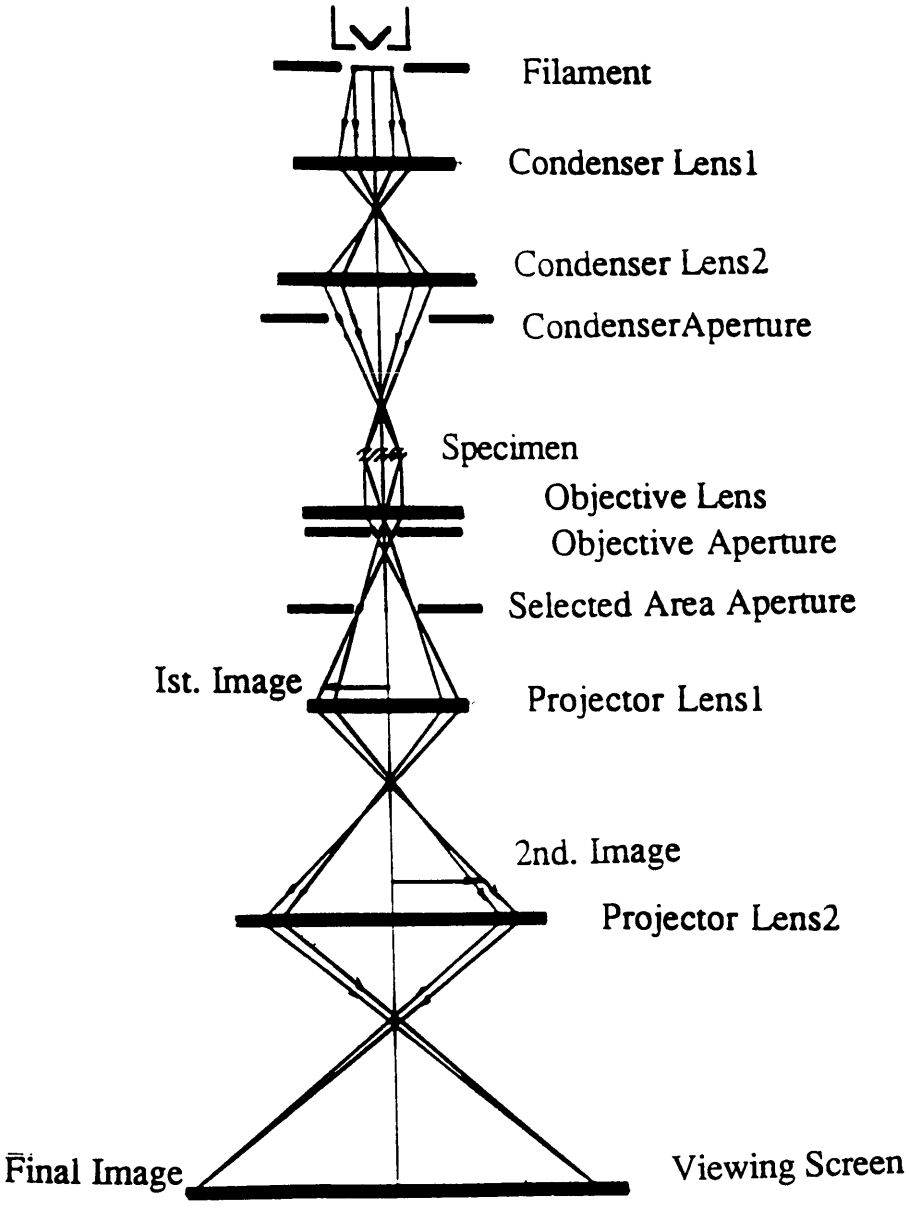

Figure 3.1: Schematic diagram of a CTEM

a tungsten filament; Reimer, 1984). The filament is mounted in a Wehnelt cylinder which contains a small aperture. A large negative potential, in this case 120kV, is applied between the filament and anode. The electrons are emitted thermionically from the filament and are accelerated and focussed by the electric field of the gun; this decreases the source size and consequently increases the current density.

The next component is the condenser lens assembly. This consists of two lenses (C1 and C2 in figure 3.1) and a fixed and a variable aperture, the latter controlling the intensity and angular convergence of the electron beam at the specimen. High resolution electron microscopy requires the use of small condenser apertures, to ensure that highly parallel coherent illumination is incident on the specimen. The use of small apertures, however, results in low current densities on the viewing screen at high magnifications. Hence high brightness electron sources are important to ensure that illumination levels adequate for focussing and astigmatism correction are obtained.

The next component is the objective lens whose design and aberrations critically affect the performance of the microscope imaging system. The most important of these is the third order spherical aberration coefficient of the lens. The effect of aberrations on the transfer of information through the microscope imaging system is considered in section 3.5.

The objective aperture, situated in the back focal plane of the objective lens, serves to limit the angular range of the scattered electrons reaching the image plane. By decreasing the aperture size the scattering contrast can be increased. However for high resolution imaging, the aperture should be as large as possible to allow high spatial frequencies to pass through and contribute to the image.

The remaining lenses, the three intermediate and projector lenses (only two of which are shown in figure 3.1), magnify the image produced by the objective lens and transfer it to the final viewing screen. Additionally,

adjustment of these lenses also allows the microscope to be operated in diffraction mode. This is discussed in the following section.

The final component of the microscope is the recording device. This is usually a photographic plate but, increasingly, low light level cameras are being used to display the image. The image can then be transferred to a computer for real time or subsequent image processing.

3.3 Electron Diffraction

For a crystalline specimen suitably oriented with respect to the incident beam sets of lattice planes scatter electrons into specific directions following Braggs Law. Scattered and unscattered beams are then focussed on the back focal plane of the objective lens and form a diffraction pattern. Varying the strengths of the remaining lenses allows either the image or the diffraction pattern to be observed on the final viewing screen. Ray diagrams showing the formation of an image and a diffraction pattern are presented in figure 3.2.

The diffraction pattern formed arises from all electrons incident on the specimen. In many cases, however, the diffraction pattern from a particular area of specimen is required. To achieve this the selected area diffraction (SAD) mode pioneered by Boersch (1936) and Le Poole (1947) can be used. This is shown schematically in figure 3.3. A diffraction pattern of the whole of the illuminated area is produced in plane C, and an image of this area is produced at D. An aperture is inserted in this plane to limit the rays which pass further down the column. Thus the diffraction pattern formed at F, by the intermediate lens, uses only those electrons which originated within the selected area. The apertures inserted in the plane at D are typically 10-50μm, which gives a minimum selected area of 0.2μm. However, the diagrams drawn correspond to perfect thin lenses, while magnetic lenses suffer from

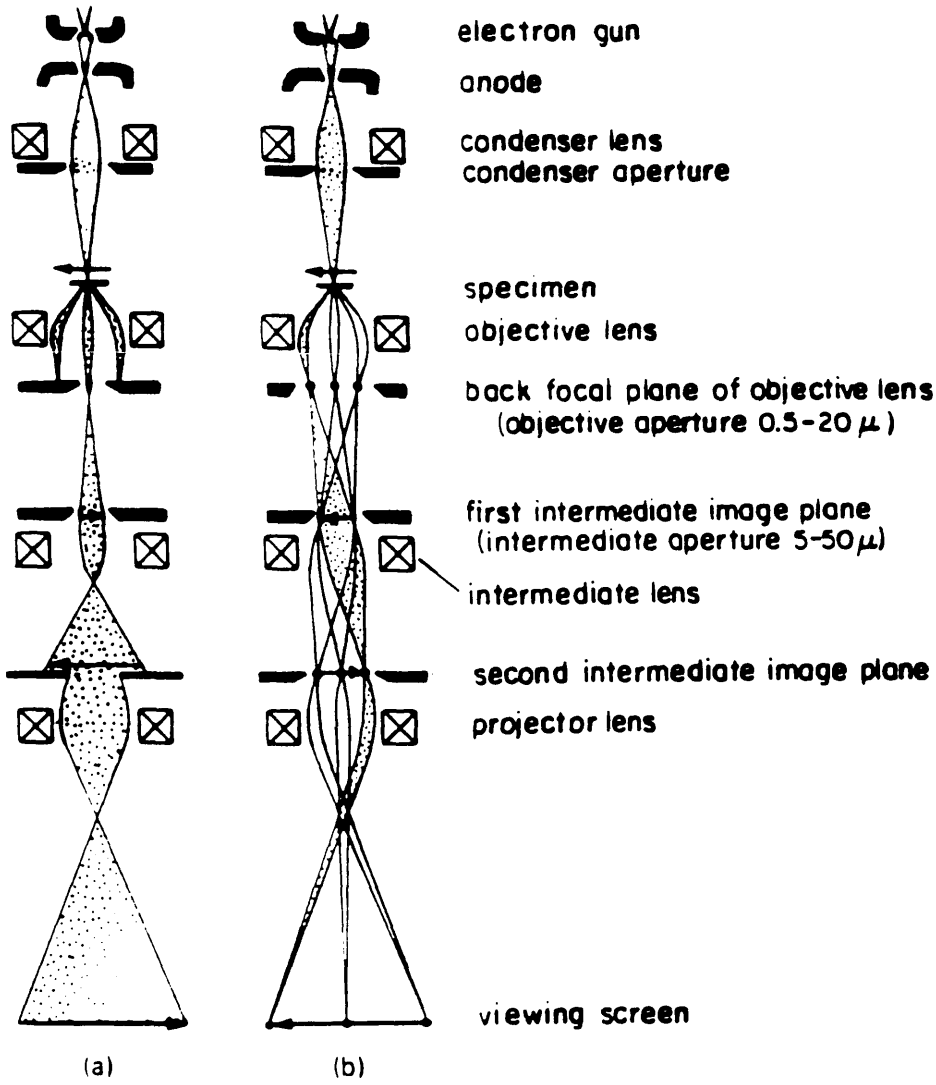

Figure 3.2: Schematic ray diagram for an electron microscope operated (a) for imaging and (b) for selected area diffraction. (from Thomas and Goringe ., 1979).

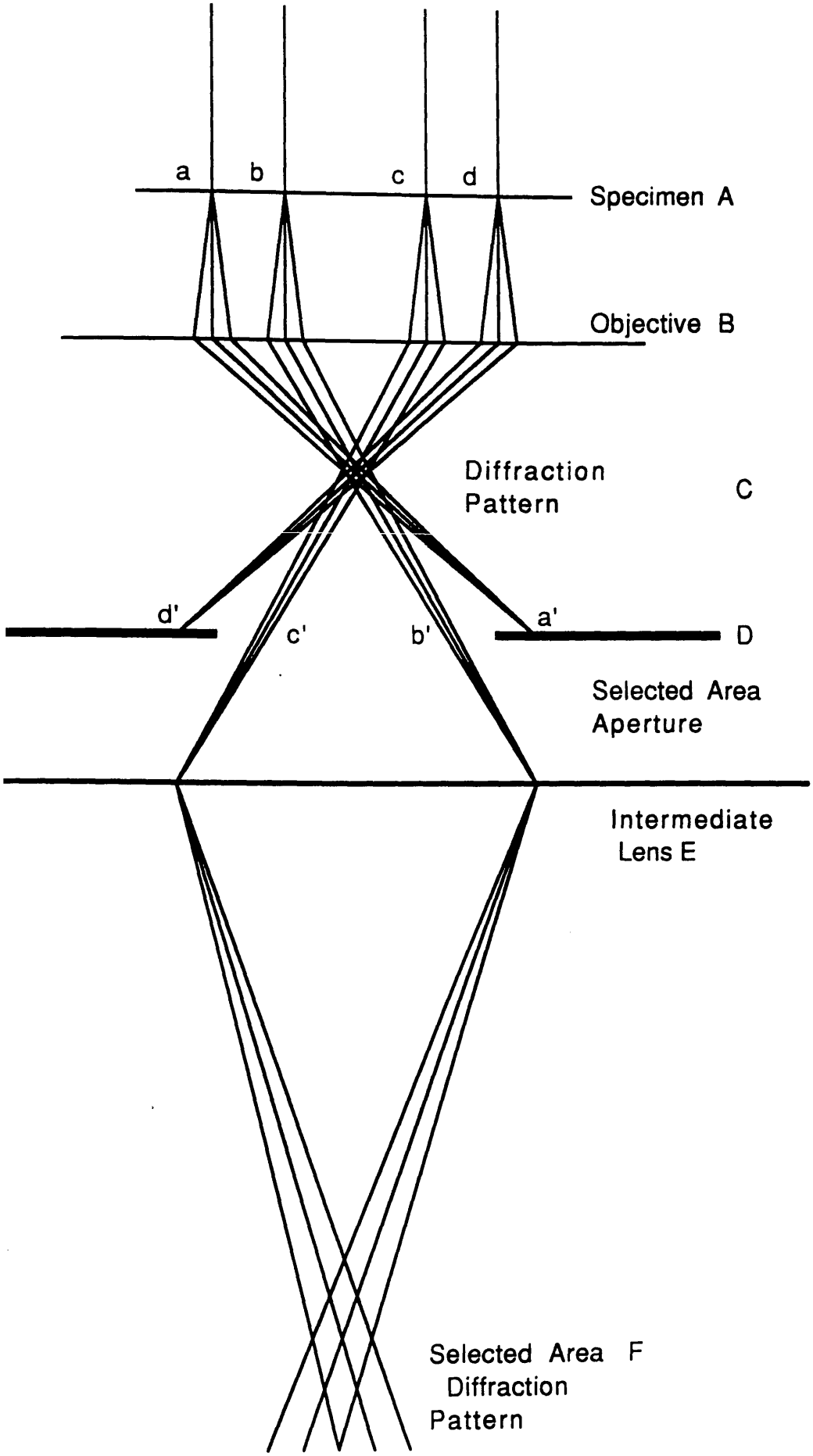

Figure 3.3: Ray diagram for selected area electron diffraction.

aberrations, in particular spherical aberration. This has the effect of causing rays inclined at an angle to the optic axis to be deviated more strongly than they would be by a perfect lens. Thus, if the image of a crystalline specimen is formed using the unscattered beam, it is brought to a focus in the plane of the selected area aperture. The image of the same area formed using a diffracted beam is brought to a focus in a plane some distance above this aperture. Because of this difference in level and also the related inclination of the diffracted beam to the axis, those electrons which come from the same area of the specimen but in different diffracted beams, do not pass through the same point in the aperture plane. The images are displaced in this plane from the zero-order image by a distance $d=MC_s\theta^3$ (where M is the magnification, C_s the spherical aberration coefficient, and θ the scattering angle). A consequence of this is that the minimum area that can be analysed is typically 0.5μm .

A schematic diagram showing the relationship between the scattering angle $2\theta_B$ and the distance D of a diffraction spot from the optic axis is shown in figure 3.4. Thus,

$$\tan(2\theta_B) = \frac{D}{L} \qquad (3.1)$$

where L is the camera length. The Bragg equation is,

$$2d \sin \theta_B = n\lambda \qquad (3.2)$$

where d is the crystal spacing and λ the electron wavelength. As the Bragg angle is small, $\sin\theta_B$ and $\tan\theta_B$ can both be approximated by θ_B giving,

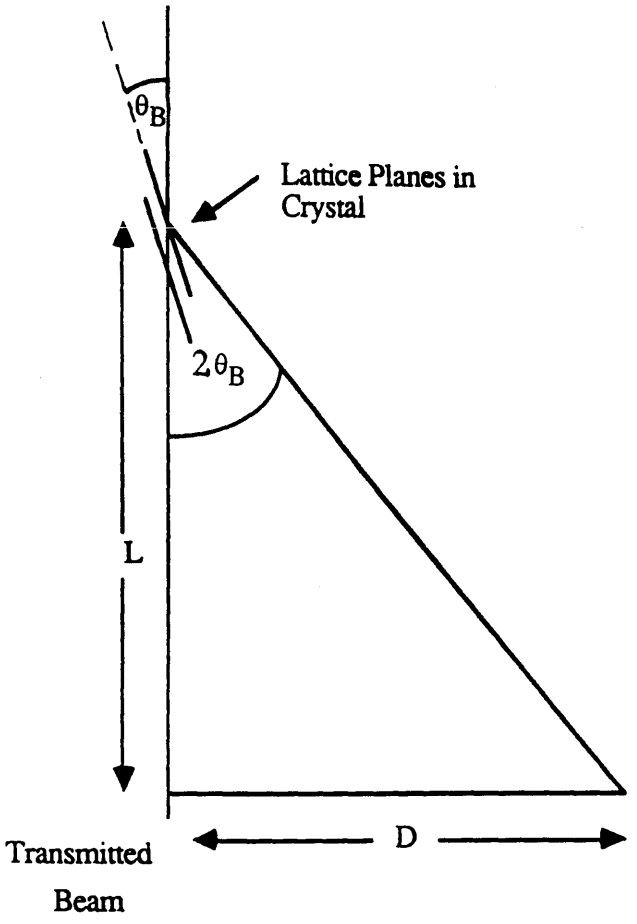

Figure 3.4: Schematic diagram showing distance of a diffraction spot from the optic axis.

$$Dd = \lambda L \qquad (3.3)$$

Knowledge of λ and the measured D spacings on the photographic emulsion together with a value for the camera length L (obtained by using a suitable standard specimen such as TlCl or Au) then enable determination of any unknown d.

3.4 Information from electron diffraction patterns

For a thin perfect crystal the electron diffraction pattern is directly related to the crystal structure. The position of the diffraction spots are a function of the crystal lattice while the intensity is dependent on the basis of the unit cell, the crystal shape and the number of unit cells contributing to the detected signal. Spot diffraction patterns obtained from single crystal specimens can be indexed allowing determination of the various lattice plane spacings in the structure. Symmetry and systematic absences in the pattern can frequently be used to obtain further information on the detailed ordering in the specimen. Diffraction patterns often contain extra spots and streaks. These provide information on deviations from perfect crystallinity and may indicate stacking faults or a twinned structure. The dose required to obtain high resolution information from a diffraction pattern is substantially less than that required to obtain an image showing comparable resolution. The reason for this is that in the former process the signal arises as a result of spatial averaging over the selected area whereas in the case of an image the signal is formed on a point by point basis. Electron diffraction has therefore been applied to many specimens whose direct imaging has been precluded due to dose constraints.

Analysis of diffraction patterns obtained from the pigmentary samples under investigation is presented in chapter 4.

3.5 Image formation in the CTEM

In the case of thin weakly scattering specimens, where a single scattering or 'kinematical', approach approximately holds, image interpretation can be considerably simplified. This allows the intensities in the image plane to be directly related to specimen structure. Image formation can be split into two parts based on the ideas of Abbe. The first step is a Fourier transform to the back focal plane of the lens giving the Fraunhofer diffraction pattern. The effects of defocus and spherical aberration can then be incorporated by modifying the amplitude and phase of the backfocal plane distribution. A second Fourier transform gives the wave function at the image plane.

In the case of a thin weakly scattering object the transmission function representing the effect of the specimen on the electron wave can be written as,

$$q(\underline{r}) = \exp[-i\sigma\phi(\underline{r})] \qquad (3.4)$$

where $\phi(\underline{r})$ is the projection of the Coulomb potential distribution in the beam direction, $\underline{r}$ is a two dimensional vector with coordinates (x,y) and σ is the interaction constant, given by $\sigma=\pi/\lambda E$ where E is the accelerating voltage. Using the weak phase approximation i.e. $\sigma\phi(\underline{r})<<1$, the transmission function can be written as,

$$q(\underline{r}) = 1 - i\sigma\phi(\underline{r}) \qquad (3.5)$$

The complex disturbance in the back focal plane of the objective lens is then given by,

$$\psi(\underline{u}) = \Im[q(\underline{r})] \cdot T(\underline{u}) \qquad (3.6)$$

In this expression $\Im$ denotes the Fourier transform, $\underline{u}$ is a reciprocal space vector with coordinates (u,v) and T($\underline{u}$) is the transfer function. This is given by,

$$T(\underline{u}) = A(\underline{u})\exp[i\chi(\underline{u})] \qquad (3.7)$$

where A($\underline{u}$) is the aperture function i.e. A($\underline{u}$)=1 within the aperture and 0 elsewhere. $\chi(\underline{u})$ is the phase shift which takes into account the effects of defocus and spherical aberration, and is given by,

$$\chi(\underline{u}) = \frac{2\pi}{\lambda}\left[\frac{C_s\lambda^4\underline{u}^4}{4} + \frac{\Delta f\lambda^2\underline{u}^2}{2}\right] \qquad (3.8)$$

The disturbance given by equation 3.6, can then be written as,

$$\psi(\underline{u}) = \partial(\underline{u}) + \sigma\Phi(\underline{u})A(\underline{u})\sin\chi(\underline{u}) - i\sigma\Phi(\underline{u})A(\underline{u})\cos\chi(\underline{u}) \qquad (3.9)$$

where ∂(u,v) represents the transmitted unscattered beam and the remaining terms represent the real and imaginary parts of the scattered amplitude.
The image disturbance is then given by,

$$\psi(\underline{r}) = 1 + \Im[\sigma\Phi(\underline{u})A(\underline{u})\sin\chi(\underline{u})] - i\Im[\sigma\Phi(\underline{u})A(\underline{u})\cos\chi(\underline{u})] \quad (3.10)$$

and the intensity distribution in the image plane is given by,

$$I(x, y) = \psi^{*}\psi \cong 1 + 2\sigma\phi(x, y) * \Im[A(u, v)\sin\chi(u, v)] \quad (3.11)$$

where * denotes a convolution. The importance of the oscillatory function $\sin\chi(\underline{u})$, the phase contrast transfer function (PCTF) can be clearly seen from equation 3.10. This determines the transfer of information to the image plane. For optimum phase contrast imaging we therefore require that $\sin\chi \sim 1$ for as wide a range of spatial frequencies as possible. This means that all spatial frequencies are transferred faithfully and the image is readily interpretable. The best general condition is obtained by balancing the effects of spherical aberration and defocus, with the optimum defocus or Scherzer focus given by,

$$\Delta f \sim 1.2(C_s\lambda)^{1/2} \quad (3.12)$$

Corresponding to this the optimum resolution attainable is given by (Eisenhandler & Siegal, 1966) as,

$$d_{min} = 0.66C_s^{1/4}\lambda^{3/4} \quad (3.13)$$

Figure 3.5, shows the PCTF for a range of defocus values applicable to the JEOL 1200EX. From equation 3.12 it can be seen that the optimum defocus value Δf is ~-900Å for C_S=1.8mm and λ=3.5pm. In this case $\sin\chi \sim 1$ for a

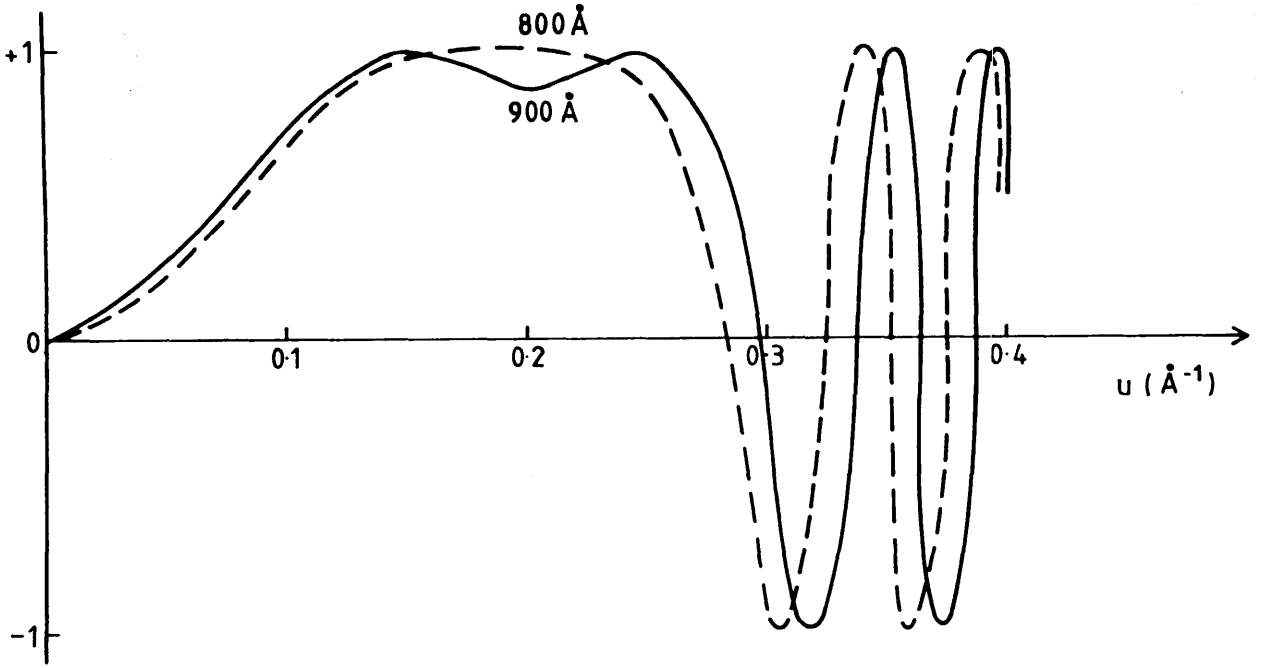

Figure 3.5: Calculated phase contrast transfer functions for the JEOL 1200EX, with Cs=1.8mm, λ=3.5pm and defocus values of -800Å and -900Å.

wide range of spatial frequencies out to a maximum value U_{max}~0.34Å^{-1}. An objective aperture is then used to cut-off higher spatial frequencies. The amplitudes of such frequency components are strongly modulated and are therefore difficult to interpret. Using equation 3.13. gives the best resolution as ~3.2Å.

The discussion so far has assumed an electron source of perfect spatial and temporal coherence. However in practice the electrons emerge from the filament with an energy spread ΔE and the electron source has a finite source size. These factors should be taken into account to give an accurate description of the transfer function. This can be achieved via the inclusion of 'envelope functions', as multiplicative terms (e.g. Frank, 1973, Krivanek, 1976 and Saxton, 1977). Humphreys and Spence (1980) showed that the damping due to chromatic aberration effects could be expressed as,

$$E_\varepsilon = \exp\left(-\frac{\pi^2}{2}\lambda^2 c_c^2 Q^2 \underline{u}^4\right) \qquad (3.14)$$

where C_c is the chromatic aberration coefficient, and Q^2 is given by,

$$Q^2 = \frac{\sigma^2(E)}{E^2} + \frac{\sigma^2(V)}{V^2} + \frac{4\sigma^2(I)}{I^2} \qquad (3.15)$$

where σ^2(E), σ^2(V), σ^2(I) are the variances in the energy spread of the electrons from the source, in the H.T. fluctuations and in the objective lens current fluctuations respectively. Using typical values for H.T. fluctuations and lens current stabilities of $\Delta V/V = 2X10^{-6}$ and $\Delta I/I = 1x10^{-6}$ respectively, allows us to calculate the form of the envelope function. This is shown in figure 3.6 (a) for the JEOL 1200EX where C_c=2mm. Values for the energy

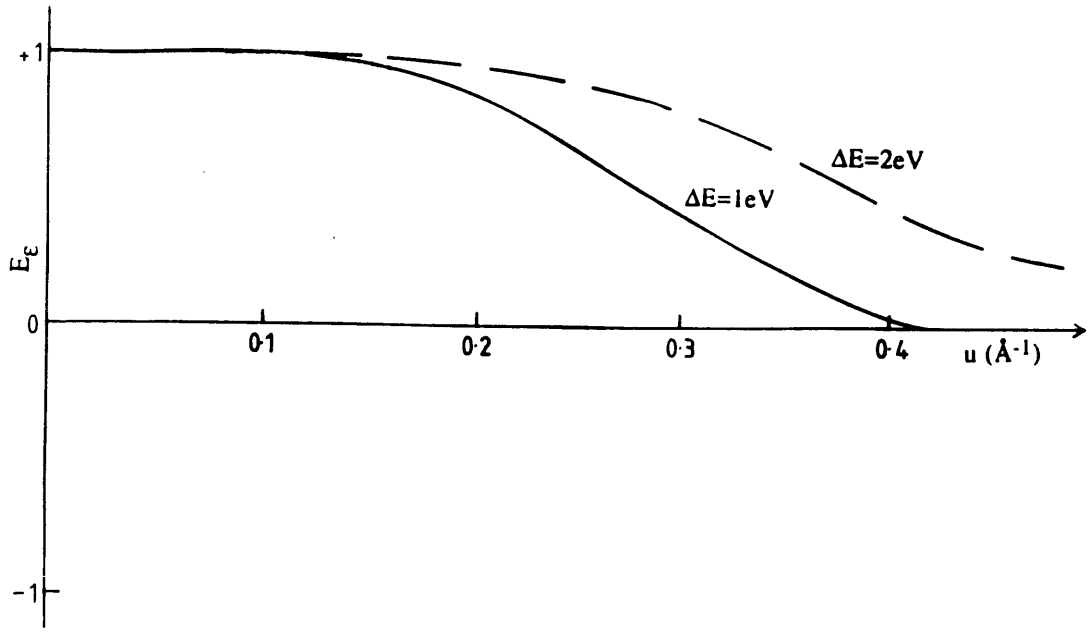

Figure 3.6(a): Calculated chromatic envelope function with Cc=2mm for ΔE=1eV and 2eV.

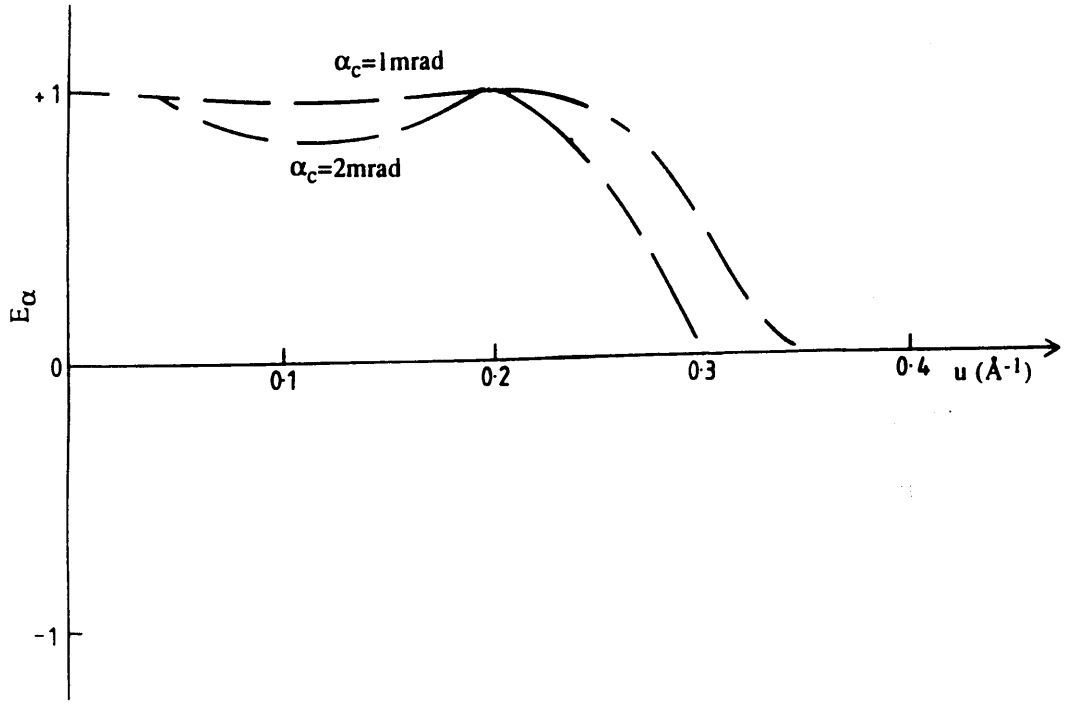

Figure 3.6(b): Partial coherence envelope function with Cs=2mm, Δf=-900Å for specimen illumination angles α_c of 1mrad and 2mrad.

spread ΔE of 1eV and 2eV are used, such values being applicable to a LaB_6 filament.

The second envelope function is due to the finite source size. This takes into account the illumination angle α_c, and is given by,

$$E_\alpha = \exp\left(-\pi^2 \alpha_c^2 \left(C_s \lambda^2 \underline{u}^3 + \Delta f \underline{u}\right)^2\right) \qquad (3.16)$$

The envelope functions for the JEOL 1200EX with α_c=1 and 2 mrad are shown in figure 3.6 (b). It can be seen that high resolution detail is lost as a result of increasing the illumination angle α_c. The resultant modified transfer function taking into account these two envelope functions can be written as,

$$T = \sin \chi E_\varepsilon E_\alpha \qquad (3.17)$$

To illustrate the effects of the aberrations on the form of the transfer function, the modified transfer function for an optimum defocus of ~-900Å and α_c=1 mrad is shown in figure 3.7. For convenience the unaberrated transfer function presented in figure 3.5 is also shown.

The description of image formation described above has assumed the 'kinematical', approach is valid. For crystalline specimens with thickness greater than ~10nm, multiple electron scattering can occur (Cowley, 1976). This considerably complicates image interpretation. Under these conditions image formation can be described by the 'multislice' approach, (Goodman and Moodie, 1974) derived from the N-beam dynamical theory of Cowley and Moodie (1957). In this dynamical approach the specimen is considered to be composed of a number of slices. The procedure is then to propagate an

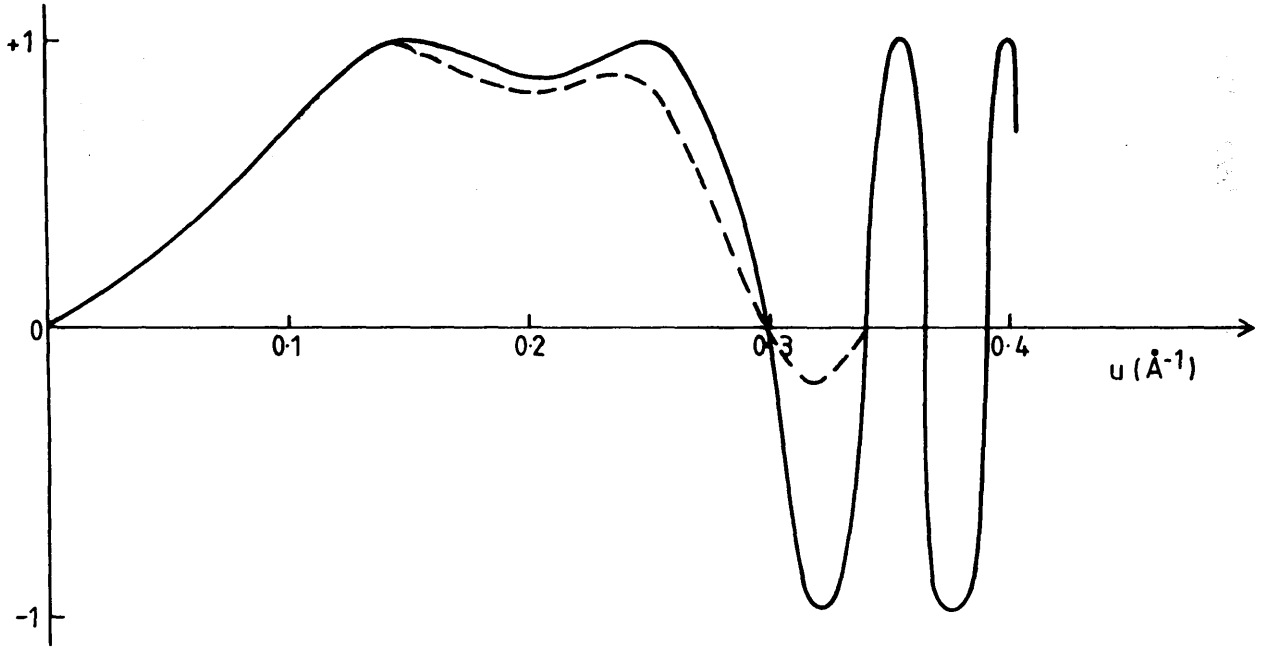

Figure 3.7: Optimum defocus PCTF, taking into account the effects of chromatic aberrations and partial coherence ($\Delta f = -900$Å; $\Delta E = 1$eV; $\alpha_c = 1$mrad).

incident wave through each slice of specimen and calculate the emergent wave function. Repeating this procedure for the entire crystal allows the exit wave at the final surface of the specimen to be readily calculated. By then propagating this wave through the remainder of the microscope imaging system, taking into account aberrations and the selected defocus value allows the final image wave function to be determined. This 'multislice' approach has been extensively used for image simulation, where factors such as specimen thickness, beam alignment, damping effects and the form of the transfer function can be investigated. These images can then be compared to images experimentally acquired using identical imaging parameters. This approach has been used in an investigation of epitaxially prepared Cl_{16}-Cu Pc (Kirkland et. al., 1980). The procedure adopted was to experimentally acquire a focal series of micrographs from the specimen and also to simulate a corresponding series using the 'multislice' technique. Determination of the appropriate focus value from the micrographs allowed the images to be matched to bands in the phase contrast transfer function. Use of this approach allowed the extraction of periodic detail to a resolution of ~1Å.

3.6 The scanning transmission electron microscope

In the STEM, images are formed by scanning a focussed electron probe across a specimen and collecting some portion of the transmitted scattered or unscattered beam by a variety of detectors. Each pixel in the resulting image is thus formed in a sequential manner unlike in the CTEM where the entire image is acquired simultaneously.

Schematic diagrams of both the CTEM and STEM are presented in figure 3.8. Application of the reciprocity principle (Cowley, 1969; Zeitler and Thomson, 1970), shows that under identical conditions, the signal recorded

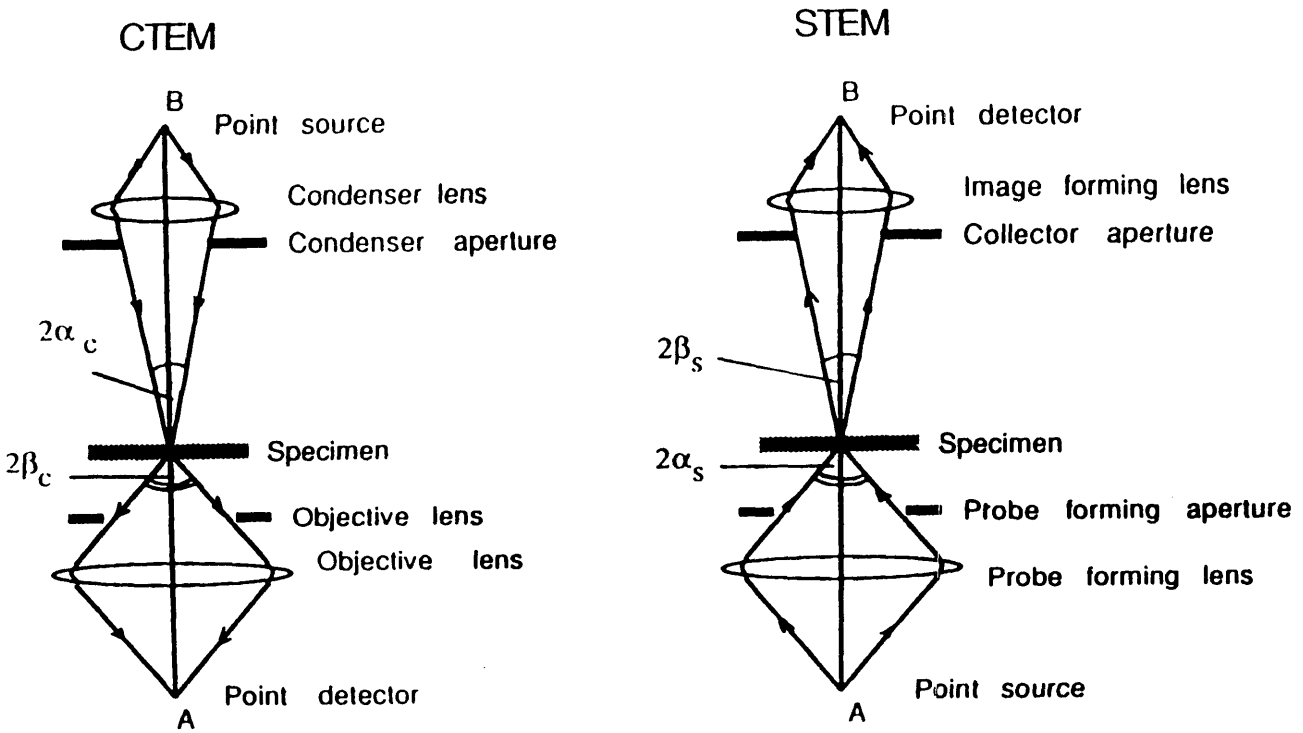

Figure 3.8: Schematic diagram illustrating the equivalence of the CTEM and the STEM.

at A from a source at B is identical to the signal which would be recorded in the CTEM case with the source at A and the detector at B. Application of this principle shows that any CTEM imaging mode can be duplicated in the STEM. This has been experimentally verified by Crewe & Wall (1970) and by Colliex et. al. (1977). The latter showed that the observed difference in the number of Fresnel fringes around a hole could be explained in terms of signal to noise considerations and did not indicate a breakdown of the reciprocity principle.

The work described in chapter 5 of this thesis was performed using an extended Vacuum Generators HB5 STEM. A schematic diagram of the microscope is presented in figure 3.9. The following paragraphs give a brief description of the major components and operational modes used in this project.

The HB5 is equipped with a field emission source (e.g. Crewe, 1971) which is a single crystal tungsten cathode welded onto a tungsten filament. The radius of the cathode tip is ~100nm and its emitting surface is a (310) face. Electrons are stripped from the surface when a potential of ~3kV is applied between the cathode and an extraction anode, creating a field of $>5x10^9$ Vm^{-1} in the source region. A second anode accelerates the electrons up to energies of 100keV. Both these components have the effect of acting as an electrostatic lens, so that the electrons appear to be originating from a virtual source, with a diameter of ~6.5nm, (Morrison, 1981). The pre-specimen optical configuration can be treated as a three lens system, comprising a double condenser lens C1 and C2 and the pre-specimen field of the objective lens. This allows considerable flexibility in the probe forming conditions. In normal imaging mode either C1 or C2 condenser lens is used to transfer an image of the virtual cross over produced by the gun to the plane of the selected area aperture (SADA). The objective lens is kept at an

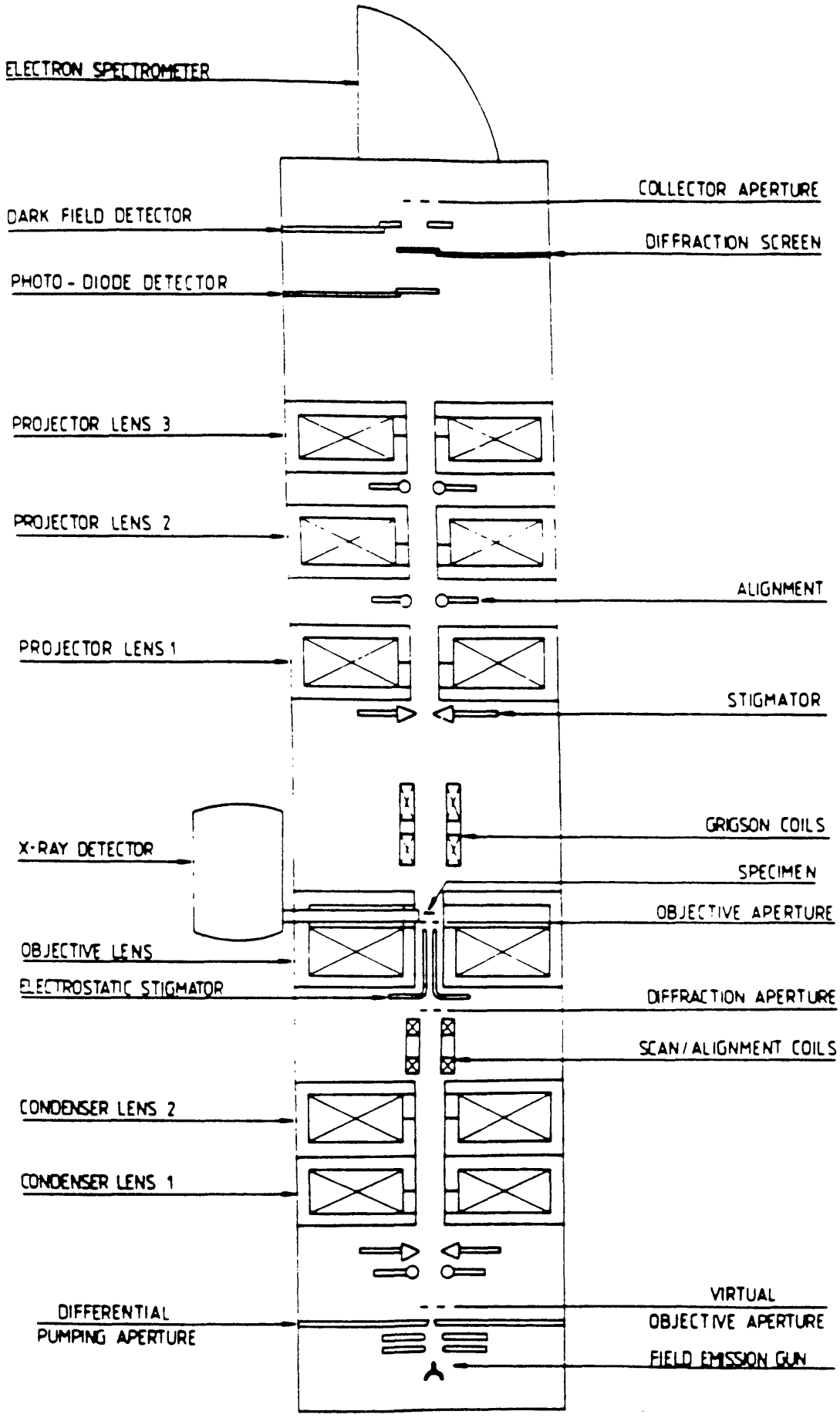

Figure 3.9: Schematic diagram showing the various components of the VG HB5 STEM.

almost constant excitation and is used to produce a demagnified image of the cross-over in the SADA plane, on the specimen plane. The objective aperture defines the probe forming semi-angle α_c. Using C2 enables the formation of a smaller probe on the specimen; however, the total current in the probe is greater when using C1. Therefore in a particular experiment, a choice exists between probe size and probe current. A discussion of the relative merits of imaging with C1 or C2 is given in chapter 5.

A feature of the modified HB5 is that it is equipped with a series of post specimen lenses. This allows the angular distribution of the electrons transmitted through the specimen to be matched to the size and shape of the electron detectors by choosing a suitable camera length. In the standard STEM configuration, the microscope is equipped with a small axial bright field detector which collects the unscattered and inelastically scattered electrons. There is also an annular dark field detector which collects electrons scattered at large angles with respect to the primary cone of electrons. A ray diagram illustrating image formation using these two detectors is presented in figure 3.10. The HB5 is also equipped with a quadrant photodiode (Centronics QD-100) detector. This is a circular detector 11mm in diameter comprising a silicon p-n junction split into 4 sections separated by inactive strips ~200μm wide. The signals from all four quadrants can be added to give an incoherent bright field image. It is also possible for the difference of the signals from any two opposite quadrants to be obtained. These difference signals are, for small shifts, directly proportional to angular shifts of the electron beam across the detector. This means that the detector has an antisymmetric response function which is dependent upon the position of the electron beam. As such it has no direct equivalent in the CTEM. It is, in theory possible to produce a similar image in the CTEM but this requires two exposures with complementary half-plane apertures, followed by the subtraction of the resulting image intensities. In

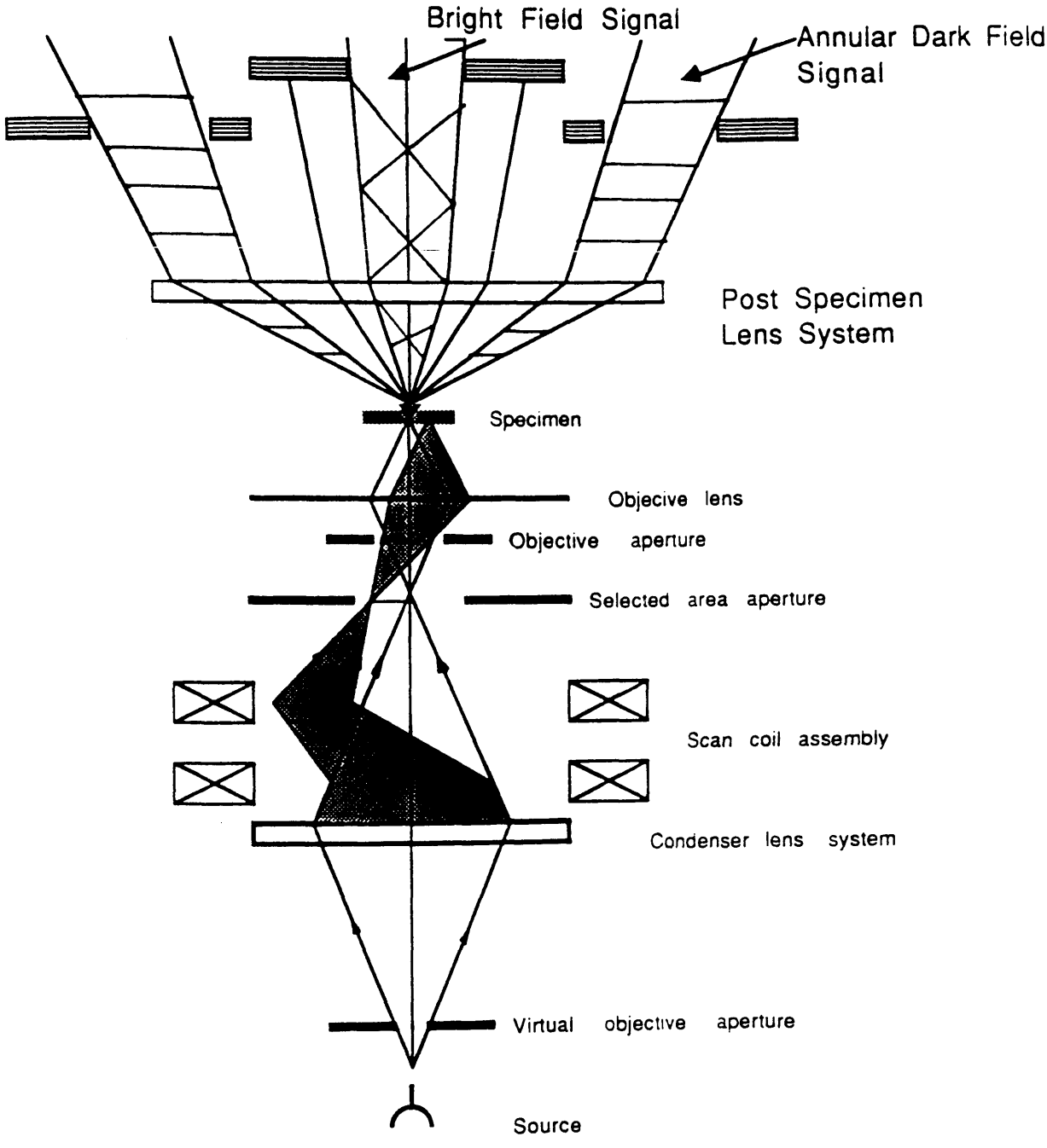

Figure 3.10: Ray diagram illustrating brightfield and darkfield imaging modes in the STEM.

practice problems of alignment of the apertures and of the resultant images makes this method impractical.

3.7 Introduction to the theory of STEM imaging

Image formation in the STEM has been covered extensively by Cowley (1976), Hawkes (1981) and Colliex and Mory (1984).

The field emission source of the STEM can be approximated by a point source. This allows the wave incident on the specimen to be expressed as the Fourier transform of the objective lens transfer function,

$$\psi_i(\underline{r}) = \Im\{A(\underline{u})\exp[i\chi(\underline{u})]\} \qquad (3.18)$$

In this expression $\Im$, A($\underline{u}$) and $\chi(\underline{u})$ have the same meaning as those defined in section 3.5.

In the STEM the image is produced by recording the variation of the detected signal as the probe is scanned across the specimen.
The exit wave can then be written as,

$$\psi_e(\underline{r},\underline{R}) = \psi(\underline{r}-\underline{R})\cdot q(\underline{r}) \qquad (3.19)$$

where q($\underline{r}$) is the specimen transmittance function and $\underline{R}$ is the position about which the probe is centred. The wave amplitude on the detector plane, neglecting a scaling factor, can be expressed as,

$$\begin{aligned}\psi_D(\underline{u},\underline{R}) &= \Im[\psi_e(\underline{r},\underline{R})] \\ &= Q(\underline{u}) * A(\underline{u})\exp[i\chi(\underline{u})]\end{aligned} \qquad (3.20)$$

where * denotes a convolution. The corresponding intensity distribution in the detector plane is given by,

$$I(\underline{u},\underline{R}) = \left|Q(\underline{u}) * A(\underline{u})\exp[i\chi(\underline{u})]\right|^2 \qquad (3.21)$$

The detected signal as a function of probe position $\underline{R}$ is then given by,

$$J(\underline{R}) = \int I(\underline{u},\underline{R})D(\underline{u})d\,\underline{u} \qquad (3.22)$$

where $D(\underline{u})$ is the detector response function. The importance of this function is discussed later in this section. Substituting the real and imaginary parts of $Q(\underline{u})$ appropriate to a weak phase object, and neglecting second and higher order terms, the bright field STEM image obtained using a small axial detector of radius u_o is given by,

$$J(\underline{R}) = \pi u_o^2[1 + \sigma\Phi(\underline{R}) * \Im[A(\underline{u})\sin\,\chi(\underline{u})]] \qquad (3.23)$$

Equation 3.23 is equivalent to the expression given by 3.11, for the CTEM, with the signal consisting of a uniform background with a small modulation. The modulation is a linear representation of the projected potential convolved with the spread function of the probe forming lens. The factor u_o^2 in equation 3.23. implies that for a small axial detector the signal obtained in STEM is low. The situation can be improved by simply increasing the dimensions of the detector. However by considering the reciprocity principle, increasing the detector dimensions in STEM is equivalent to increasing the source size in the CTEM, thus resulting in low coherence and poor phase contrast effects. This is discussed in detail by

Butler and Cowley (1983). The consequence of this poor signal to noise ratio for standard STEM lattice imaging is now discussed with special reference to beam sensitive specimens.

In STEM lattice imaging, the electron distribution in the detector plane is a convergent beam diffraction pattern composed of a series of discs whose radius is determined by the probe half-angle and whose position is determined by the scattering angle θ, where $\theta=\lambda/d$. Formation of a lattice image requires that the probe angle must be sufficiently large to allow the discs to overlap and that a small axial detector is placed in this overlap region. This has been discussed in detail by Cowley & Spence (1979). As noted previously the signal to noise ratio in the lattice image is dependent on the detector dimensions, so use of a large collection angle should be beneficial. However as this angle approaches the dimensions of the probe angle the contrast of the lattice fringes decreases to zero, (Cowley & Au., 1978).

The collection efficiency of STEM brightfield imaging is approximately $(\beta_s/\alpha_s)^2$ where α_s is the angle subtended by the probe and β_s that by the detector as illustrated in figure 3.8. For high resolution lattice imaging typical values for α_s and β_s are $\sim 7.5\times10^{-3}$ and 10^{-3}-10^{-4} radians respectively which implies standard STEM brightfield imaging is <5% efficient. A consequence of this low collection efficiency is that standard STEM lattice imaging is ill suited to the investigation of radiation sensitive specimens, as achieving comparable images requires irradiating the specimen with a considerably greater electron dose. There is therefore a considerable incentive for investigating new imaging modes in the STEM to increase the electron efficiency.

The detector response function, denoted $D(\underline{u})$ in equation 3.22, can be varied by developing novel detector configurations which have no easily

implemented counterpart in the CTEM. One such detector is the split detector of Dekkers and de Lang (1977). This comprises a large axial detector split into two independent semicircular areas. This detector is, however, insensitive to deflections parallel to the split. The problem is conveniently solved by using a detector split into 4 quadrants (Rose, 1977). A further detector configuration is the multi-annular detector of Rose (1974). In this detector the dimensions of the annuli are matched to the positions in reciprocal space where the contrast transfer function changes sign. The resultant signals obtained from various annuli can therefore be added together constructively, increasing the efficiency of bright field imaging. This scheme is however dependent on selecting the correct radii of the detector rings.

A further technique based on the differential phase contrast (DPC) mode of microscopy, utilising the properties of the quadrant detector described above has been developed. This technique offers an efficient use of electrons and provides simultaneously topographic information and high contrast lattice fringes.

3.8 Principles of DPC image formation

The aim of this section is to discuss the principles of DPC imaging, with particular reference to obtaining topographic and structural information. In the DPC imaging mode, difference signals from opposite segments of a quadrant detector, give a signal which is linearly related to the phase gradient of the specimen transmittance (Dekkers & de Lang, 1977).

Denoting the thickness of the specimen by $t(\underline{r})$ and the inner potential function of the crystalline specimen by $V(\underline{r},z)$, the phase excursion is given by

$$\phi(\underline{r}) = \pi \left[\int_0^{t(\underline{r})} V(\underline{r}, z)dz \right] / (\lambda E_o) \qquad (3.24)$$

where λ is the electron wavelength, E_0 the energy of the electron beam and z is the co-ordinate along the optic axis. Assuming the potential variation along the z-axis is negligible, equation 3.24 can be written as,

$$\phi(\underline{r}) = \pi V(\underline{r}) t(\underline{r}) / \lambda E_o \qquad (3.25)$$

Therefore taking difference signals from opposite segments of a quadrant detector gives images which can be regarded as maps of two orthogonal components of the phase gradient of the specimen transmittance i.e.

$$\nabla_x \phi(\underline{r}) = \frac{\pi \nabla_x (V(\underline{r}) t(\underline{r}))}{\lambda E_o} \qquad (3.26)$$

$$\nabla_y \phi(\underline{r}) = \frac{\pi \nabla_y (V(\underline{r}) t(\underline{r}))}{\lambda E_o} \qquad (3.27)$$

A schematic diagram showing how topographic contrast arises in the DPC imaging mode is presented in figure 3.11.

The above expressions show that at low resolution, where the variation in the mean inner potential is below the resolution limit, the images obtained are to a good approximation directly proportional to the thickness gradient $t(\underline{r})$.

At higher resolution, we are concerned with the variation of the specimen potential. For simplicity in the following discussion of the form of the DPC signal obtained from a specimen with a periodic internal structure, a one dimensional approach is adopted. It should be noted that if required the

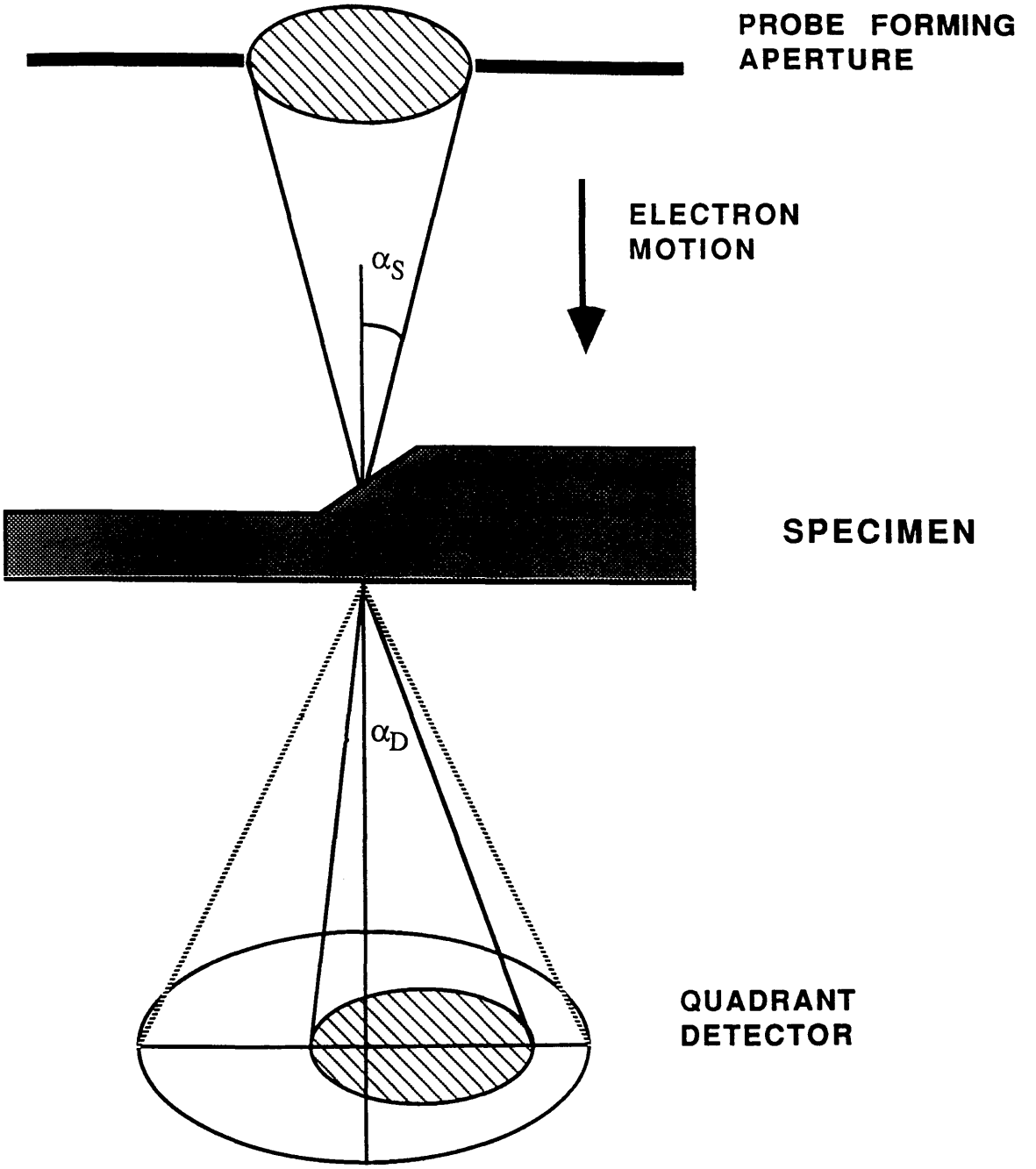

Figure 3.11: Schematic diagram showing how topographic contrast arises in the DPC imaging mode.

derived expressions can be easily extended. In the former case the inner potential function of a 1-dimensional periodic structure can be expressed to first order as,

$$V(x) = V_o + V_1 \sin(2\pi x / \Lambda) \qquad (3.28)$$

The first term of this equation represents the mean inner potential of the specimen. The second term represents a particular internal periodic structure in the unit cell. These terms are related to the structure factor F_{hkl}. The relationship is given by,

$$F_{hkl} = 2\pi m_o e \frac{V_{hkl}}{h^2} \qquad (3.29)$$

where m_o is the rest mass of the electron and h is Planck's constant. For Cl_{16}-Cu Pc, V_o is associated with the structure factor of F_{000} and V_1 with a particular internal periodicity. The periodicities of greatest interest correspond to the (110) and (001) reflections. Using data from Hirsch et. al. (1965) values for V_{000}, V_{110} and V_{001} were calculated to be 9.88V, 1.78 and 9V respectively.

To reveal the internal structure of specimens by DPC lattice imaging requires that the diffracted beams emerging from the specimen overlap with the unscattered central beam. In the case of a weakly scattering object, with the phase varying sinusoidally with periodicity Λ, the specimen transmittance can be written as,

$$h(x) = 1 + i\phi_o \sin\left(\frac{2\pi x}{\Lambda}\right) \qquad (3.30)$$

A schematic diagram showing the overlap of the diffraction discs is presented

in figure 3.12. If the specimen is illuminated by a coherent probe, subtending an angle α_S, then the outgoing wave after traversing the specimen will consist of three components, namely the unscattered beam and two diffracted beams. To satisfy the overlap condition requires $\alpha_S > \theta_B$. The amplitude in the detector plane ψ_d can be expressed (Dekkers and de Lang, 1977) as,

$$\psi_d(x_o, x_d, y_d) = \psi_o(x_d, y_d) + \frac{1}{2}\phi_o\psi_o(x_d + X, y_d)e^{\frac{2\pi i x_o}{\Lambda}} - \frac{1}{2}\phi_o\psi_o(x_d - X, y_d)e^{-\frac{2\pi i x_o}{\Lambda}} \qquad (3.31)$$

where the last two terms in (3.31)represent the two diffracted beams which are centred a distance $X=L\theta$ away from the optic axis.

The amplitude and phase of ψ_d can be treated as constant within the brightfield cone, thus $\psi_o(x_d,y_d)=A_o$. Neglecting terms involving powers of ϕ_o^2 the intensity in area Q_{+1} can be expressed as,

$$I_{A1} = A_o^2\left(1 + \tfrac{1}{2}\phi_0 e^{\frac{i2\pi x_o}{\Lambda}}\right)\left(1 + \tfrac{1}{2}\phi_0 e^{-\frac{i2\pi x_o}{\Lambda}}\right)$$
$$= A_o^2\left[1 + \phi_o \cos\left(\frac{2\pi x_o}{\Lambda}\right)\right] \qquad (3.32)$$

while for area Q_{-1} the intensity is given by,

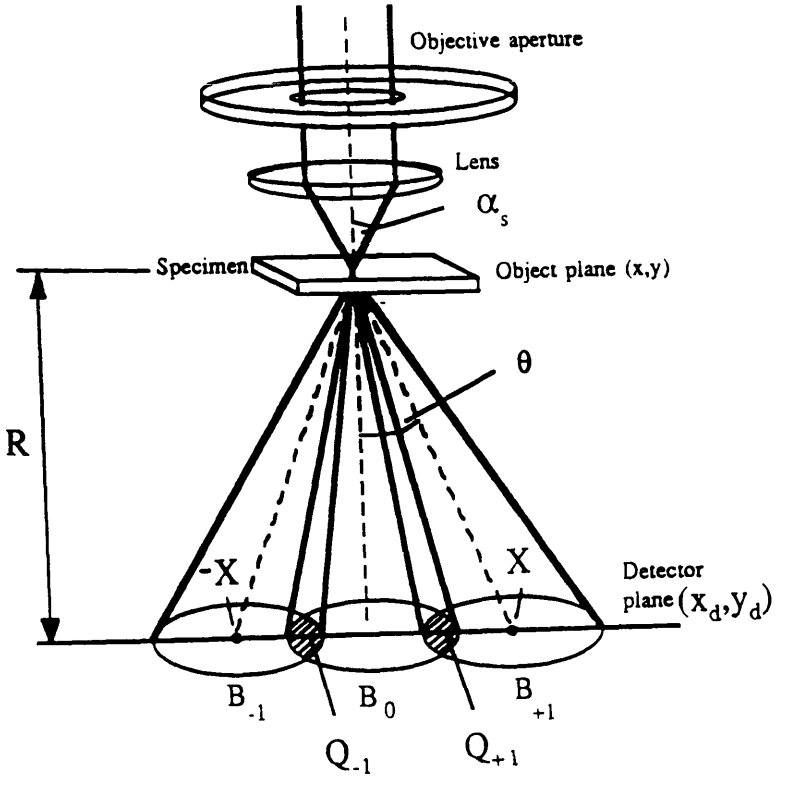

Figure 3.12: Schematic diagram showing the overlap of discs in the diffraction pattern.

$$I_{A2} = A_o^2\left(1 - \tfrac{1}{2}\phi_0 e^{\frac{i2\pi x_o}{\Lambda}}\right)\left(1 - \tfrac{1}{2}\phi_0 e^{-\frac{i2\pi x_o}{\Lambda}}\right)$$
$$= A_o^2\left[1 - \phi_o \cos\left(\frac{2\pi x_o}{\Lambda}\right)\right] \qquad (3.33)$$

Therefore by dividing the detector into two semicircular areas and subtracting the signal falling on opposite segments of the detector gives a resultant signal,

$$S(x_o) \propto 2A_o^2 \phi_o O_A \cos\left(\frac{2\pi x_o}{\Lambda}\right) \qquad (3.34)$$

where O_A denotes the area of overlap in angle space.

From equation 3.34. it can be seen that the signal obtained as the electron probe is scanned across the specimen surface is directly proportional to the phase gradient of the specimen transmittance.

As the total current I_p incident on the detector plane is proportional to $\pi\alpha_s^2$, the ratio of the information containing current from the detector to the current in the probe is given by,

$$\frac{I(x_o)}{I_P} = 2\phi_o O_A \cos\left(\frac{2\pi x_o}{\Lambda}\right) / (\pi\alpha_s^2) \qquad (3.35)$$

with the corresponding maximum value given by,

$$\frac{I_{\max}}{I_P} = 2\phi_o O_A / (\pi\alpha_s^2) \qquad (3.36)$$

In this expression $0_A/\pi\alpha_s^2$ represents the fraction of the brightfield cone which is involved in an overlap.

The maximum signal expressed as a number of electrons is given by,

$$S_{max} = \frac{2\phi_o O_A I_p \tau}{\pi \alpha_s^2 e} \qquad (3.37)$$

where τ is the recording period. The corresponding noise N, assuming only Poisson noise need be considered, is related to the sum of the variances of the charge falling on the two halves of the detector, i.e.

$$N = \left[\left(\frac{I_p \tau}{2e}\right) + \left(\frac{I_p \tau}{2e}\right)\right]^{1/2} \qquad (3.38)$$

The resultant $(S/N)_{max}$ is therefore given by,

$$\left(\frac{S}{N}\right)_{max} = \frac{2\phi_o O_A}{\pi \alpha_s^2}\left(\frac{I_p \tau}{e}\right)^{\frac{1}{2}} \qquad (3.39)$$

The discussion so far has assumed an in focus system with no aberrations. In practice however both spherical aberration and defocus have to be taken into account.

3.9 The DPC transfer function

The form of the transfer function for image formation in the CTEM was

discussed previously in this chapter, where it was shown that to allow the image to be readily interpreted it was important that all spatial frequencies of interest were transferred faithfully. In a similar manner it is important to discuss the form of the transfer function for DPC STEM imaging. Of particular importance in this discussion is the effect of the probe forming semi-angle and aberrations on the form of this function. As discussed previously in this chapter the probe forming semi-angle is defined by the real objective aperture, and in this project two apertures of diameter 25μm and 50μm were used. They subtended angles of 4.16mrad and 8.32mrad respectively. Before examining the aberrated system it is instructive to describe the DPC transfer function for an aberration free system. In an aberration-free system the transfer function is proportional to the areas of overlap Q_{-1} and Q_{+1}, shown schematically in figure 3.12. It should be noted, that at lower spatial frequencies the two diffracted beams themselves overlap and as their contributions are in anti-phase, signal cancellation occurs and no phase information can be derived from electrons falling on these portions of the detector. The form of the transfer function for the aberration-free system is presented in figure 3.13. It can be seen that efficiency of transfer of phase information falls at low and high spatial frequencies and for an aberration-free system the maximum DPC transfer is achieved at $\alpha_s/\theta_B \sim 2.2$. The form of the DPC transfer function for an aberrated system has been discussed in detail by Su (1989). The results from these calculations showed that for small values of α_s, the resultant transfer function was relatively insensitive to the defocus value, for α_s=4.16 mrad the optimum value being Δf=-26nm. However, as the probe forming semi-angle was increased the resultant transfer function was very sensitive to the defocus value selected, and for α_s=8.32 mrad the optimum value was determined to be Δf=-110nm. The form of the transfer function and the signal to noise ratio are presented in

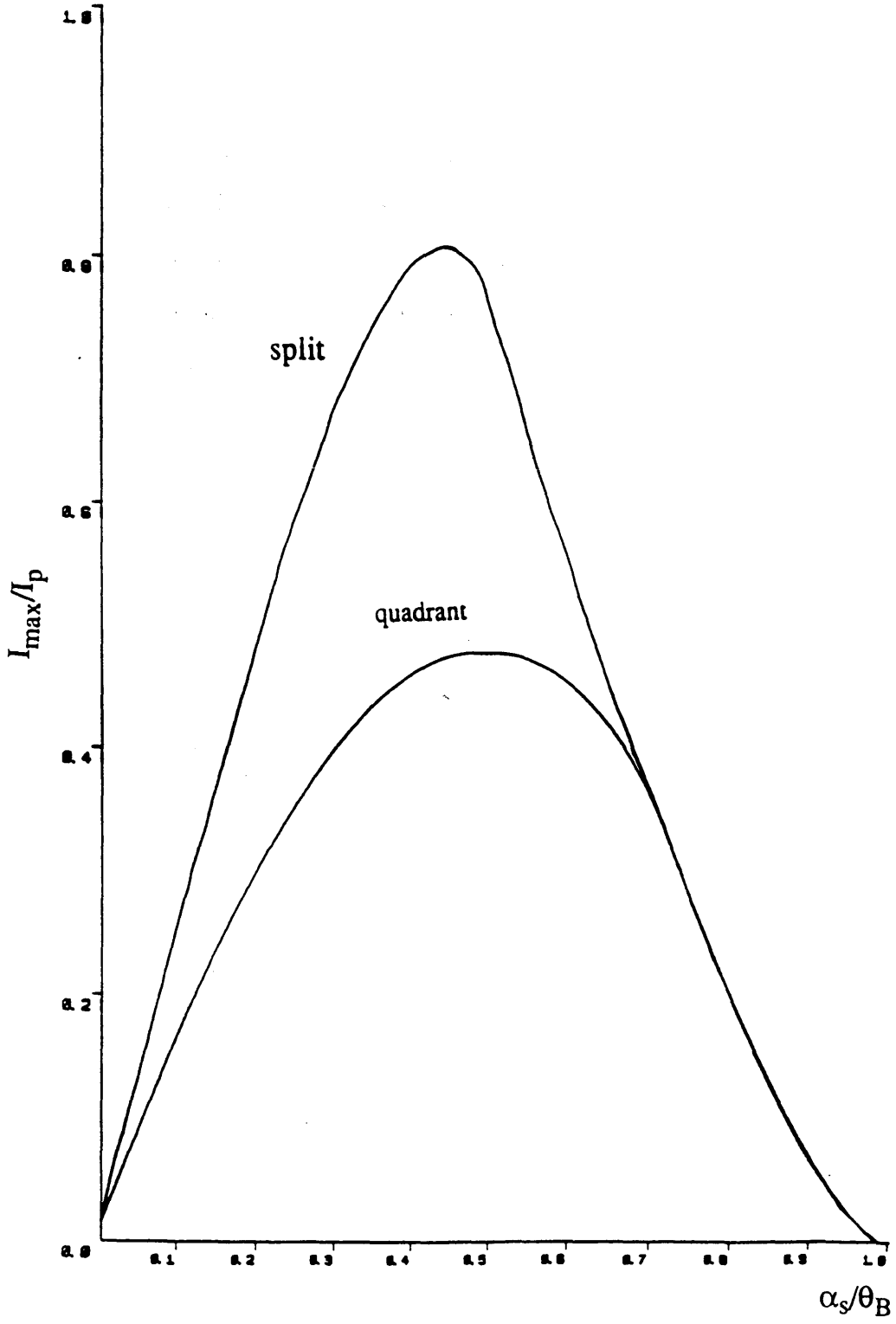

Figure 3.13: DPC transfer function for split and quadrant detectors in an aberration free system.

figures 3.14 and 3.15 respectively. The results show that for small values of α_s, spherical aberration is not too severe and the transfer function remains high over a wide range of spatial frequencies (or as presented in figure 3.15. periodicities in real space). For the case of α_s=8.32 mrad, the transfer function is still fairly high, for a range of spatial frequencies, though its magnitude is less than that obtained with α_s=4.16 mrad. It should be noted, however, that the use of a larger aperture is essential if smaller periodicities in the object are to be resolved. Using a larger aperture, such as α_s=12.48 mrad leads to poor quality image and is therefore not suitable for a lens with the spherical aberration coefficient of the objective lens in the HB5.

3.10 Efficiency of the various imaging modes.

As discussed in chapter 2, investigation of organic materials by electron microscopy is limited due to severe dose constraints. It is therefore essential that efficient imaging modes are used in the investigation of these specimens to ensure that the maximum amount of useful information is obtained before significant specimen degradation occurs. The aim of this section is to assess the relative efficiency of the various imaging modes described in this chapter, namely CTEM, STEM and DPC STEM.

For brightfield imaging in the CTEM the image intensity was shown to consist of a periodic modulation superimposed on a constant background. In the case of thin weakly scattering specimens the signal S is proportional to $2\phi_0$(Misell, 1977). The maximum signal S_{max} can be expressed as,

$$S_{max} = 2\phi_o n_o \qquad (3.40)$$

where n_0 is the number of detected electrons per pixel of the detector, n_0 is

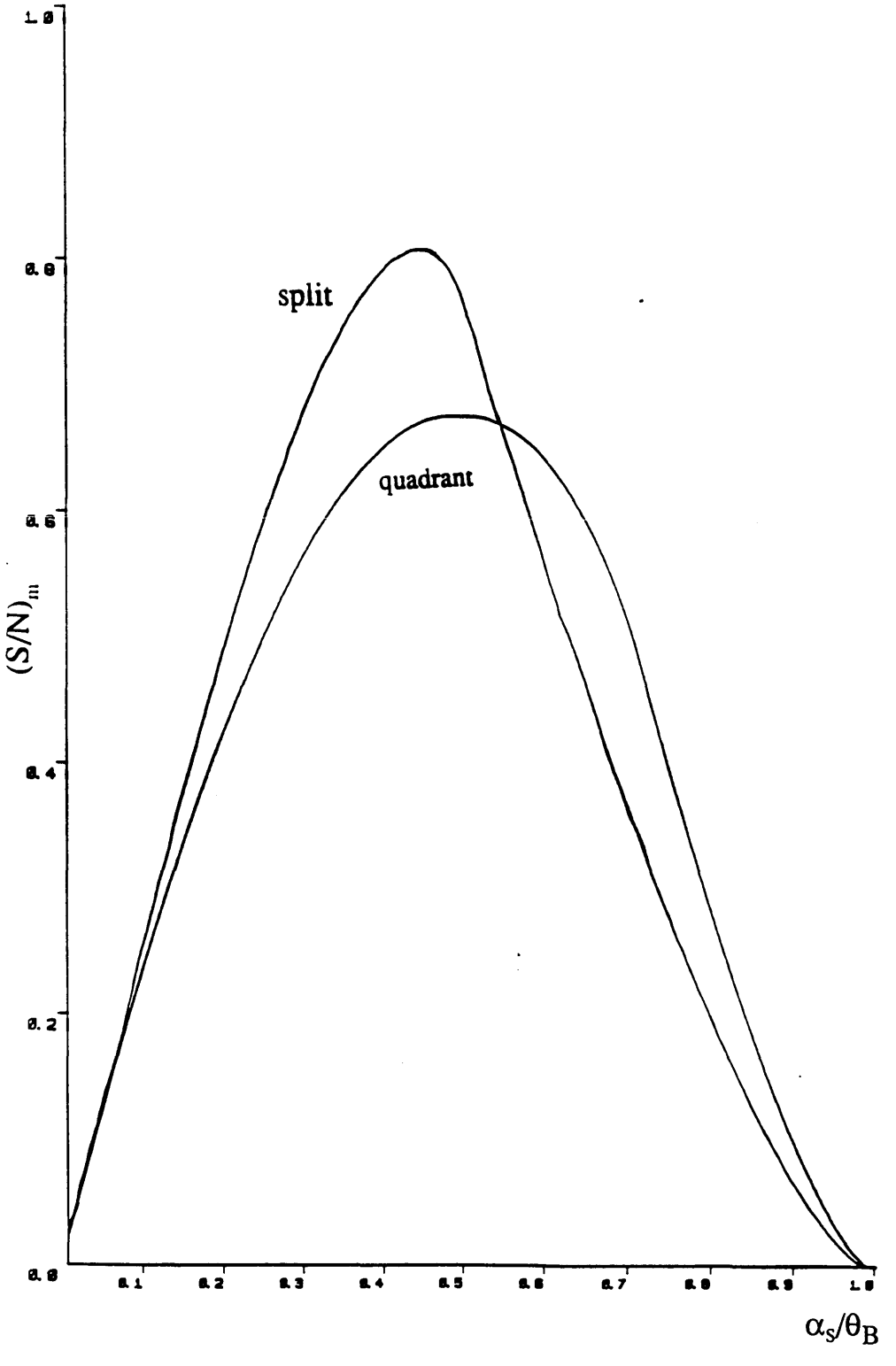

Figure 3.14: The signal to noise ratio for DPC imaging in an aberration-free system using both split and quadrant detectors.

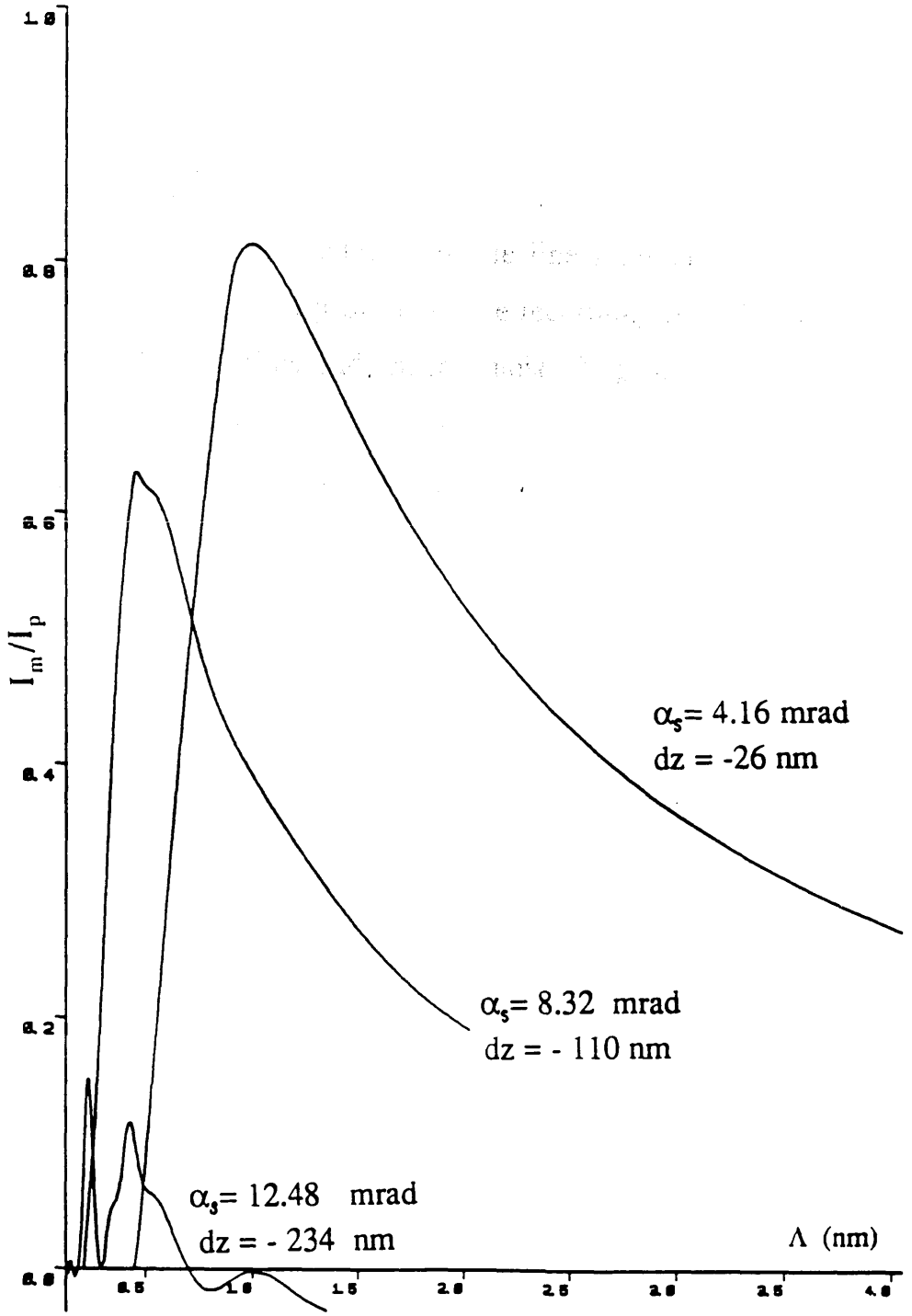

Figure 3.15: Calculated DPC transfer for different aperture sizes and optimum defoci with a split detector (Cs=3.3mm).

given by,

$$n_o = \frac{\pi B_o \alpha^2{}_c \delta^2 \tau}{e} \qquad (3.41)$$

where B_o is the source brightness, δ the linear dimensions of the pixel referred back to the object plane and τ the recording time. The noise arises from statistical fluctuations and substrate noise. Neglecting the effects of the support film, the noise signal N is determined by Poisson statistics and is given by, $N=n_o{}^{1/2}$. The signal to noise ratio is therefore given by,

$$\left(\frac{S}{N}\right)_{max} = 2\phi_o \left\{ B_o \pi \alpha_c^2 \frac{\delta^2 \tau}{e} \right\}^{1/2} \qquad (3.42)$$

This can be expressed in a simpler manner by noting that the current hitting each pixel is given by, $I_p=B_o\pi\alpha_s{}^2\delta^2$ therefore equation 3.42, can be rewritten as,

$$\left(\frac{S}{N}\right)_{max} = 2\phi_o \left\{ \frac{I_p \tau}{e} \right\}^{\frac{1}{2}} \qquad (3.43)$$

we note that in the approximations used here all the electrons going through the specimen reach the image recording plane. In the STEM the maximum signal collected by the detector can be expressed as,

$$S_{max} = 2\phi_o \frac{I_p \tau}{e} \frac{\beta_s^2}{\alpha_s^2} \qquad (3.44)$$

It should be noted that the factor $(\beta_s/\alpha_s)^2$ represents the ratio of the number of electrons collected to those incident on the specimen.

The noise can be expressed as

$$N = \left(\beta_s^2 I_p \tau / (\alpha_s^2 e)\right)^{\frac{1}{2}} \qquad (3.45)$$

The signal to noise ratio is therefore given by,

$$\left(\frac{S}{N}\right)_{max} = 2\phi_o \left\{\frac{I_p \tau}{e}\right\}^{1/2} \left(\frac{\beta_s^2}{\alpha_s^2}\right)^{\frac{1}{2}} \qquad (3.46)$$

However as discussed previously for good phase contrast effects we require $\alpha_S >> \beta_S$. This presents severe difficulties when investigating radiation sensitive specimens as the dose to which the specimen must be subjected to achieve comparable images is increased by a factor $(\alpha_S/\beta_S)^2$.

In DPC STEM the signal to noise ratio can be written as,

$$\left(\frac{S}{N}\right)_{max} = 2\phi_o\left(\frac{I_p\tau}{e}\right)^{\frac{1}{2}}\frac{O_A}{\pi\alpha_s^2} \qquad (3.47)$$

The detection efficiency is therefore seen to be dependent on $O_A/(\pi\alpha_S{}^2)$ Thus it can be seen that relative to standard STEM lattice imaging DPC STEM lattice imaging is a factor of $O_A/(\pi\alpha_S\beta_S)$ times more efficient.

In conclusion this chapter has described diffraction and image formation in the CTEM and has given a brief introduction to the theory of image formation in the STEM. The latter instrument allows a variety of novel imaging techniques such as DPC microscopy which can provide information on specimen structure not readily obtainable by other techniques.

Results obtained from the application of DPC imaging to the pigmentary materials are presented in chapter 5.

Chapter 4

CTEM IMAGING AND DIFFRACTION STUDIES OF HALOGENATED COPPER PHTHALOCYANINE PIGMENTS.

4.1 Introduction

As discussed in chapter 1, the effectiveness of a pigment in colouring the medium into which it is incorporated is strongly dependent on the size, shape and internal structure of the individual pigmentary particles. There is therefore considerable incentive to investigate these parameters for the various pigmentary samples of interest in this project. This chapter describes the application of electron diffraction and imaging techniques available in the CTEM to various forms of industrially prepared X-Cu Pc. The results obtained from the diffraction studies undertaken are presented in section 4.2. Analysis of these patterns is described in section 4.3. Electron diffraction provides information on the internal structure of the pigmentary particles; however, we are often concerned with the relation of the internal structure to the external habit of the particle. Lattice imaging provides information on the internal structure, extent of crystallinity, presence of defects and some information on the particle size and shape. The principles and instrumental considerations required for lattice imaging are considered in section 4.4. Lattice images acquired from the various materials are presented in section 4.5.

4.2 Diffraction studies of industrially prepared X-Cu Pc pigmentary materials

In chapter 3, it was shown that using the selected area diffraction

technique the smallest area from which diffraction patterns could be obtained was ~0.5μm^2. As individual pigmentary particles have dimensions significantly less than this lower limit, the only viable way of examining single particles is to have either a low particle density covering the specimen and isolate one particle within the area defining aperture or to have a selection of particles on the specimen grid. In this way there is a possibility that one of the particles will be in the correct orientation to present a prominent reciprocal lattice plane to the incident beam, while the others will simply contribute to the background intensity.

The instrumental conditions for electron diffraction required that highly coherent illumination was incident on the specimen. These conditions could be met using a small (20μm) condenser apertures and spot size 3. The procedure adopted to select suitable areas from which to acquire diffraction patterns, was to traverse the specimen in diffraction mode and select areas in this manner. This proved more successful than viewing what appeared to be a good area of specimen and then examining the corresponding diffraction pattern. Series of diffraction patterns (typically three in number) were acquired from each area using exposure times of 2,4, and 8s. This allowed both the low and high order spot spacings to be accurately measured. Determination of the lattice parameters from the spot spacings on the photographic emulsion requires an accurate determination of the camera length. This was achieved by using a standard TlCl specimen which gave a value for the camera length of (109$\pm$ 2)cm for a nominal value of 120cm.

Several industrially prepared pigmentary samples were investigated in this work. Sample A was a very highly chlorinated sample in which it was hoped that all the peripheral hydrogen atoms had been substituted by chlorine. Sample B, although also highly chlorinated, was known to retain some hydrogen. Samples C and D had both chlorine and bromine present.

The expected ratios were 15 to 1, and 3 to 13 respectively, and hydrogen was once again believed to be absent. Specimen E was a brominated sample which had been halogenated with approximately 8 bromine atoms per molecule. Sample F had both chlorine and bromine present in the expected ratio of 4 to 3. The first four materials are commercial samples, and the bulk of the investigations was concerned with these materials. The last two materials are experimental samples and were studied in the later stages of the project.

Figures 4.1 (a)-(h), show a selection of spot diffraction patterns obtained from the various pigmentary samples. Streaking was frequently observed in the patterns and indicated that the pigmentary particles had an element of disorder predominantly along one particular direction. This is discussed in section 4.3. A schematic diagram of the indexed diffraction pattern is shown in figure 4.2.

Figures 4.1 (a)-(d) are from the chlorinated samples. Considerable variations in spot spacings were present in the various chlorinated samples, and also between patterns obtained from the same material. Figures 4.1 (a) and (b) are from sample A, and have lattice spacings of 1.3 ± 0.02nm and 1.5 ± 0.02nm respectively, the distance to the outer arcs was 0.33 ± 0.02nm and 0.37 ± 0.02nm respectively. The angle between the central line of spots and the outer line is 68 ± 2^{o}. Figures 4.1 (c) and (d) are from sample B, the former has a lattice spacing of 1.5 ± 0.02nm, while the distance to the outer arcs is 0.36 ± 0.02nm. Figure 4.1 (d), shows two central lines of spots of spacing 1.4 ± 0.02nm, with the angle between the line of spots being $\sim20^{o}$. The distance to the outer arcs is 0.35 ± 0.02nm. The two lines of spots are probably due to the overlap of two suitably oriented particles.

Diffraction patterns from the highly brominated sample D are presented in figures 4.1 (e)-(h). The patterns show less streaking than those presented

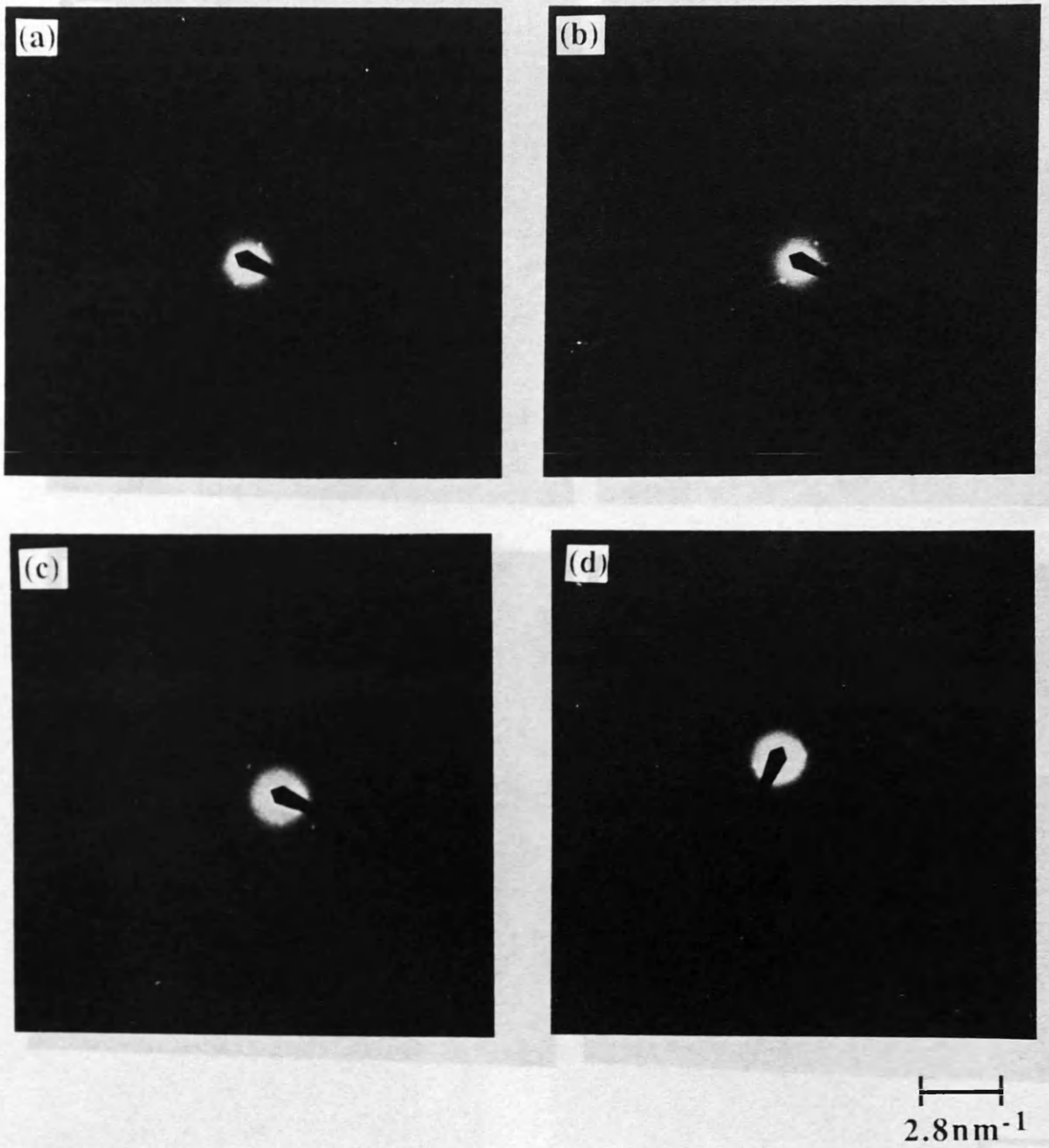

Figure 4.1: (a)-(d) Diffraction patterns obtained from the highly chlorinated pigmentary samples.

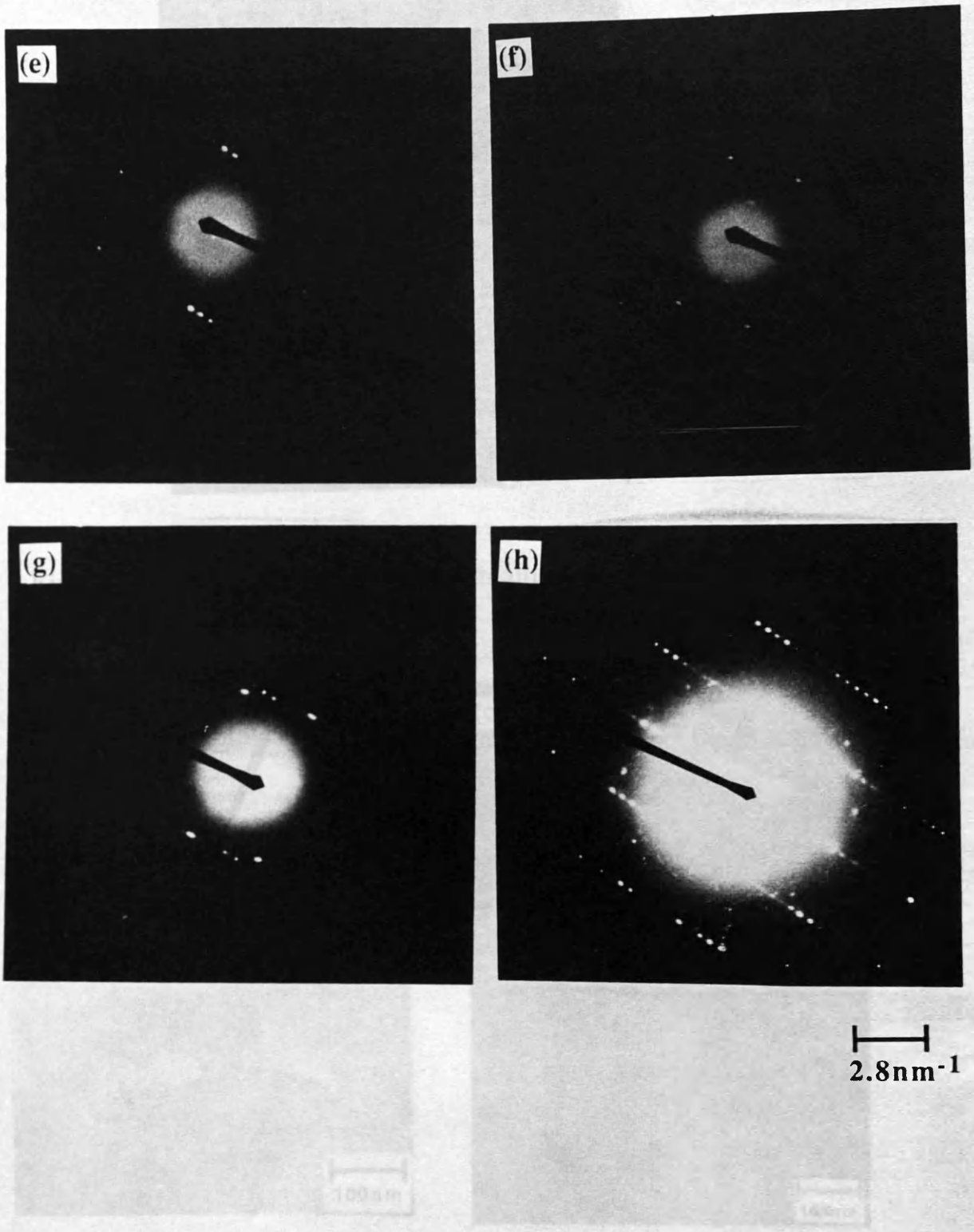

Figure 4.1: (e)-(h) Diffraction patterns obtained from the highly brominated pigmentary sample D.

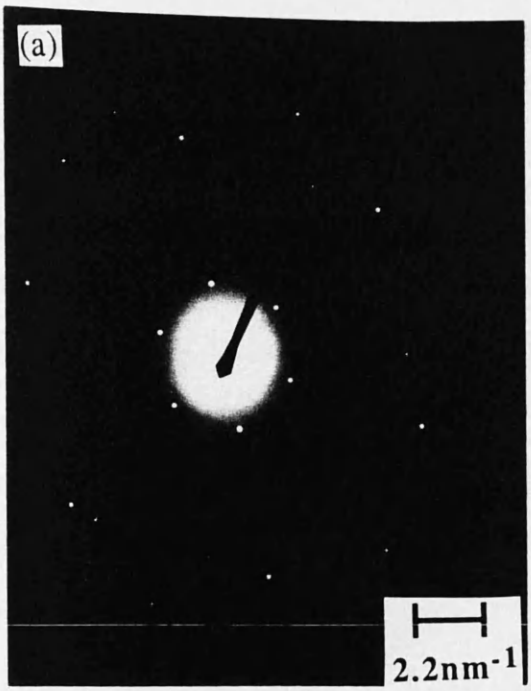

Figure 4.3: (a) Diffraction pattern obtained from the impurity material.

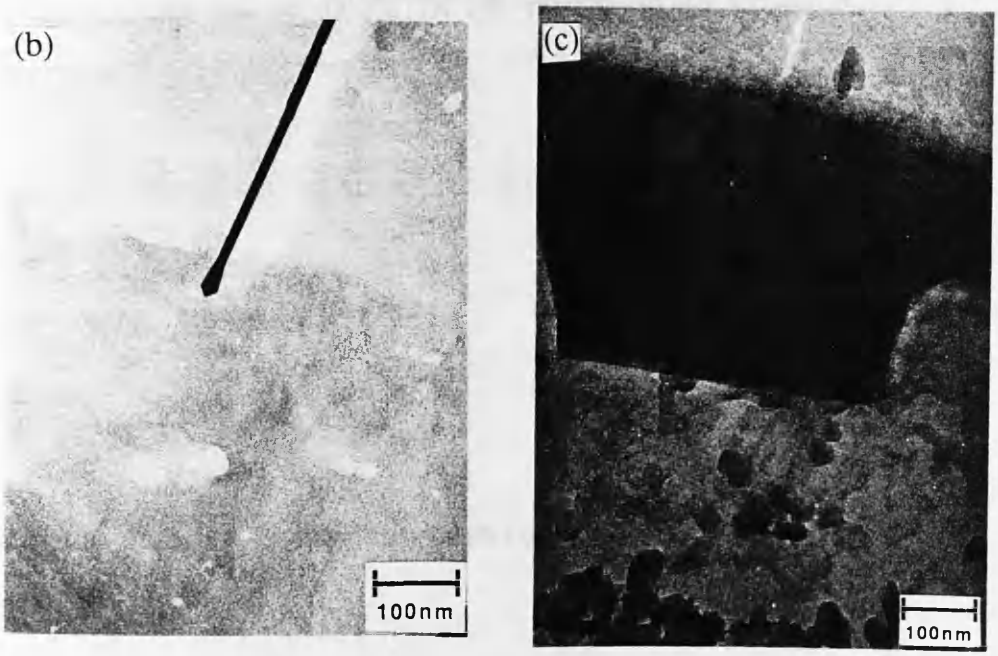

Figure 4.3: (b)-(c) Typical areas of specimen giving rise to the type of diffraction pattern shown above.

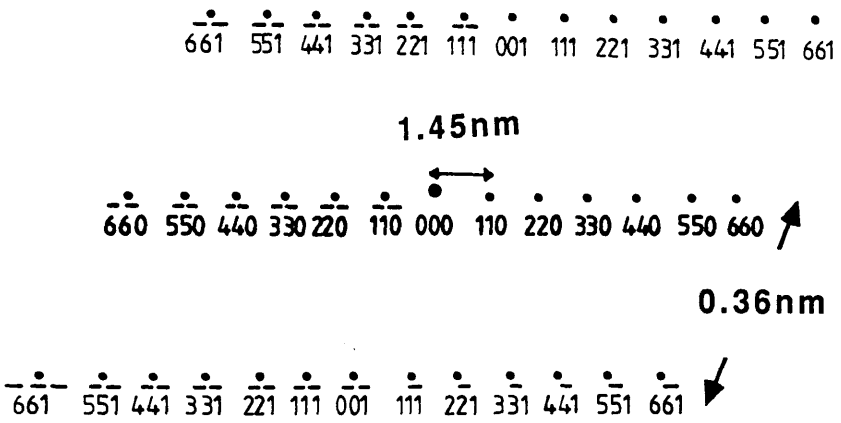

Figure 4.2: Experimentally observed reciprocal lattice plane with zone axis [110].

in (a)-(d), and in some cases particularly (e) and (h), several lines of well defined spots are present. The lattice spacing in figures 4.1 (f) and (g) was determined to be 1.4±0.02nm. The distance to the outer arcs were 0.38±0.02nm. The spacings of the spots in figure 4.1 (e) and (h), were both 2.5±0.02nm. The distance to the outer line of spots in these patterns was 0.37±0.02nm and 0.39±0.02nm respectively. The larger spacing (2.5nm) observed in figures 4.1 (e) and (h) is discussed in the following section.

It was not possible to obtain good quality diffraction patterns from the lower halogenated materials (samples E & F). The patterns consisted of faint diffuse spots on a high background, and as such these proved difficult to analyse.

One further prominent feature which was observed when scanning the specimens in diffraction mode was the occurrence of rather different two dimensional diffraction patterns, such as that shown in figure 4.3 (a). These patterns possessed six-fold symmetry with the angle between any triangular grouping being 60.0°±0.5°, with lattice spacing of 0.45±0.02nm. The patterns, were more frequently observed in sample D than in the highly chlorinated materials, and could be associated with extremely thin slabs of material of dimensions considerably greater than the pigmentary particles, as shown in figures 4.3 (b) and (c). Using EDX microanalysis on the JEM 100C, it was not possible to definitively identify the elements present in these slabs. The two major reasons for this were that the count rate from these thin slabs was very low and that, in addition to the aluminium peak, which was believed to be characteristic of the impurity material, titanium, chlorine, copper and bromine peaks were also present in the spectra. The titanium peak was due to scattering of electrons onto the specimen grid and the last three peaks were due to scattering onto pigmentary particles in the surrounding area.

To try to identify this unknown material it is instructive to examine possible impurities that could have been introduced in the industrial

preparation of the material. These include sodium chloride, aluminium chloride and aluminum hydroxide. Neither sodium nor aluminium chloride can give a diffraction pattern of the type observed, (Drummond, 1985). The last material aluminium hydroxide exists in many crystalline forms, one of which is, Type A β aluminium hydroxide (commonly called bayerite), which forms a hexagonal crystalline structure with d=4.38Å (determined by powder x-ray diffraction). As bayerite is of the correct crystal type and has comparable lattice dimensions to the impurity observed, it seems a likely candidate for the unknown structure.

4.3 Analysis of diffraction patterns

The major lattice spacings and angles between the reciprocal lattice vectors are presented in figure 4.4. To calculate these parameters the structure of the pigment was taken to be that of the epitaxially prepared fully chlorinated Cu Pc. This was found by Uyeda et. al. (1972) to be a monoclinic c-face centred lattice with the following unit cell dimensions.

a=1.96nm
b=2.6nm
c=0.36nm
β=116.5°
Space group C2/c or C2/m.

The spacings obtained from figures 4.1 (a)-(d) could therefore be assigned to the (110) or (020) and (001) reflections. The angle between the (020) and the (001) reciprocal lattice vectors is, however, 90°, whilst that between (110) and (001) is 68°. This means that the spots can be indexed only

in terms of the (110) and (001) lattice vectors. From the spot indexing described above, the zone axis [uvw] could be readily calculated, and was determined to be [110]. In the case of the epitaxial material a zone axis of [001] is observed. To understand why a different zone axis is observed in the pigmentary material it is instructive to examine the different growth mechanisms involved. As discussed in chapter 1, epitaxial growth results in extensive crystalline regions in the a-b or molecular plane. Tilting through 26° about the column axis then results in the incident beam passing along the [001] zone axis presenting the a*-b* reciprocal lattice plane. In the case of the pigmentary material, where the constraints imposed on epitaxial growth are absent, the molecules initially tend to form long oblique columns. These columns are then attracted together by weaker Van der Waals forces. Due to the weak nature of the bonding between the columns, variations in the crystal form adopted are to be expected. The separation of the molecules in the highly chlorinated materials was determined to be 0.33 ± 0.02nm, 0.36 ± 0.02nm, 0.35 ± 0.02nm and 0.37 ± 0.02nm for figures 4.1 (a), (b), (c) and (d) respectively. In the highly brominated sample the corresponding spacings were 0.37 ± 0.02nm, 0.38 ± 0.02nm, 0.38 ± 0.02nm and 0.39 ± 0.02nm for figures 4.1 (e), (f), (g) and (h) respectively. The measured column spacings in the highly brominated sample were greater than in the chlorinated samples; this suggests that packing the large bromine atoms into the structure is not as effective as packing the chlorine atoms, and that expansion in the column axis is a consequence of this. This is in accordance with the fact that the covalent radii for bromine is 0.115nm which is greater than that of chlorine which is 0.099nm. The difference in these two values is approximately equal to the measured differences obtained from the diffraction patterns.

The 2.5nm spacing, observed in figures 4.1 (e) and (h) cannot be indexed

in terms of the reciprocal lattice vectors presented in figure 4.4. To ensure that the spacings were being accurately measured, a further series of diffraction patterns were obtained from sample D using a larger camera length (200cm). The camera length was recalibrated using the TlCl specimen which gave a value of 189±2cm for the nominal value of 200cm. The values obtained for the spacing were the same as those previously determined. To try and explain this spacing, which was only observed in sample D, it is again instructive to examine the ways in which the molecules can stack in these molecular crystals. In Cu Pc, there are essentially two ways in which effectively planar molecules can stack together and these are shown schematically in figure 4.5 (a) and (b). The major differences between α and β Cu Pc has been discussed by Fryer et. al. (1979). In the α-phase, all the molecules are stacked in parallel, whereas in the β-phase, the planar molecules are stacked in zig-zag columns, such that the copper atom in one molecule is above a nitrogen atom in the underlying molecule. This permits octahedral coordination of the copper atom and accounts for the higher stability of this phase. It was also shown that the lattice structure of a growing crystal can have a marked effect on its morphology. For example in β-Cu Pc the stacking sequence and differing number of molecular contacts in different directions confer marked anisotropy on this phase. This is shown in figures 4.6 (a) and (b). For example a (010) plane at the surface of a growing crystal exposes the faces of the Cu Pc molecules. In contrast the (201) and (001) planes would reveal only the edges of the molecules. Thus, in the absence of external constraints, additional Cu Pc molecules are most readily attached to the crystal by superimposition on to (010) crystal faces, and least readily attached to the (201) and (001) faces. Consequently, crystals tend to adopt a brick shape, growth being most rapid in the direction of the b-axis perpendicular to the (010) plane. Additionally, octahedral coordination will also favour addition to the (010) faces. The sides of the crystals will be

Spot Indices (hkl)	Lattice Spacings (nm)	Angle between pairs of reciprocal lattice vectors.	
200	0.88		
		90°	
020	1.30		
		56°	64°
110	1.45		
		68°	
001	0.36		

Figure 4.4 : Lattice spacings corresponding to various diffraction spots and the angles between the {hkl} planes.

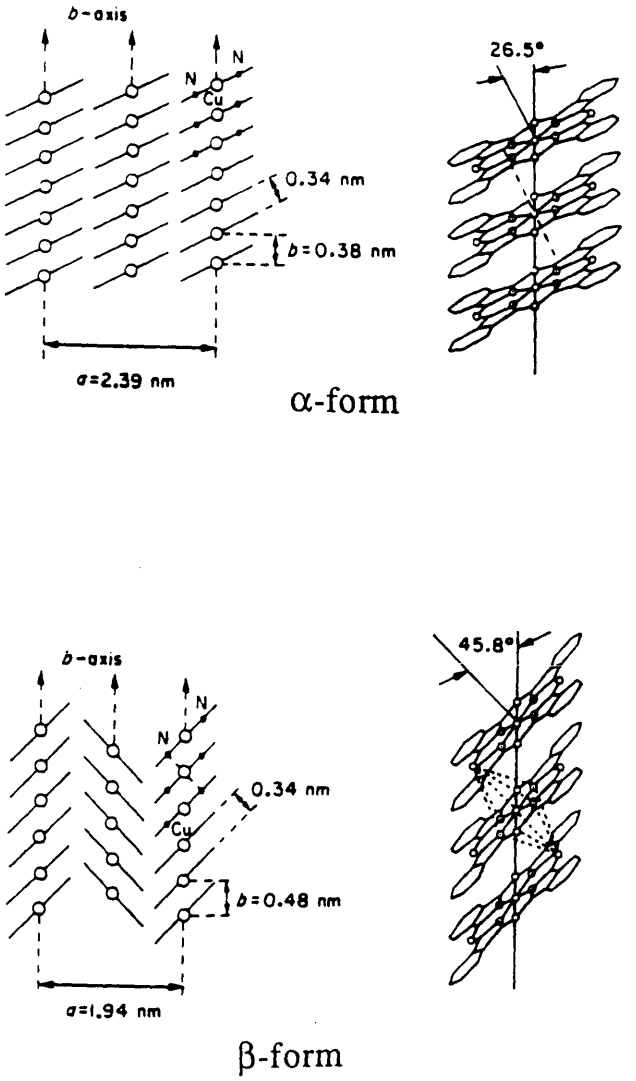

Figure 4.5 : Schematic representations of the α and β-crystal modifications of copper phthalocyanine showing the differences in stacking arrangements and the octahedral coordinations of the central copper atom in the β phase (after Honigmann and Horn, 1968).

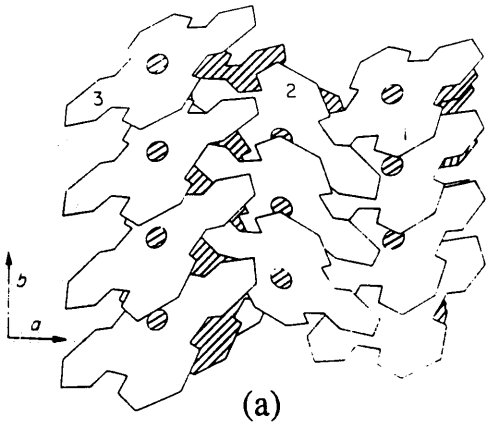

(a)

Figure 4.6 (a) : The β-phase crystal viewed in perspective from the {001} direction, i.e. at right angles to the b-axis. The numbered molecules are also shown in figure 4.6 (b).

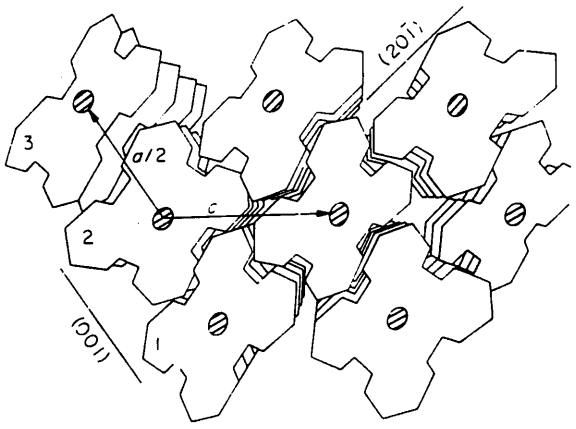

(b)

Figure 4.6 (b) : The β-phase crystal viewed in perspective from the [010] direction, parallel to the b-axis. Unit cell axes and principal growth planes are delineated (after Fryer et. al., 1979).

bounded by the (201) and (001) faces, and their ends will consist of (010) faces.

In the α-phase, there are no planes with a high density of near-neighbour contacts, and in the absence of octahedral coordination reduces the attraction of the β-axis as the predominant direction of growth. Thus, the potential for growth would be expected to be similar in all three directions.

The results presented suggest that in the highly chlorinated materials an α-type stacking is adopted, with the molecules stacking in parallel. This form of stacking in chlorinated Cu Pc's has been discussed by Fryer (1977). Streaking in the diffraction patterns indicates that deviations in this stacking sequence are present, a defect structure is described later on in this section to account for the observed streaking. The results obtained from the highly brominated materials suggest that they sometimes adopt a β-type configuration. This is discussed more fully in section 4.5.

Reference to a collection of standard diffraction patterns (e.g. Harburn et. al., 1975) shows that the observed streaking can be explained on the basis of several defect models. A common feature of these defect models is that ordering is altered along one direction whilst being preserved along the other. Streaking is then introduced along the direction in which a departure from the periodic structure can be viewed. The results obtained suggests that the highly chlorinated samples have a defect structure comprising twinning about a [110] twin plane and that the molecules lie on the substrate with this axis approximately parallel to the incident beam. This structure is shown schematically in figure 4.7. The effect of this twin structure is to superimpose a second array of spots similar to the original pattern but reflected through a plane perpendicular to the inner line of spots. The (001) spot is at an angle of 68° to the central line and the (331) spot is at an angle of 72° on the other side. In a twinned structure the spots will therefore appear at

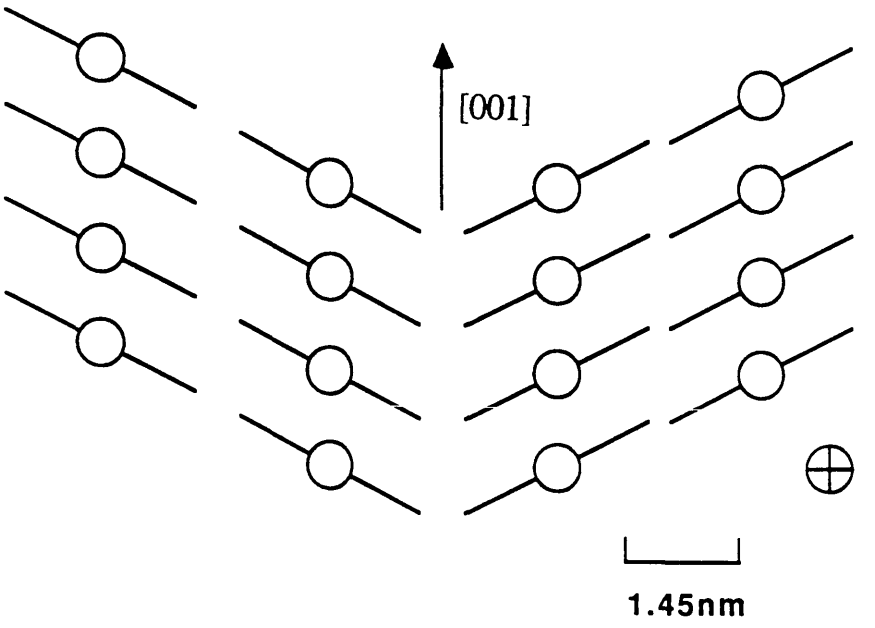

Figure 4.7 : Schematic diagram of a twinned structure.

68° and 72° on both sides. The streaking observed in many of the patterns precludes measuring the spot positions accurately and so the twin contributions are concealed. In figure 4.1 (e), the outer line seems to have a single prominent spot at 68° to the inner line, whereas, figures 4.1 (f), (g) and (h), have two bright spots at 68° on either side rather than one at 68° and 72°.

The fact that twinning is observed to be extensive simply reflects the small difference in energy that is involved when columns of molecules bind in almost equivalent orientations. Experimental evidence for twinning in molecular crystals, has been obtained by (Kobayashi et. al., 1982) who observed twinning in Zn Pc using high resolution electron microscopy (HREM), and by Drummond (1985) who used diffraction in a STEM to make a detailed investigation of the internal structure of highly chlorinated Cu Pc pigmentary particles.

4.4 Instrumental considerations for lattice imaging

The aim of this section is to give a brief description of the instrumental requirements for lattice imaging in the CTEM. The basic principle of lattice imaging is that interference between the diffracted and undiffracted beams gives rise to an image intensity which consists of a constant background superimposed on which is a modulation with the period of the lattice. The scattering and subsequent interference of beams from crystal planes is illustrated schematically in figure 4.8.

To obtain high contrast lattice fringes, it is important that highly coherent incident illumination is used. Conditions similar to those discussed in section 4.2 were adopted, with a condenser aperture of 20μm and spot size 2 being used. A further important factor in obtaining good quality images is the

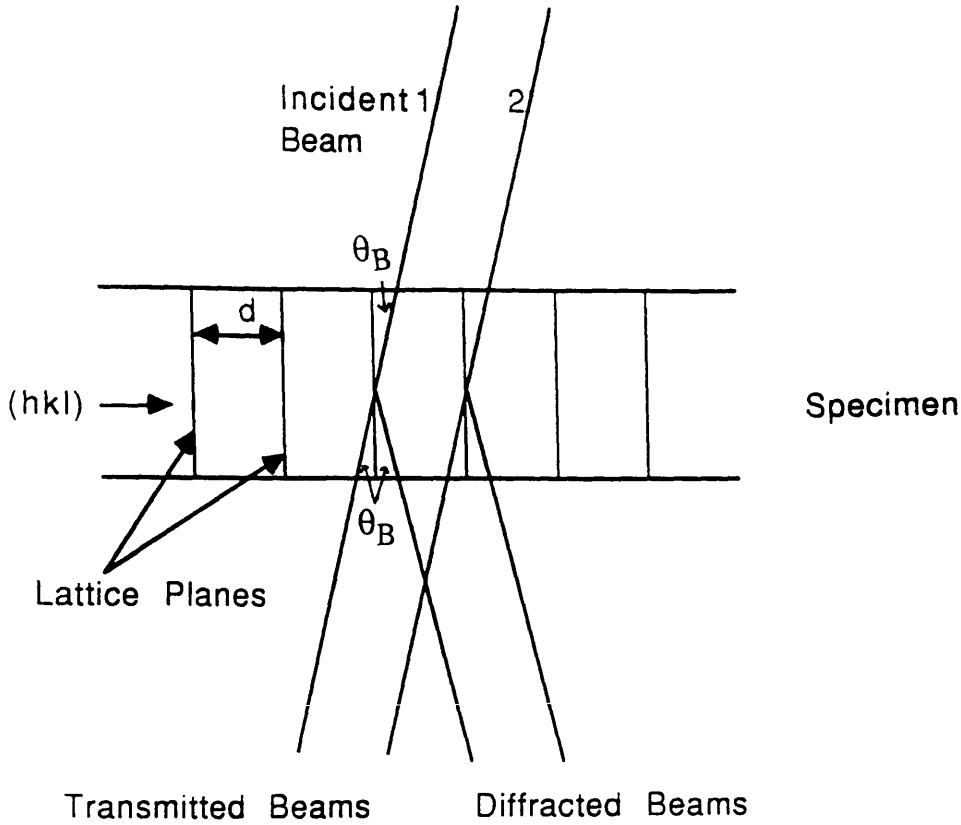

Figure 4.8 : Schematic diagram showing formation of a lattice image.

correction of objective lens astigmatism. The holey carbon films used to support the pigmentary material were useful for this purpose since, at low magnification <100kX, astigmatism can be corrected by using the underfocus and overfocus Fresnel fringes around the perimeter of a small hole by making adjustments so that the fringe is symmetrical. At higher magnifications a more accurate test uses the 'grainy' structure of the carbon film itself. The criterion for correction is that there should be no obvious directionality in the appearance of the film. The discussion regarding instrumental conditions pertinent to lattice imaging so far have been applicable to any specimen. However, as discussed in chapter 2, other factors are important when investigating radiation sensitive specimens. In particular it is essential that the electron dose be kept as low as possible to minimise the damage experienced by the specimen. The use of a MDS to satisfy these requirements was discussed in chapter 2, and was used extensively in this project. To allow low exposure times to be employed, the use of fast photographic emulsions are important. To satisfy this requirement x-ray film was found to be appropriate. The type of film used in this project was CEA Reflex-15 which allowed high contrast images to be obtained using an exposure time of 1s and a current density of ~1pAcm^{-2} (measured at the viewing screen). As this corresponds to a dose of ~1Ccm^{-2}, which is substantially less than the critical dose for these materials (Table 2.1), the images obtained are virtually free from damage. Also used in this project to acquire images was a video system. This comprised a camera with a silicon intensifier target tube (SIT) viewing a single crystal YAG screen which was located underneath the camera chamber. Images were then transferred to an Arlunya image processor. This system allows real time noise reduction and image enhancement to be performed. The resultant image can then be transferred and stored on videotape.

4.5 Experimentally obtained images

Two studies were undertaken to characterise as fully as possible the shape and structure of the various pigmentary samples. The first was to record series of low magnification images (75kX) of all the pigmentary samples. These allowed the size and shape of the particles to be assessed. The second set of images were acquired at higher magnifications (150-200kX); these provided information on the internal structure of the particles through the presence of lattice fringes.

4.5 (a) Low magnification results

Low magnification images from the highly chlorinated samples are presented in figures 4.9 (a)-(c). In all of the figures the shape and size of the individual particles is similar, the particles appear to have similar dimensions in all directions with typical dimensions ~50nm (close to the optimum particle size). Also shown for reference in figure 4.9 (d) is the unhalogenated parent material α Cu Pc. The particles in this sample appear more rod like with typical dimensions 50-100nm. Images from the highly brominated particles are presented in figure 4.9 (e). The particle shape is quite different from those in the previous images. The particles are more elongated, approximately brick-shaped with the major axis of the particle being greater than 50nm. Figure 4.9 (f), from the lower halogenated sample E shows considerable variations in particle size and shape. There are irregular shaped particles of dimensions ~50-100nm and also thin elongated particles of dimensions greater than 200nm. Images from sample F are presented in figures 4.9 (g) and (h). Striking variations in the particle size and shape are apparent in these images. There are fairly regularly shaped particles of

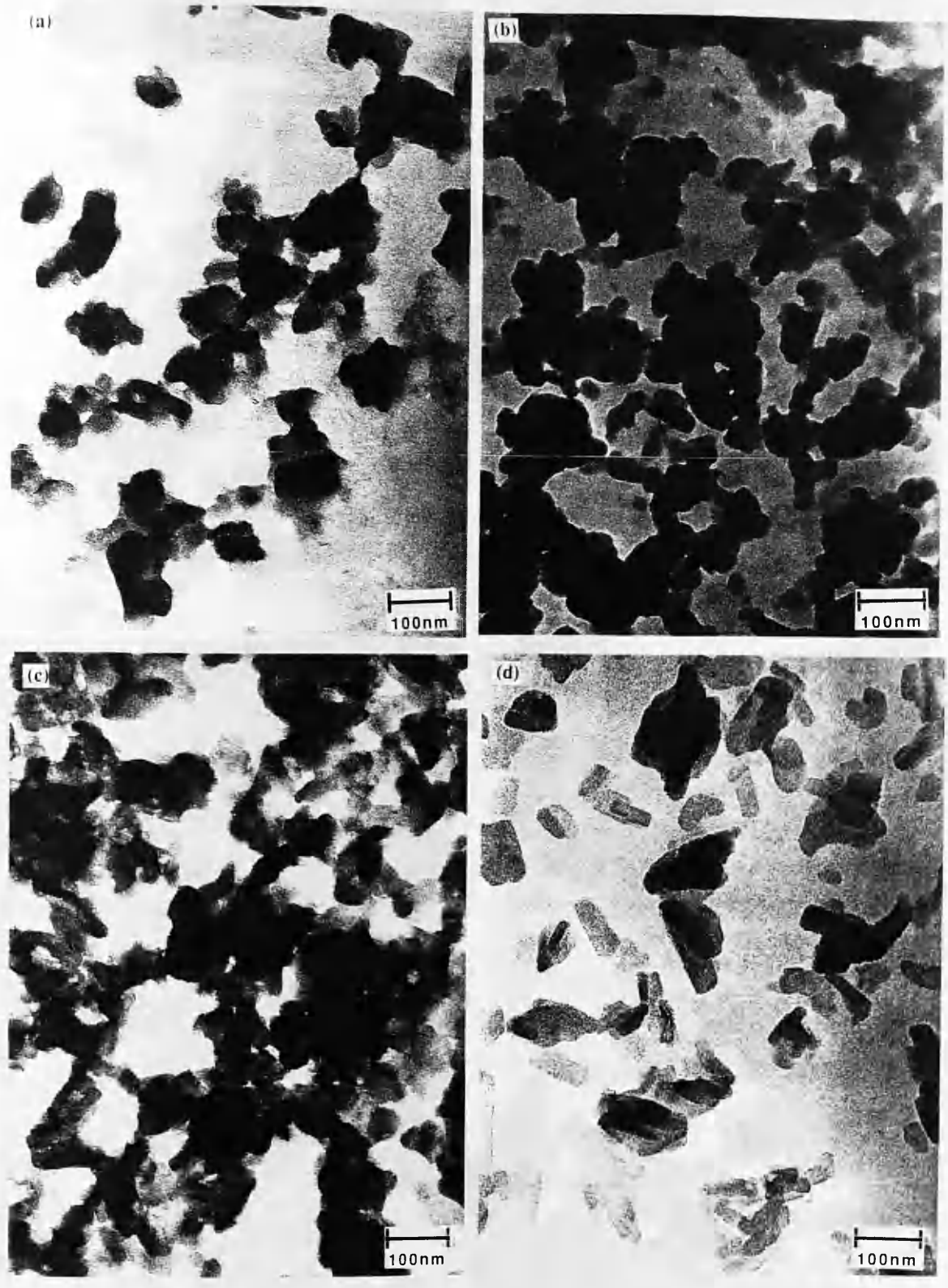

Figure 4.9: (a)-(c) Low magnification images from the highly chlorinated pigmentary samples (d) is from the unhalogenated α Cu Pc.

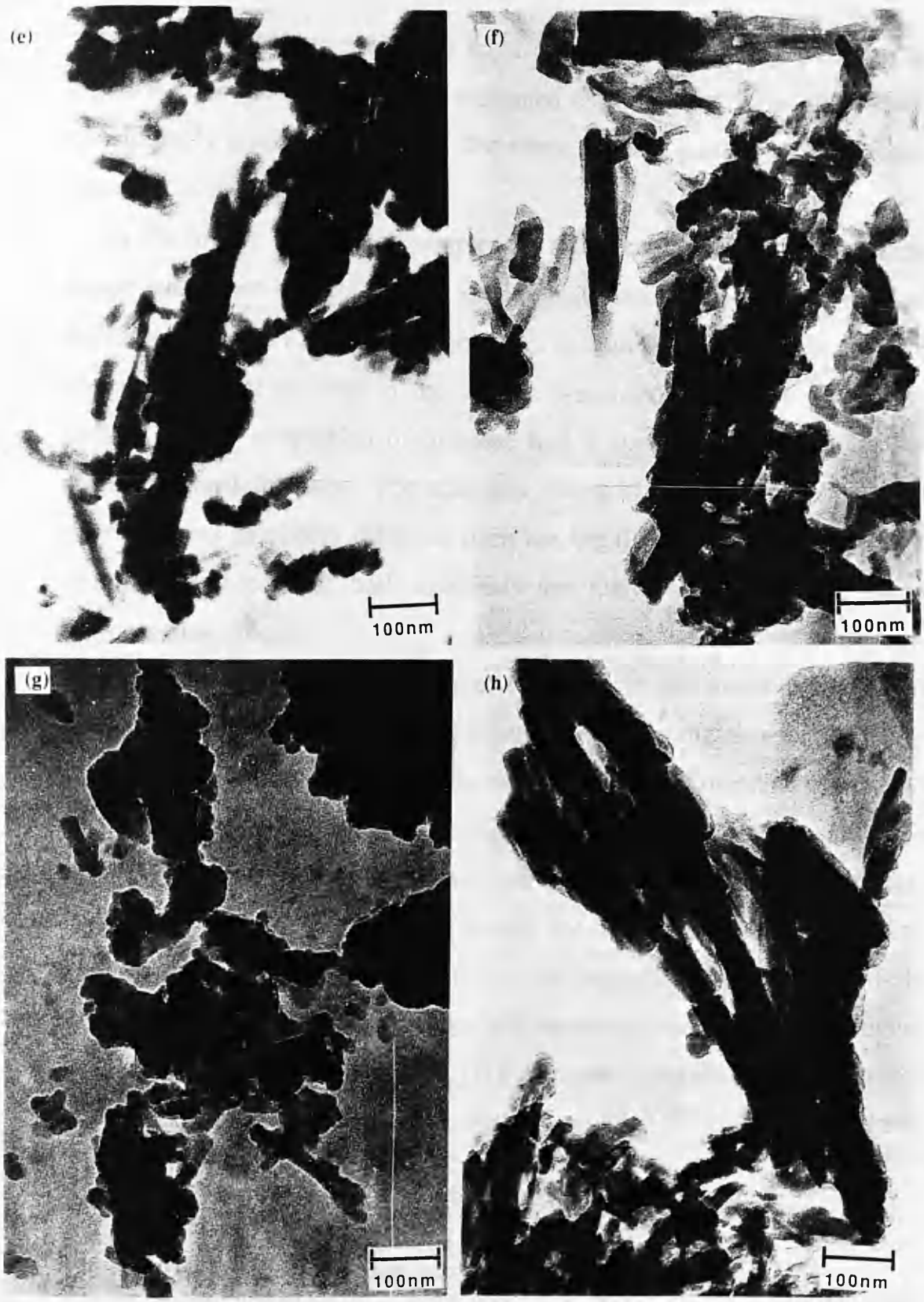

Figure 4.9: (e) Low magnification image from the highly brominated sample D, (f) and (g) are from the lower halogenated sample E and (h) is from sample F.

dimensions 50-100nm present in areas of figure 4.9 (g). The particles in figure 4.9 (h), however, are thin elongated entities with larger dimensions considerably greater than 200nm. The shape of these particles is even more pronounced than in sample E.

In the highly chlorinated samples no significant difference in particle shape was observed between the various materials. The low proportion of bromine added to sample B did not seem to significantly alter the particle shape. However as seen in the images presented in figures 4.9 (e)-(f) increasing the proportion of bromine had a considerable effect on the resulting particle shape. The size and shape of the highly brominated particles was markedly different from the highly chlorinated samples. It should be noted that both materials are manufactured by the same pigmentation process.

A variety of particle shapes was observed in the lower halogenated samples. The fact that these are experimental samples suggests that this may be a consequence of variations in the substitution of hydrogen atoms around the periphery of the molecule by halogen atoms, the resultant shape being a function of the bromine/chlorine content of the individual particles. Unfortunately this could not be tested due to difficulties in obtaining compositional information from individual pigmentary particles. This is discussed in detail in chapter 7, where it is shown that to obtain compositional information with an accuracy of ± 0.5 halogen atoms/molecule requires analysis of volumes containing approximately 10^8 molecules (~1500 particles).

4.5 (b) High magnification results

Lattice images obtained from the highly chlorinated samples are

presented in figures 4.10 (a)-(d). In all of these images extensive lattice fringes are present. Figure 4.10 (a) is from sample A and (b) from sample B. Lattice fringes of 1.4nm are present in both these images, corresponding to the (110) lattice spacings. Figure 4.10 (c) and (d) are from the sample B. In the former image lattice fringes of 1.4nm and 0.57nm can be clearly seen and correspond to the (110) and (310) lattice spacings. This indicates a zone axis of [001] and not [110] as presented previously. In figure 4.10 (d), several regions of fringes can be discerned, with bending of fringes present at (A) and a small disordered region of fringes at (B).

Lattice fringes from the highly brominated sample are presented in figures 4.11 (a)-(f). In figure 4.11 (a), the particles are elongated approximately brick shaped particles with roughly rectangular corners. Lattice fringes of spacing 1.4nm lie approximately parallel to the major axis of the particles. The next image, figure 4.11 (b) shows several fringe separations of 1.2nm, 1.4nm and 2.2nm respectively. Series of fringes can be seen to change into larger fringes of approximately twice this dimension. This fringe spacing is comparable to that obtained in some of the diffraction patterns. A similar result has been obtained by Howitt (1976) in β Cu Pc, again suggesting a strong similarity between the highly brominated material and β Cu Pc. Figure 4.11 (c) shows a highly disordered region of specimen. Severe bending of lattice fringes is observed at A. Notable is that lattice fringes, whilst suffering severe bending, can remain continuous throughout the crystal. The presence of an edge dislocation is observed at B.

Figure 4.11 (d) shows two edge dislocations lying approximately anti-parallel. A schematic diagram of their relative orientation is shown in the top left hand corner for convenience. Edge dislocations, oriented in this manner, can recombine to form a row of vacancies or interstitials which is normally an energetically favourable process since the elastic strains are largely eliminated, as has been discussed by Van Bueren (1960). The following

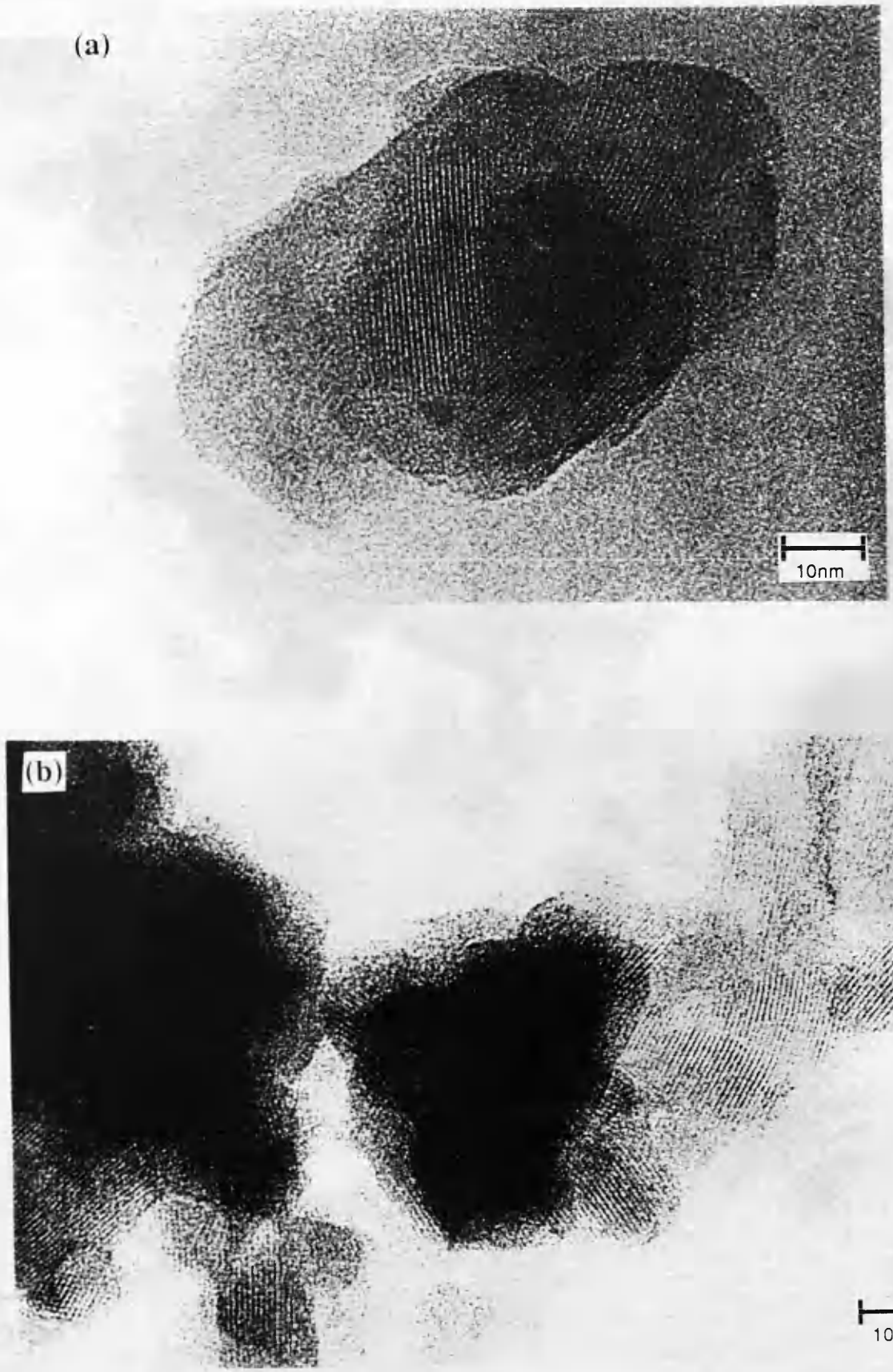

Figure 4.10: (a)-(b) Lattice images from the highly chlorinated pigmentary particles.

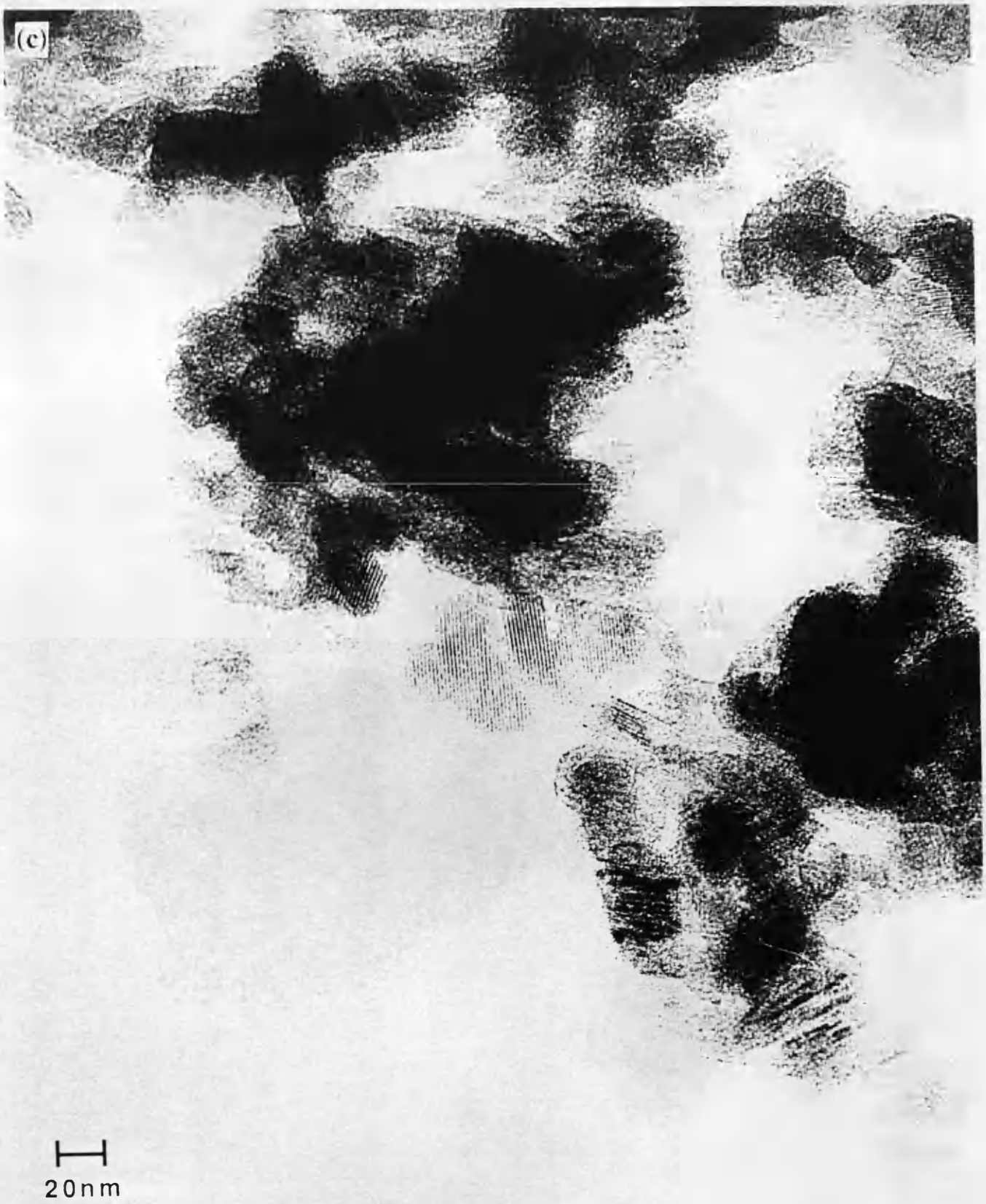

Figure 4.10: (c) Lattice image from the highly chlorinated pigmentary particles.

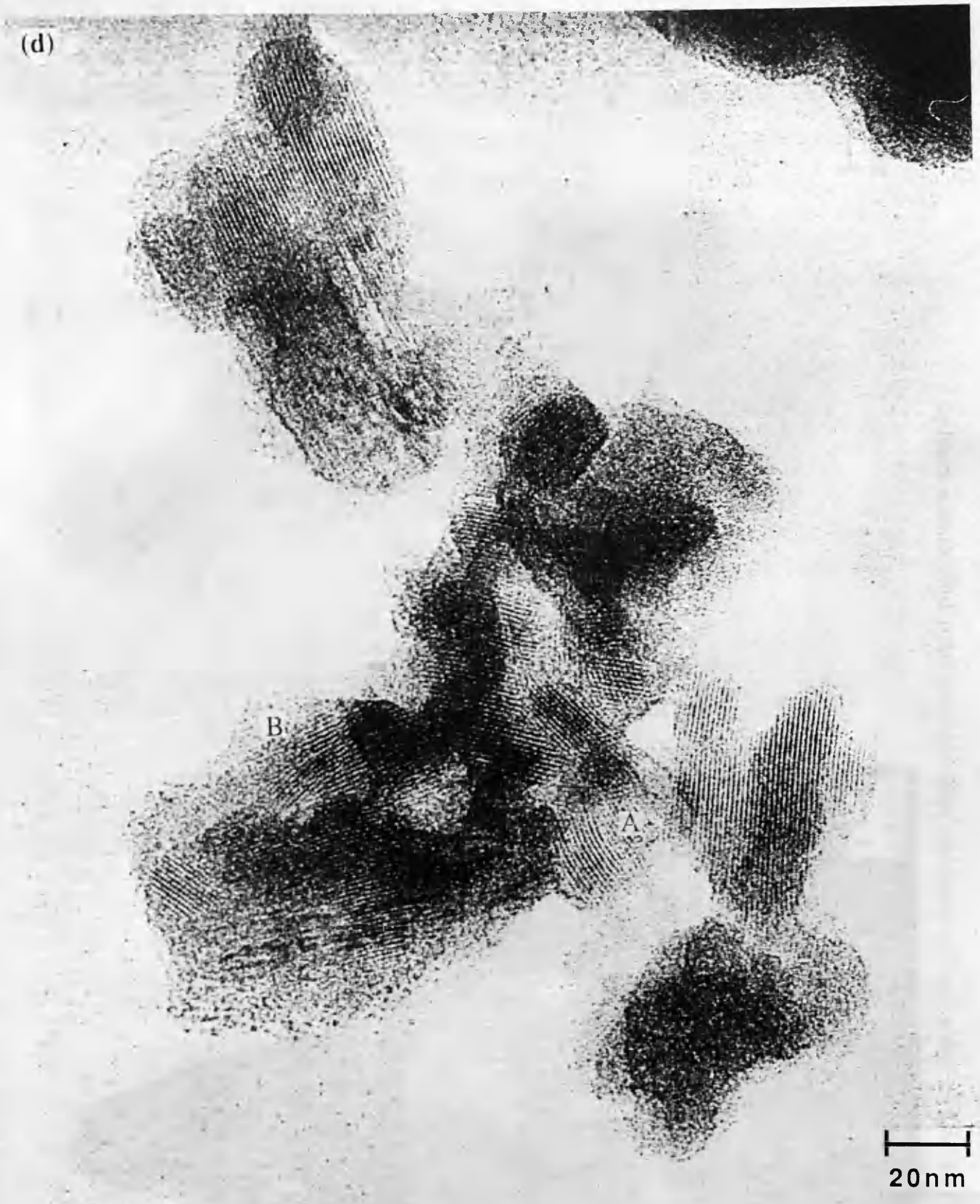

Figure 4.10: (d) Lattice image from the highly chlorinated pigmentary particles.

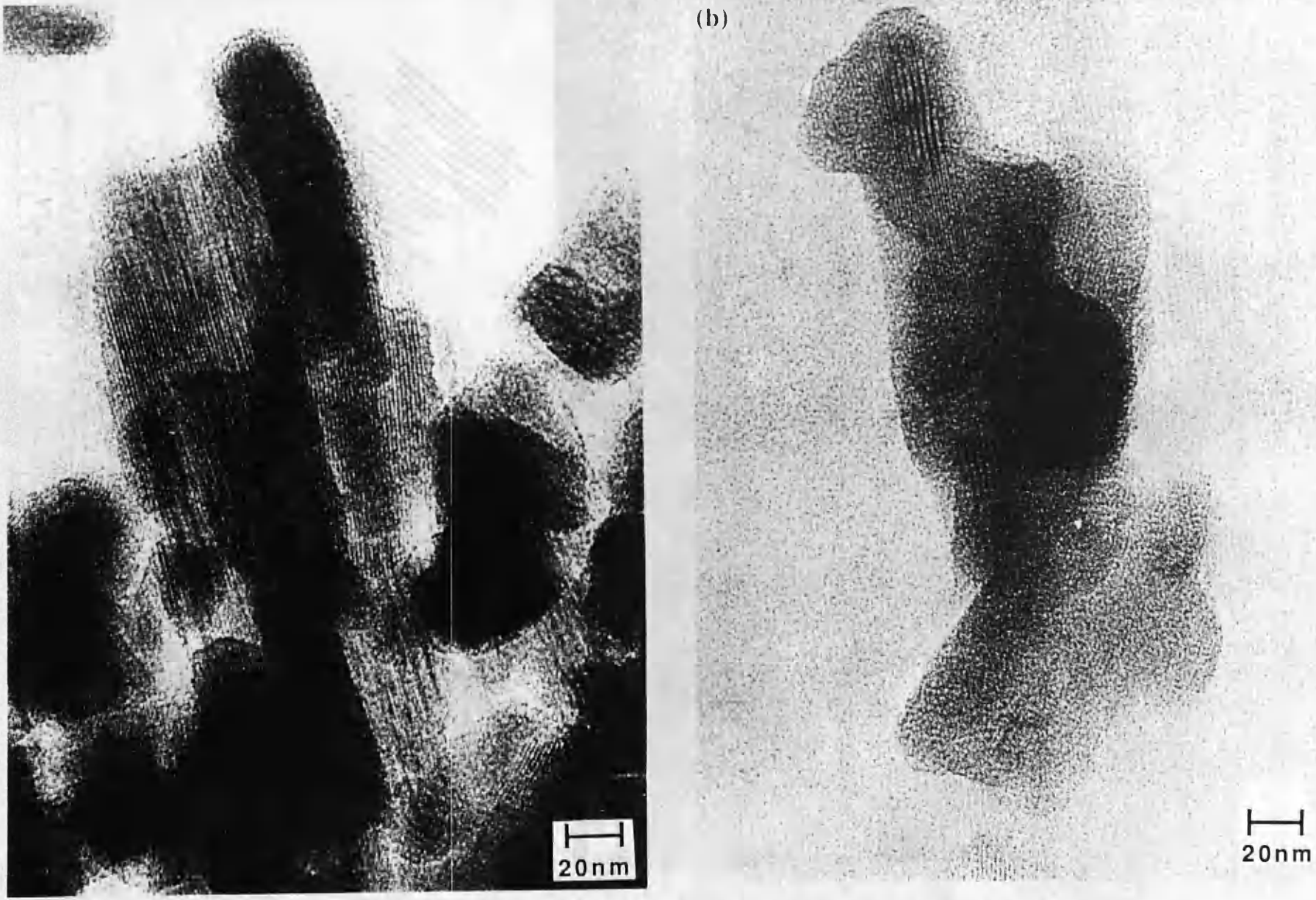

Figure 4.11: (a)-(b) Lattice images from the highly brominated pigmentary sample.

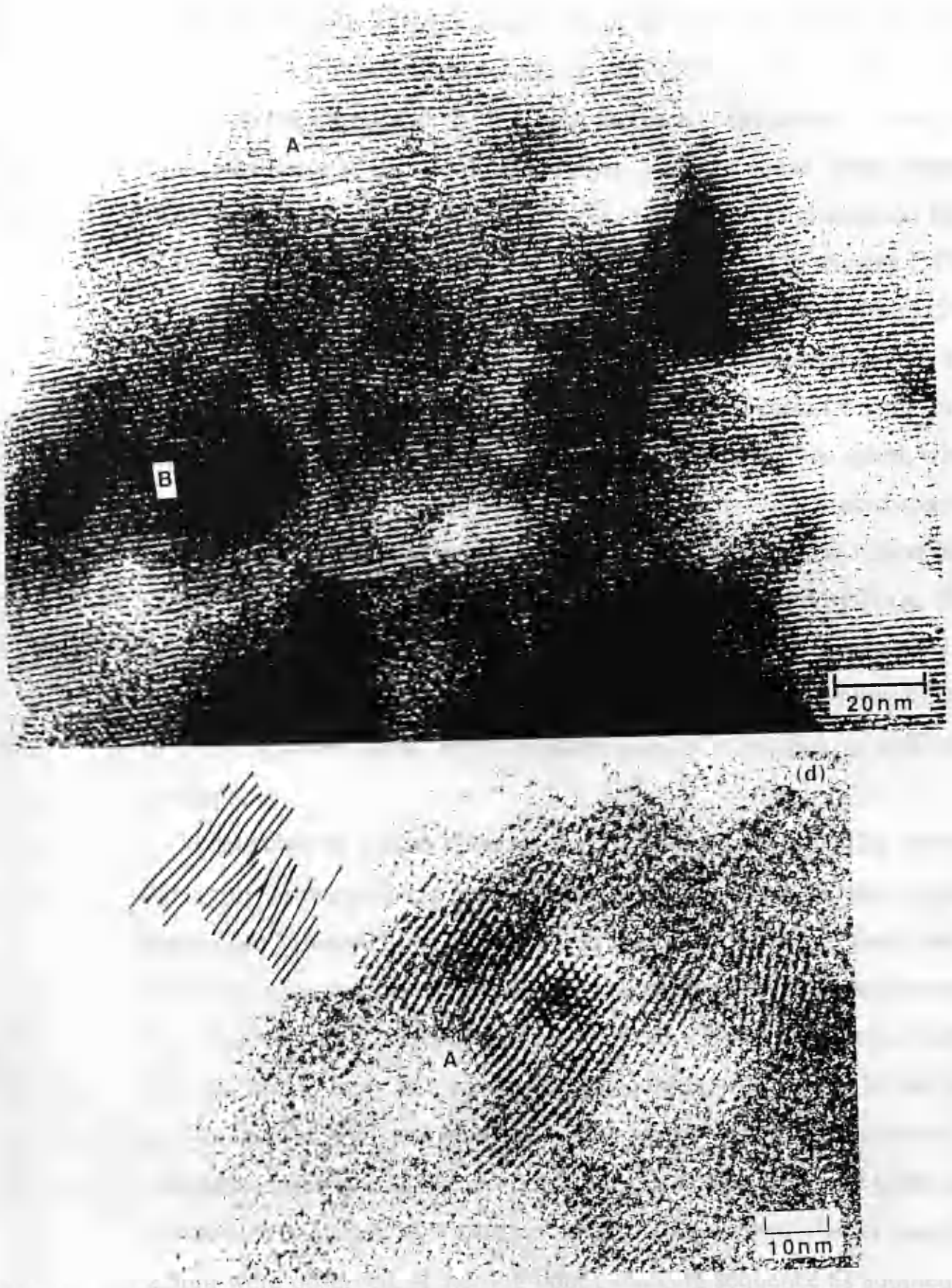

Figure 4.11: (c)-(d) Lattice images from the highly brominated pigmentary sample

image, figure 4.11 (e) shows an extensive region of crossed lattice fringes. The fringe spacing corresponding to the (110) and (020) lattice spacings. It can be seen that this indicates a zone axis of [001] i.e. the incident beam is parallel to the c-axis and the resulting image is a projection of the planar molecules stacked in columns. Images such as these were observed infrequently and suggest that this was an unfavourable orientation for the pigmentary material dispersed on the grids as described in chapter 1. Figure 4.11 (f), shows a vortex like structure of dimensions ~ 40nmx50nm. Formation of features such as this are frequently associated with spiral growth, initiated by the presence of a screw dislocation on the crystal surface. Significant thickness variations are evident across the spiral, with the maximum thickness being in the dark central regions. This is consistent with spiral growth, producing a layered structure, with the central region having the greatest thickness. A similar feature has been reported by Fryer (1980), in the highly chlorinated material. The formation of such features has been discussed in detail by Verma (1953), though it should be noted that formation of such features from approximately planar molecules is difficult to envisage.

In this chapter results obtained from diffraction and imaging studies of the highly chlorinated and highly brominated materials have been presented. Significant differences in the shape and internal structure of these particles have been observed. In the chlorinated materials an α-type stacking sequence was adopted, though streaking in many of the diffraction patterns indicated that deviations from this configuration could readily occur. In the highly brominated material, the spacings in the majority of the diffraction patterns and lattice images, could be interpreted in an analogous manner to the highly chlorinated material. However, in some of the patterns larger spacing of 2.5nm were observed. A 'herring-bone', stacking sequence as adopted in β-

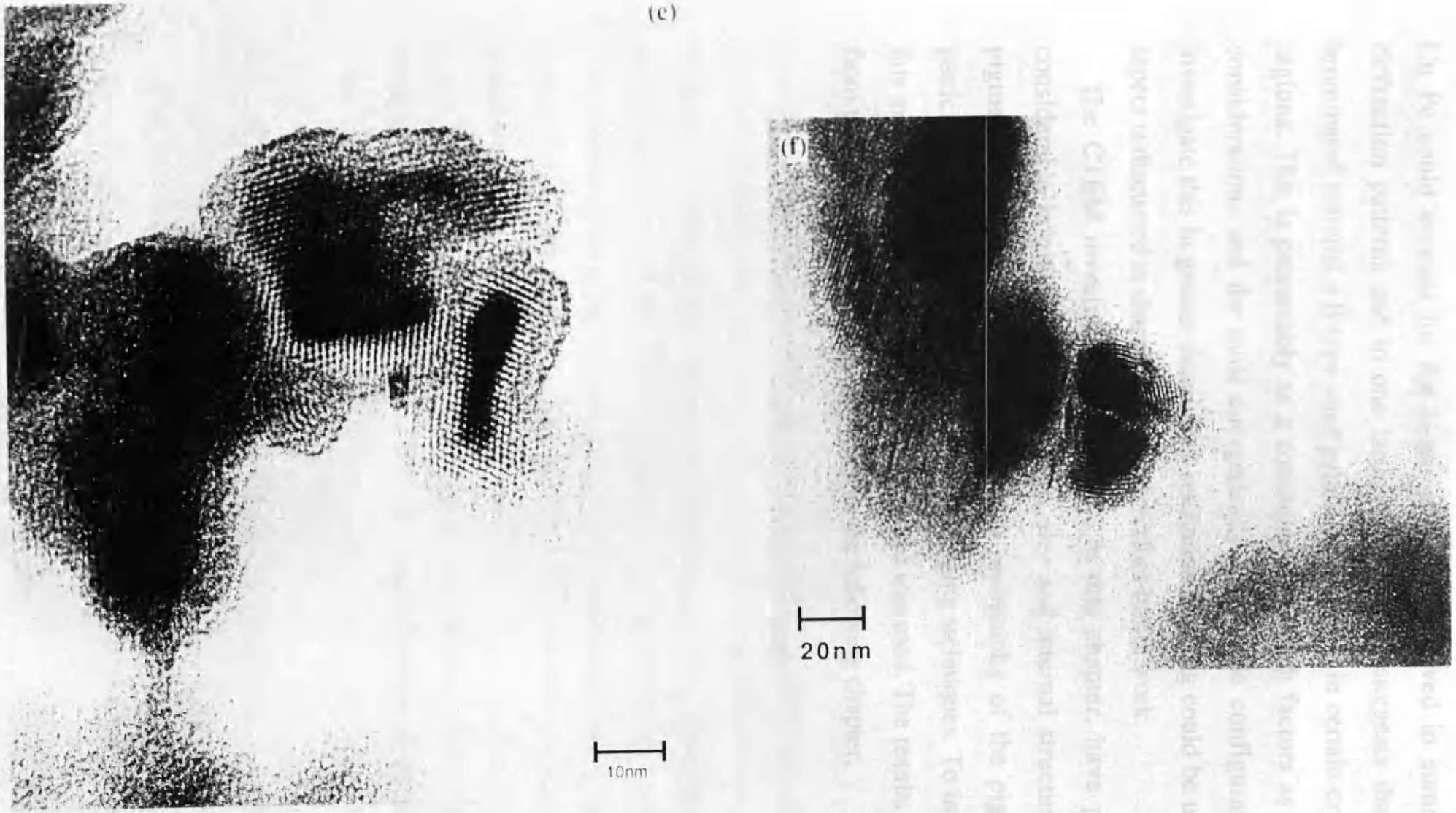

Figure 4.11: (e)-(f) Lattice images from the highly brominated pigmentary sample.

Cu Pc could account for the larger spacings observed in some of the diffraction patterns and in one lattice image. This suggests that in the brominated material a β-type configuration is adopted in certain crystalline regions. This is presumably as a consequence of such factors as packing considerations and the most energetically favourable configuration. To investigate this in greater detail high resolution imaging could be used; this aspect is discussed in chapter 8, which describes future work.

The CTEM investigations described in this chapter, have provided considerable information on the shape, size and internal structure of the pigmentary particles. Information on the topography of the pigmentary particles is however limited using CTEM imaging techniques. To investigate this in greater detail, DPC imaging in a STEM was used. The results obtained from these investigations are presented in the following chapter.

Chapter 5

DIFFERENTIAL PHASE CONTRAST IMAGING OF HALOGENATED COPPER PHTHALOCYANINE PIGMENTS

5.1 Introduction

The CTEM investigations presented in the previous chapter allowed the size and shape of the individual pigmentary particles to be assessed, and provided some information on the internal structure of the particles, through diffraction studies and lattice imaging. Access to information on the detailed topography of the particles is, however, limited using bright field CTEM imaging techniques. The DPC mode of microscopy was discussed in chapter 3, and was shown to be capable of providing simultaneously topographic and structural information. The aim of this chapter is to describe the application of this technique to the various pigmentary samples. The instrumental conditions required for DPC imaging are considered in section 5.2. Comparison of imaging conditions for DPC microscopy are discussed in section 5.3. In section 5.4, images obtained from the various materials are presented.

As both the CTEM and the STEM were used to study these materials a comparison can be drawn regarding the relative merits of each. This is presented in section 5.5.

5.2 Instrumental considerations for DPC imaging

The DPC mode of microscopy was discussed in detail in chapter 3, where it was shown that contrast could be generated in a number of ways. For

example, in the case of particles, small shifts in the bright field cone away from the symmetry position on a quadrant detector are related to thickness gradients in the particles (Chapman & Morrison, 1983) from which their detailed topography can be recovered. To reveal the internal structure of the particles by DPC lattice imaging it is neccesary that the diffraction discs, corresponding to scattering through $+2\theta_B$ and $-2\theta_B$ (where θ_B is the relevant Bragg angle) should overlap with the bright field cone and again difference signals from opposite segments of a quadrant detector are taken as a small focussed probe of electrons is scanned across the specimen. In this case the signal obtained is dependent on the area of overlap and so it is important to choose an optical configuration which maximises this overlap area.

All investigations were carried out in an extended VG HB5 STEM. The high brightness source of a field emission gun is particularly suitable for producing a small probe on the specimen. For example, it is possible to produce a probe with a lateral dimension of <1nm and a primary current of ~0.2nA, this is important in ensuring that images with good signal to noise ratios can be obtained in reasonable acquisition periods.

There is considerable flexibility in the probe forming conditions for imaging in the HB5. The electron optical components used in imaging consisted of a single condenser lens (C1 or C2) plus the highly excited objective lens. As discussed in chapter 3, two apertures of diameter 25μm and 50μm were used here. They subtended angles of 4.16 mrad and 8.32 mrad respectively. A detailed discussion of the relative merits of these various imaging conditions is presented in section 5.3.

Post specimen lenses (PSL's) were used to transfer the electron distribution leaving the specimen to the quadrant detector which was sited in the far field. For a probe forming semi-angle of 4.16 mrad suitable values for the PSL's were determined to be; PSL1 0 (coarse control), 7.45 (fine control) PSL2

off, PSL3 +11 (coarse control), 4.83 (fine control). This gave a camera length of 70cm. For a probe forming semi-angle of 8.32mrad appropriate values for the PSL's were; PSL1 1 (coarse control), 4.95 (fine control) PSL2 off, PSL3 0 (coarse control), 6.0 (fine control). This gave a camera length of 35cm.

Descan coils situated before the first PSL were used to ensure that in the absence of any specimen interaction the electron distribution in the detector plane remained stationary about the centre of the detector irrespective of the position of the probe in the specimen plane

Image acquisition could be performed in analogue or digital mode, the latter being accomplished using a Link AN10000 image acquisition and processing system. Images were recorded at a resolution of 256x256 at 8 bits per pixel. The recommended dwell times of the beam at each pixel was 51μs. Two images were obtained in each set. These corresponded to differentiation in two orthogonal directions. A beam blanking unit was used between acquisitions. This allowed the preceding image to be assessed and saved to disk before the next image was acquired, thus eliminating unnecessary irradiation of the sample.

5.3 Comparison of imaging conditions for DPC microscopy

To extract the maximum information concerning the topography and internal structure of the pigmentary particles, it is important to optimise the imaging conditions. This was achieved through a systematic study in which investigations were made of the effects of using various probes on the topographic and structural information obtainable. Three imaging configurations were used; they were

1. C1 25μm ROA.

2. C1 50μm ROA.

3. C2 50μm ROA.

When using conditions 2, topographic and structural information faded after only a few seconds due to the increased electron dose hitting the specimen (typically a factor of 4X greater than using conditions 1 and 3). The tip extraction voltage was therefore adjusted until the current was ~1/4 of its original value. To ensure that the conditions stayed constant during the course of the experiments, the current was continuously monitored using a picoammeter connected to the virtual objective aperture (VOA).

Low magnification DPC images with two orthogonal differentiation directions were acquired from the same highly chlorinated pigmentary sample using the three optical conditions defined above, these are presented in figures 5.1-5.3. It should be noted that it was not possible to obtain images from identical particles using the three imaging configurations i.e. there was no standard particle. The conclusions reached were obtained by studying several images in each study, and a typical example of each is shown. Figure 5.1, show images obtained using conditions 1. Figure 5.1 (a), shows relatively little surface detail; however, bright and dark regions are evident which denote regions where the thickness is varying and hence delineate the edges of the particles. In figure 5.1 (b) the surface again appears fairly smooth except for a region at A, where there are bright and dark features. These will be discussed later in this section. Images obtained using conditions 2, are presented in figures 5.2. In figure 5.2 (a), the edges of several particles can be observed, giving a strong impression of several particles overlaying one another, also strong bright and dark features are evident at A. In figure 5.2 (b), relatively small thickness variations are observed on the particle surface, though again the edges of the particles are discernible. Images

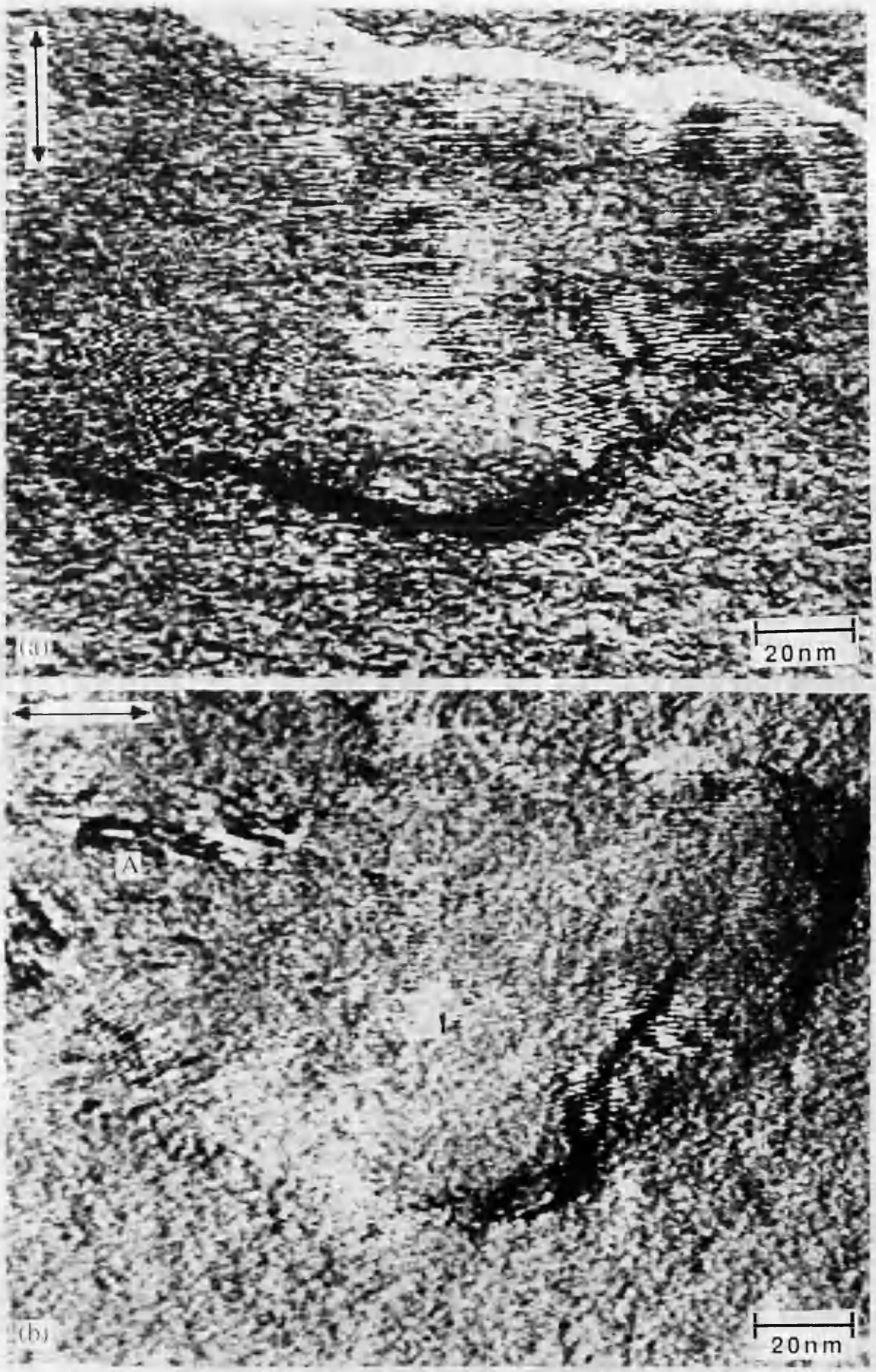

Figure 5.1: (a)-(b) Low magnification DPC STEM images of highly deformated particles obtained using conditions I. Arrows denote the differentiation direction.

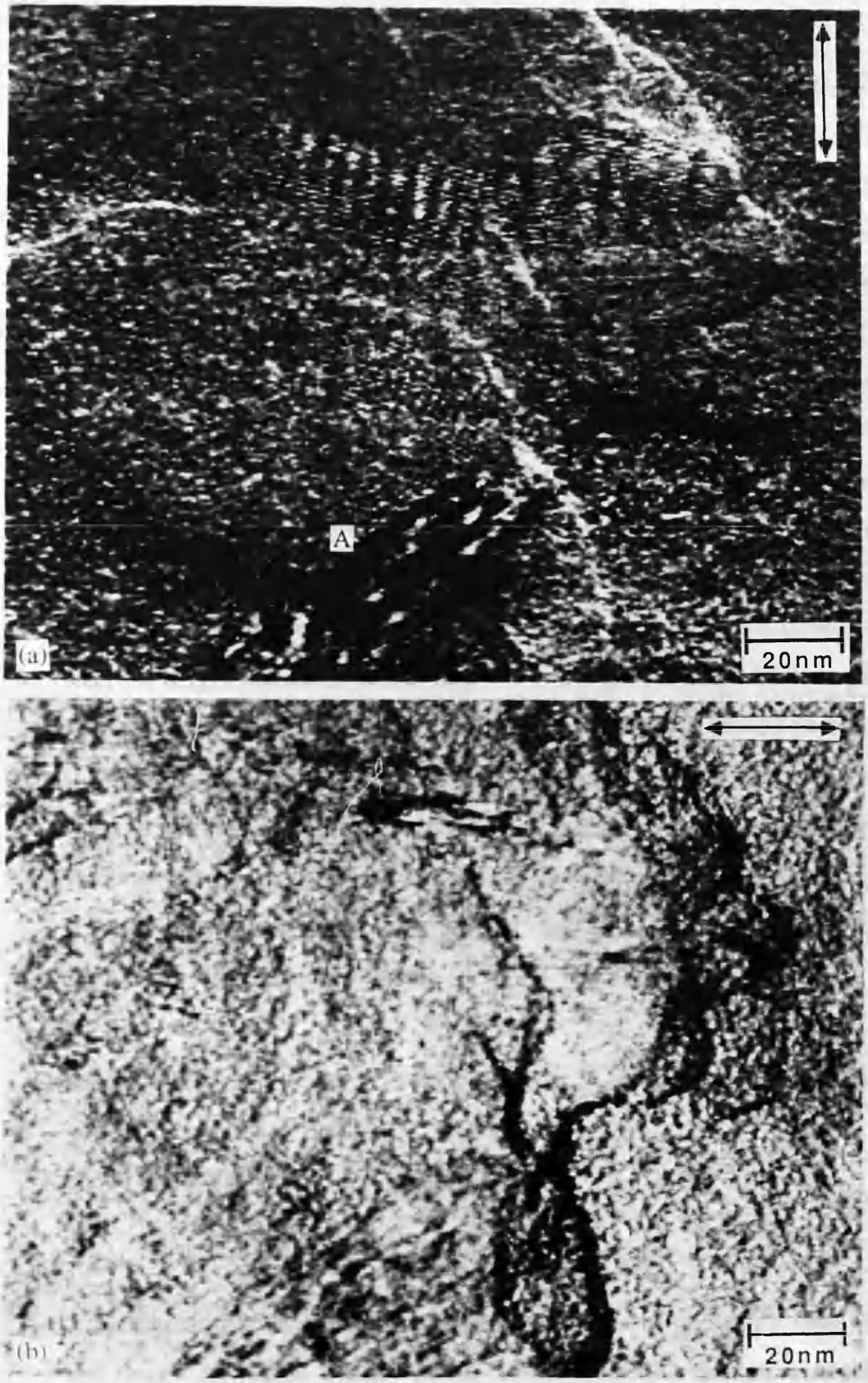

Figure 5.2: (a)-(b) Low magnification DPC STEM images of highly chlorinated particles obtained using conditions 2.

acquired using conditions 3, are presented in figure 5.3. In figure 5.3 (a), it can be seen that several particles are overlapping. In figure 5.3 (b), very strong and extensive bright and dark features are evident in region (A). These features and those indicated in the previous figures cannot be interpreted as thickness variations in the specimen. The reasons for this are evident if figures 5.3 (a) and (b) are studied. In figure 5.3 (b), the strong black and white features would be interpreted as pronounced ridges and troughs on the particle surface, however if these were genuine thickness gradients they would also be evident in figure 5.3 (a). As these are not visible in this image they cannot be interpreted in this way. It is therefore important to determine what contrast mechanism can give rise to these features. As discussed previously, contrast can arise due to overlap of diffraction spots with the brightfield cone. This therefore could provide a possible explanation for the observed features. The diffraction pattern presented in figure 4.2, showed that the spacing of stacks of molecules corresponding to the (110) spacing was ~1.4nm. The separation of molecules corresponding to the (001) spacing was ~0.36nm. These have Bragg angles of 1.32 mrad and 5.14 mrad respectively. Using the values for the optical conditions employed in the studies described above, namely.

Conditions 1	Conditions 2 and 3
α_s=4.16 mrad	α_s=8.32 mrad
L=0.7m	L=0.35m

One can readily calculate the spacing and extent of the bright field cone and the Bragg diffracted beams on the 11mm quadrant detector. A schematic diagram showing the position of the beams is presented in figure 5.4. Using

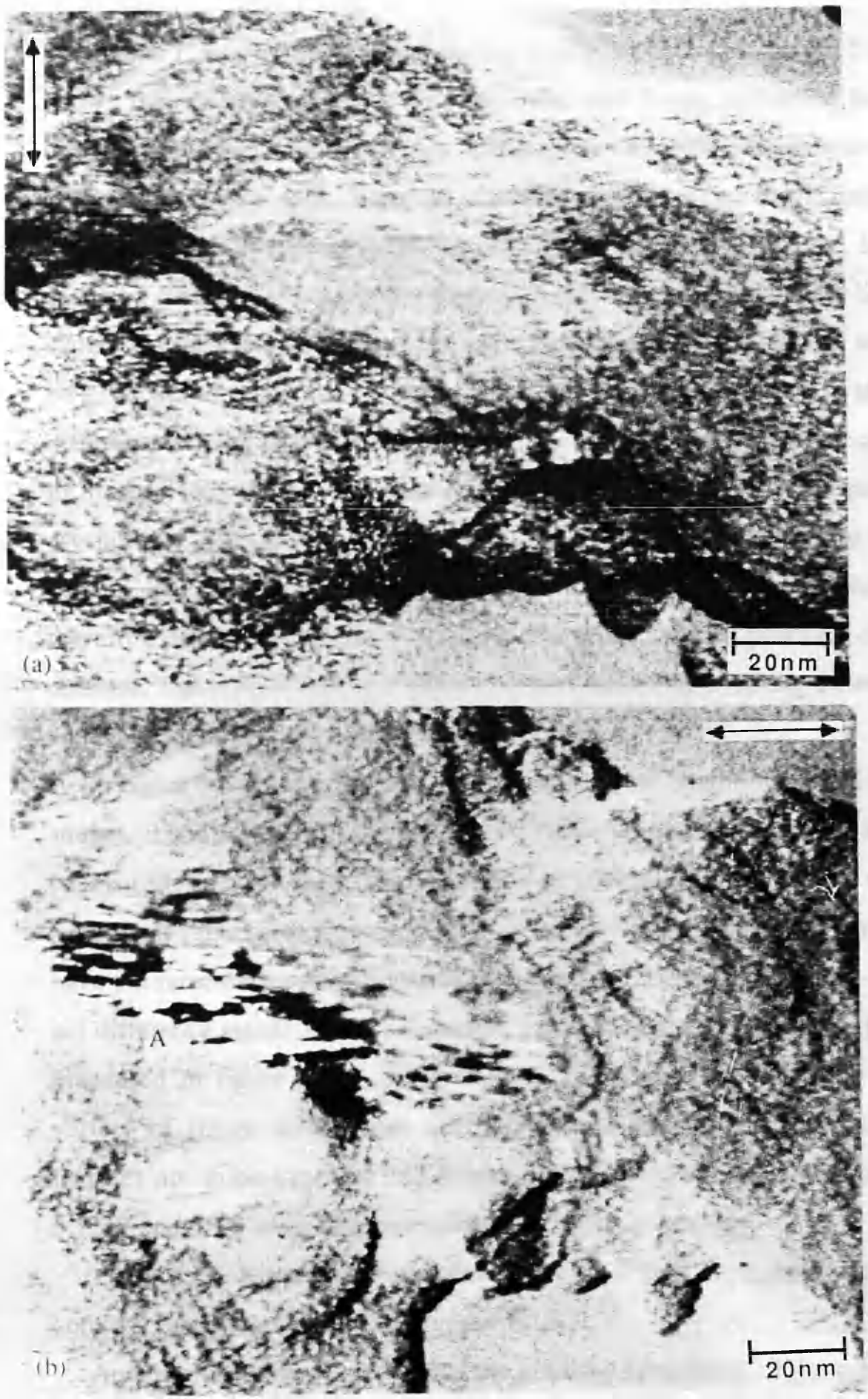

Figure 5.3: (a)-(b) Low magnification DPC STEM images of highly chlorinated particles obtained using conditions 3.

conditions 1, bright and dark features are visible in figure 5.1. Figure 5.4 (a) shows the position of the brightfield cone and Bragg diffracted beams ($2\theta_{110}$) and ($2\theta_{001}$). It can be seen that centre of the (001) Bragg beam lies outside the detector area . However, a portion of the disc lies on the detector surface, though overlap between the brightfield cone does not occur. In the case of a perfect crystal, suitably oriented with respect to the incident beam, signal cancellation would therefore be expected to occur as the beams would be expected to fall symmetrically on the detector surface and upon taking difference signals cancellation would occur. However, the results presented in the previous chapter, showed that considerable deviation from perfect crystallinity existed, severe bending of lattice planes and dislocations were present. Thus asymmetry in the beam positions are to be expected and can therefore result in variations in the intensity on various portions of the detector. Therefore a resultant signal is to be expected upon taking difference signals from opposite quadrants of the detector.

In figure 5.4 (b), the position of the beams using conditions 2 and 3 are shown, it can be seen that overlap between the brightfield cone and the Bragg beams ($2\theta_{110}$) and ($2\theta_{001}$) occurs. Therefore taking difference signals (4-2), a resultant signal proportional to $\cos(2\pi x/\Lambda)$ is obtained, where the symbols have the same meaning as chapter 3. Upon taking difference signals (3-1), no net difference signal occurs. Of course, it should be noted that the diagrams presented in figure 5.4, assume a particular fringe orientation. A wide variety of fringe orientations are present and therefore strong contrast features are to be expected and indeed are observed (as shown by figures 5.1,5.2 and 5.3), when differentiating in different directions.

This section has therefore provided a plausible explanation for the contrast variations observed in figures 5.1-5.3.

An additional observation is that the granular appearance of the substrate and particle surface is considerably less in figure 5.3 than in the other

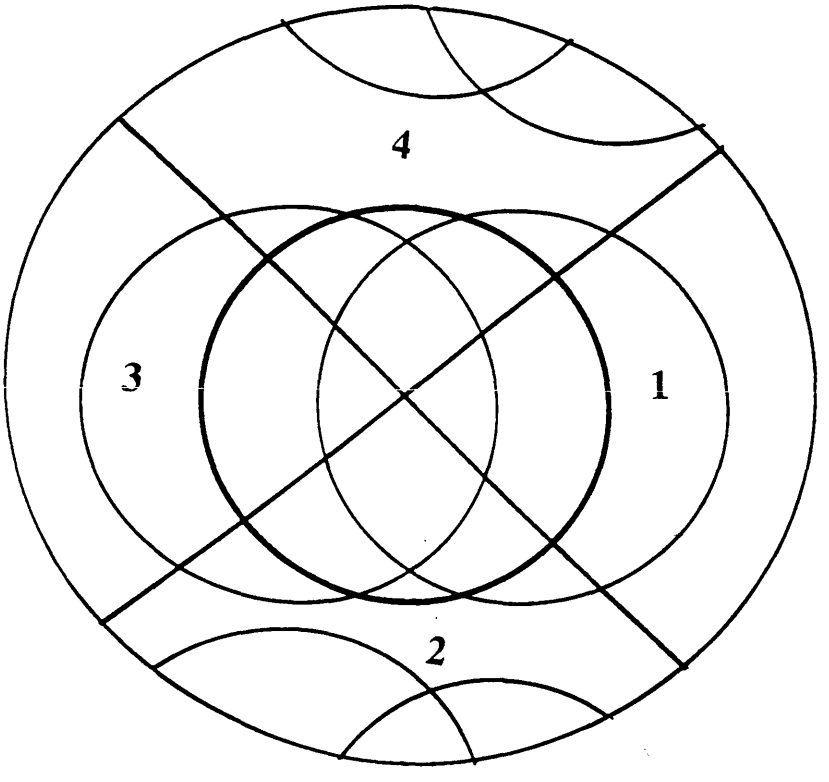

Figure 5.4 (a): Schematic diagram showing the position of the discs on the quadrant detector using conditions 1.

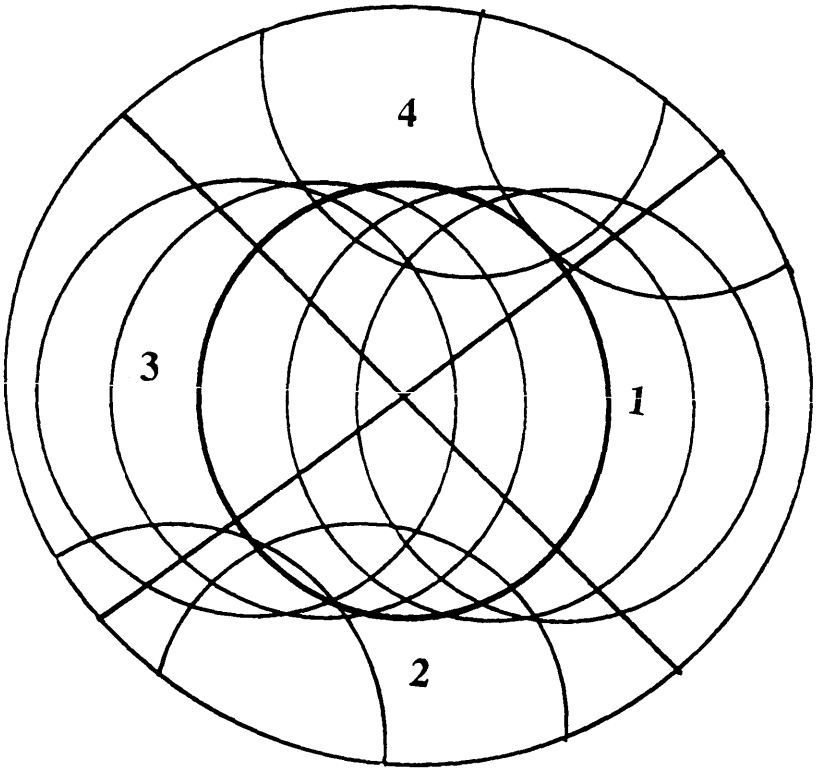

Figure 5.4 (b): Schematic diagram showing the position of the discs on the quadrant detector using conditions 2 and 3.

figures. This means that surface features are clearer and finer features can be discerned. Whether this is a consequence of the particular imaging conditions used or it was due to variations in the particular areas of specimen being examined is unclear.

Comparison of the three imaging configurations used suggests that for topographic information similar images can be obtained using any of the configurations described.

One aim of this section was to assess the various possible imaging configurations to determine which was the most suitable for revealing topographic detail. However, as discussed previously, we are also interested in revealing the internal structure of the particles through the presence of lattice fringes. Therefore, the studies were repeated at higher magnification to assess the quality of the lattice images obtained using each of the imaging configurations.

The results obtained from these studies are presented in figures 5.5.-5.7. Figure 5.5 (a) shows a large number of high contrast lattice fringes lying across the particle surface. Significant disruption is evident in this image. In figure 5.5 (b) no fringes can be observed. This is in accordance with the fact that no information is transferred from an orientation parallel to the direction of differentiation. Images obtained using conditions 2, are presented in figure 5.6. Few lattice fringes are visible in figure 5.6 (a). In figure 5.6 (b) however several separate crystalline regions are evident.

Figure 5.7 shows images obtained using conditions 3. A large number of high contrast fringes are evident in figure 5.7 (a). The visibility of fringes in figure 5.7 (b) is low. The results presented in this section suggest that images showing structural and topographic information can be obtained using any of the configurations. The transfer function presented in figure 3.15, showed that for fringes >1nm, the transfer of this information was higher using a

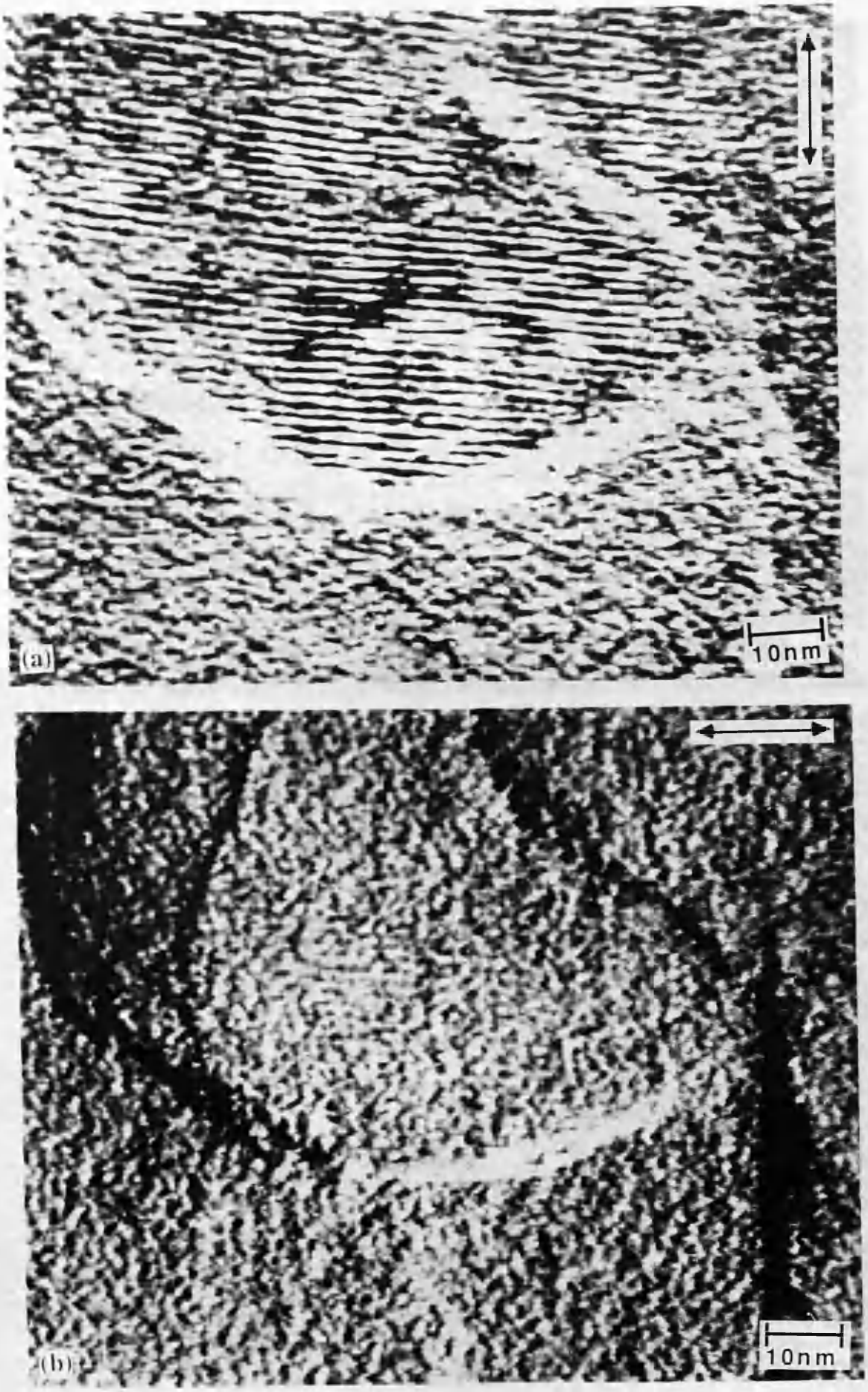

Figure 5.5 : (a)-(b) High magnification DPC STEM images of highly chlorinated particles obtained using conditions 1.

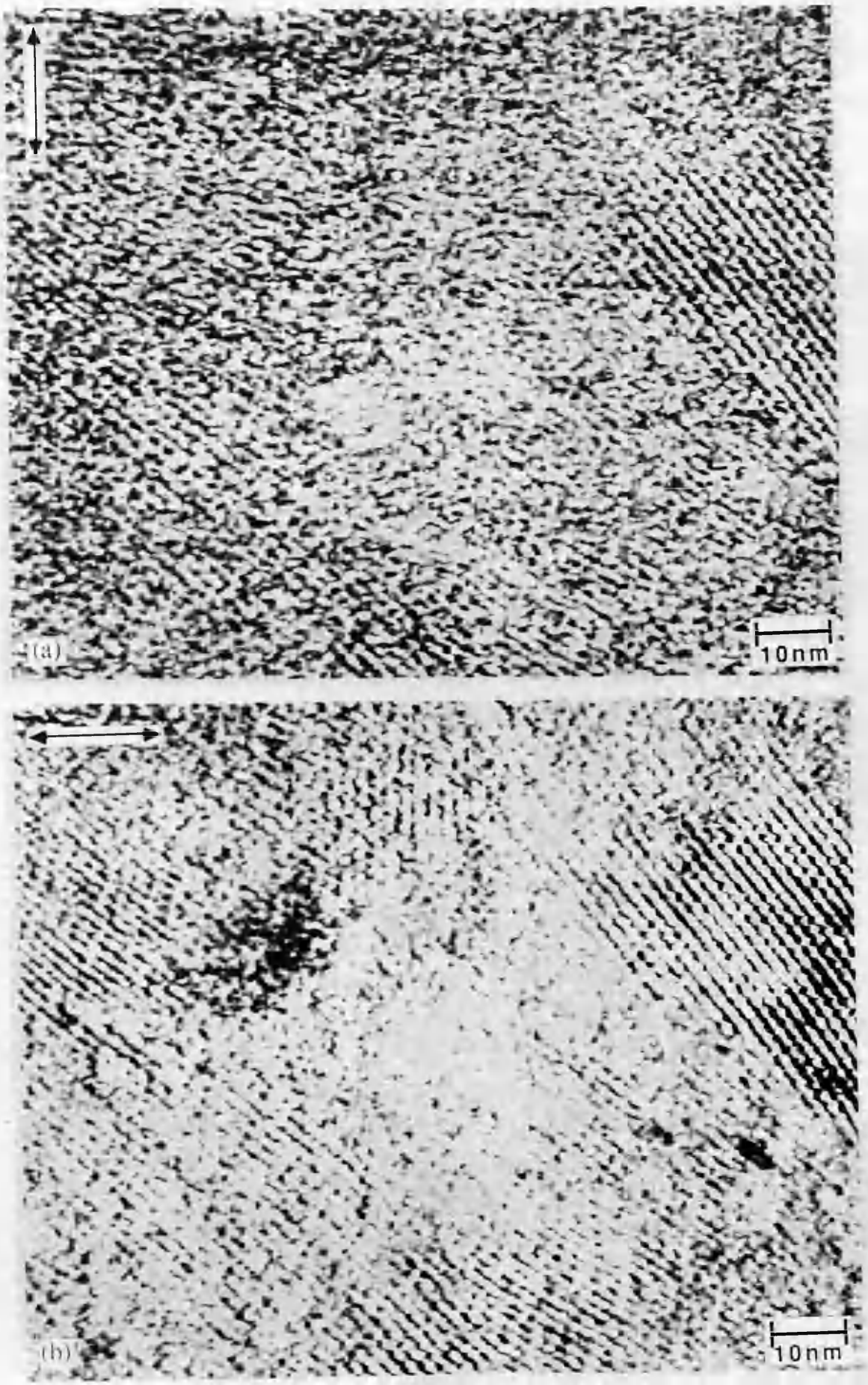

Figure 5.6 : (a)-(b) High magnification DPC STEM images of highly deformated particles obtained using conditions 2.

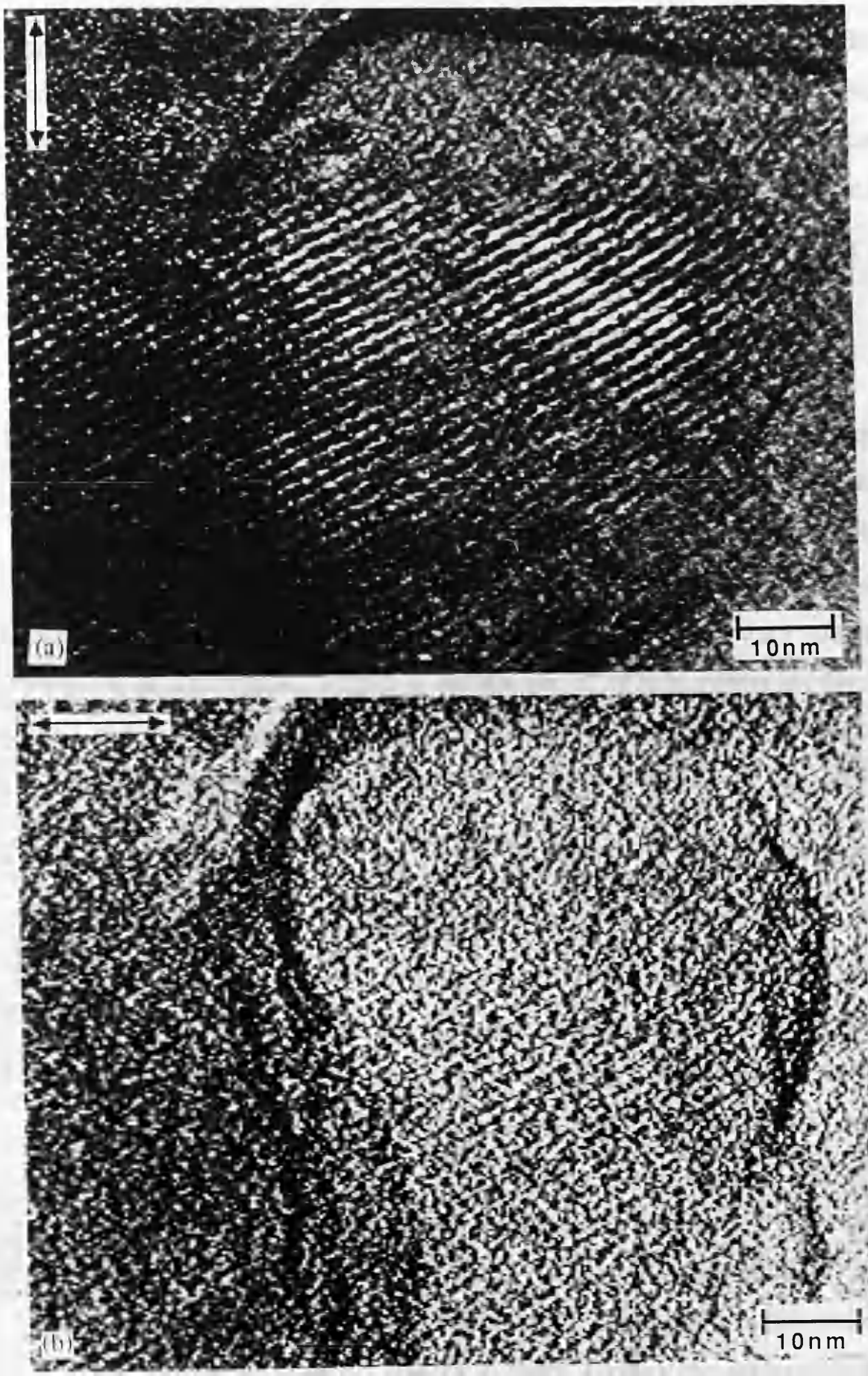

Figure 5.7 : (a)-(b) High magnification DPC STEM images of highly chlorinated particles obtained using conditions 3.

probe forming semi-angle of α_s=4.16mrad than α_s=8.32 mrad. It should be noted that to observe finer periodicities in the object, such as the 0.36nm spacing, corresponding to the separation of the molecules perpendicular to their plane the use of a larger aperture is essential as using α_s=4.16 mrad limits the resolution to ~0.5nm.

5.4 Experimentally obtained images of pigmentary X-Cu Pc.

In an analogous manner to the results presented in the preceding chapter, two studies were undertaken using the DPC imaging mode. The first was to record series of low magnification images from the various samples. These provided information on the shape and topography of the individual particles, factors which have a significant effect on the pigmentary properties of the material. The second set of images recorded at higher magnification provided information on the internal structure of the particles through the presence of lattice fringes which are present simultaneously with the topographic information.

5.4 (a) Low magnification results

Several images from the highly chlorinated particles were presented in the previous section. These images showed particles in which dimensions in all directions were similar. This is in agreement with the CTEM results presented in chapter 4.

Images obtained from the highly brominated particles are presented in figures 5.8 and 5.9. The images show elongated, approximately brick shaped, particles. The edges of the particles are clearly discernible and irregular surface features and faceting is evident. Of particular interest in the

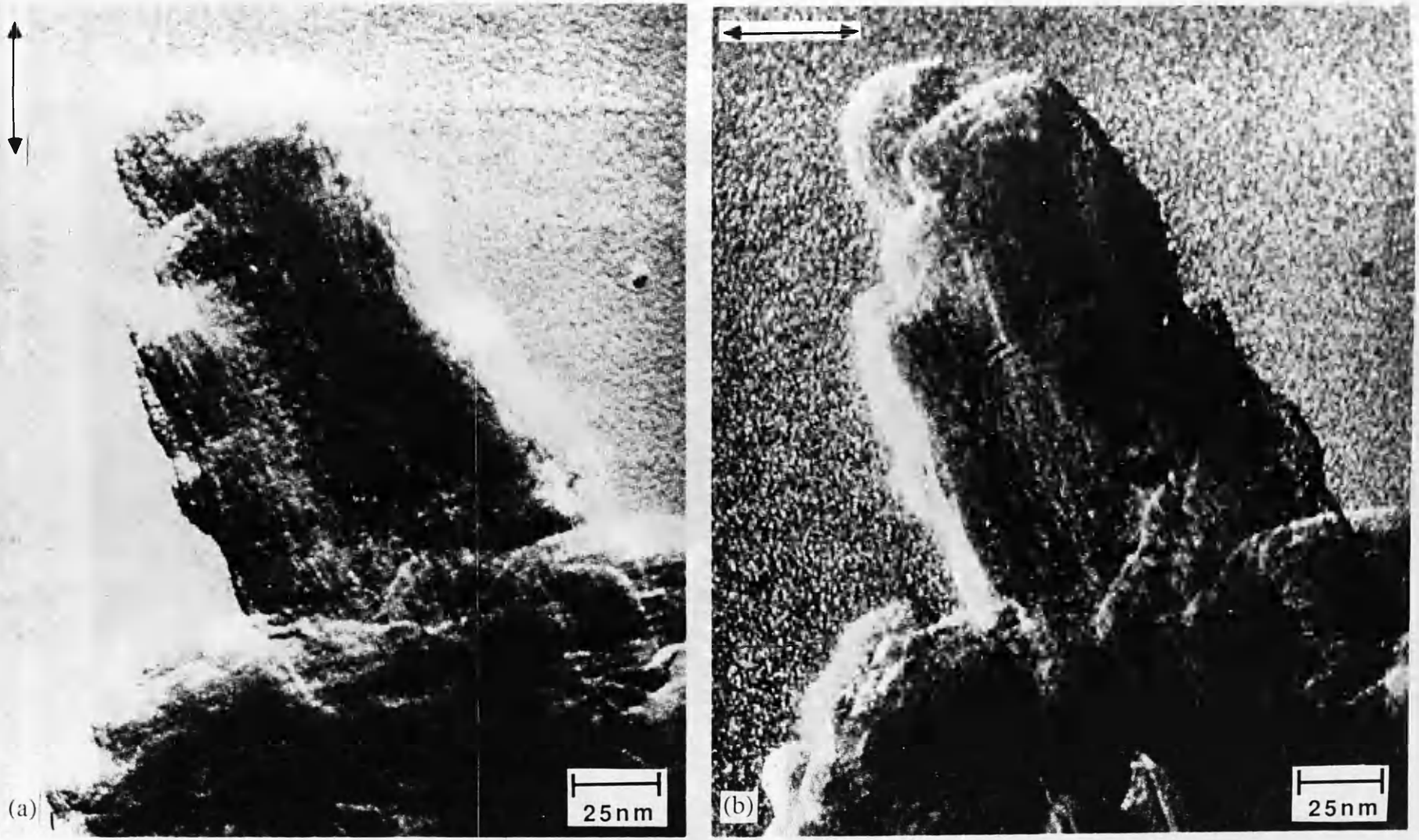

Figure 5.8:(a)-(b) Low magnification DPC STEM images of highly brominated particles.

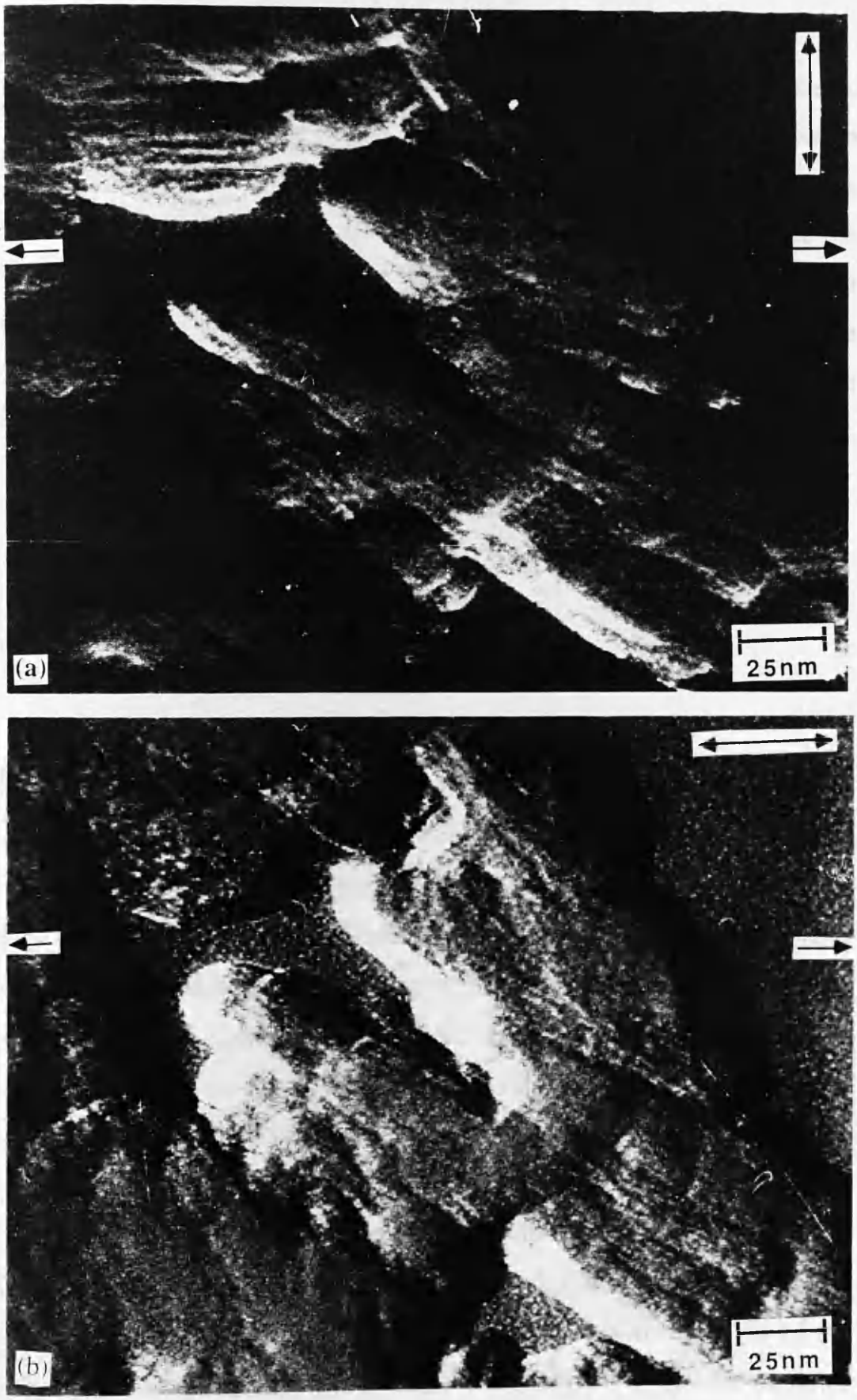

Figure 5.9:(a)-(b) Low magnification DPC STEM images of highly brominated particles.

study of the particle shape is the extent of edge features and surface steps. These can be most satisfactorally be explored using the images shown in figure 5.9 which were recorded digitally. There are various procedures available for edge detection. The majority of these approaches involve the convolution of the original image with a suitable mask. Examples of such masks are the Laplacian, Sobel, Roberts or Kirsch operators. These are designed to locate regions of high spatial frequency. It was found that the Sobel's operator was the most appropriate and has the form

$$\begin{bmatrix} -1 & 0 & 1 \\ -2 & 0 & 2 \\ -1 & 0 & 1 \end{bmatrix} \quad \text{followed by} \quad \begin{bmatrix} 1 & 2 & 1 \\ 0 & 0 & 2 \\ -1 & -2 & 1 \end{bmatrix} \qquad (5.1)$$

The resulting gradient image after convolution will typically be dark in regions where changes in intensity are subtle, and bright in regions of rapid intensity variation. In some regions of the image noise is present, this can be removed by applying a suitable threshold to the image, i.e. setting all pixels below a certain threshold value to zero. This was achieved by selecting a substrate region i.e. one which contained no particles, and monitoring the signal variation in this region as the threshold value was adjusted. It should be noted that the threshold value was set as low as possible to reduce noise but not remove information on genuine thickness variations present in the image. The procedure was applied to the highly brominated sample presented in figure 5.9. The results are shown in figure 5.10. Figures 5.10 (a) and (b), show that the particles have pronounced surface steps at the edges of the particles. Additionally finer lines can be seen, suggesting that the particles possess a terraced structure at the edges of the particles, the top surface in

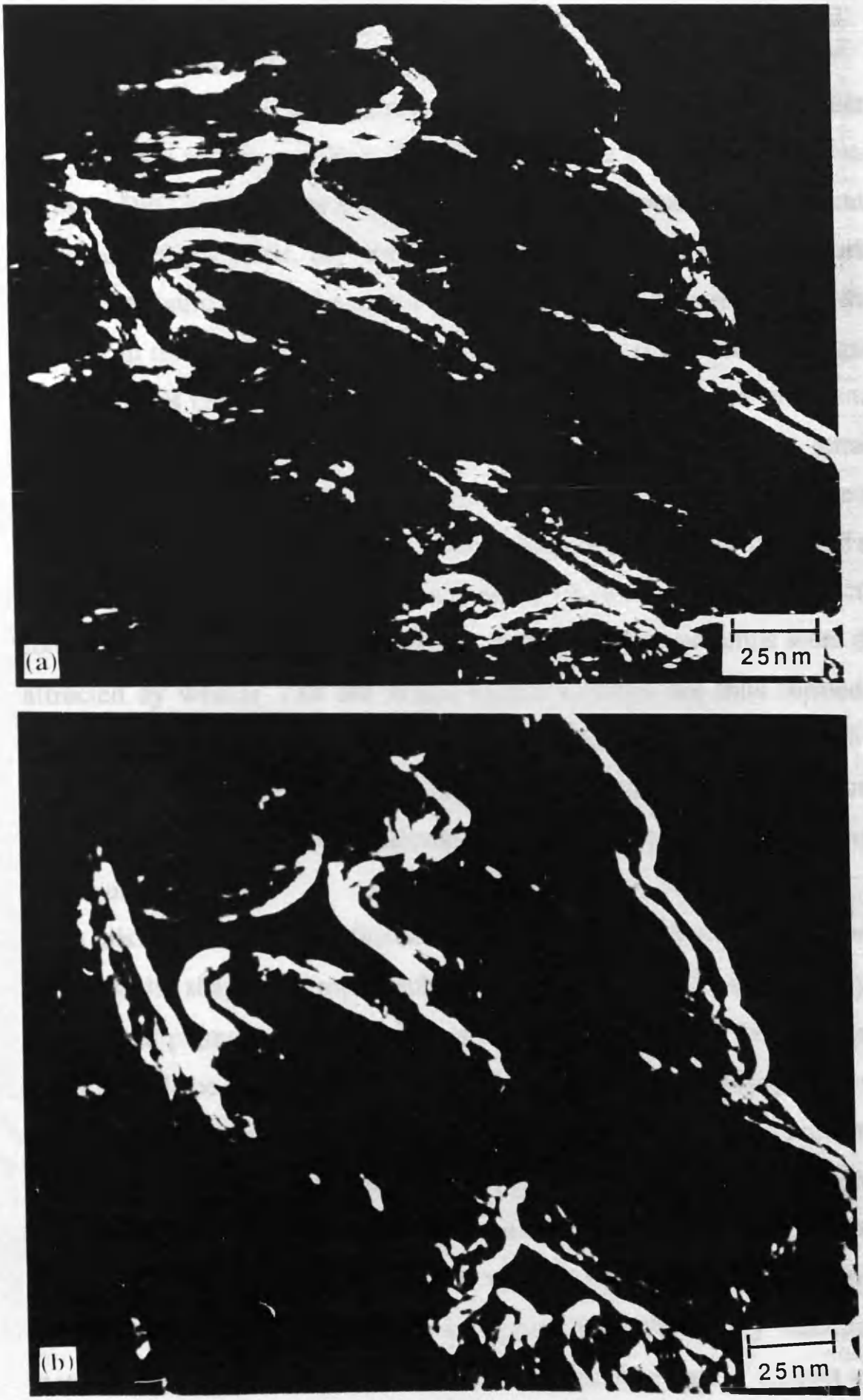

Figure 5.10:(a)-(b) Processed images showing edge features of the highly brominated particles.

comparison being relatively flat.

A further technique that can provide information on thickness gradient in the specimen is line profiling. A single line trace of the signal variation across a DPC image, gives a profile which is proportional to the gradient of the specimen thickness, i.e. t(x). Line profiles obtained from the marked regions of figure 5.9 are presented in figure 5.11 (a). Interpretation of these profiles in terms of the topography of the particles is presented in figures 5.11 (b). It is clear from these figures that the particles have pronounced edges and have a terraced structure. The typical dimensions of these terraces is ~2nm. It is important to discuss what crystal growth processes can give rise to these terraces. In the previous chapter crystal formation was discussed as a two stage process. Firstly long chains of approximately planar molecules formed as a result of π-orbital overlap. Secondly these columns were then attracted by weaker Van der Waals forces. Crystals are thus formed by stacking planes of molecules on top of each other. These terraces which are of the dimensions of individual halogenated molecules (~2nm) can thus be interpretated directly at the molecular level as arising from the stacking of planes of molecules.

In this section low magnification DPC STEM images have been presented showing the shape and topography of the highly chlorinated and highly brominated pigmentary particles. It is instructive to discuss the importance of particle shape and topography with reference to the pigmentary properties of the materials. As discussed in chapter 1, the effectiveness of a pigment in colouring the medium into which it is incorporated is strongly dependent on achieving a good dispersion. The results presented in this section in conjunction with those in chapter 4, suggest that the highly brominated material will be less effective as a pigment than the highly chlorinated material. The reasons for this are that the large surface area of contact along

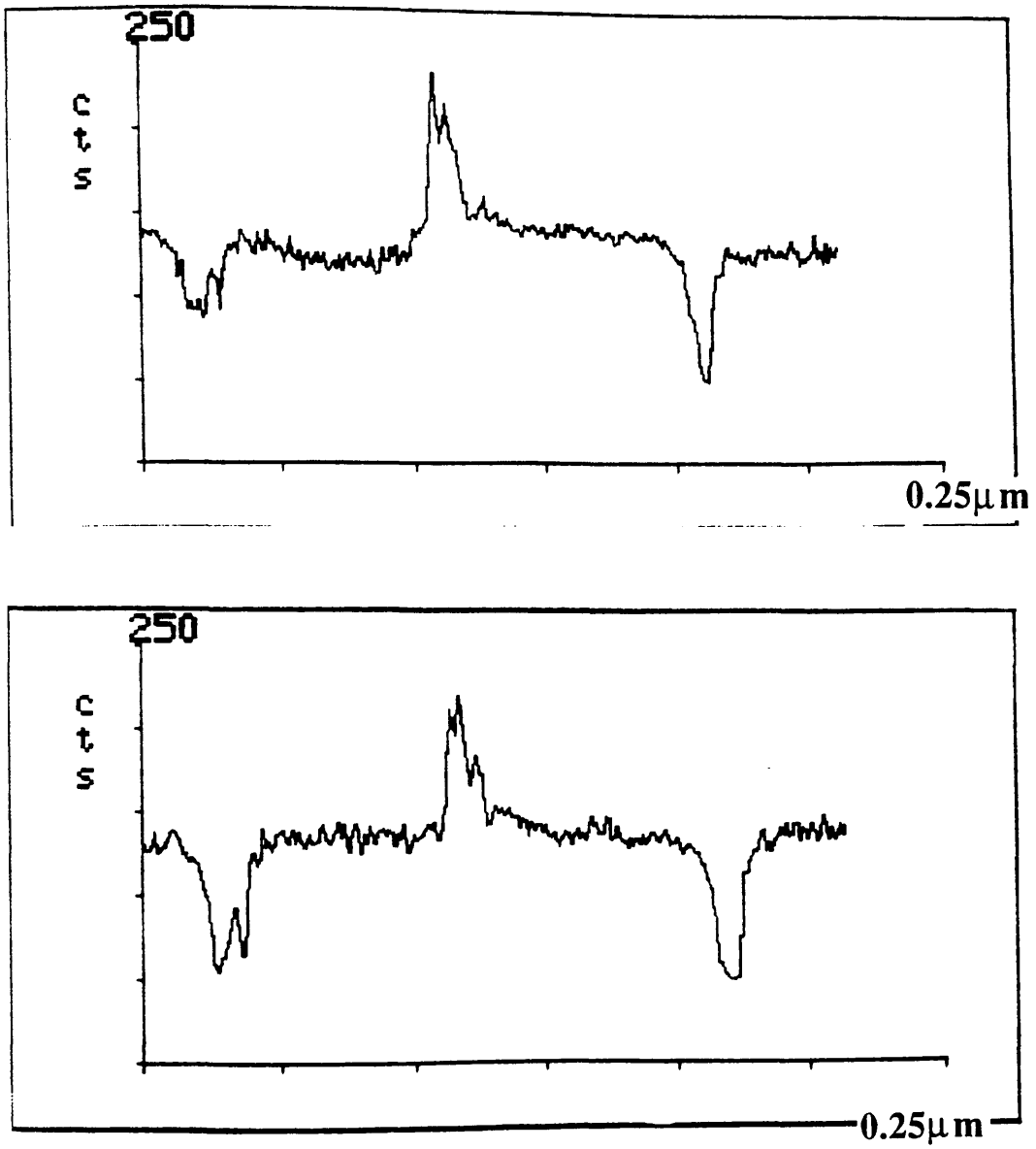

Figure 5.11 (a): Line profiles obtained from the selected regions of figures 5.9 (a) and (b).

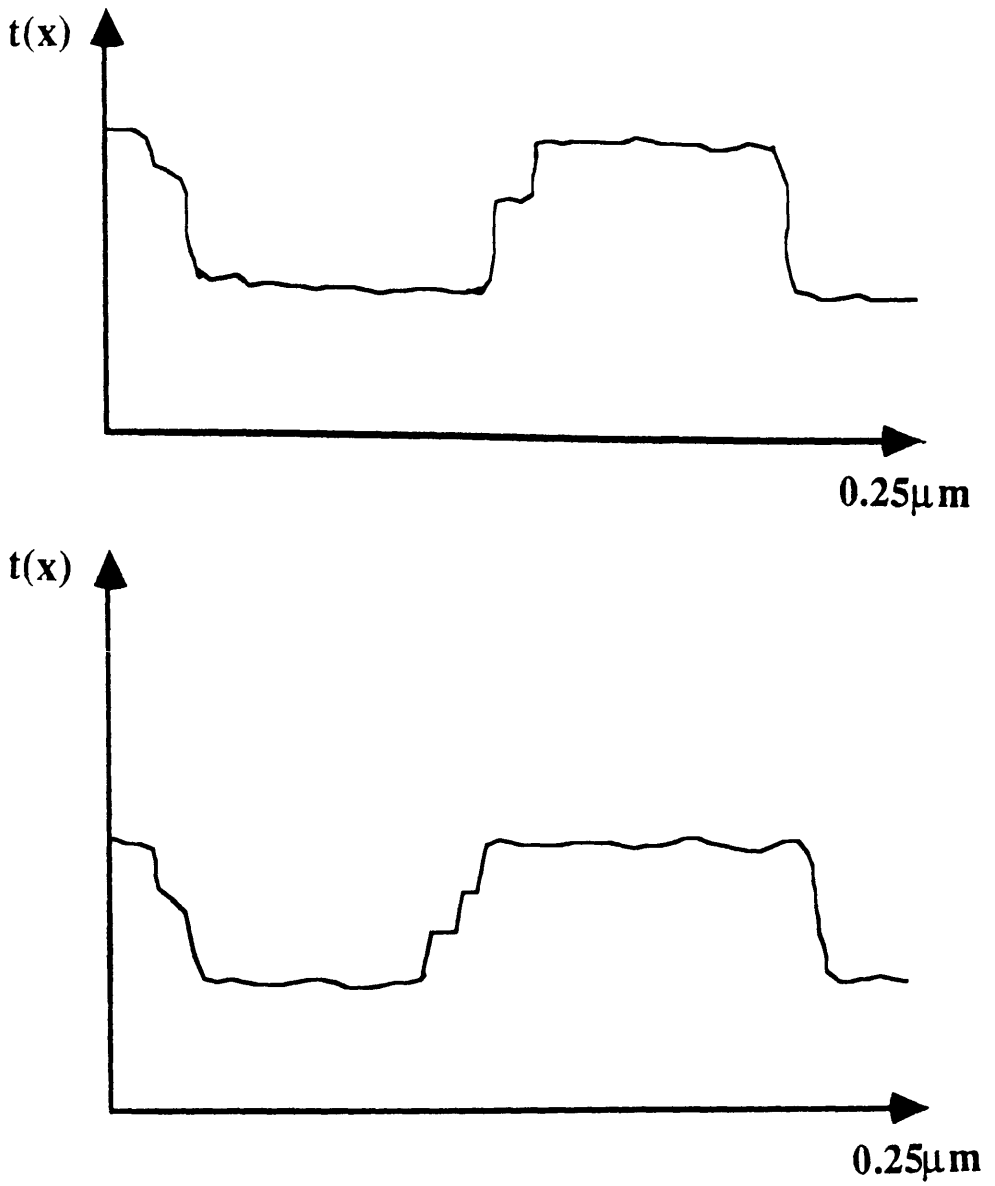

Figure 5.11 (b): Thickness profiles corresponding to the line profiles presented in figure 5.11 (a).

the major axis of the particle is likely to result in strong aggregation of particles. A consequence of this is that it decreases the effective surface area of the particles with a corresponding decrease in their pigmentary effectiveness. Improvements in the pigmentary properties of this material could be obtained if the particle shape could be altered to be similar to those of the highly chlorinated particles.

5.4 (b) High magnification results

DPC lattice images obtained from the highly chlorinated sample A are presented in figures 5.12 and 5.13. Figures 5.12 (a) and (b), show a pair of DPC lattice images; note that in these images the information on specimen topography is present simultaneously. Irregular surface features and pronounced thickness variations are evident. A wide variety of fringe orientations are clearly visible in each image, only those very close to a differentiation direction (e.g. at A & B) being absent in the other image. This emphasises that information is unlikely to be lost through the use of a 'directional', imaging technique. The availability of information on the internal structure and topography of the particles, in comparison to the CTEM lattice images presented in the previous chapter, helps greatly in the provision of a full description of the particles. Figures 5.13 (a) and (b) show images obtained from sample B. A large number of lattice fringes of spacing 1.4nm are visible in these figures. Additionally bending of lattice fringes and several dislocations are evident; the positions of these are indicated. A region of crossed fringes is observed in the top right hand corner of the image. Figure 5.14 (a) and (b), shows DPC lattice images from the highly brominated material. Extensive crystalline fringe patterns are evident in these images.

In an attempt to characterise as fully as possible the internal structure of

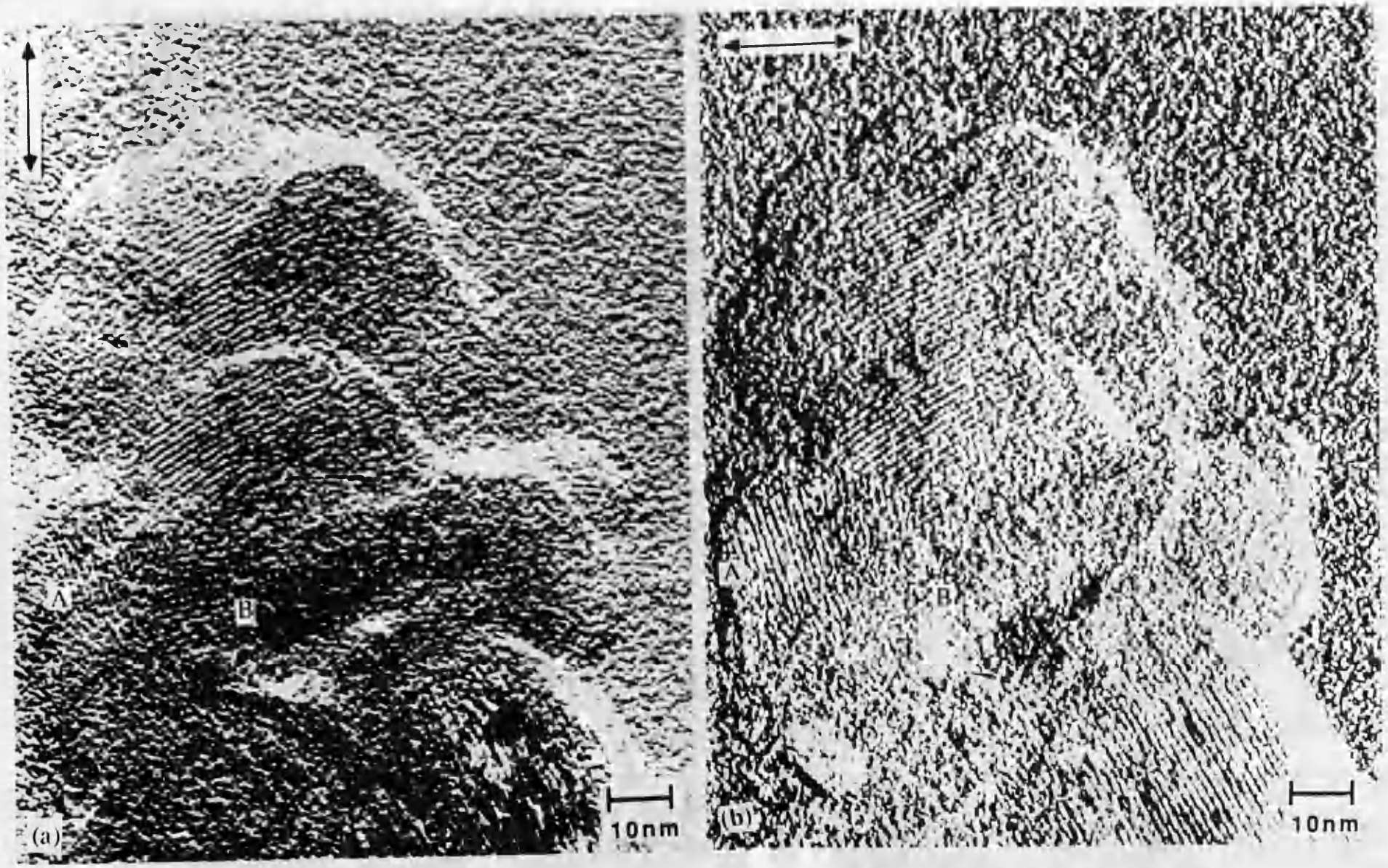

Figure 5.12: (a)-(b) High magnification DPC STEM lattice images of highly chlorinated particles.

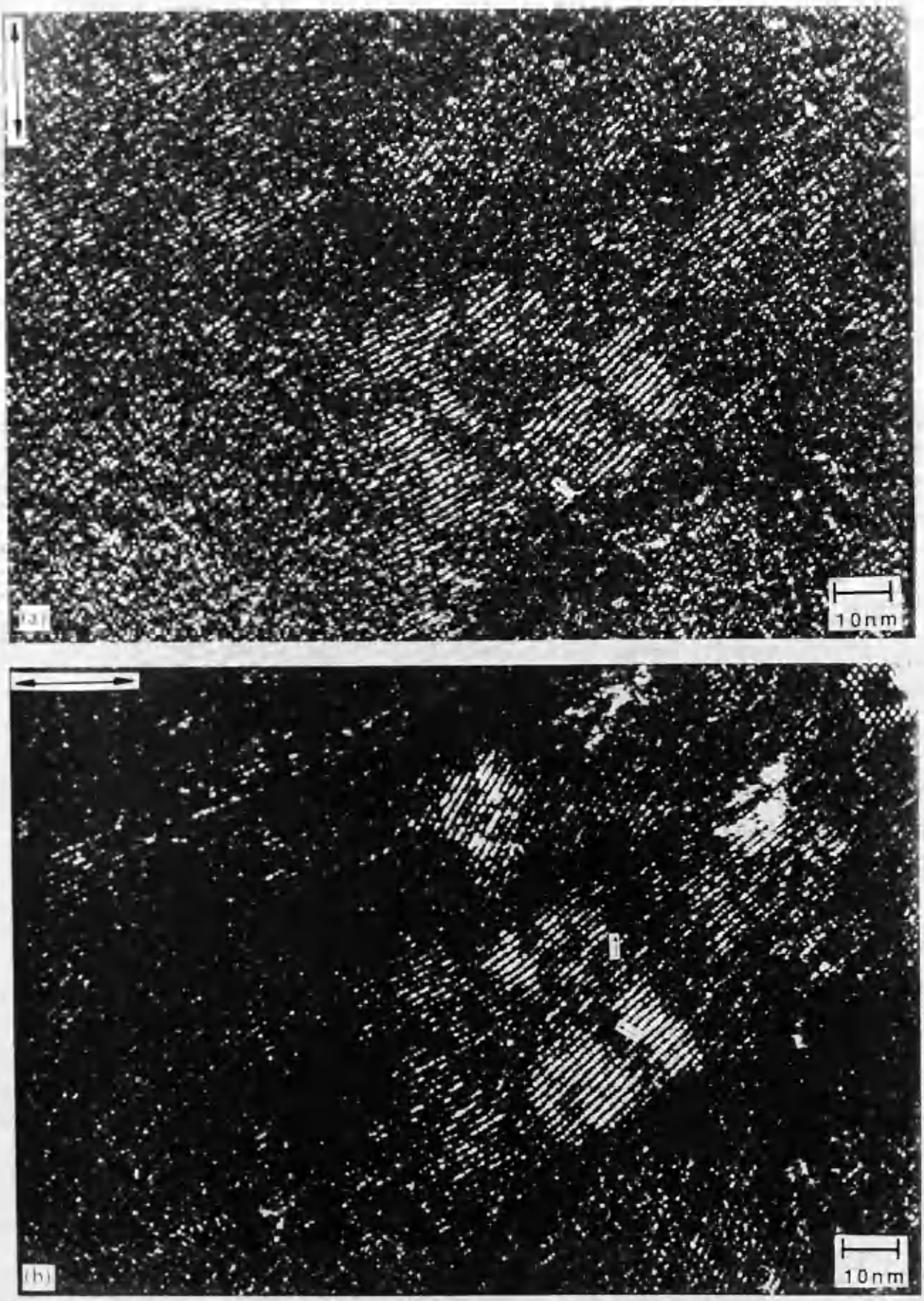

Figure 5.13: (a)-(b) High magnification DPC STEM lattice images of highly chlorinated particles.

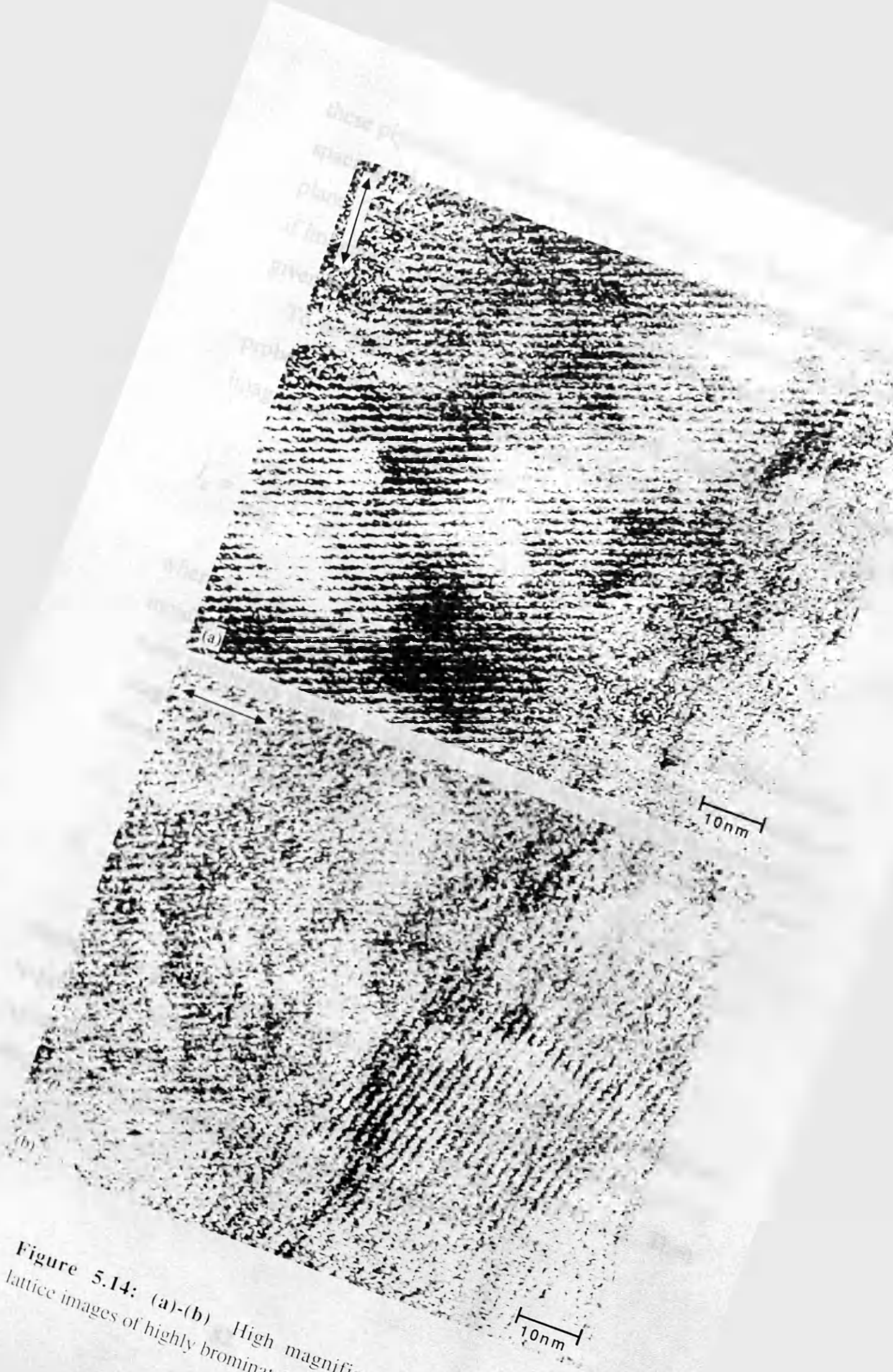

Figure 5.14: **(a)-(b)** High magnification DPC STEM lattice images of highly brominated particles.

these pigmentary particles several attempts were made to observe the 0.36nm spacing, corresponding to the separation of molecules perpendicular to their plane. This proved unsuccessful. A calculation was performed to determine if imaging the 0.36nm periodicity was feasible. Details of this calculation are given below.

To be able to image a periodic structure of periodicity Λ requires the probe size d to be ~$\Lambda/2$. The image signal (I_S) obtained using the DPC imaging mode can be written as,

$$I_s = \frac{O_A}{\pi\alpha_s^2}\Gamma\frac{I_p\tau}{e} \qquad (5.2)$$

where Γ is the proportion of current in the particular Bragg diffracted beam, incident on the detector, the remaining symbols have the same meaning as those previously defined in chapter 3. To allow the object to be detected this image signal must be considerably greater than the inherent statistical noise, this noise can be expressed as,

$$N = k\left(\frac{I_p\tau}{e}\right)^{\frac{1}{2}} \qquad (5.3)$$

where k is a physiologically-determined signal-to-noise ratio, typically >5 required for recognition of detail (Rose, 1948). For convenience the expression for the overlap area in equation 5.2 will be rewritten as η . Then using equations (5.2) and (5.3) leads to the inequality,

$$\eta\Gamma\left(\frac{I_p\tau}{e}\right)^{\frac{1}{2}} > k \qquad (5.4)$$

The dose D_c hitting the specimen can be written as,

$$D_c = \frac{I_p\tau}{d^2} \qquad (5.5)$$

Substituting this expression into equation 5.4 and rearranging leads to,

$$\Lambda^2 > \frac{4k^2e}{D_c\Gamma^2\eta^2} \qquad (5.6)$$

Using appropriate values for the parameters in this equation, i.e. taking the critical dose D_c for these materials as ~10Ccm^{-2}, a value for Γ of ~0.05 and from figure 3.15 η is ~1/3 at Λ=0.36nm. This gives the minimum resolvable feature as ~0.8nm. Thus it can be seen that for the beam sensitive specimens under investigation, resolving the 1.3nm periodicity is straightforward, however imaging the 0.36nm periodicity is unfeasible. However, to demonstrate that this resolution is attainable using DPC lattice imaging, high contrast lattice fringes (0.34nm) were recorded from a graphitised carbon specimen. A typical example of the images obtained is presented in figures 5.15 (a) and (b). It is worth noting that these fringes were considerably easier to observe using DPC microscopy than by conventional STEM lattice imaging.

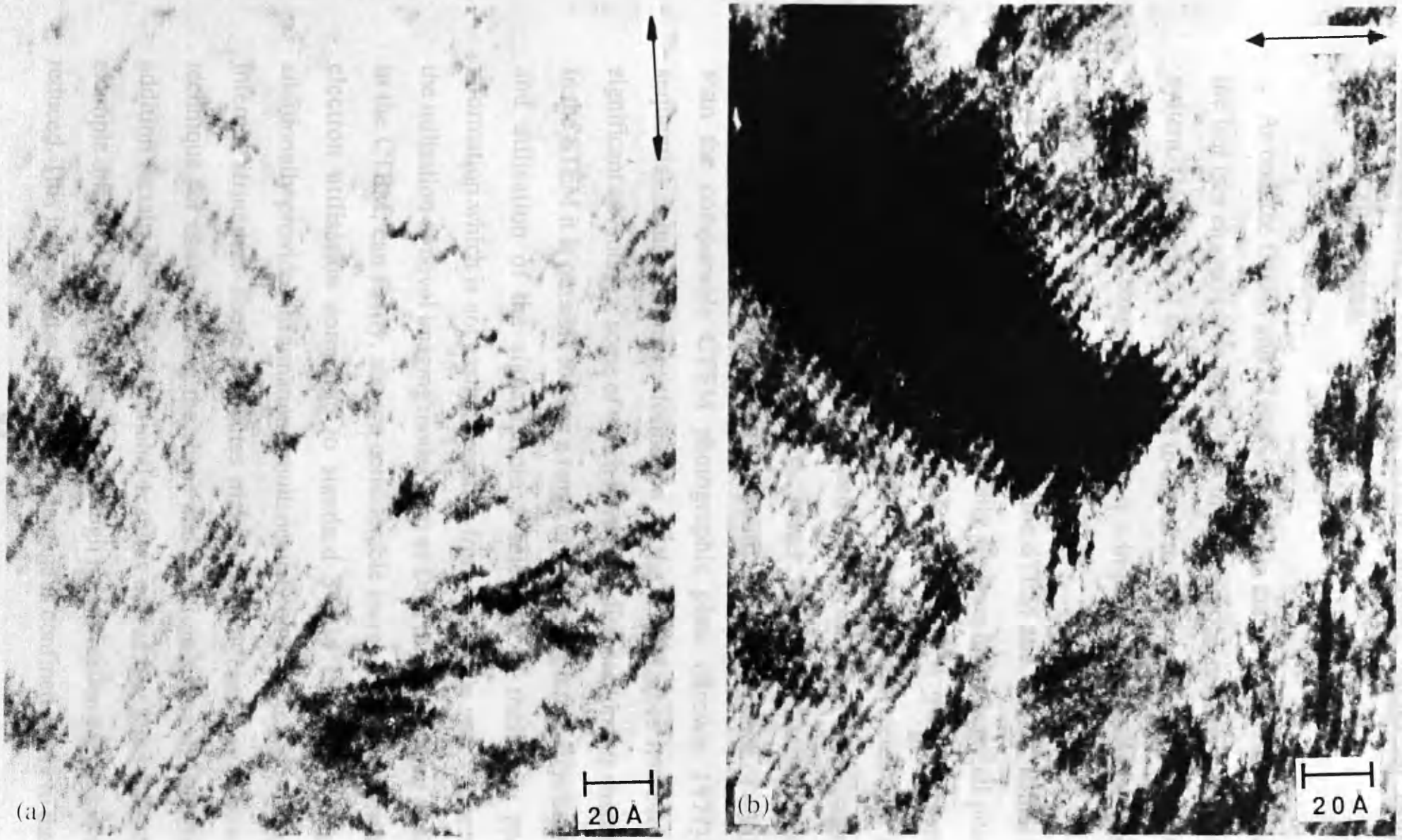

Figure 5.15: (a)-(b) High magnification DPC STEM lattice images of graphitised carbon.

5.5 Comparison of CTEM and STEM imaging modes for radiation sensitive specimens.

As both the CTEM and STEM were used in the investigations described in the last two chapters it is instructive to compare the relative merits of each system. One facet of this related to signal to noise considerations and these were compared in chapter 3. However it is important to discuss the merits of each system in a wider context.

A fundamental difference between the STEM and CTEM, is that in the former the image is acquired sequentially whereas in the latter all pixels are acquired simultaneously. The latter approach is advantageous for investigating beam sensitive materials, since parallel recording offers significant benefits in terms of speed and, in the case of photographic emulsions, the number of pixels in the image. The CRT recording screen for example has between 1-2x10^6 picture points, which is a factor of ~36X less than the comparable CTEM photographic plate (Brown, 1977). The sequential nature of image formation in the STEM does however offer significant advantages, some of which have been discussed in this chapter.

In the STEM it is possible to have a range of detectors present simultaneously and utilisation of the signals from a selection of these can provide information which is not easily accessible from any single one. Furthermore, the utilisation of novel imaging modes such as DPC microscopy not attainable in the CTEM, can firstly, allow a considerable increase in the efficiency of electron utilisation compared to standard STEM lattice imaging and additionally provides information simultaneously on particle topography and internal structure. These attributes makes DPC microscopy a powerful technique for characterising the shape and structure of small particles. In addition certain desirable operational features accrue using the STEM. For example difficulties in selecting areas at high magnification are considerably reduced. This is due to the fact that any damage is confined solely to the area

observed on the viewing screen. Therefore operations such as focussing and astigmatism correction can be carried out on an area adjacent to the region of interest. The desired area can then be brought quickly into the field of view and the image acquired.

Chapter 6

CONSIDERATIONS FOR ENERGY DISPERSIVE X-RAY MICROANALYSIS

6.1 Introduction

As discussed in chapter 1, the industrial preparation of the pigmentary material involved substituting halogen atoms for the hydrogen atoms around the periphery of the copper phthalocyanine molecule. The resultant properties of the pigment, in particular the shade, are strongly dependent on the quantity and type of halogen added. Variations in shade can occur between batches prepared under standard manufacturing conditions indicating a differing level of incorporation of halogen into the pigment. The purpose of these investigations was therefore to provide compositional information, of the highest possible accuracy, to determine whether variations in chemical composition were present on a microscopic scale. The technique used was EDX microanalysis and the specific measurements made were of the halogen to copper ratios. As virtually all the molecules were believed to contain a central copper atom the values obtained can be interpreted as the mean halogen content per molecule for each of the samples investigated. The advantage of EDX microanalysis over standard chemical analysis is that compositional information is available on a microscopic scale and the accuracy achievable is greater than chemical analysis which at best is $\pm$ 1 halogen atom/molecule (Vass, 1988). However, the information that can be obtained by any electron beam technique is limited by the damage the material suffers during electron irradiation. This chapter is therefore concerned with various aspects of EDX which enable

extraction of the maximum amount of information from the beam sensitive pigmentary samples under investigation. The production of characteristic x-rays, and the procedure adopted to convert the number of detected x-ray counts to elemental concentrations, is described in section 6.2. Absorption of characteristic x-rays before detection can lead to erroneous conclusions on specimen composition. Section 6.3 discusses two aspects of absorption, namely self-absorption in the specimen and absorption in the EDX detector. A major problem in obtaining accurate compositional information from organic materials is that a substantial degree of mass loss can occur during electron irradiation. Techniques which minimise this mass loss are thus of considerable interest, offering the possibility of obtaining a more meaningful analysis. One such approach involves keeping the specimen at cryogenic temperatures. The rationale for this is that the mobility of the molecular fragments produced by bond breakage should be substantially reduced at lower temperatures, this is discussed in section 6.4. The instrumental requirements for EDX analysis of the beam sensitive specimens is discussed in section 6.5. Included in this section is a discussion of the performance of the low temperature x-ray rod, designed to investigate the effect of specimen cooling on the rate of halogen loss.

6.2 Ionisation cross-sections

EDX microanalysis is an established technique for determining specimen composition in the electron microscope (Cliff & Lorimer, 1975). There are two completely different mechanisms by which x-rays can be produced when electrons with energies around 100keV are incident on a thin foil target. Bremsstrahlung photons are produced when the incident electrons are accelerated in the field of the atomic nuclei in the specimen. This gives a continuous background in the spectrum which decreases in magnitude with increasing photon energy. As the shape of the spectrum is similar for all elements it yields no direct information on specimen composition. A detailed discussion of the bremsstrahlung component of an EDX spectrum is given by Chapman et. al. (1984). Characteristic photons may be produced when an atom de-excites following the ionisation of an inner atomic shell by an incident electron. The emitted photon of energy hν is characteristic of the atom and so a peak appears in the spectrum centred about this energy. It is the characteristic photons which provide information on specimen composition. In this work only transitions to the K-shell are considered. Quantitative EDX microanalysis then requires an accurate knowledge of K-shell ionisation cross-sections. In the case of thin specimens, where the mean energy loss is substantially less than the initial energy, the probability for ionisation of a particular inner shell is described by the relevant cross-section. The K-shell ionisation cross-section σ_{iK} is frequently calculated using a simple functional form. One suitable form is the Bethe model (Bethe, 1930). Using the Bethe model the total ionisation cross section for K-shell transitions, σ_{iK} is given by,

$$\sigma_{iK} = 2\pi e^4 b_K / n\left(\frac{c_K T_0}{I_K}\right)\frac{1}{T_0 I_K} \qquad (6.1)$$

where I_K is the K-shell binding energy and b_K and c_K are parameters which can be evaluated empirically. Following Gray et. al. (1983), the values of b_K and c_K used for elements of interest in this work were 0.67 and 0.89 respectively. Analysis of Kα peaks requires the calculation of cross-sections for x-ray production per unit solid angle. These were obtained using,

$$\sigma_{cK} = \frac{s_K \omega_K \sigma_{iK}}{4\pi} \qquad (6.2)$$

The fraction of ionisation events which result in emission of an x-ray photon rather than an Auger electron is described by the fluorescence yield ω_K. Values for the fluorescence yield were obtained from Langenberg & Van Eck (1979). The partition function S_K expresses the probability of a transition to the K-shell originating from a particular higher order shell and is defined as

$$s_K = \frac{N_\alpha}{N_\alpha + N_\beta} \qquad (6.3)$$

where N_α and N_β are the number of transitions from the L-shell and M-shell respectively. Values for S_K, were obtained from Khan & Karami (1980). Figure 6.1, lists values for I_K, hν, ω_K, s_K and σ_{cK} for the elements of interest in this thesis.

Element	I_K (keV)	$h\nu$ (keV)	ω_K	s_K	σ_{cK} ($\times 10^{-32}$ m^2 sr^{-1})
Chlorine	2.82	2.62	0.098	0.92	7.5
Copper	8.98	8.04	0.44	0.88	6.7
Bromine	13.48	11.9	0.62	0.86	5.1

Figure 6.1: Values for I_K,$h\nu$,ω_K,s_K and σ_{iK} for the elements of interest in this thesis.

The information on specimen composition usually requires the ratio of the number of atoms of two elements in the irradiated volume. The ratio N_a/N_b for two atomic species a and b, is related to the peak intensities P_a/P_b by,

$$\frac{N_a}{N_b} = \frac{\varepsilon(h\nu_b)\sigma_{cKb}}{\varepsilon(h\nu_a)\sigma_{cKa}}\frac{P_a}{P_b} \qquad (6.4)$$

The equation is conveniently rewritten as

$$\frac{N_a}{N_b} = k_{ab}\frac{P_a}{P_b} \qquad (6.5)$$

where k_{ab} is given by

$$k_{ab} = \frac{\varepsilon(h\nu_b)\sigma_{cKb}}{\varepsilon(h\nu_a)\sigma_{cKa}} \qquad (6.6)$$

The k-factor, relates the relative efficiency of production and detection of the characteristic signals. Knowledge of this k-factor for the two elements of interest enables calculation of the relative atomic fractions from the ratio of counts in the x-ray peaks (Cliff & Lorimer, 1975). Determination of the k-

factor requires information on the efficiency of the x-ray detector at the photon energies of interest. Evaluation of these parameters is described in the following section.

6.3 Self-absorption of characteristic x-rays and low energy detection efficiencies

Absorption of characteristic x-ray photons, before they are detected, can seriously affect the measured elemental composition from the irradiated volume. The two major absorption processes which need to be considered are specimen self-absorption and absorption in the EDX detector. Self absorption of characteristic x-rays by the specimen is relevant particularly to the Cl K x-ray (2.6keV). Using the approach of Goldstein (1979), the magnitude of absorption of characteristic x-rays within the specimen can be calculated. The absorption factor can be written as

$$I_a = I_0 \frac{\left[1 - \exp\left\{-\left(\frac{\mu}{\rho}\right)\rho t \operatorname{cosec}\alpha\right\}\right]}{\left(\frac{\mu}{\rho}\right)\rho t} \qquad (6.7)$$

where α is the detector take off angle, (μ/ρ) is the mass absorption coefficient for the material and ρ is the density. In this case the absorbing material is a mixture of various elements. An effective value for (μ/ρ) is calculated using,

$$\left(\frac{\mu}{\rho}\right) = \sum_j \left(\frac{\mu}{\rho}\right)_j C_j \qquad (6.8)$$

where $(\mu/\rho)_j$ is the mass absorption coefficient for element j and c_j is the mass fraction for element j. Values for the mass absorption coefficients were obtained from an extensive tabulation by Heinrich (1987). As anticipated, absorption correction primarily affects the low energy photons; for the thickness of interest in this work (~100nm) the absorption correction is small, ~1% for chlorine and negligible for copper and bromine.

The second absorption process of concern is absorption by the EDX detector. At the front end of the Si(Li) detector is a thin Be window typically 8μm thick. This isolates the detector vacuum from the outside world. A thin evaporated layer of gold (~20nm) acts as a contact on the front surface of the Si (Li) crystal. An incident photon, passing through the Be window and gold contact layer, may be absorbed in the 'active region' of the silicon crystal, ionising the silicon atoms and resulting in the emission of photoelectrons. These then lose energy in the crystal, causing a cascade of electron-hole pairs. The number of such pairs is proportional to the initial energy of the photon. These electrons and holes are swept apart by the applied bias, forming a charge pulse, whose magnitude in turn is proportional to the incident photon energy. The pulse is amplified by a FET, located directly behind the crystal, and fed to a multichannel analyser where it is displayed as a histogram of counts against energy.

The efficiency of an x-ray detector falls below unity at low photon energies due to absorption of the incoming photons before they arrive at the active portion of the detector crystal. Absorption occurs in the Be window, the Au contact, and a silicon 'dead layer'. The first of these is the most important, and it is convenient to describe the efficiency of the detector in terms of an effective Be thickness τ_{Be} (Gray et. al., 1983). In this work a value of 10μm was appropriate. At low photon energies $\varepsilon(h\nu)$ is given by,

$$\varepsilon(h\nu) = \exp\left[-\left(\frac{\mu}{\rho}\right)_{Be} \rho_{Be}\tau_{Be}\right] \qquad (6.9)$$

where ρ_{Be} is the density of Be, $(\mu/\rho)_{Be}$ is the mass absorption coefficient for the photon energy of interest in Be and is again evaluated following Heinrich (1987). Calculation of the detection efficiencies at the photon energies of interest gave 0.95 for chlorine, and 1.0 for copper and bromine to an accuracy of <2%, (Chapman et. al., 1983).

6.4 Low temperature EDX microanalysis

The information that can be obtained from the analysis of organic materials such as the phthalocyanines by EDX microanalysis is limited due to damage of the material upon electron irradiation. Primary damage arises due to ionisation of the specimen by the incident electron beam. Secondary damage processes such as diffusion then lead to a loss of peripheral halogen atoms and thus to a reduction in the halogen to copper ratio. As we are interested in determining halogen to copper ratios with the highest possible accuracy, it is clearly important to reduce the rate at which halogen is lost. As diffusion is strongly temperature dependent, it should be possible to reduce the mobility of the halogens by cooling the specimen to lower temperatures. This avenue has been investigated by, for example, Shuman et. al. (1976) and Egerton (1980). Results from these investigations demonstrated that the rate of mass loss was substantially reduced upon cooling to liquid nitrogen temperatures. Additionally, if the rate of halogen loss could be significantly

reduced, it would be possible to increase the electron dose incident on the specimen, with a corresponding increase in analytical accuracy.

6.5 Instrumental Considerations

EDX microanalysis is based on detecting and quantifying the characteristic x-ray photons generated within a volume of sample upon irradiation by the electron beam. It is therefore important that the detected x-rays should arise solely from the volume under analysis. Unfortunately stray electrons passing down the column and electrons scattered from the specimen and its support can cause additional contributions whose nature is unrelated to the region of specimen under analysis. In order to identify and reduce the sources of extraneous background, the environment of the JEOL JEM 100C electron microscope has been extensively modified (Nicholson et. al., 1982). Instrumental contributions from the specimen surroundings and the x-ray collimator have been reduced to such an extent that by far the largest source now arises from the support grid and specimen rod. Specimens were prepared on 75-mesh titanium grids. These were chosen for several reasons; they offer small instrumental backgrounds provided the beam is kept sufficiently far from the grid bar, they have an easily identifiable characteristic line in the x-ray spectrum at 4.5 keV which is well separated from the elements of interest and, additionally, they allow a large area of specimen to be analysed. A spectrum acquired from the $Cl_{14.5}$ Cu Pc sample showing the major x-ray peaks is presented in figure 6.2; the extraneous titanium peaks are due to the specimen grid and the top plate of the rod.

The low temperature x-ray rod used to investigate the effect of low temperature on the rate of halogen loss from several halogenated copper phthalocyanine pigmentary samples is illustrated in figures 6.3 and 6.4. The

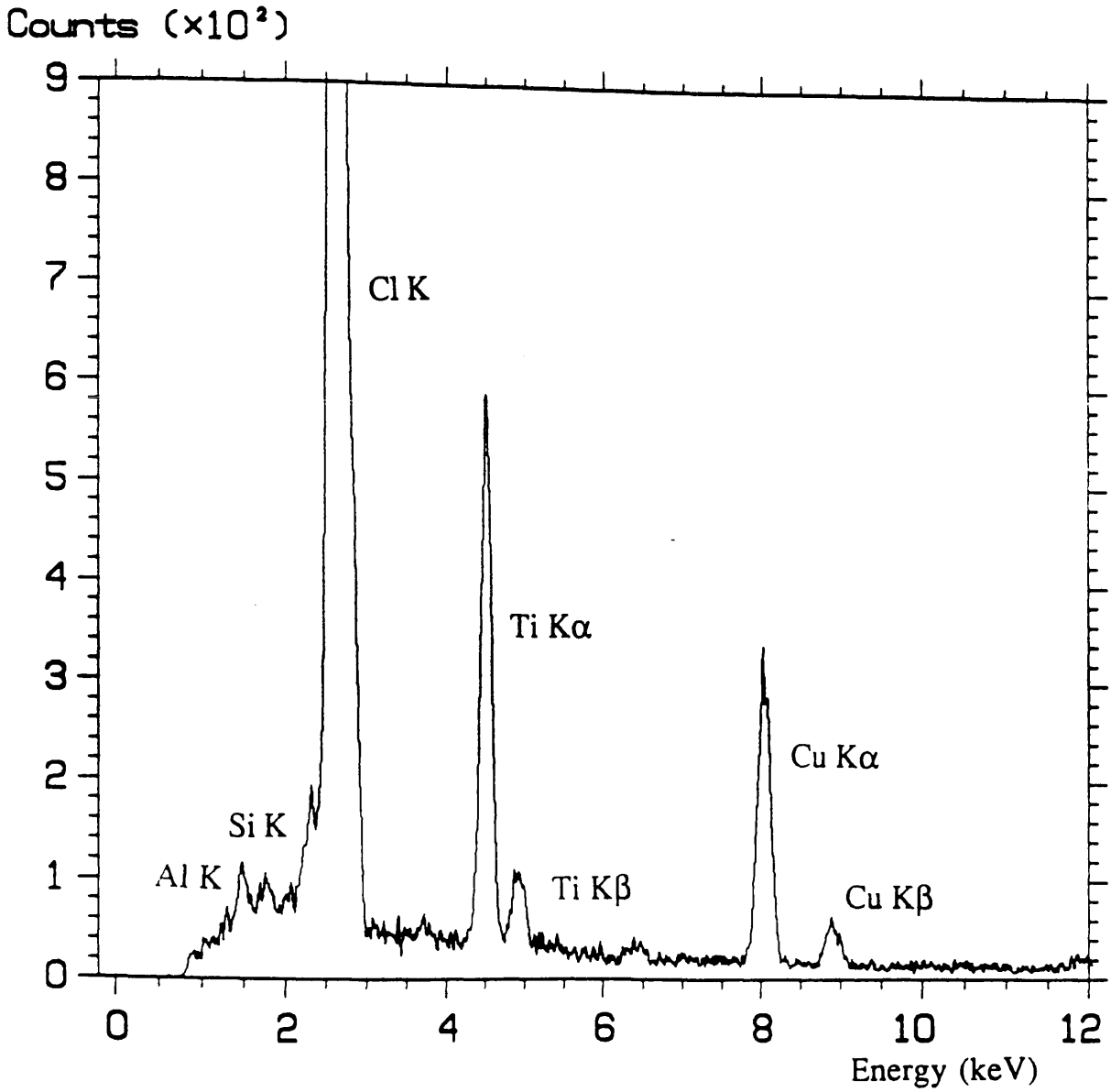

Figure 6.2: Typical EDX spectrum from ~$Cl_{14.5}$ Cu Pc.

Figure 6.3: The low temperature x-ray rod.

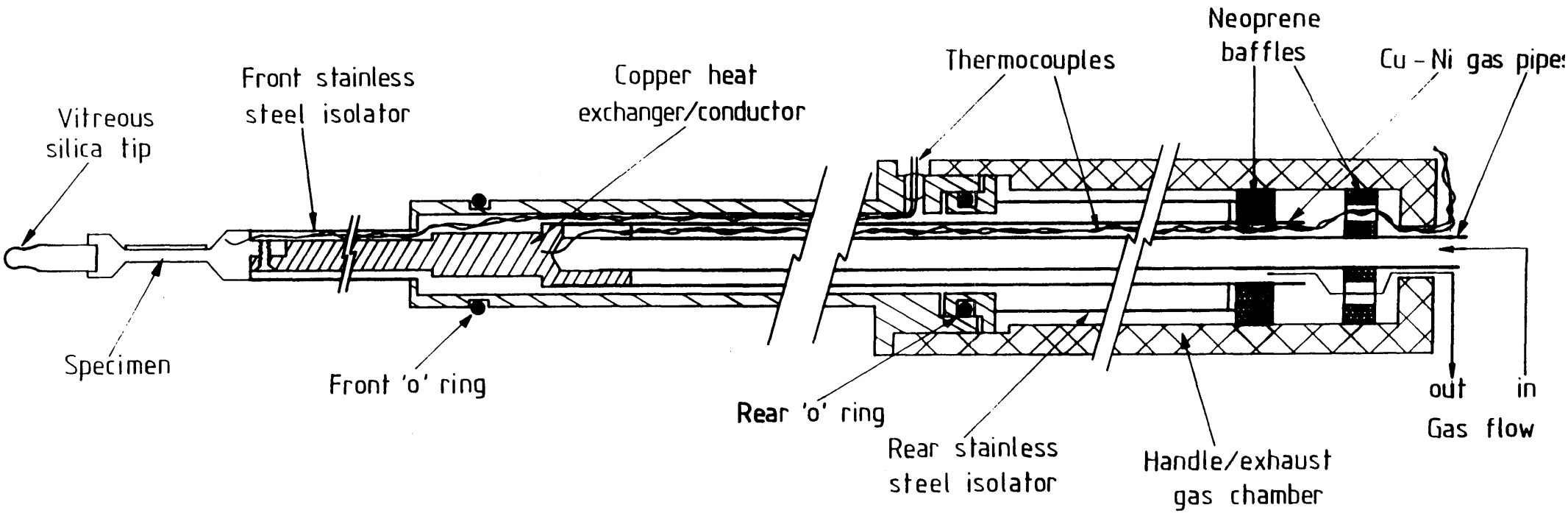

Figure 6.4: Schematic diagram of the low temperature x-ray rod.

rod was designed by Dr W.A.P. Nicholson of the Department of Physics and Astronomy, Glasgow University and was constructed in the mechanical workshop of that department. The rod was designed to have excellent x-ray analytical properties without compromising its low temperature performance.

A schematic diagram of the specimen rod and detector environment in the JEM 100C electron microscope is shown in figure 6.5. As the detector is perpendicular to the incident beam direction it is neccesary to tilt the specimen from the normal to allow the generated x-rays to be detected. A consequence of this geometry is that it is important to retain as little bulk material above the specimen as possible to minimise shadowing in the direction of the beam. Similar considerations apply to the underside of the rod, with a minimum of material being used close to the specimen to reduce the material that can be struck by electrons scattered by the specimen. These considerations led to the design for the upper section of the x-ray rod as shown in figure 6.6.

The construction material for the upper section of the rod was oxygen free copper, chosen for its high thermal conductivity. However, as we are interested in the copper content of the phthalocyanines, it is essential that no copper signal from the rod should contribute to the spectrum. The upper section was heavily coated in successive layers of carbon dag. A spectrum recorded from a thin aluminium specimen of comparable mass thickness to the pigmentary samples is presented in figure 6.7. No copper signal is visible above the background. Thus the copper signal visible in spectra recorded from the pigments can be attributed entirely to the phthalocyanine samples.

Cooling in the low temperature x-ray rod is achieved by the flow of cold high purity nitrogen gas in the vicinity of the specimen. This involves precooling the gas in a copper coil (12 turns, 50mm diameter, 6mm tube) in a 25 litre dewar of liquid nitrogen. The gas then passes via an insulated tube to

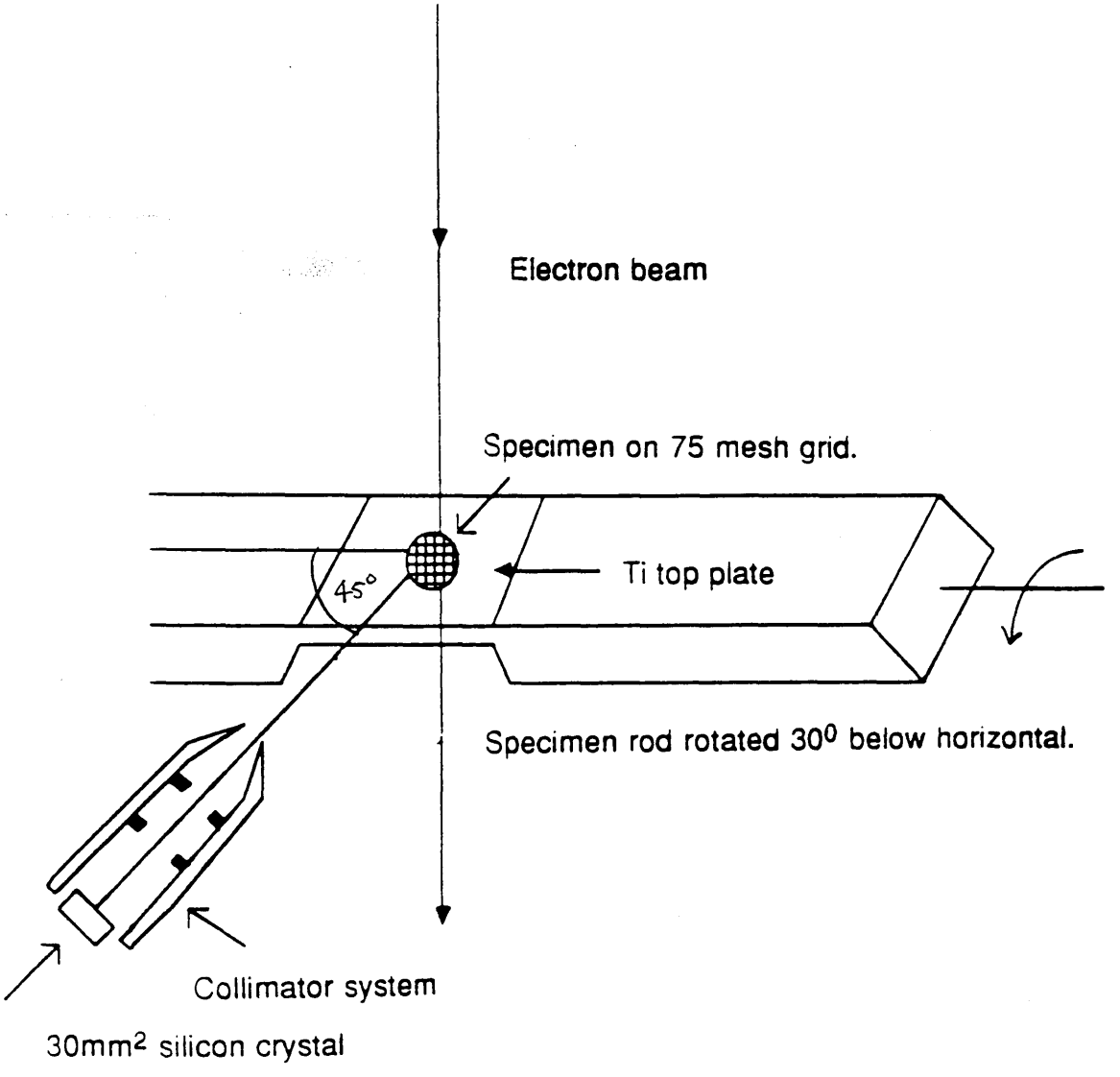

Figure 6.5: Schematic diagram of specimen and detector arrangement for x-ray microanalysis in the JEM 100C.

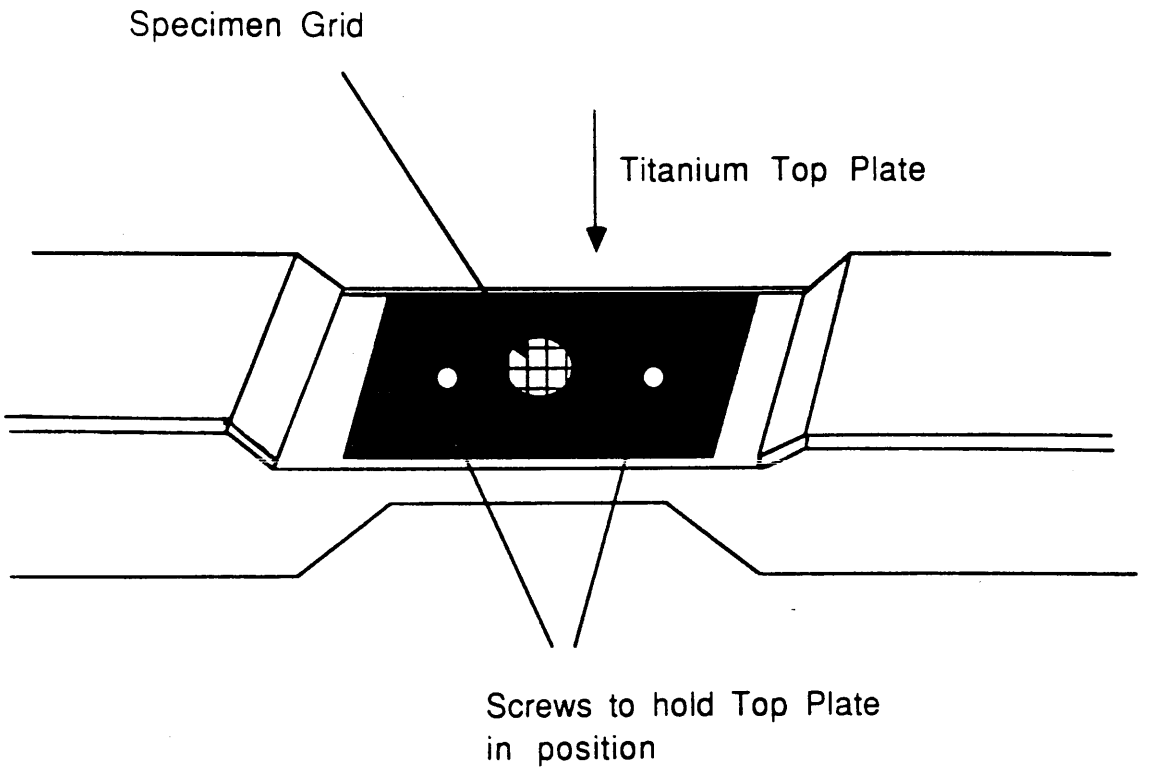

Figure 6.6: Schematic diagram of the top section of the low temperature x-ray rod.

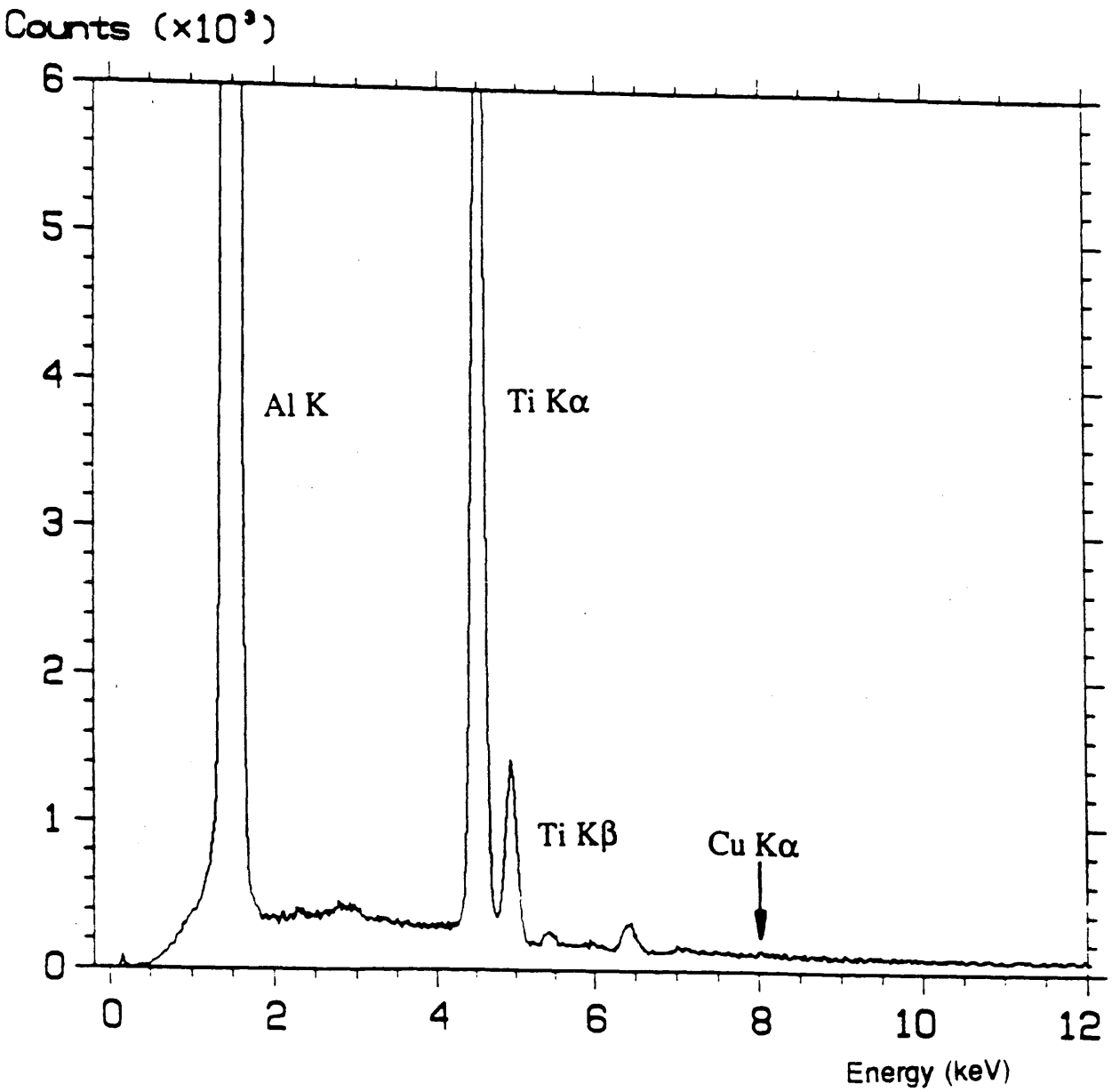

Figure 6.7: Spectrum from aluminium specimen showing no copper peak above the background.

a second copper cooling coil (6 turns, 100mm diameter, 6 mm tube) in a 2 litre dewar of liquid nitrogen mounted close to the microscope column. The gas is fed to the inner Cu-Ni tube of the low temperature rod via small nickel bellows, the return path being provided by the outer tube. All exposed copper tubing was shielded in neoprane to minimise heat losses. The temperature of the rod was monitored using two copper/copper-nickel thermocouples, one located at the heat exchanger, the other as close to the specimen as possible. The temperature was displayed on a Comark digital thermometer to an accuracy of <0.2 K. The response of the system upon cooling is shown in figure 6.8, the difference in temperature between the two thermocouples (typically 10K) was used during development of the rod to indicate the magnitude of heat leaks in the rod.

An important requirement when using gas cooled low temperature stages is that drift rates are sufficiently low as not to interfere with the analysis. The variation of operating temperature with flow rate is shown in figure 6.9. The lowest temperature attainable was ~100K. However this required considerably increasing the flow rate which resulted in high drift rates. A flow rate of 5L/minute was found to be a compromise, allowing an operating temperature of 110K to be achieved, with an acceptable specimen drift. Drift rates of 0.2-0.3nms^{-1}, were measured at an operating temperature of 110K, after allowing the system ~30 minutes to reach thermal equilibrium. The experimental procedure (described in detail in the following chapter) typically involved acquisition of 10 spectra in a series, each of 24s duration. Therefore drift was not a problem in the analysis of areas typically 5-10μm^2. The experimental equipment used in the low temperature EDX studies is shown in figures 6.10 and 6.11.

To investigate the response of the various samples to electron irradiation, information on the electron dose incident on the specimen is required. This

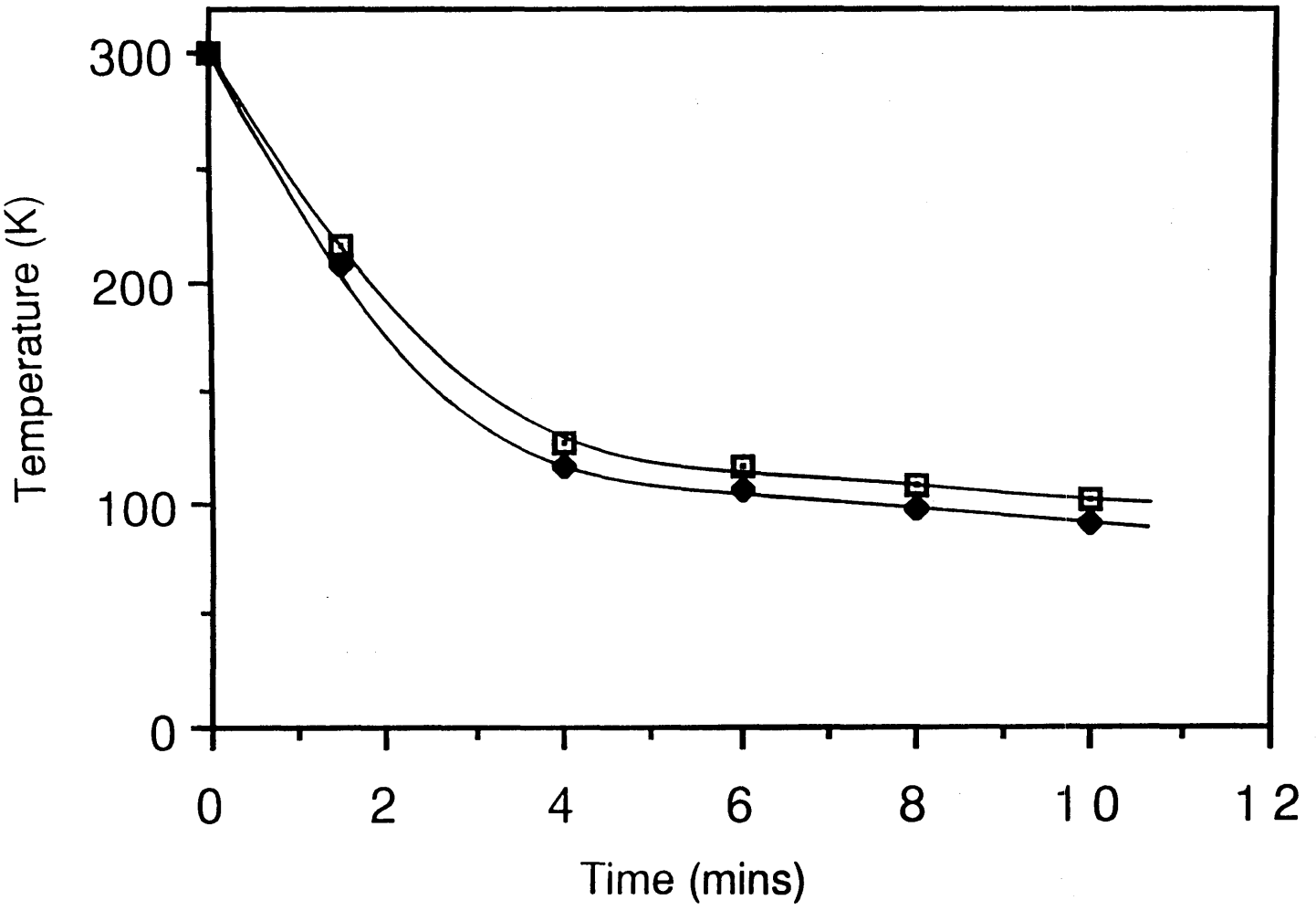

Figure 6.8: Variation of the operating temperature with cooling period, using a flow rate of 5 L/minute.

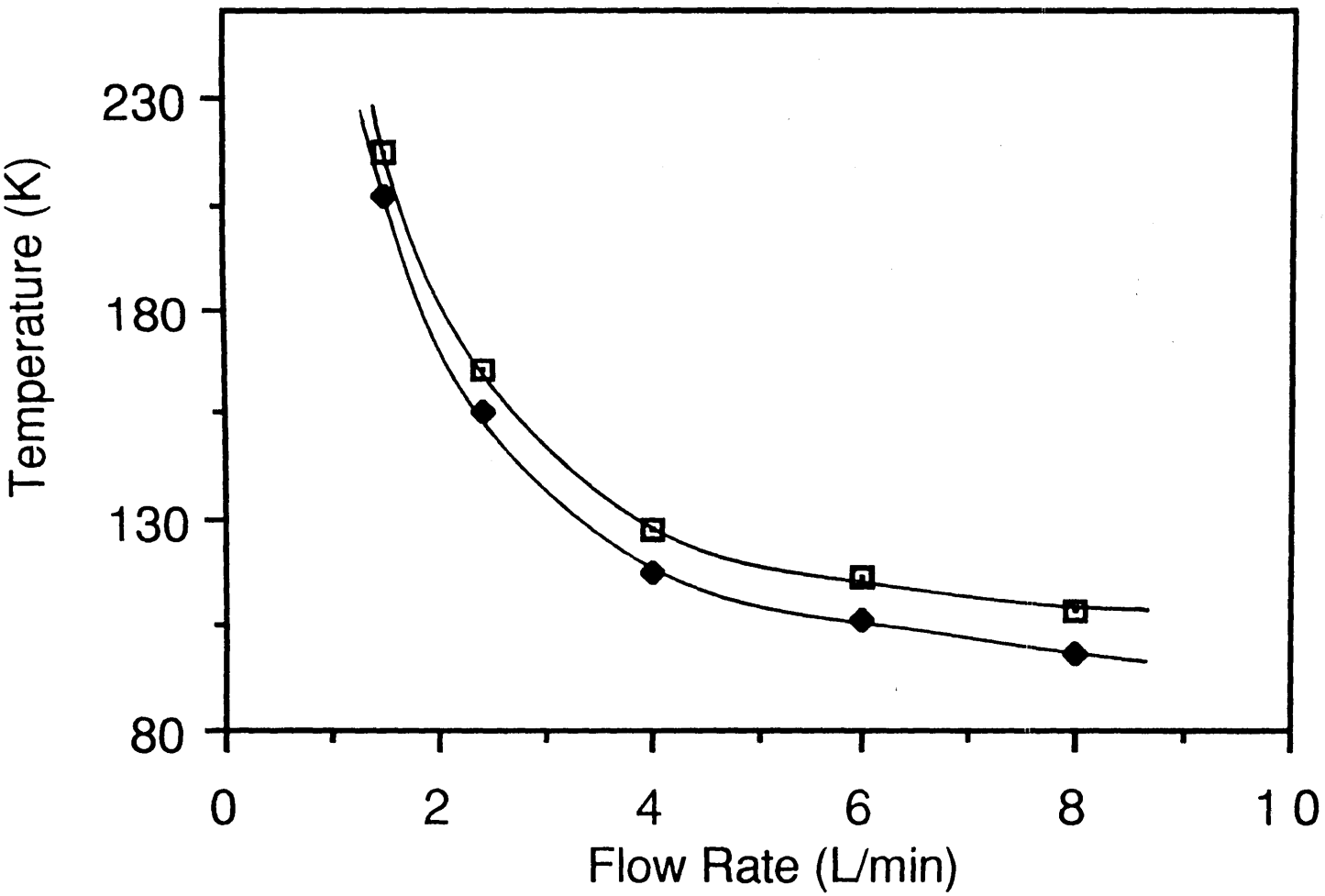

Figure 6.9: Variation of the operating temperature with flow rate.

Figure 6.10: The experimental arrangement used in low temperature EDX investigations.

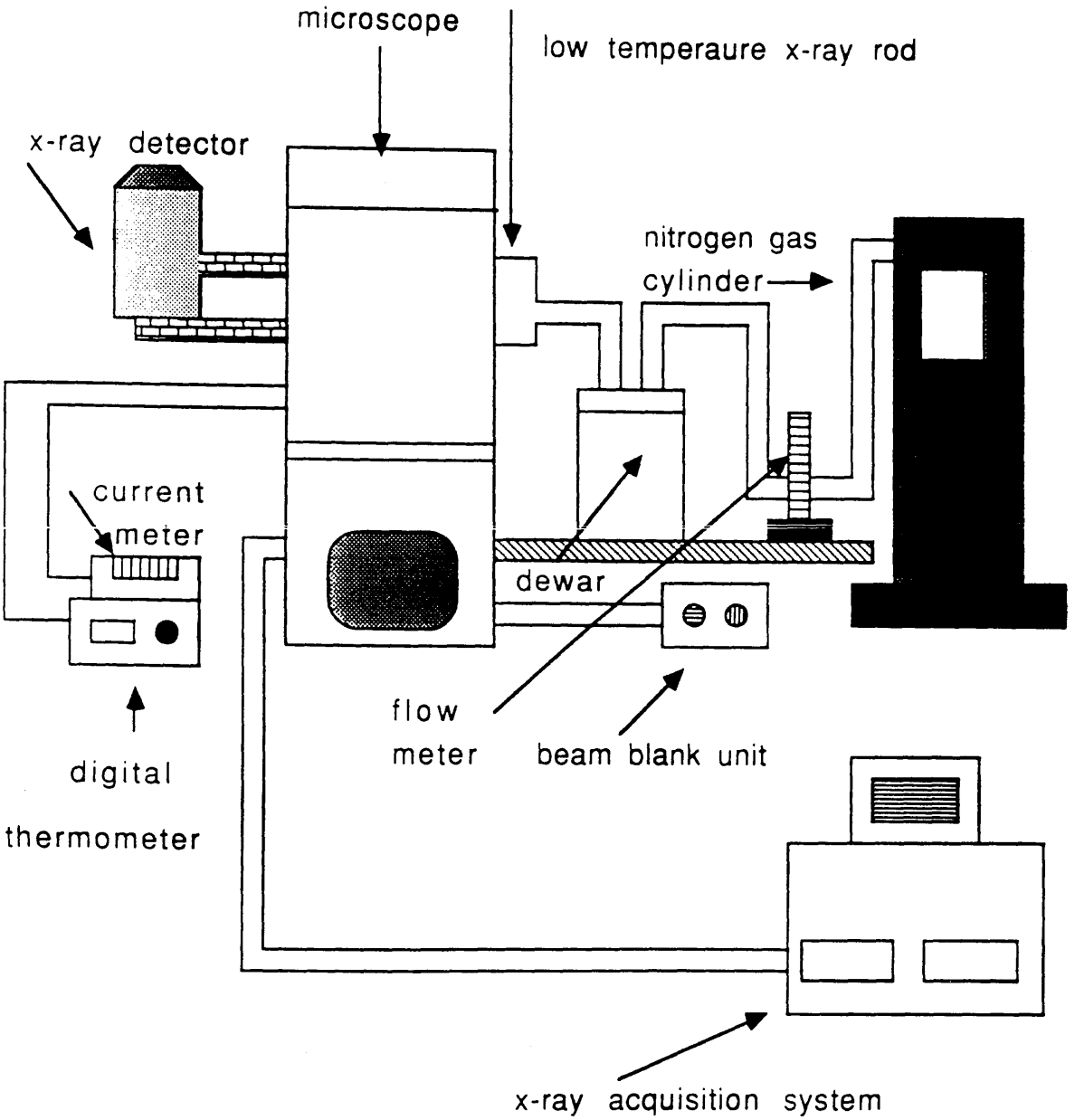

Figure 6.11: Schematic diagram of the experimental arrangement used in low temperature EDX investigations.

was obtained by measuring the incident current using a Faraday cage located in the viewing chamber of the electron microscope in conjunction with a Keithley 616 electrometer. The microscope was equipped with a Link Si (Li) x-ray detector which has a crystal of active area $30mm^2$ that subtended a solid angle of ~ 0.02 steradians in its normal position with respect to the specimen. Spectra were acquired using a Link Systems 860 x-ray acquisition and analysis system. This system allows spectra to be acquired and stored on floppy disk, and provided some processing routines. Included amongst the processing options are the ability to set windows on regions of interest to calculate the peak and background contributions in the spectrum. The data were then transferred to a micro-computer where programs were written to analyse the data. This involved calculation of the elemental composition and the errors involved.

The results obtained from the low temperature investigations are described in the next chapter.

Chapter 7

EXPERIMENTAL RESULTS FROM EDX MICROANALYSIS OF VARIOUS HALOGENATED COPPER PHTHALOCYANINE PIGMENTS

7.1 Introduction

In this chapter the application of EDX microanalysis to several halogenated copper phthalocyanine pigmentary samples is discussed. The basic principles of this technique were outlined in chapter 1 and the instrumental requirements discussed in chapter 6. This chapter concerns those aspects of the technique which allow compositional information of the highest accuracy to be obtained from the radiation sensitive specimens under investigation. This is important not only in determining as accurately as possible the local specimen composition, but in assessing whether variations in specimen composition on a microscopic scale are present in these samples. However, the information that can be obtained using electron beam techniques is limited by the damage the material suffers during electron irradiation. Damage results in a reduction in the number of halogen atoms in the analysed volume, due to diffusion following bond breakage; the number of copper atoms in contrast remains unchanged. Thus there is a reduction in the halogen to copper ratio as irradiation proceeds. Analysis based on a single measurement is therefore of limited accuracy in determining the halogen to copper ratio. To obtain accurate analyses from small volumes of material it is therefore important to reduce the rate at which halogen is lost, and towards this end, low temperature EDX microanalysis has been investigated. The experimental procedure developed for low temperature EDX is described in

detail in section 7.2. The spectral processing required to extract elemental concentrations from these series of spectra is described in section 7.3. The effects of radiation damage on the elemental composition of the areas of the specimens under investigation are discussed in section 7.4. Results are presented showing the rate of halogen loss as a function of electron dose at room temperature and low temperature. This served two purposes. Firstly it allowed a comparison to be made between room and low temperature microanalysis of similar regions of specimen under carefully controlled experimental conditions. Secondly, and more importantly in providing information on the pigments themselves, by extrapolation of these data to zero dose the composition of the undamaged material could be recovered. The extrapolation procedure developed is described in section 7.5. The results obtained from the extrapolations are presented in section 7.6. Comparison of room and low temperature microanalysis is described in section 7.7.

7.2 Experimental details

Several industrially prepared pigmentary samples were investigated in this project. Details of these materials were given in chapter 4.

As discussed previously, damage results in the loss of peripheral halogen atoms and thus to a reduction in the halogen to copper ratio. To avoid obtaining inaccurate results on specimen composition it is essential to reduce this loss to a negligible level, or accurately monitor its progress as irradiation proceeds. The former option is not feasible as the dose would have to be so severely restricted that the characteristic peaks would be statistically insignificant. The latter approach was therefore adopted. In order to investigate the response of the material, it is essential that specimen

irradiation outwith spectral acquisition be minimised. Preliminary examination of the sample was therefore undertaken using a low electron dose <0.01Ccm^{-2}. Upon finding a suitable area, the probe was reduced in size to match the area of specimen selected for analysis and the beam blanked using a beam blanking unit. Areas typically 5-10μm^2 were selected for analysis. The time required for the whole of the initial procedure was typically <5s and an offset to account for irradiation of the sample in this time was calculated and added to the dose measurements. Secondly, synchronisation of spectral acquisition and irradiation periods ensured that irradiation of the sample outwith spectral acquisition was eliminated. An important requirement for accurate microanalysis is the reproducibility of the probe position. Observation at the highest magnification used in microanalysis (20kX) showed no shift in position on its return and following blanking no drift over the acquisition times used in the analyses.

Series of x-ray spectra were acquired from the same small volumes of specimen with the beam being re-blanked after each acquisition. Preliminary experiments had revealed that a serious loss of halogen (up to 30%) could occur when the specimen was subjected to a dose of 10 Ccm^{-2} and for this reason individual spectra were acquired using a dose of between 0.5 Ccm^{-2} and 1 Ccm^{-2}. The accuracy with which compositional information can be obtained depends largely on the number of counts in the characteristic peaks and in this case was substantially limited by those in the Cu Kα peak. To ensure that halogen to copper ratios could be determined from each spectrum with a statistical accuracy better than 3% (corresponding to an accuracy of <0.5 halogen atoms per phthalocyanine molecule), a useful lower bound to the number of Cu Kα counts was set at 1500. Thus in a particular experiment the thickness of the specimen and the dose to which the specimen can be subjected are both fixed. Establishing the number of counts required in a particular peak then determines uniquely the charge that must be incident on

the specimen which should be illuminated by the partly focussed beam. For the conditions described above appropriate values for the two quantities are 5nC and $5\mu m^2$ respectively. Thus the volume of specimen analysed must contain $\sim 10^8$ molecules which corresponds to ~1500 particles of X-Cu Pc. The charge incident on the specimen is the product of the probe current and the spectral acquisition time and these quantities can be chosen for convenience. In practice a probe current of 0.2nA, set using a Faraday cage, and a time of 24s was selected. Using this experimental procedure allowed the variation in the halogen to copper ratio to be determined as a function of the dose to which the specimen was subjected. Extrapolation of each series of spectra to zero dose then enabled the composition of the undamaged material to be recovered. After acquiring series of spectra at room temperature the system was cooled to 110K. The experimental procedure described above was then repeated. Care was taken to traverse the grid in a systematic manner to ensure that previously irradiated areas of sample were not re-analysed.

7.3 Spectral processing

A typical area of specimen selected for EDX microanalysis is presented in figure 7.1. A typical EDX spectrum from $\sim Cl_{14.5}$ Cu Pc is shown in figure 7.2. The major peaks are from chlorine, copper Kα and Kβ and titanium Kα and Kβ. The titanium peaks are due to the specimen grid and top-plate of the x-ray rod. Small impurity peaks due to aluminium and silicon are also present. The former comes from aluminium hydroxide as discussed in chapter 4; the small silicon peak is probably due to vacuum oil contamination.

Analysis of the acquired spectra requires the conversion of the number of detected counts in the x-ray peaks to the corresponding elemental

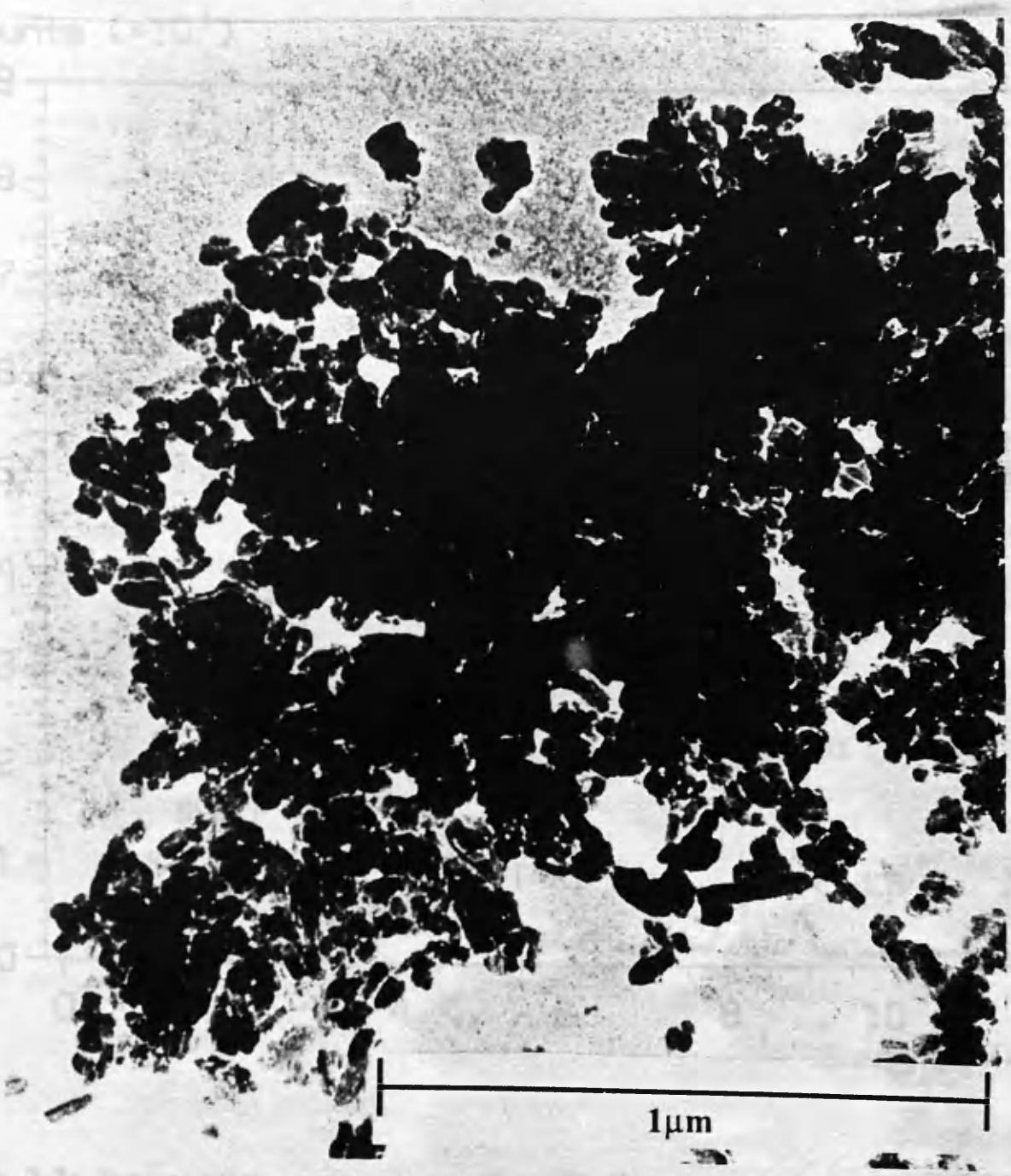

Figure 7.1: Typical area selected for EDX microanalysis.

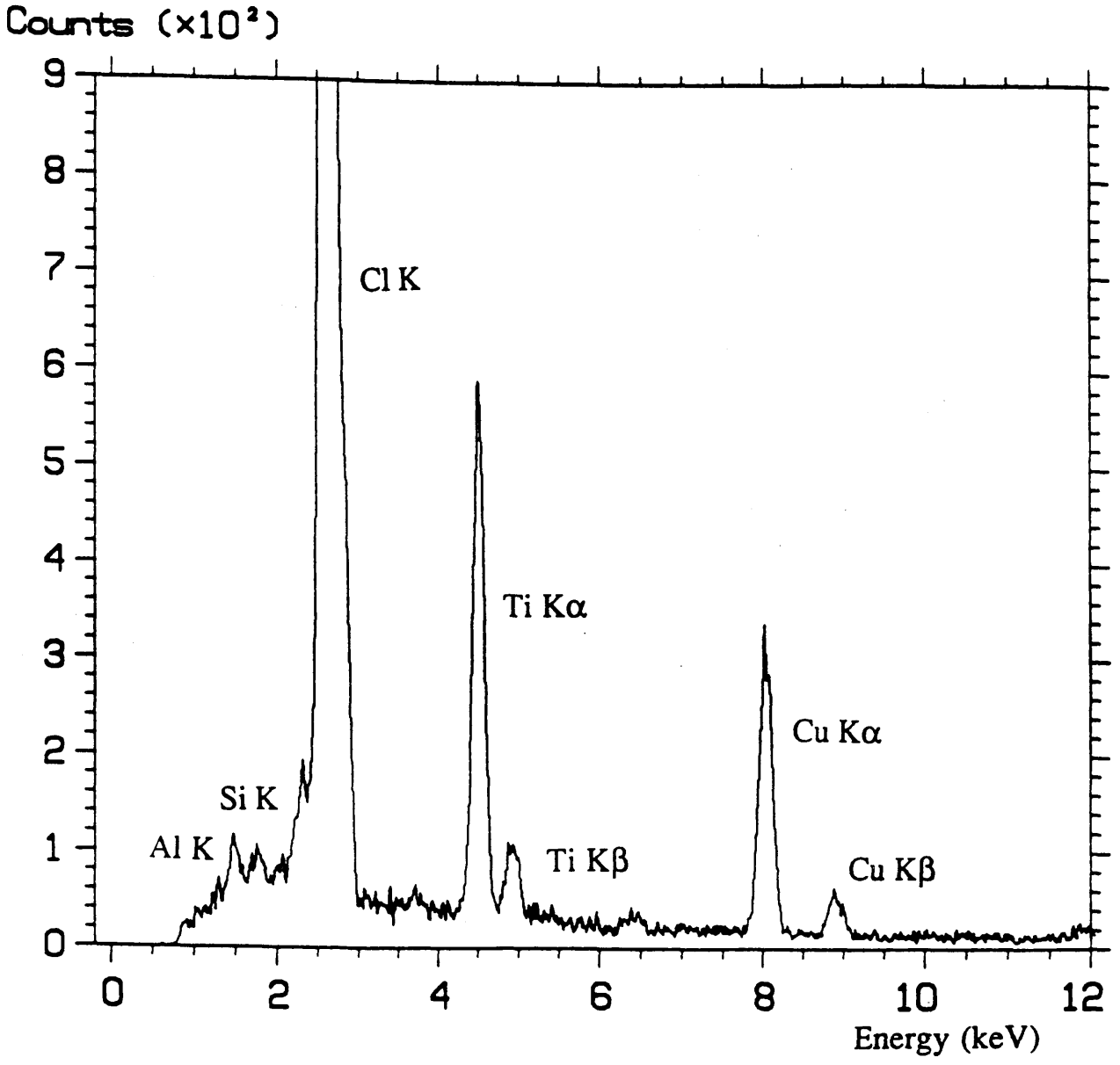

Figure 7.2: Typical EDX spectrum from ~$Cl_{14.5}$ Cu Pc.

concentration. The analysis involves two stages. Firstly, the uninformative bremsstrahlung background was subtracted from the spectrum to isolate the characteristic peaks of interest. As the background was small and its energy variation slow, a linear interpolation of the background on either side of the characteristic peaks was used to determine its magnitude. This is shown schematically in figure 7.3. The errors in the extracted characteristic signals are essentially governed by Poisson statistics of the counts in the energy ranges or 'windows' of interest.

If G denotes the number of gross counts in the peak and B is the number of counts calculated for the background contribution, the number of characteristic counts P is defined as

$$P = G - B \tag{7.1}$$

where B is given by,

$$B = N_P B = \frac{1}{2} N_P \left(\frac{B1}{N1} + \frac{B2}{N2} \right) \tag{7.2}$$

B_1 and B_2 are the number of counts in the selected background windows of width N_1 and N_2 and N_p is the number of channels in the peak. The error δP in determining P is given by

$$\delta P = (\delta G^2 + N_p^{\,2} \, \delta B^2)^{\frac{1}{2}} \tag{7.3}$$

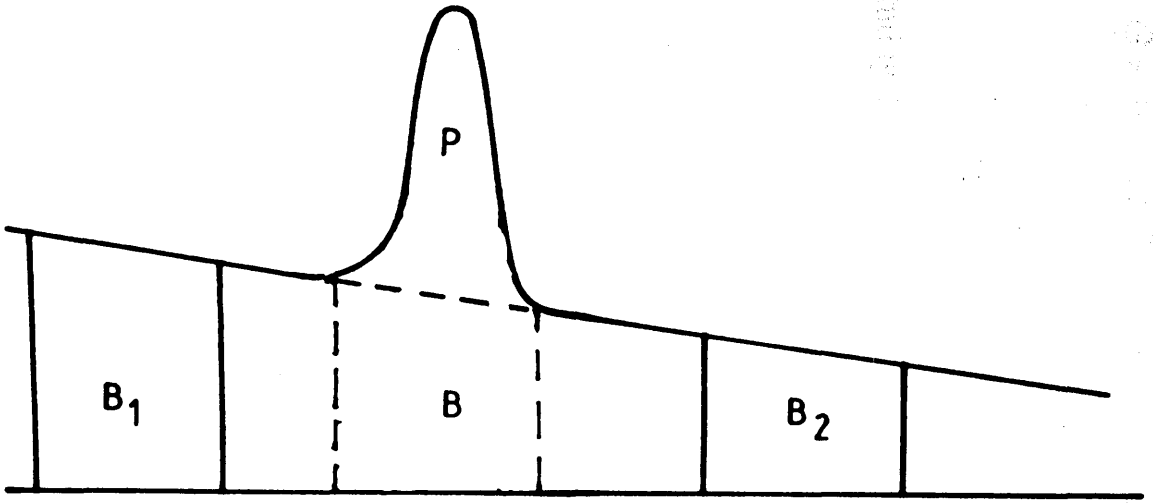

Figure 7.3: Schematic diagram showing peak extraction.

where δG^2 and δB^2 are given by,

$$\delta G^2 = G = P + N_p B \qquad and \qquad \delta B^2 = \frac{\delta B_1^2}{N_1^2} + \frac{\delta B_2^2}{N_2^2} \tag{7.4}$$

Substituting these last two expressions into equation (7.1) gives

$$\delta P = \left[P + N_p B + \frac{N_p^2}{4}\left(\frac{B_1}{N_1^2} + \frac{B_2}{N_2^2} \right) \right]^{\frac{1}{2}} \tag{7.5}$$

The errors discussed above apply to individual measurements of the ratio of the two elements.

The second stage of analysis relates the number of detected counts in the peak to elemental concentrations using the ratio technique of Cliff and Lorimer (1975). This relates the number of atoms of two species A and B (n_x/n_{Cu}) in the analysed volume to the ratio of the counts in their characteristic peaks (P_x/P_{Cu}) through the equation

$$\frac{n_x}{n_{Cu}} = k_{x\,Cu} \frac{P_x}{P_{Cu}} \tag{7.6}$$

In the absence of suitable standards relating Cu, Cl and Br theoretical values following the approach of Chapman et. al. (1984) were used. Using the values from figure 6.1 and the efficiencies of x-ray detection at the appropriate peaks given in section 6.3, the resulting values for $k_{Cu\ Cl}$ and $k_{Cu\ Br}$ were calculated to be 0.99 and 1.29 respectively. Their accuracy was estimated to be ~3%.

7.4 Radiation damage in industrially prepared pigmentary materials

Most of the series of spectra acquired comprised 10 spectra so that the total electron dose to which a particular area was subjected never exceeded $10Ccm^{-2}$. Many such series of spectra were recorded from each of the samples. In each case the variation in the halogen to copper ratio was plotted as a function of dose. As discussed in the introduction this enables the composition of the undamaged material to be obtained upon extrapolation.

Typical results obtained from the samples are shown in figures 7.4-7.10. In all cases the solid black squares are from runs at 300K whilst the outlined squares represent data acquired at 110K. Figure 7.4 shows results obtained from sample A and it is immediately apparent that the rate of loss of chlorine is significantly reduced at the lower temperature. More specifically, by a dose of $5Ccm^{-2}$ the results suggest that whilst a chlorine loss of ~25% is experienced at room temperature the loss at 110K is approximately 1/3 of this value. The improvement in stability of a factor of 3 is in accord with the results of Egerton (1986). Also noteworthy is the fact that at low temperatures the variation of the Cl/Cu ratio with dose appears to a very good approximation to be linear whilst that at room temperature curves markedly. This suggests that fitting a straight line to the experimental data

** To allow the rate of loss of halogen at room temperature to be more easily assessed, smooth curves fitted by eye have been drawn through the room temperature data.

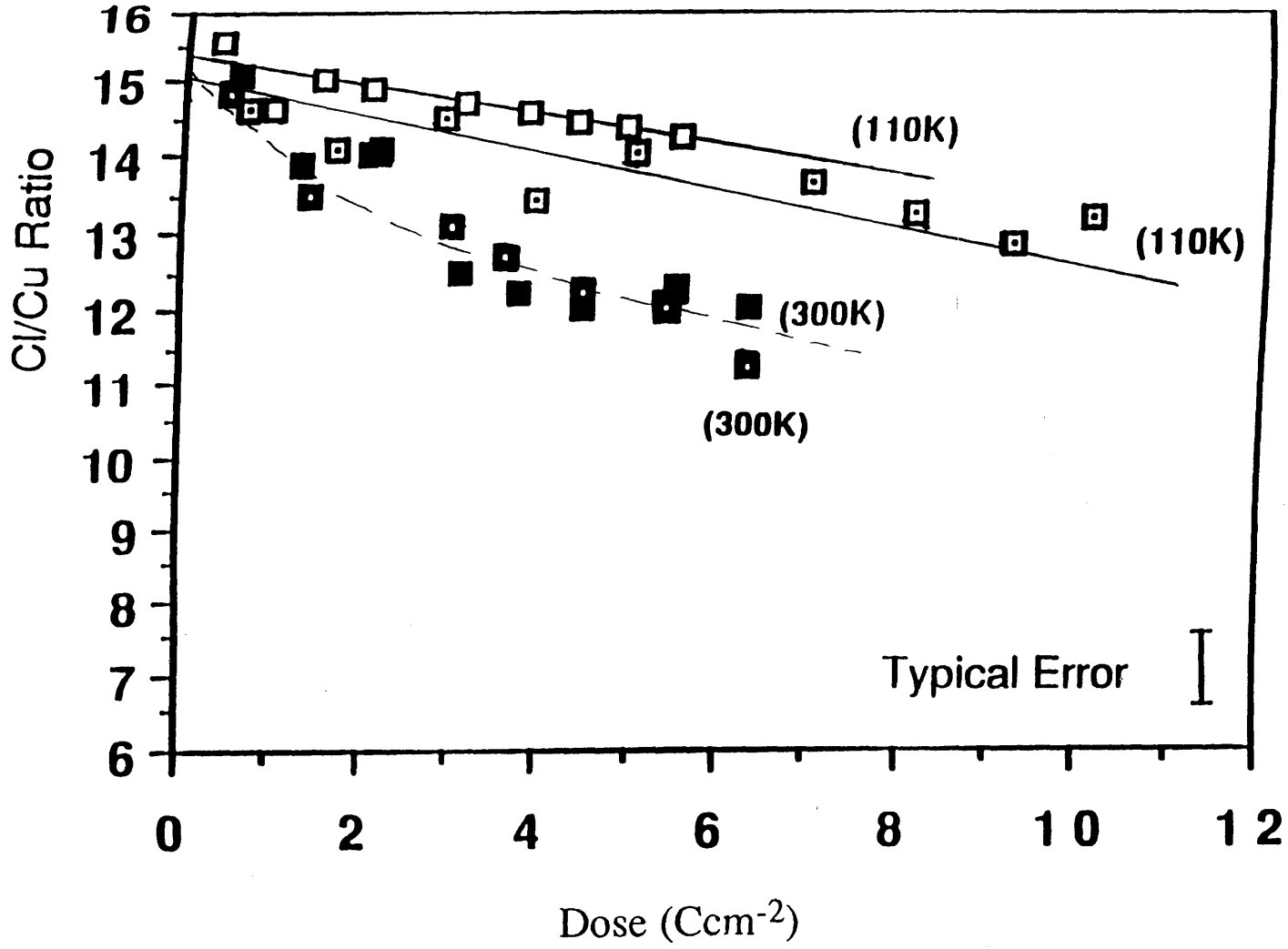

Figure 7.4: Variation of the chlorine to copper ratio with dose at room temperature (300K) and low temperature (110K). (Sample A).

from the cold runs and extrapolating to the ordinate axis should provide an accurate measure of the pigment composition. No such straightforward empirical procedure can be used on the room temperature data. The detailed description of the extrapolation method is discussed in the following section. Figure 7.5 shows data from sample B and once again the benefit of cooling is apparent, albeit the rate of loss of chlorine is only reduced by ~2 compared with the room temperature data. As before, the chlorine content appears to decrease linearly with dose at 110K whilst, at 300K, its initial loss differs markedly from that after a dose of ~2Ccm^{-2}. Thus extrapolation of room temperature data to zero dose would have a large error associated with it whilst much more reliable results should be obtainable from the cold runs.

Comparison of the results shown in figures 7.4 and 7.5 shows that the rate of chlorine loss is considerably more rapid from sample B than in sample A. This is in accordance with the results of Clark et. al. (1980) who found that structural degradation under electron irradiation was related to the hydrogen content remaining in X-Cu Pc's following halogenation. Whilst the strengths of a carbon-hydrogen and a carbon-halogen bond are comparable, hydrogen is much more mobile than a halogen atom (due to its lower mass) and so diffuses rapidly away from its original site after bond breakage. In progressing through the sample it possesses sufficient energy to promote further damage. In addition, the higher proportion of unfilled space in less halogenated samples allows halogen atoms or any molecular fragments produced by secondary damage processes to diffuse away from their original sites more easily.

Results from three analyses of specimen C are presented in figure 7.6. Figures 7.6 (a) and (b) show how the Cl/Cu and Br/Cu ratios respectively vary with dose. Once again the beneficial effects of cooling on chlorine confinement are apparent and it is noteworthy that the rate at which chlorine is lost is less than that for either of the previous two samples. Retention of

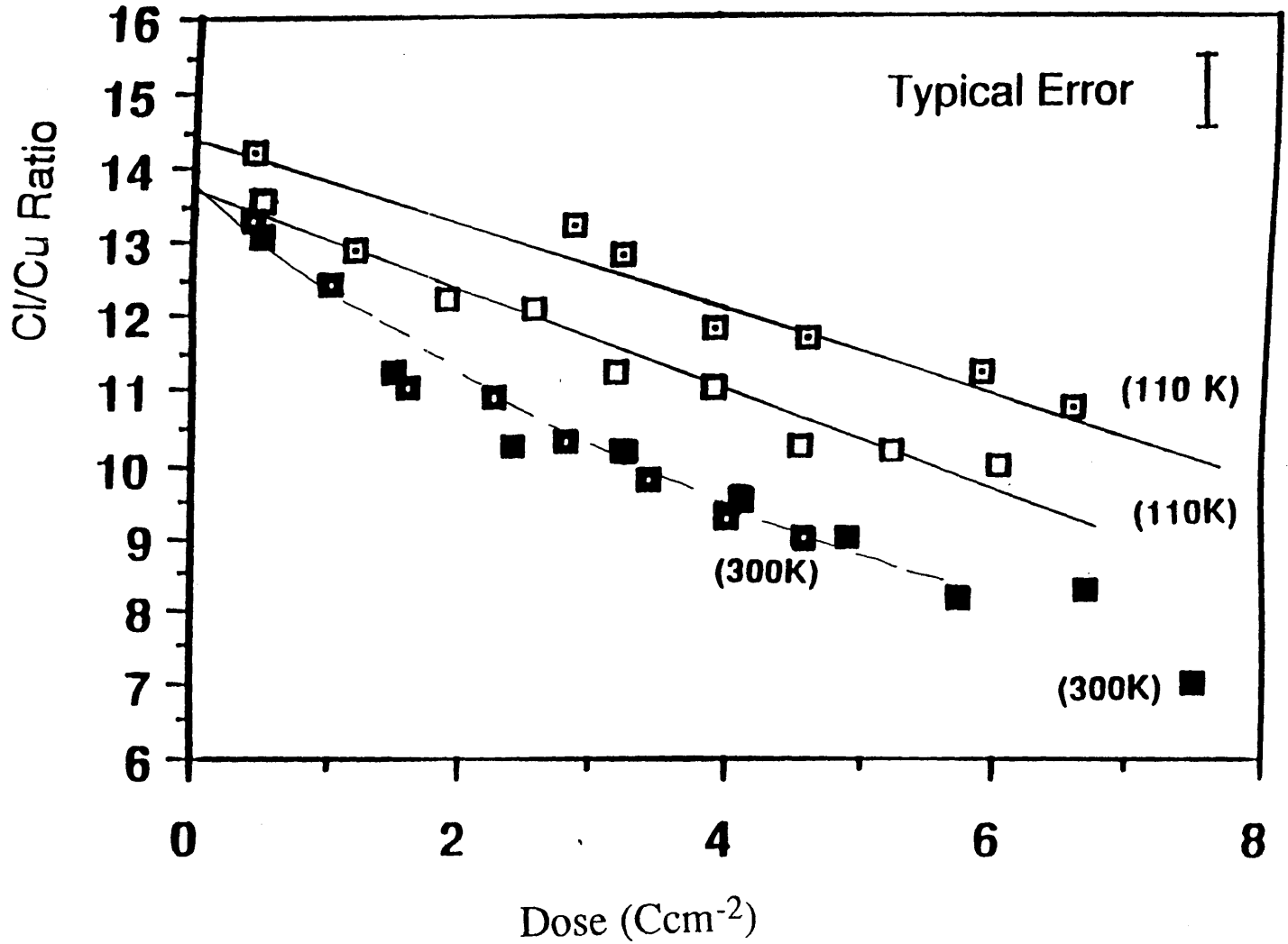

Figure 7.5: Variation of the chlorine to copper ratio with dose at room temperature (300K) and low temperature (110K). (Sample B).

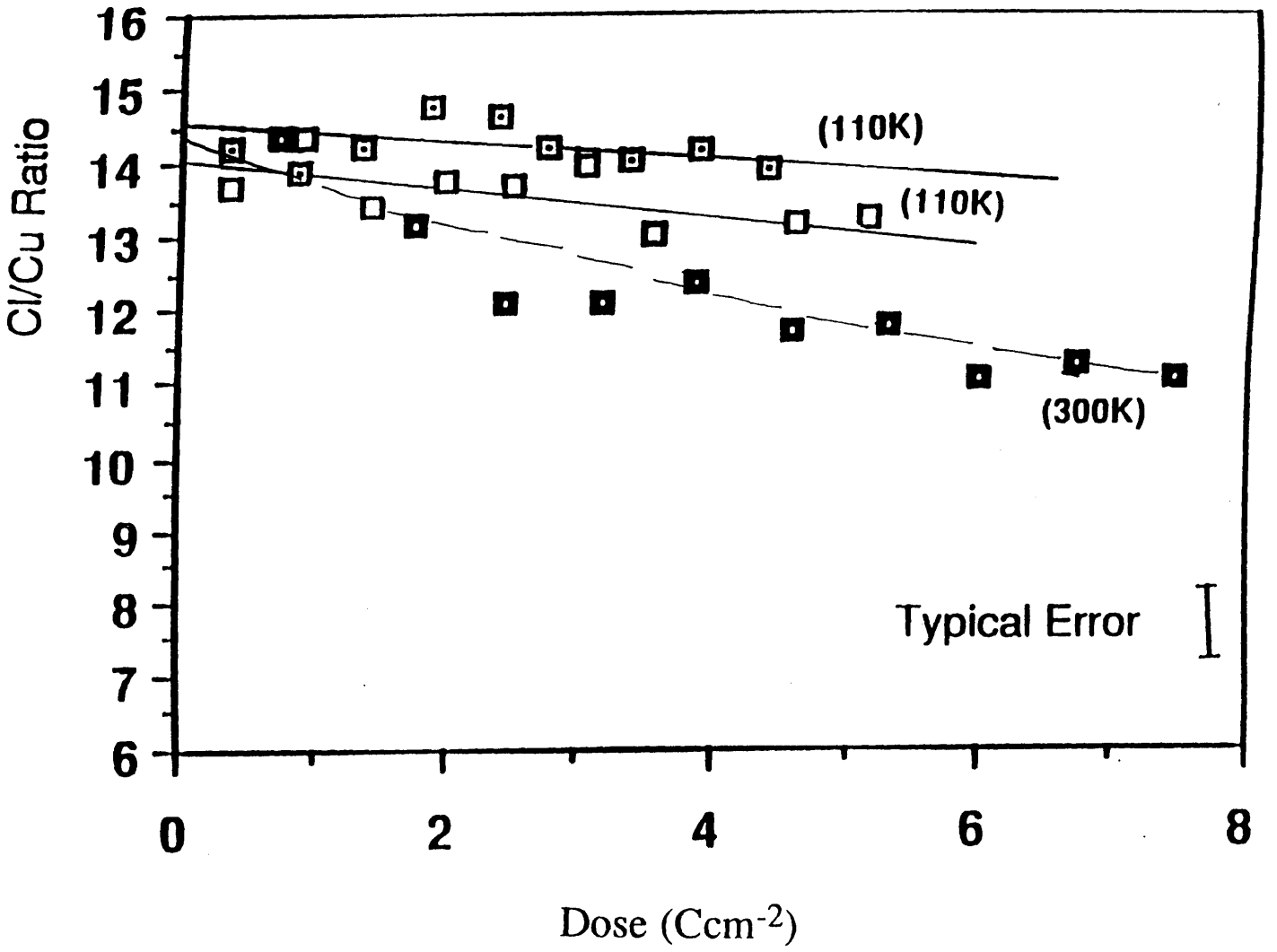

Figure 7.6 (a): Variation of the chlorine to copper ratio with dose at room temperature (300K) and low temperature (110K). (Sample C).

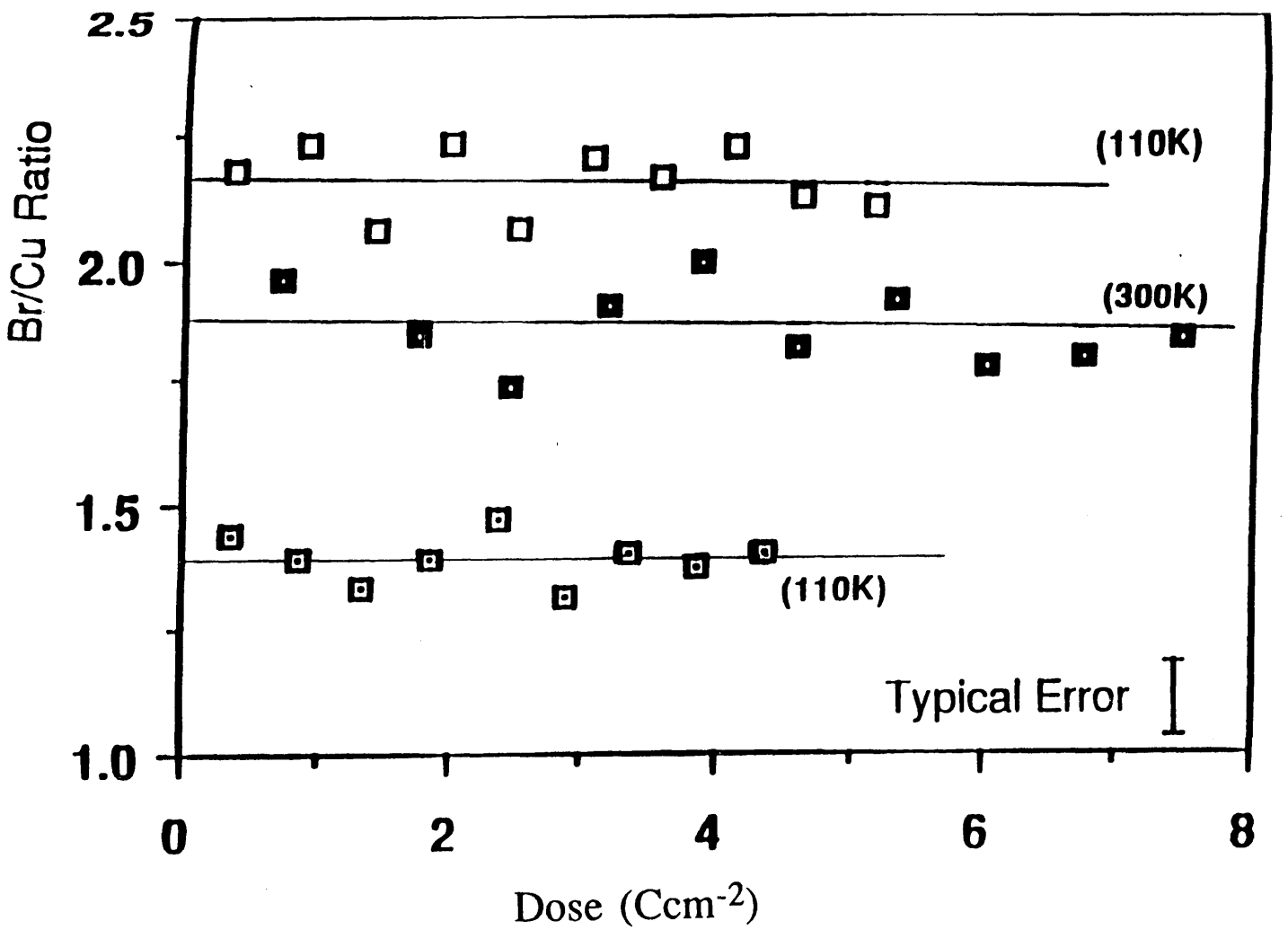

Figure 7.6 (b): Variation of the bromine to copper ratio with dose at room temperature (300K) and low temperature (110K).

(Sample C).

bromine within the analysed volume is even more marked and figure 7.6 (b) suggests that there is no significant loss at either room temperature or 110K. That this is so is presumably due to the high mass of the bromine atoms. This leads to slow diffusion rates and consequently there is a relatively high probability that bond reformation will take place leaving the bromine atoms in their original sites.

An analysis of specimen D is shown in figure 7.7. The rate of chlorine loss is again reduced upon cooling to 110K. At room temperature ~25% of chlorine has been lost after a dose of ~10Ccm^{-2}, whereas the loss at 110K is approximately 1/4 of this value. Significant improvements in the confinement of bromine within the analysed volume is obtained upon cooling. At room temperature ~15% of bromine is lost after a dose of ~10Ccm^{-2}, whereas at low temperature the loss is ~1/3 of this value. The total halogen content of this sample is approximately equal to that of specimen C; however, the rate of loss of chlorine and bromine is greater in this sample. This suggests that the rate of damage may depend on the extent of close packing in the molecular structure. In the case of specimen D, the high proportion of large bromine atoms is less likely to give a compact structure and the increased damage rate may be a consequence of this.

Results from an analysis of specimen E are presented in figure 7.8. At room temperature, the bromine to copper ratio falls to a plateau after a dose of ~ 4Ccm^{-2} after which it remains relatively stable out to a dose of ~14Ccm^{-2}. Considerable improvement in the confinement of the bromine data is obtained upon cooling with <5% bromine having being lost after a dose of ~10Ccm^{-2} compared to ~25% at room temperature. Significant is that the initial rapid loss of bromine has been eliminated in the low temperature data. This again allows a more straightforward extrapolation to zero dose yielding accurate information on the halogen to copper ratio.

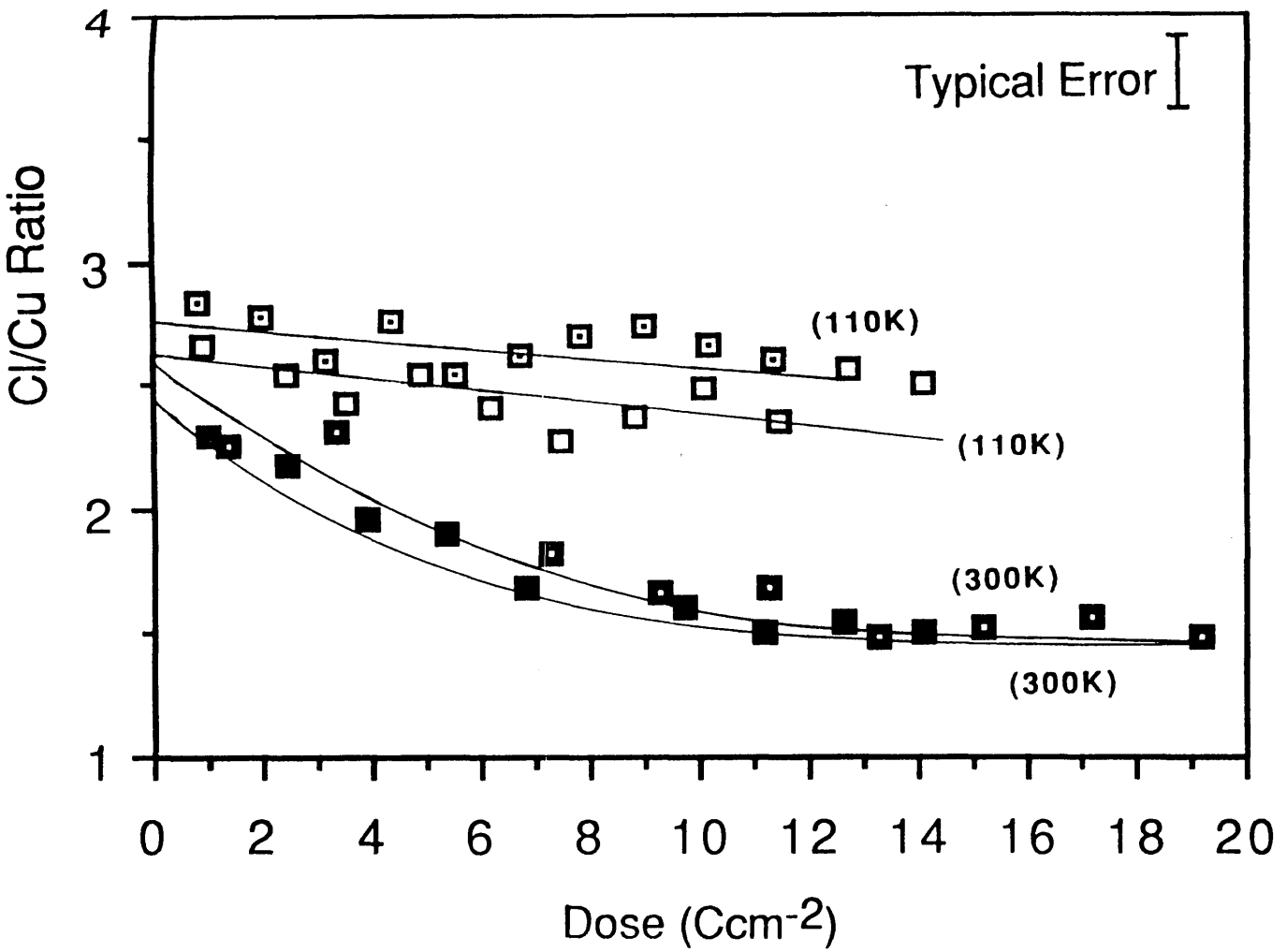

Figure 7.7 (a): Variation of the chlorine to copper ratio with dose at room temperature (300K) and low temperature (110K).

(Sample D).

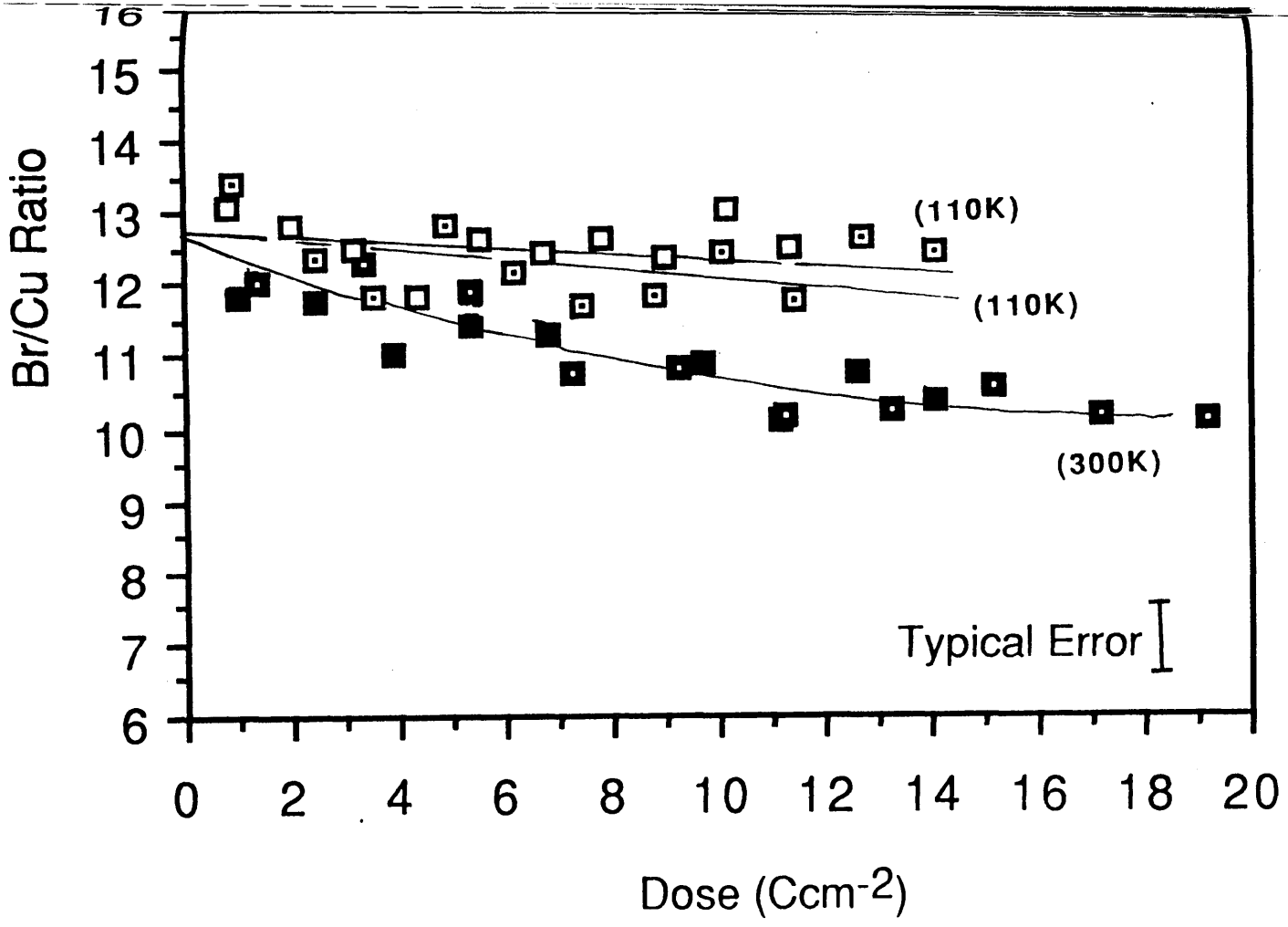

Figure 7.7 (b): Variation of the bromine to copper ratio with dose at room temperature (300K) and low temperature (110K).

(Sample D).

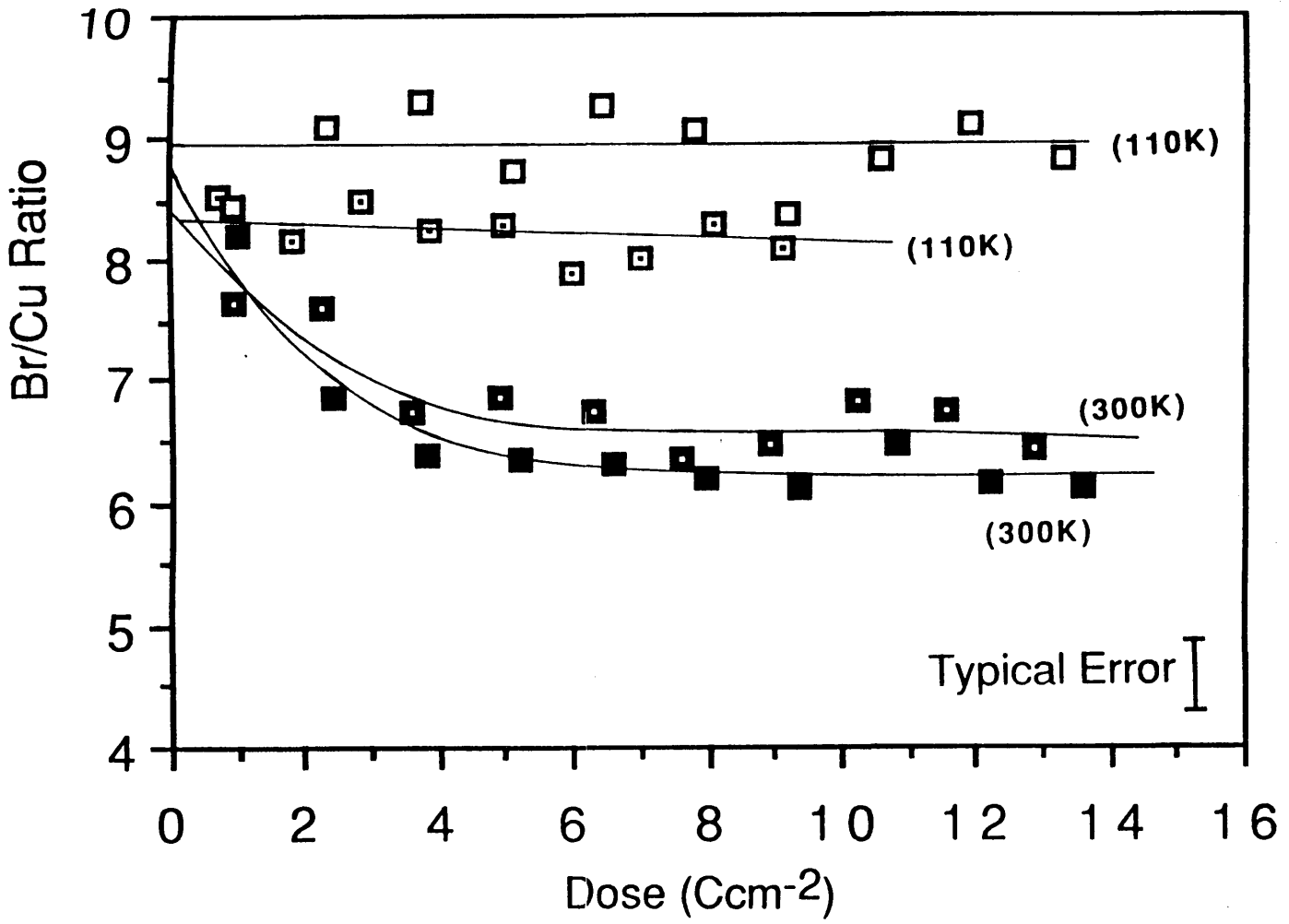

Figure 7.8: Variation of the bromine to copper ratio with dose at room temperature (300K) and low temperature (110K). (Sample E).

Results from an analysis of material F are presented in figure 7.9. Figures 7.9 (a) and (b) show how the Cl/Cu and Br/Cu ratios respectively vary with dose. At room temperature the chlorine to copper ratio falls to a plateau after a dose of ~2Ccm^{-2} after which the concentration remains relatively constant out to a dose of ~8Ccm^{-2}. The difference in the variation of the chlorine to copper ratio with electron dose at room temperature and low temperature is striking. Results show ~50% of the chlorine has been lost after a dose of ~12Ccm^{-2} at room temperature, whereas no significant loss was detected upon cooling to 110K. The rapid loss of chlorine at room temperature can be explained on the basis of the high proportion of hydrogen in this sample, the importance of hydrogen in determining the rate of damage was discussed previously. The bromine data is considerably more stable than the chlorine data at room temperature with ~15% of bromine being lost compared to 50% of chlorine after a comparable dose. Upon cooling no significant bromine loss was detected. The improvement in the confinement of chlorine and bromine in this sample upon cooling to 110K is surprising. The rate of halogen loss is significantly less than that observed in samples A, B and D, in which the total halogen content is significantly higher. A further analysis was undertaken to try to determine what factors could account for the observed improvement. The experiment consisted of acquiring series of spectra from small volumes of sample at 110K. The sample was then returned to room temperature and measurements made on the Cl/Cu and Br/Cu ratios ~1 hour after allowing the specimen to return to room temperature. Results obtained from these analyses are presented in figure 7.10. The results indicate that in this sample, the amount of damage produced upon returning the sample to room temperature is substantially less than that obtained in a room temperature analysis. This suggests that a considerable degree of bond reformation has occurred in this sample by cooling the sample to 110K. It is

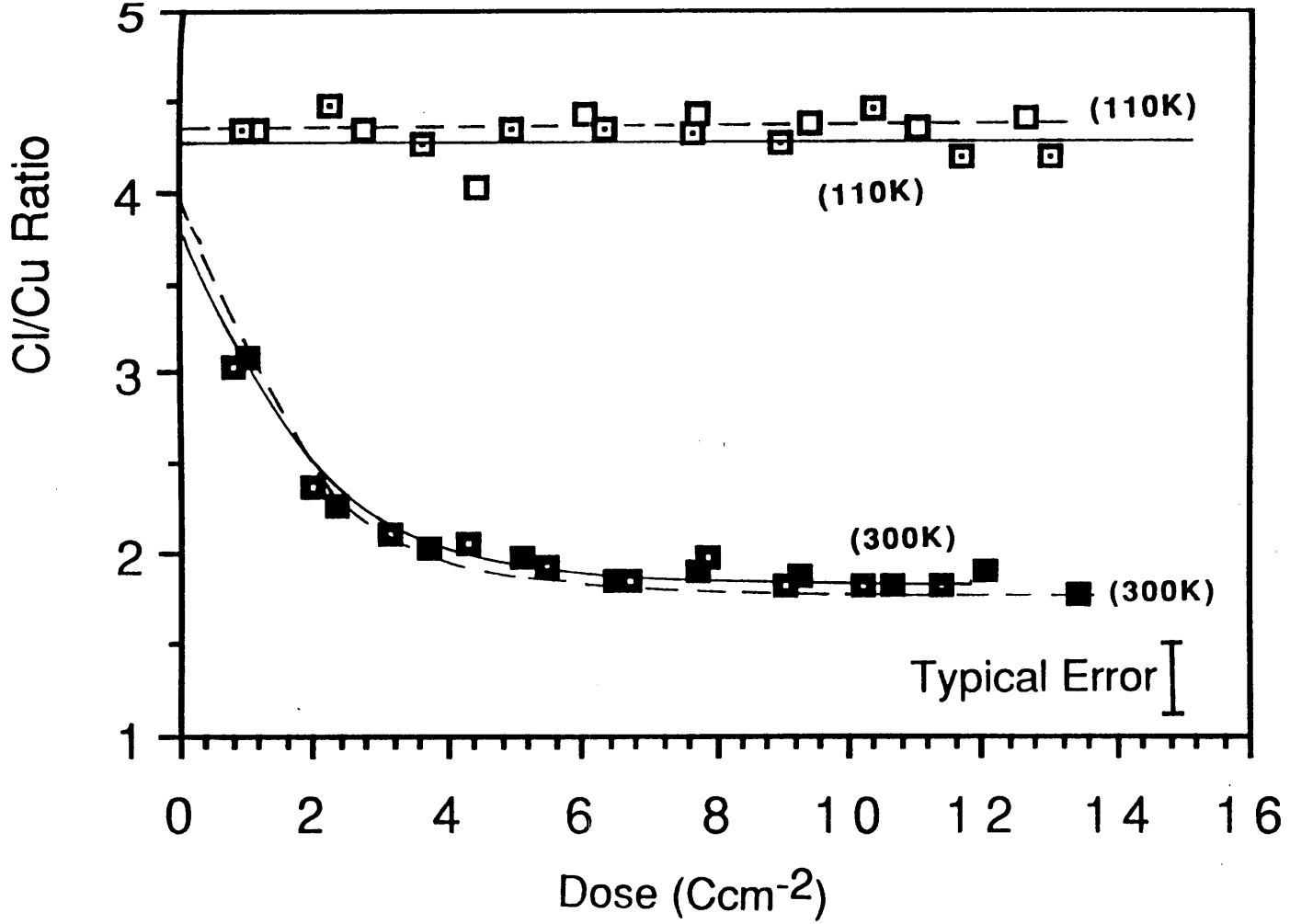

Figure 7.9 (a): Variation of the chlorine to copper ratio with dose at room temperature (300K) and low temperature (110K).

(sample F)

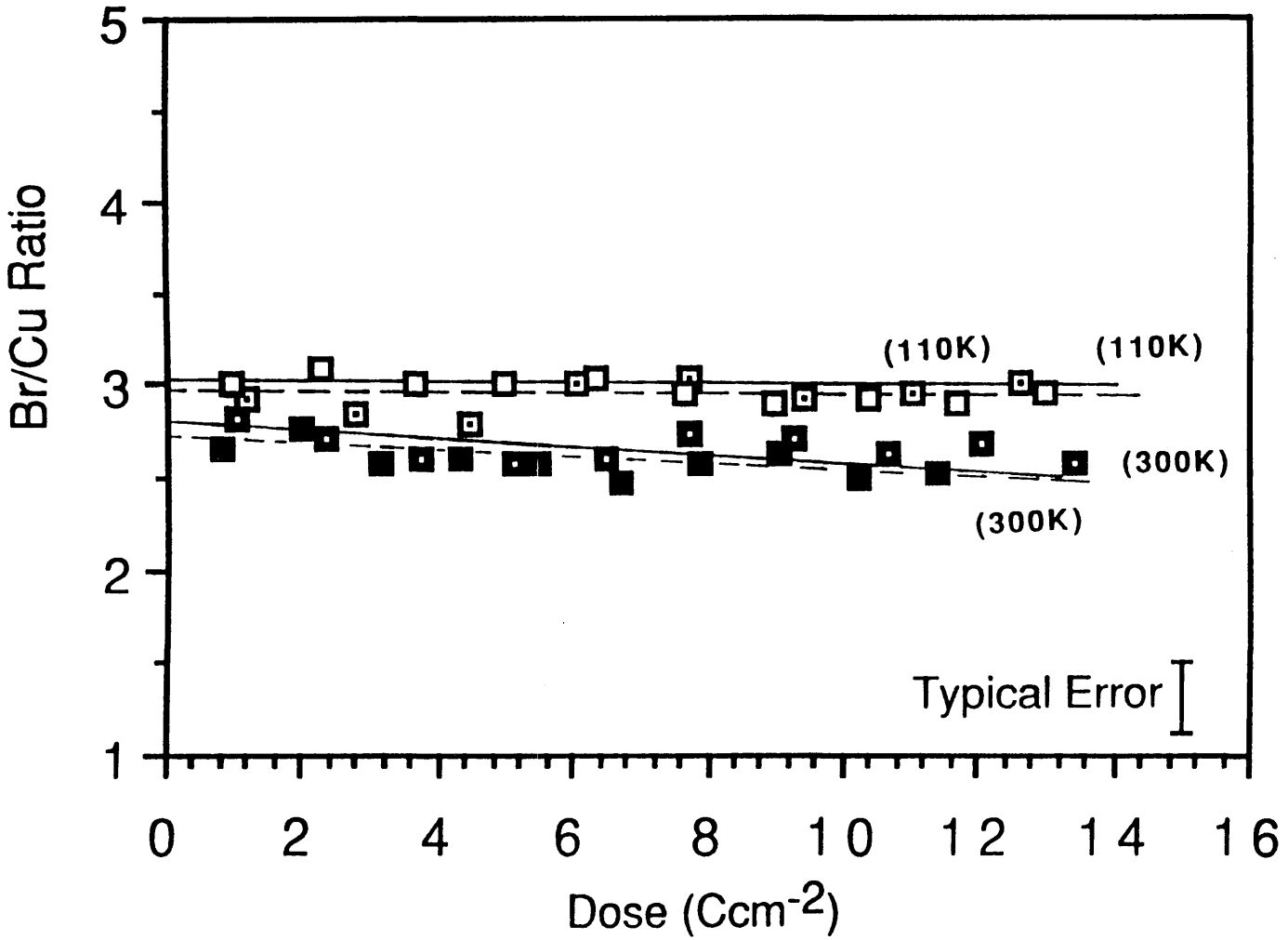

Figure 7.9 (b): Variation of the bromine to copper ratio with dose at room temperature (300K) and low temperature (110K).

(Sample F)

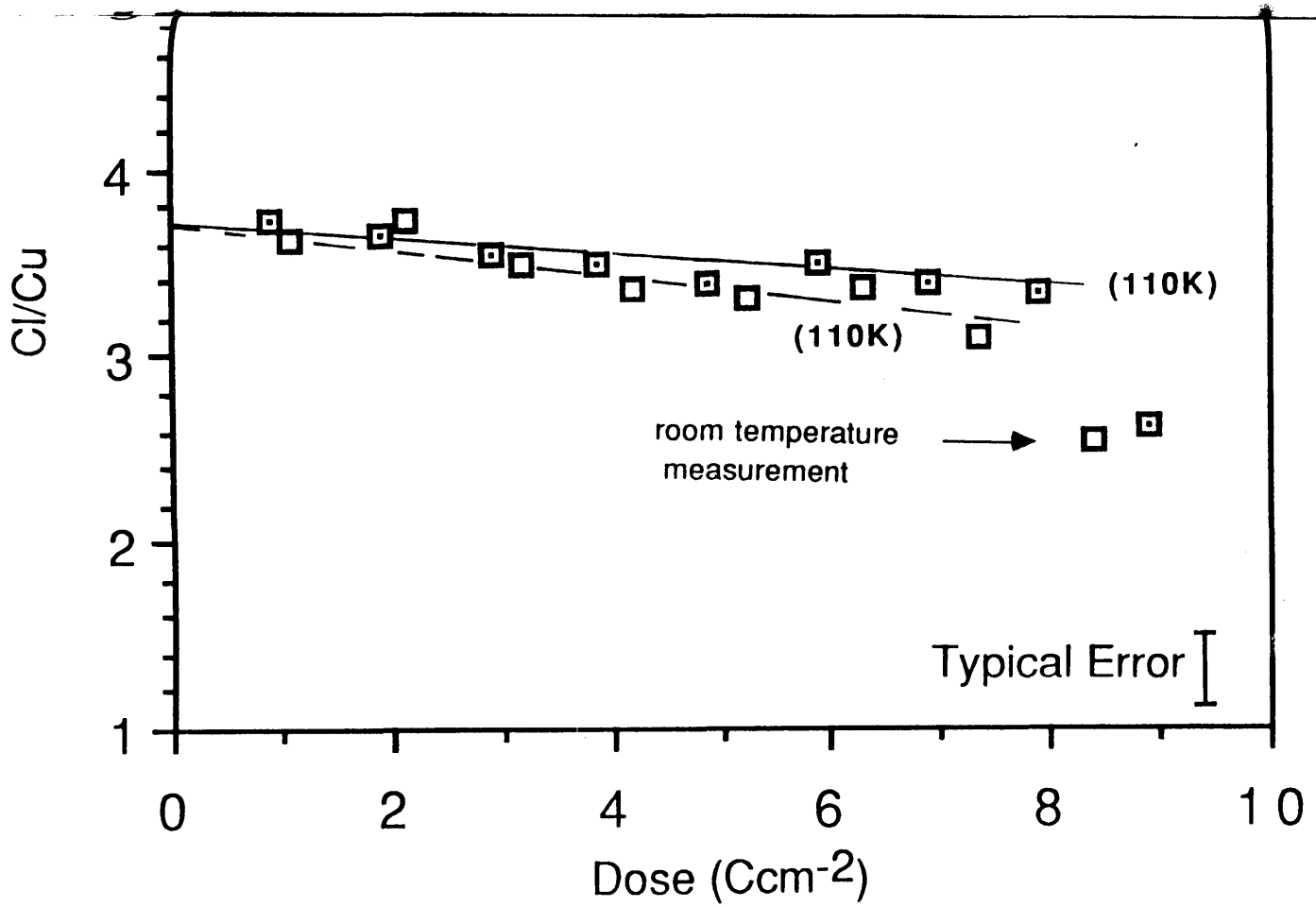

Figure 7.10 (a): Variation of the chlorine to copper ratio with dose at low temperature (110K) and upon returning to room temperature (300K).

(sample F)

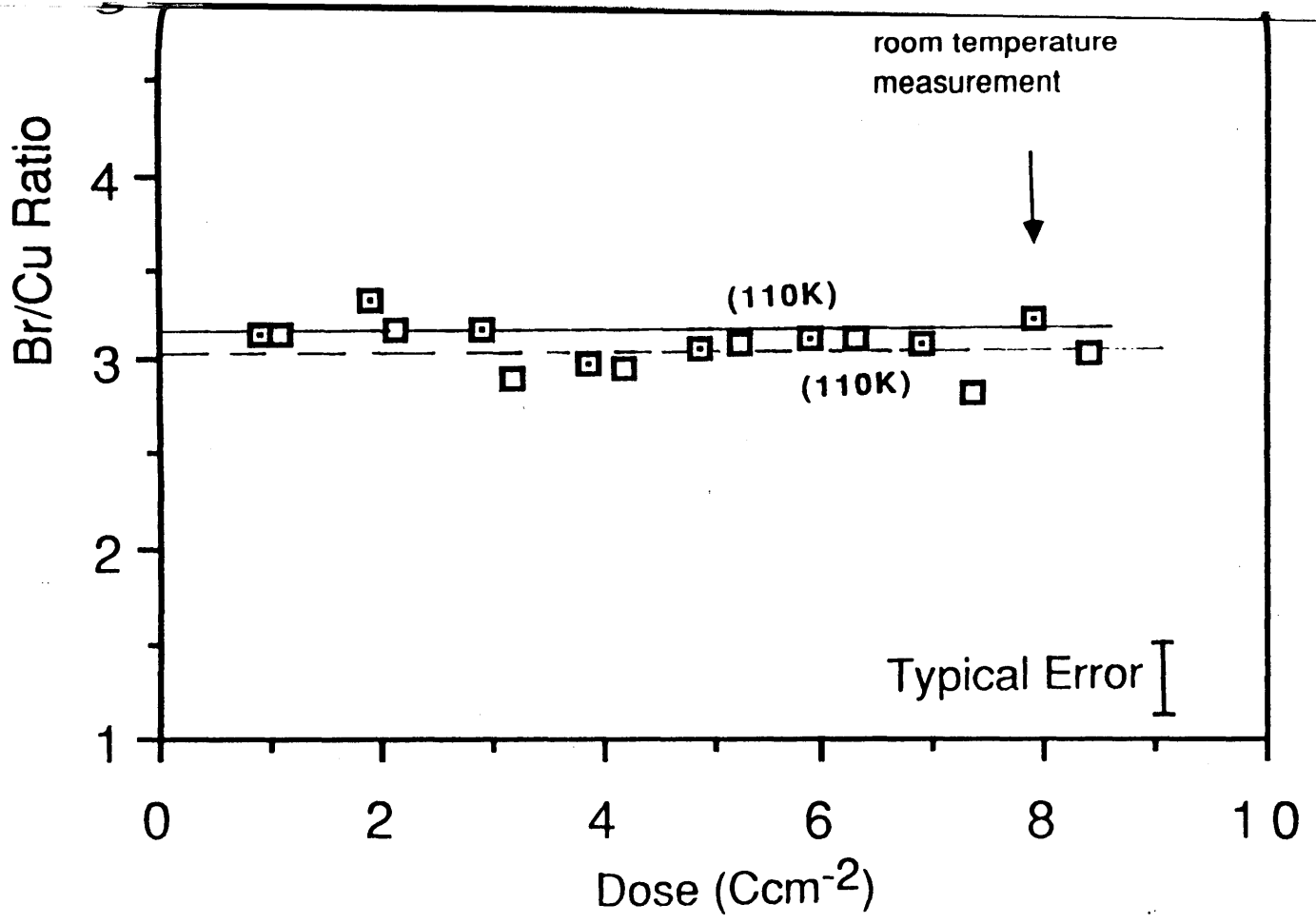

Figure 7.10 (b): Variation of the bromine to copper ratio with dose at low temperature (110K) and upon returning to room temperature (300K).

(sample F)

from each spectral series can be presented in the form $\alpha \pm \delta\alpha$ where, for a 95% confidence interval, $\delta\alpha$ is given for the chlorine data by

$$\delta\alpha = t\left(n-2, 1-\tfrac{1}{2}\eta\right)\left\{\frac{\sum x_i^2}{n\sum\left(x_i-\bar{x}\right)^2}\right\}^{\frac{1}{2}} . S_1 \qquad (7.11)$$

where t{n-2,1-1/2η} is the (1-1/2η) percentage point of a t-distribution with (n-2) degrees of freedom and

$$S_1 = \left\{\frac{\sum\left(y_i-\alpha-\beta x_i\right)^2}{(n-2)}\right\}^{\frac{1}{2}} \qquad (7.12)$$

In determination of the bromine content $\delta\alpha$ is given by

$$\delta\alpha = t\left(n-1, 1-\frac{1}{2}\eta\right)S_2/(n)^{\frac{1}{2}} \qquad (7.13)$$

where

$$S_2 = \left\{\frac{\left(y_i-\alpha\right)^2}{(n-1)}\right\}^{\frac{1}{2}} \qquad (7.14)$$

Analysis of the data using the expressions detailed above was carried out using a 'Minitab' statistical application package (Ryan et. al., 1985).

7.6 Results obtained from extrapolations

Results obtained from the extrapolations for each of the samples are presented in tables 7.1-7.6. From the data presented in the tables it was possible to calculate the mean values of α together with the standard deviations ($\Delta\alpha$) and standard errors in the means. The results for each sample are given in the appropriate table. For samples A and B the best estimates of the undamaged Cl/Cu ratios with their associated standard errors were 15.0 ± 0.1 and 13.9 ± 0.2 respectively. Thus it is seen that the degree of chlorination in A is greater than in B. This is as expected and is in accord with the observation that the sample containing more hydrogen damages more rapidly. It is also apparent though that the degree of chlorination in A falls significantly short of the maximum value showing the difficulty of effecting a complete replacement of all 16 peripheral hydrogen atoms by chlorine. The standard deviations in the distributions for A and B are 0.3 and 0.7 respectively. Comparison of these figures with the corresponding extrapolation errors $\delta\alpha$ in table 7.1 and 7.2 show them to be generally comparable from which we deduce that there is no detectable variation in composition within these samples on the scale of the microanalysis undertaken here.

For sample C the mean values of the Cl/Cu and Br/Cu ratios are 13.8 ± 0.2 and 1.8 ± 0.1 respectively. This leads to a mean total halogen to copper ratio of 15.6 which is higher than that achieved in either of the other two samples and is likely to be the main reason why C degrades more slowly under irradiation than A or B. Examination of table 3 allows further deductions to be made. Firstly, it is clear that the accuracy with which the bromine content can be determined is an order of magnitude better than that pertaining to chlorine as a result of the greater stability of the bromine; indeed individual

Br/Cu ratios were determined with an error $\delta\alpha<0.1$. This figure is considerably less than the standard deviation $\Delta\alpha$ in the distribution of measured Br/Cu ratios. Thus in this instance the results show that significant variations in chemical composition are detectable in the small volumes of material analysed and the standard deviation can be regarded as a measure of the degree of inhomogeneity rather than as a measure of the accuracy with which the analyses were made.

For sample D the best estimate of the Cl/Cu and Br/Cu ratios are 2.58 ± 0.06 and 12.63 ± 0.20. This leads to a mean total halogen to copper ratio of 15.21, again emphasising the difficulties in achieving a complete substitution of all the peripheral halogen atoms.

For sample E, the best estimate of the Br/Cu was 8.7 ± 0.2. The standard deviation is 0.4. Comparison with the corresponding extrapolation error $\delta\alpha$, shows that they are of equal magnitude and therefore no significant variation in composition on the scale investigated could be detected.

For sample F, the mean values of the Cl/Cu and Br/Cu ratios are 4.35 ± 0.12 and 3.02 ± 0.02 respectively. The accuracy with which the bromine content can be determined is significantly higher than that obtainable for the majority of the chlorine data. Individual Br/Cu ratios were determined with a precision $\delta\alpha$ of typically <0.1. However as the standard deviation of the distribution of results is 0.02, no detectable variation in specimen composition could be observed on the scale of the analysis undertaken.

7.7 Comparisons between room and low temperature microanalysis

In section 7.4, results were presented showing the variation of the Cl/Cu

and Br/Cu ratio with dose for the various samples under investigation at room temperature (300K) and low temperature (110K). The aim of this section is to determine the improvement conferred by using low temperature EDX microanalysis. Results showing the rate of chlorine loss at 300K and 110K are presented in table 7.7. The first column shows the rate of chlorine loss at 300K. From these results it can be seen that the rate of chlorine loss increases as the halogen content of the X-Cu Pc decreases. This is in agreement with the results of Clark et. al. (1980), as has been discussed previously. Comparison of the rate of chlorine loss at 300K and 110K shows that in all the samples analysed, the rate of chlorine loss was significantly reduced upon cooling to 110K. For specimens A, B, C, and D the rate of chlorine loss was reduced by a factor of 2-3 upon cooling. For specimen F the rate of chlorine loss was reduced by a factor of ~10 upon cooling to 110K.

Comparison of the rate of bromine loss at 300K and 110K is presented in Table 7.8. These results show that the rate of bromine loss was significantly reduced upon cooling to 110K. Sample B showed exceptional stability at both room and low temperature; no significant loss was observed at either temperature.

Results presented in the previous sections have shown the beneficial effects of cooling the sample in reducing the rate of halogen loss from the pigmentary samples investigated. The rate of damage was found to be different for the various materials investigated, the quantity and type of halogen present in the sample being of considerable importance in determining the rate of damage. Analysis of the mixed halogen samples, enables a comparison to be made between the rate of chlorine and bromine loss at room and low temperature under fixed experimental conditions. Results at room temperature are presented in table 7.9. The results indicate

Material	Measured Chlorine to Copper ratio (α)	Error in Extrapolation ($\delta\alpha$)
A	14.6	0.4
	14.9	0.5
	15.3	0.5
	14.9	0.7
	15.2	0.4
	14.8	0.6
	15.1	0.4
	15.2	0.5

Mean chlorine to copper ratio=15.0
Standard Deviation ($\Delta\alpha$) of Distribution of Results=0.3
Standard Error=0.1.

Table 7.1: Results from analyses of Material A.

Material	Measured Chlorine to Copper ratio	Error in Extrapolation
B	(α)	($\delta\alpha$)
	13.6	0.5
	14.1	0.7
	12.7	0.9
	14.3	1.0
	14.4	1.0
	14.5	0.8
	14.2	0.6
	13.0	0.7

Mean chlorine to copper ratio=13.9
Standard Deviation ($\Delta\alpha$) of Distribution of Results=0.7
Standard Error=0.2.

Table 7.2 : Results from analyses of Material B.

Material	Measured chlorine to copper ratio	Error in Extrapolation	Measured bromine to copper ratio	Error in Extrapolation
C	(α)	($\delta\alpha$)	(α)	($\delta\alpha$)
	14.4	0.3	1.3	0.05
	13.7	0.2	1.76	0.02
	13.8	0.7	1.85	0.07
	14.4	0.6	1.47	0.05
	14.2	0.3	1.39	0.04
	14.1	0.6	2.2	0.05
	14.4	0.6	1.8	0.06
	14.6	0.9	1.75	0.13
	13.4	0.8	1.87	0.07
	12.6	0.6	2.69	0.22
	13.7	0.7	1.8	0.04
	12.6	0.6	1.9	0.03
	14.3	0.5	1.37	0.03
	14.0	0.4	1.69	0.12

Mean chlorine to copper ratio=13.8
Standard Deviation ($\Delta\alpha$) of Distribution of Results=0.7
Standard Error=0.2.

Mean bromine to copper ratio=1.76
Standard Deviation ($\Delta\alpha$) of Distribution of Results=0.3
Standard Error=0.09.

Table 7.3 : Results from analyses of Material C.

Material D	Measured chlorine to copper ratio (α)	Error in Extrapolation ($\delta\alpha$)	Measured bromine to copper ratio (α)	Error in Extrapolation ($\delta\alpha$)
	2.57	0.15	12.3	0.4
	2.6	0.08	12.5	0.26
	2.57	0.17	12.5	0.27
	2.5	0.08	12.8	0.4
	2.67	0.08	12.62	0.6
	2.83	0.35	13.3	0.3
	3.0	0.2	13.1	0.3
	2.9	0.28	12.2	0.7
	3.0	0.2	13.3	0.5
	2.6	0.4	12.6	0.7

Mean chlorine to copper ratio=2.58
Standard Deviation ($\Delta\alpha$) of Distribution of Results=0.15.
Standard Error=0.02.

Mean bromine to copper ratio=12.63
Standard Deviation ($\Delta\alpha$) of Distribution of Results=0.4.
Standard Error=0.2.

Table 7.4 : Results from analyses of Material D.

Material	Measured Chlorine to Copper ratio	Error in Extrapolation
E	(α)	($\delta\alpha$)
	8.3	0.2
	8.8	0.3
	9.3	0.2
	8.9	0.2
	8.4	0.3
	8.4	0.3

Mean bromine to copper ratio=8.7
Standard Deviation ($\Delta\alpha$) of Distribution of Results=0.4.
Standard Error=0.2.

Table 7.5 : Results from analyses of Material E.

Material F	Measured Chlorine to Copper ratio (α)	Error in Extrapolation ($\delta\alpha$)	Measured Bromine to Copper ratio (α)	Error in Extrapolation ($\delta\alpha$)
	4.3	0.07	2.98	0.04
	4.6	0.04	3.03	0.06
	4.3	0.1	2.95	0.07
	3.5	0.3	3.03	0.05
	4.3	0.2	2.9	0.06
	4.6	0.35	3.0	0.07
	4.3	0.3	3.05	0.06
	4.9	0.15	3.2	0.1
	4.4	0.2	3.0	0.1
	4.5	0.3	3.02	0.06

Mean chlorine to copper ratio=4.35
Standard Deviation ($\Delta\alpha$) of Distribution of Results=0.35.
Standard Error=0.11.

Mean bromine to copper ratio=3.02
Standard Deviation ($\Delta\alpha$) of Distribution of Results=0.08.
Standard Error=0.02.

Table 7.6 : Results from analyses of Material F.

Material	% chlorine Loss for dose ~6Ccm^{-2} (300K)	% chlorine Loss for dose ~6Ccm^{-2} (110K)	% chlorine loss (300K) / % chlorine loss (110K)
A	~25%	~10%	~2.5
B	~30%	~20%	~2
C	~20%	~7%	~3
D	~20%	~7%	~3
F	15%	<5%	~3

Table 7.7 : Rate of chlorine loss at room temperature (300K) and low temperature (110K) for the pigmentary samples investigated.

Material	% bromine Loss for dose ~6Ccm^{-2} (300K)	% bromine Loss for dose ~6Ccm^{-2} (110K)	% bromine loss (300K) / % bromine loss (110K)
E	~25%	~10%	~2.5
C	<5%	<5%	~1
D	~15%	~5%	~3
F	~15%	<5%	~3

Table 7.8 : Rate of bromine loss at room temperature (300K) and low temperature (110K) for the pigmentary samples investigated.

Material	% chlorine loss for dose ~6Ccm^{-2} (300K)	% bromine loss for dose ~6Ccm^{-2} (300K)	% chlorine loss / % bromine loss
C	~20%	<5%	~4
D	~25%	~15%	~1.7
F	50-60%	~15%	~4

Table 7.9 : Rate of chlorine and bromine loss at room temperature (300K) for the mixed halogen pigmentary samples investigated.

Material	% chlorine Loss for dose ~6Ccm^{-2} (110K)	% bromine Loss for dose ~6Ccm^{-2} (110K)	% chlorine loss / % bromine loss
C	~7%	<5%	~1.5
D	~10%	~5%	~2
F	<5%	<5%	~1

Table 7.10 : Rate of chlorine and bromine loss at low temperature (110K) for the mixed halogen pigmentary samples investigated.

that the rate of chlorine loss is 1.5-4 times more rapid than the rate of bromine loss at room temperature. This emphasises that diffusion of the more massive bromine atoms is substantially less than that of chlorine atoms. A comparison of the rates of chlorine and bromine loss at low temperature are presented in table 7.10. The results show that the rate of chlorine loss is ~1-2 times more rapid than bromine loss. Comparison of these results with those presented in table 7.9, shows that the rate of chlorine loss relative to the rate of bromine loss has been reduced upon cooling to 110K.

In conclusion, the experimental procedure of cooling the sample to 110K and acquiring series of spectra using a limited electron dose from small volumes typically containing 10^8 molecules allows accurate compositional information to be obtained from these radiation sensitive materials. The advantage of low temperature is that the rate of halogen loss is significantly reduced upon cooling to 110K and assumes a simpler variation with dose.

Chapter 8

CONCLUSIONS AND SUGGESTIONS FOR FUTURE WORK

8.1 Summary of work undertaken

The materials investigated in this project were halogenated copper phthalocyanine pigmentary samples. These materials are prepared industrially by ICI and in the blue/green colour areas represent the most important class of organic pigments. One of the main reasons for investigating these materials was that, under nominally identical preparation conditions, variations arose in the final colour properties of the pigment. Therefore, the aim of the project was to characterise the materials as fully as possible, using analytical techniques available in electron microscopy, to try to determine how the observed variations could arise. Specifically, this characterisation required determination of structural and compositional information of the highest possible accuracy. The major difficulties encountered in the investigations were that the specimens suffered radiation damage during irradiation by the electron beam. Therefore special experimental procedures were adopted. Without these, results obtained pertained to the significantly damaged material whose structure and composition may be markedly different from the original material.

The structure of the pigments were investigated in the CTEM using electron diffraction and lattice imaging. Initial low magnification studies showed that there were considerable variations in particle shape between the

highly chlorinated and highly brominated pigmentary particles. The highly chlorinated particles were fairly round smooth shaped particles of typical dimensions 50nm. The highly brominated particles, tended to be more elongated and approximately brick shaped with the longest dimension of the particles being typically >50nm. The lower halogenated materials investigated showed considerable variations in particle size and shape.

Electron diffraction patterns obtained from the highly chlorinated particles showed streaking parallel to the centre line of spots, indicating that there was considerable disruption of the crystal structure. A defect structure incorporating twinning along the [110] direction, was proposed which accounted for the observed diffraction patterns. That twinning is observed in these materials is not surprising given the small difference in energy that is involved when columns of molecules bind in almost equivalent orientations. The majority of diffraction patterns obtained from the highly brominated particles showed a similar stacking sequence to that observed in the chlorinated samples, however in some of the patterns a periodicity of ~2.5nm was observed. This suggests that in certain crystalline regions, the molecules stack together in a 'herring-bone', configuration of the type observed in β-Cu Pc. This configuration can have a marked effect on crystal growth. This results in preferential growth along the column axis, and therefore provides an explanation to account for the marked differences in the shape of the brominated material.

Lattice imaging showed a 1-D fringe pattern exhibiting periodicities in the range 1.3-1.5nm, comparable to the (110) plane spacing in the epitaxial prepared material. In the chlorinated particles, a large number of such fringes with different orientations were observed. In the highly brominated material the fringes tended to lie along the major axis of the particles. Also observed in many regions of the brominated particles was bending of lattice

planes and dislocations. These indicated that there were considerable deviations from perfect crystallinity in the brominated pigmentary particles, and suggested that stacking of the large bromine atoms in the structure, gave rise to the observed differences. Noteworthy was that severe bending of lattice fringes could be accommodated with the fringes remaining continuous over appreciable distances in the crystals.

The CTEM studies provided information on the particle size and internal structure. However, information on the topography of the particles was limited.

The DPC mode of microscopy was described in chapter 3, where it was shown to be capable of providing information simultaneously on the internal structure and specimen topography. Results obtained from the pigmentary materials using the DPC mode of microscopy were presented in chapter 5. Low magnification images provided information on the size and topography of the highly chlorinated and highly brominated materials. The particles were shown to have sharp edges and terraces. The latter could be interpreted as arising from stacking of planes of molecules to form the particles. The results presented in chapter 5, in conjunction with the CTEM investigations suggested that the highly brominated material would be a less effective pigment. The major reason for this is the large area of contact of the approximately brick shaped particles will result in strong aggregation. This reduces the effective surface area of the particles and thus their pigmentary effectiveness. Aggregation is less of a problem in the chlorinated samples due to the small area of contact.

EDX microanalysis was used to determine halogen to copper ratios with an accuracy $\lesssim$ 0.5 halogen atoms/molecule. This was the upper limit on the accuracy required to determine if compositional variations were present between small volumes of supposedly similar samples. A major problem in obtaining accurate analyses was that during electron irradiation damage

occurred resulting in a loss of halogen atoms and thus to a reduction in the halogen to copper ratio. It was therefore essential to reduce the rate at which halogen was lost if accurate compositional information was to be obtained. The experimental procedure developed of cooling the sample to close to liquid nitrogen temperature and acquiring series of spectra was described in chapters 6 and 7. The results obtained were presented in chapter 7, and showed that the rate of halogen loss was significantly reduced upon cooling to liquid nitrogen temperatures. Extrapolation of each series back to zero dose allowed the composition of the undamaged material to be recovered. The extrapolation procedure developed was described in chapter 7. Results from these extrapolations showed that chlorine to copper ratios could be determined with a precision of typically 0.2-0.4 chlorine atoms/molecule. In several of the samples no significant bromine loss was detectable, this allowed bromine to copper ratios to be determined with a precision of <0.1 bromine atoms/molecule. Compositional information of this accuracy showed that in one of the materials (sample C) significant compositional variations were present between the small volumes of sample analysed.

8.2 Future work

There are several areas in which further investigations could be conducted, followed on from the present work. Those of greatest interest are outlined below:

[1] The results presented in chapter 4, suggested significant differences were present in the stacking configuration adopted in the chlorinated and brominated materials. These conclusions were reached using electron diffraction techniques. To. investigate this further high resolution imaging

could be used. Using the present electron microscope, this was limited due to the instrumental resolution achievable. Using a 200kV microscope, with λ=2.7pm, Cs=0.5mm and Cc=1mm would give a point resolution of 0.194nm. This would enable more detailed information on the specimen structure, to be obtained complementing the diffraction studies and providing information on the relationship between the internal structure and external habitat of the crystal.

[2] In the DPC imaging mode, future improvements would allow the signals from various segments of the quadrant detector to be acquired and displayed simultaneously. This approach would significantly reduce the dose to which the specimen was subjected.

[3] The experimental results presented in chapter 7 monitored the loss of halogen atoms as irradiation proceeds. However to understand in greater detail the damage mechanism, information on the rate of loss of other elements in the sample would be of considerable benefit. The rate of nitrogen loss could be measured using a windowless EDX detector. However, the production and detection efficiencies for low atomic number elements are low. The recent development of parallel EELS systems, offers a powerful alternative technique for monitoring simultaneously the loss of several species from the sample. For example, the loss of nitrogen, chlorine and bromine could be monitored simultaneously. The relative rates of loss of the species in peripheral molecular sites to those of nitrogen at room and low temperature, would provide important indications on the major damage processes.

[4] The low temperature EDX studies and the extrapolation procedure

developed, were applied to the investigation of X-Cu Pc's. However, the experimental procedure and analysis scheme developed should be applicable to many other specimens. The loss of chlorine from several polymer samples has been investigated by Vesely (1984). The resulting mass-loss curves were complex and required complicated extrapolation procedures to model the data. Cooling the samples to liquid nitrogen temperatures should reduce the rate of chlorine loss and allow a simple extrapolation procedure to be adopted, with a corresponding increase in analytical accuracy.

References

CHAPTER 1

Brockes, A. (1964) Optik 21, (10), 550.

Cosslett, V.E. (1978) J. Microsc, 113, Pt. 2, 113.

Drummond, M.J., Chapman, J.N. and Nicholson, W.A.P. (1981)
In : Proc EMAG 81. Ed. Goringe, M.J., IOP Conf. Ser.61., p.11.

Fryer, J.R. (1977) In : Proc EMAG 77 Ed. Misell, D., IOP Conf. Ser.36., p.423.

Fryer, J.R. (1980) J. Microsc, 119, Pt. 3, 1.

Fryer, J.R. and Holland, F. (1984) Proc. Roy. Soc. (London) A393, 353.

Horn, D. and Honigman, B. (1974)
Polymorphic des Kupferphthalocyanine, XII Fatipec Congress.

Kobayashi, T., Fujiyoshi, Y. and Uyeda, N. (1982) Acta Cryst., A38, 356.

Lippel et. al. (1989) Physical Review Letters, Vol 62, No 2, 171.

Moser, F.H. and Thomas, A.L. (1983) The Phthalocyanines (CRC, Boca Raton,)

Smith, D.J., Fryer, J.R. and Camps, R.A. (1986) Ultramicroscopy 19, 279.

Uyeda, N., Kobayashi, T., Ishizuka, K. and Fujiyoshi, Y. (1978) Chemica Scripta, 14, 47.

CHAPTER 2

Bahr, G., Johnson, F.R. and Zeitler, E. (1965) Laboratory Investigations 14, 1115.

Box, H.C. (1961) Annual Review of Science, 22, 355.

Box, H.C. (1975) In " Physical Aspects of Electron Microscopy and

Microbeam Analysis ", Wiley, New York, Eds. Siegal, B.M. and Beaman, D.R., 279.

Chapman, J.N., Craven, A.J. and Scott, C.P. (1989) Ultramicroscopy 28, 108.

Chiu, W. and Glaeser, R.M. (1980) In " Electron Microscopy at Molecular Dimensions ", Springer Verlag, Eds. Baumeister, W. and Vogell, W. p.194.

Clark, W.R.K., Chapman, J.N., MacLeod, A.M. and Ferrier, R.P. (1980) Ultramicroscopy, 5, 195.

Clark, W.R.K. (1979) Ph.D. Thesis, University of Glasgow.

Colliex, C. and Mory, C. (1984) : In " Quantitative Electron Microscopy ", Eds. Chapman, J.N. and Craven, A.J. SUSSP publications, Edinburgh, chapter 4.

Cosslett, V.E. (1974) Proceeding of the Royal Society of London, A338, 1.

Crozier, P.A. Chapman, J.N., Craven, A.J. and Titchmarsh, J.M. (1984) : In Analytical Electron Microscopy 1984, San Francisco Press, Ed. Williams and Joy, D.C., p. 79.

Downing, K.H. and Grano, D.A. (1982) Ultramicroscopy, 7, 381.

Egerton, R.F. (1976) Phys. Status Solidi (a) 37, 663.

Egerton, R.F. (1979) Ultramicroscopy 4, 169.

Egerton, R.F. (1980) Ultramicroscopy 5, 521.

Egerton, R.F. (1980) J. Microsc, Vol 118, Pt. 4, 163.

Egerton, R.F. (1986) Electron Energy-Loss Spectroscopy in the Electron Microscope, Plenum, New York, 324.

Egerton, R.F. and Crozier, P.A. (1987) Ultramicroscopy 23, 305.

Experimental Study Group, (1986) J. Microsc, Vol 141, Pt 3, p. 385.

Fujiyoshi, Y., Kobayashi, T., Tsuji, M. and Uyeda, N. (1982) Proceeding of

International Congress on Electron Microscopy, Hamburg 2, 461.

Koster, A.J., Van den Bos, A and Van der Mast, K.D. (1987) Ultramicroscopy, 21, 209.

Martinez, J.P., Locatelli, D., Balladore, J.L. and Trinquier, J. (1982) Ultramicroscopy, 8, 437.

Murata, Y., Fryer, J.R. and Baird, T. (1976) Nature, 263, No.5576, 401.

Murata, Y., (1978) In Electron Microscopy 1978 (Proc. 9th Intern. Cong. on Electron Microscopy, Toronto, 1978) ed. J.H. Sturgess Vol. 3, p.49.

Ramamurti, K., Crewe. A.V. and Isaacson, M.S. (1975) Ultramicroscopy, 1, 156.

Reimer, L. (1960) Zeitschrift Naturforschung, A, 15, 405.

Reimer, L. and Spruth, J. (1982) Ultramicroscopy, 10, 199.

Reimer, L. (1984) In " Transmission Electron Microscopy ", Springer Verlag, p 135.

Roberts, P.T.E. Chapman, J.N. and MacLeod, A.M. (1982) Ultramicroscopy 8, 385.

Rose, A. (1948) Advances in Electronics, I, 131.

Saxton, W.O., Smith, D.J. and Erasmus, S.J. (1983) J. Microsc. 130, 187.

Salih, S.M. and Cosslett, V.E. (1974) Physical Review, A9, 1041.

Siegal, B.M. (1972) Zeitschrift Natursforsch, A27, 325.

Smith, D.J., Camps, R.A., Freeman, L.A., O' Keefe, M.A., Saxton, W.O. and Wood, G.J. (1985) Ultramicroscopy 18, 63.

Smith, D.J., Fryer, J.R. and Camps, R.A. (1986) Ultramicroscopy 19, 279.

Thomas, L.E. (1984) In " Analytical Electron Microscopy 1984 ", San Francisco Press, Eds. Williams and Joy, D.C., p. 358.

Unwin, P.N.T. and Henderson, R. (1975) Journal of Molecular Biology, 94, 425.

Uyeda, N., Kobayashi, T., Ohara, M. and Harada, Y. (1972) Proceedings of the 5th European Congress on Electron Microscopy, The Institute of Physics, London, 566.

Uyeda, N., Kobayashi, T., Ishizuka, K. and Fujiyoshi, Y. (1978) Chemica Scripta, 14, 47.

Williams, R.C. and Fisher, H.W. (1970) Journal of Molecular Biology, 52, 121.

Uyeda, N., Kobayashi, T., Suito, E., Harada, Y. and Watanabe, M. J. (1970) J. Microscopie Electronique, Grenoble, 1, 23.

CHAPTER 3

Boersch, H. (1947) Zeitschrift Naturforsch, 2a, 615.

Butler, J.H. and Cowley, J.M. (1983) Ultramicroscopy, 12, 29.

Clark, W.R.K., Chapman, J.N., MacLeod, A.M. and Ferrier, R.P. (1980) Ultramicroscopy, 5, 195.

Colliex, C., Craven, A.J. and Wilson, C.J. (1977) Ultramicroscopy, 6, 71.

Colliex, C. and Mory, C. (1984) In " Quantitative Electron Microscopy ". Eds. Chapman, J.N. and Craven, A.J. SUSSP publications, Edinburgh, p 149.

Cowley, J.M. and Moodie, A.F. (1957) Acta Crystallographica, 10, 609.

Cowley, J.M. (1969) Applied Physics Letters, 15, No. 2, 58.

Cowley, J.M. (1976) Ultramicroscopy 2, 251.

Cowley, J.M. and Au, A.Y. (1978) Scanning Electron Microscopy I, SEM Inc., AMF O' Hare, Chicago, 53.

Cowley, J.M. and Spence, J.C.H. (1979) Ultramicroscopy 3, 433.

Crewe, A.V. and Wall, J. (1970) Journal of Molecular Biology, 48, 375.

Crewe, A.V. (1971) In " Electron Microscopy and Material Science ", Ed. Valdre, U, 162.

Dekkers, N.H. and de Lang, H (1974) Optik 44, 452.

Frank, J. (1973) Optik 38, 519.

Hawkes, P.W. (1984) In " Quantitative Electron Microscopy ", Eds. Chapman, J.N. and Craven, A.J. SUSSP publications, p.351.

Lynch, D.F. and Moodie, A.F. (1975) Acta Cryst, A31, 300.

Morrison, G.R. (1981) Ph.D. Thesis, University of Glasgow.

Rose, H. (1974) Optik, 39, 416.

Rose, H. (1977) Ultramicroscopy 2, 251.

Scherzer, O. (1949) J. Appl. Phys. 20, 20.

Su, Y. (1989) M.Sc. Thesis, University of Glasgow.

Zeitler, E. and Thomson, M.G.R. (1970) Optik 31, 258.

CHAPTER 4

Drummond, M.J., Chapman, J.N. and Nicholson, W.A.P. (1981) In Proc EMAG 81 Ed. Goringe, M.J. IOP Conf. Ser.61., p.11.

Drummond, M.J. (1985) Ph. D. Thesis, University of Glasgow.

Fryer J.R. (1980) J. Electron Microsc. 23, 79.

Harburn, G., Taylor, C.A. and Welberry, T.R. (1975) In " Atlas of Optical Transforms ", Camelot Press.

Howitt, D. (1976) Ph. D. Thesis, University of California, Berkely.

Kobayashi, T., Fujiyoshi, Y. and Uyeda, N. (1982) Acta Cryst., A38, 356.

Verma, A.R. (1953) In " Crystal Growth and Dislocations ", Butterworth Scientific Publications.

the 10th International Congress on Electron Microscopy, Hamburg 1, 217.

Glaeser, R.M. (1971) Journal of Ultrastructure Research, 36, 466.

Glaeser, R.M. (1975) In " Physical Aspects of Electron Microscopy and Microbeam Analysis ", Wiley, New York, Eds. Siegal, B.M. and Beaman, D.R., 205.

Grubb, D.T. and Groves, G.W. (1971) Philosophical Magazine, 24, 815.

Hall, T.A. and Gupta, B.L. (1974) J. Microsc, 100, Pt. 2, 177.

Hayward, S.B. and Glaeser, R.M. (1980) In " Electron Microscopy at Molecular Dimensions ", Eds. Baumeister, E. and Vogell, W. p. 226.

Herrman, K.H. (1984) : In " Quantitative Electron Microscopy ", Eds. Chapman, J.N. and Craven, A.J. SUSSP publications, Edinburgh, p 119.

Herrman, K.H. and Krahl, D. (1984) Adv. Opt, Electron Microsc. 9, 1.

Hobbs, L.W. (1979) In " Introduction to Analytical Electron Microscopy ", Eds. Hren, J.J. Goldstein, J.I. and Joy, D.C., Chapter 17.

Howitt, D.G., Thomas, G. and Toutolima, W. (1976) J. Appl. Phys. 47, 4.

Isaacson, M. Johnston, D. and Crewe, A.V. (1973) Radiation Research, 55, 205.

Isaacson, M. (1975) In " Physical Aspects of Electron Microscopy and Microbeam Analysis ", Wiley, New York, Eds. Siegal, B.M. and Beaman, D.R., 247.

Kessel, M., Frank. and Goldfarb, W. (1980) In " Electron Microscopy at Molecular Dimensions" Springer Verlag, Eds. Baumeister, W. and Vogell, W. p.154.

Kirkland, E.J., Siegal, B.M., Uyeda, N. and Fujiyoshi, Y. (1980) Ultramicroscopy, 5, 479.

Kobayashi, K. and Sakaoku, K. (1965) Laboratory Investigations, 14, No. 6, Pt. 2, 359.

Kobayashi, T., Murata, H. and Uyeda, N. (1982) Proceedings of the 10th

CHAPTER 5

Chapman, J.N. and Morrison, G.M. (1984) J. Microsc. Spectrosc. Electron. Vol. 9. 329.

Brown L.M. (1977) "Electron Microscopy and Analysis 1977", p 141 Ed.D.L. Misell (IOP: Bristol)

Rose, A. (1948) Advances in Electronics, I, 131.

CHAPTER 6

Bethe. H.A. (1930) Annalen de. Phys. 5, 325.

Berenyi, D and Hock, G. (1978) Jap. J. Appl. Phys 12(2) 78.

Chapman, J.N., Gray, C.C., Robertson, B.W. and Nicholson, W.A.P. (1983) X-ray spectrom 12 (4), 153.

Chapman, J.N., Nicholson, W.A.P. and Crozier, P.A. (1984) J. Microsc. 136, 179.

Cliff, G. and Lorimer, G.W. (1975) J. Microsc. 103, 203.

Egerton, R.F. (1980) J. Microsc, Vol 118, Pt. 4, 389.

Goldstein, J.I. (1979) In " Introduction to Analytical Electron Microscopy". Eds. Hren, J.J., Goldstein, J.I. and Joy, D.C. chapter 3, 83.

Gray, C.C., Chapman, J.N., Nicholson, W.A.P., Robertson B.W. and Ferrier, R.P. (1983) X-ray Spectrom. 12, 163.

Heinrich, K.F.J. (1987) In EMSA proceedings.

Khan, Md.R and Karami, M. (1980) X-ray Spectrom. 9, No 1, 32.

Langenberg, A. and van Eck, J. (1979) Journal of Physics B: Atomic and Molecular Physics 12, No 8, 1331.

Nicholson, W.A.P., Biddlecombe, W.H. and Elder, H.Y. (1982) J. Microsc. 126, 307.

Shuman, H., Somlyo, A.V. and Somlyo, A.P. (1980) In " Microbeam Analysis ", San Francisco Press Inc., Ed. Wittry, D.B.,275.

Vass, D. (1988) Private communication

CHAPTER 7

Chapman, J.N., Nicholson, W.A.P. and Crozier, P.A. (1984)
J. Microsc. 136, 179.

Clark, W.R.K., Chapman, J.N., MacLeod, A.M. and Ferrier, R.P. (1980)
Ultramicroscopy, 5, 195

Cliff, G. and Lorimer, G.W. (1975) J. Microsc. 103, 203.

Egerton, R. F.(1986) Electron Energy Loss Spectroscopy in the Electron Microscope, Plenum, New York, 324.

CHAPTER 8

Vesely, D. (1984) Ultramicroscopy, 14, 279.